Aeroelastic Modelling and Analysis of Highly Curved Composite Propeller Blades

P. M. van Veen

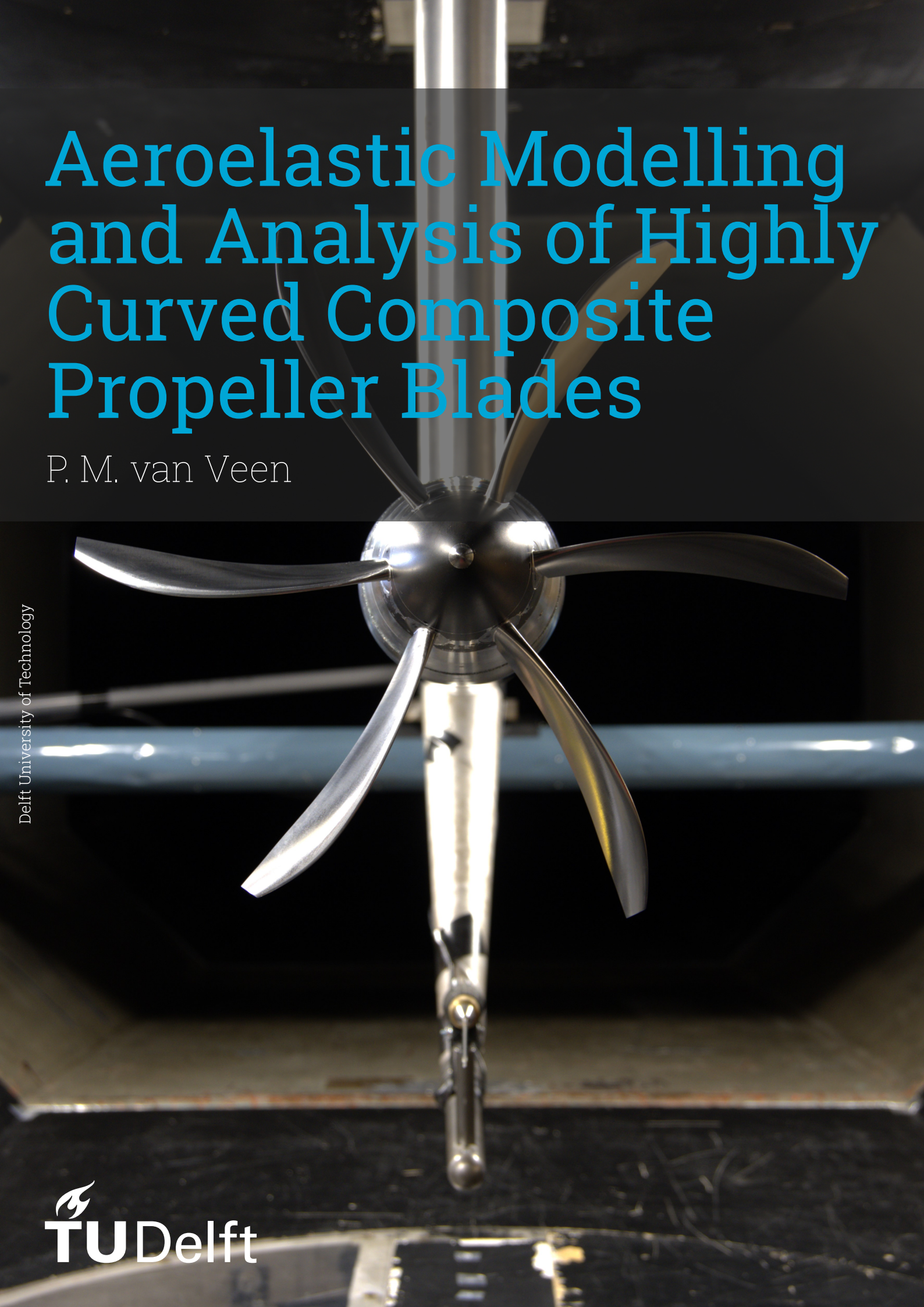

Delft University of Technology

TU Delft

Aeroelastic Modelling and Analysis of Highly Curved Composite Propeller Blades

by

P. M. van Veen

to obtain the degree of Master of Science
at the Delft University of Technology,
to be defended on Thursday, 27 November 2025, at 09:30 AM.

Student number:	4854594	
Project duration:	February, 2025 – November, 2025	
Thesis supervisors:	Dr. ir. T. Sinnige,	TU Delft
	Dr. J. Sodja,	TU Delft
Chairman:	Prof. dr. ing. G. Eitelberg,	TU Delft
Examiner:	Prof. dr. ir. R. de Breuker,	TU Delft

Cover: TUD-XPROP-Λ Propeller in the Low Turbulence Tunnel
by Tomas Sinnige

An electronic version of this thesis is available at http://repository.tudelft.nl/.

TU Delft

Preface

With the completion of this work, my time as a student at Delft University of Technology is nearly coming to an end. The past months have been challenging to say the least, and I am glad to say that it is almost finished. Now, the time has come to look back on this wonderful journey.

Three years ago, in the autumn of 2022, I could never have imagined that I would one day graduate as an Aerospace Engineer, because, at the time, I was deeply immersed in the field of theoretical physics. However, driven by long-lasting curiosity, and perhaps also by a lack of motivation to write a thesis in the field of Particle and Astrophysics, I made a last-minute decision to start studying in Delft, just in time to join midway through the academic year. Although joining the program without a bachelor's degree in Aerospace Engineering came with its challenges, looking back, it turned out to be one of the best decisions I could have made. After two more years of coursework, travelling with my girlfriend, and an internship at ASML, the moment I could no longer avoid arrived: it was time to start writing my Master's thesis.

At first, I was overwhelmed by the complexity of this project. I have to admit that progress during the first half was slower than I expected, and I would be lying if I said I didn't consider quitting this thesis multiple times. This was undoubtedly one of the toughest challenges of my life, but as my dad once told me: "The bigger the battle, the greater the feeling of victory". Therefore, after months of hard work, I am proud to present the results of my research. With that, it is time to thank the people who made all of this possible.

First of all, I would like to sincerely thank my supervisors, Tomas Sinnige and Jurij Sodja, for offering me this project and for their continuous guidance throughout. The journey has been challenging, with many ups and downs, particularly during the first half, and I could not have completed this work without your mentorship. Fortunately, I feel that things truly fell into place toward the end. I would also like to thank former TU Delft student Koen Prud'homme van Reine for sharing his wind tunnel test data, which greatly supported this work.

During this time, I had the pleasure to work alongside one of my closest friends, Sam, even though we were writing our theses in completely different fields of science. Sam, I would like to thank you for the countless enjoyable conversations we had during our many coffee and lunch breaks, the shared complaints about our theses, and the long hours we spent together in the library. Since we are both about to graduate, the time has come for us, after studying together for over ten years, to go our separate ways. I am excited to see what the future holds for each of us, and I hope our paths will continue to cross.

I am deeply grateful to my parents for their unconditional love and support, both financially and emotionally. I could not have come this far without either of you. You have given me the foundation to pursue my dreams, and I will always be grateful. Thank you from the bottom of my heart.

Lastly, and above all, I would like to thank my girlfriend, Iris. Thank you for your encouraging words during difficult times, for always believing in me, for your love, and simply for being there for me. Without you, I might have given up on this thesis countless times. I am grateful for everything you did to support me, in particular near the end of this project. Now that this chapter has come to an end, I look forward to enjoying our time together in our apartment, free from deadlines and stress. I am sure this new phase will bring us both joy, and I can't wait to share many new adventures with you.

Philip van Veen
Nijmegen, November 2025

Abstract

Propellers are a promising option for future sustainable aviation, as they can be powered by electric or hybrid-electric systems and, for a given thrust requirement, can achieve higher potential propulsive efficiency than ducted fans. This efficiency advantage comes from their ability to operate at larger diameters without incurring significant nacelle drag and weight penalties. The main challenge for propeller-driven aircraft is to reduce noise while maintaining high efficiency. Unlike turbofans, propellers lack a nacelle for acoustic liners, so noise reduction relies on optimization of blade geometry and operating conditions. Modern propeller designs therefore feature advanced sweep and lean distributions. Sweep is used to enhance both aerodynamic and acoustic performance by inducing destructive interference in noise signals and reducing aerodynamic losses associated with shock wave formation, thereby reducing noise emissions and enhancing efficiency. Lean, in turn, is introduced to alleviate the structural stresses that arise in swept blades. The objective of this work is to develop an aeroelastic analysis tool for propeller blades with sweep and lean, based on a low-fidelity aerodynamic model tightly coupled to a structural model, and to use this tool to study the effect of sweep and lean on the aerodynamic performance and structural response of composite propeller blades.

The aerodynamic loads were computed using blade element momentum (BEM) theory, which does not inherently account for sweep and lean. To include these effects, sweep was modelled by the quarter-chord alignment, while lean was represented by the face alignment. The corresponding sweep and lean angles were defined as the angles between these alignments and the pitch axis. A correction for sweep was applied to the BEM model, as it changes the orientation of the airfoils relative to the blade's rotational velocity. No correction was needed for lean, because it does not directly affect the airfoil orientation. The aerodynamic model was validated against experimental data for two baseline propellers: the unswept *TUD-XPROP* and the swept *TUD-XPROP-*Λ. While BEM tends to overestimate the aerodynamic performance of these blades, it accurately captures the trends in thrust as well as the sensitivity of thrust and efficiency to sweep. Additionally, both the experimental measurements and the BEM results indicated that, for the low freestream Mach number and modest sweep amplitude considered, the effects of sweep and lean on aerodynamic performance are limited.

Aeroelastic analysis was performed using *PROTEUS*, developed by TU Delft. Within this tool, the BEM model is tightly coupled to the structural model through sensitivities of the aerodynamic, centrifugal, and structural loads with respect to structural deformations. These aerodynamic sensitivities of the extended BEM model were analytically derived in this work to reduce computational cost. Comparison with numerical sensitivity computations confirmed that these analytical expressions accurately predict aerodynamic sensitivities in all required degrees of freedom. Compared to the loosely coupled method, which computes aerodynamic and structural loads iteratively, this tightly coupled approach reduced the computational time of the aeroelastic analysis by approximately 30%.

A parameter study was conducted to investigate the effects of sweep and lean on the aerodynamic performance and structural response of flexible propeller blades. Sweep was parametrized using scaled *TUD-XPROP-*Λ blades, while lean employed fully up- or downstream distributions. Flexible blades were first compared to rigid counterparts, showing that flexibility affects the thrust and power coefficients but has a minimal impact on peak aerodynamic efficiency, with differences typically within $\pm$0.3%. Next, the aerodynamic performance of flexible curved blades was compared to that of the straight blade under constant thrust coefficient T_C. Blades combining backward sweep with upstream lean achieved the highest efficiency, with gains up to 1.7%. Part of this efficiency gain, however, was attributed to the increased disk area of propellers with curved blades. Finally, the blades' structural response was assessed under constant thrust. Blades with backward sweep and upstream lean experienced most stress. The root bending moment was dominated by the moment about the x-axis, which could be reduced significantly by applying upstream lean. Additionally, analysis at doubled thrust showed that obtained values depend on operating conditions, which were not optimized, so emphasis should be on the trends rather than absolute values when interpreting the results of this work.

Nomenclature

Abbreviations

Abbreviation	Definition
BS	Backward Sweep
BE	Blade Element
BEM	Blade Element Momentum
CFD	Computational Fluid Dynamics
DL	Downstream Lean
FS	Forward Sweep
FPP	Flight Performance and Propulsion
LC	Loosely Coupled
LE	Leading Edge
LLT	Lifting-Line Theory
MDO	Multi-disciplinary Design Optimization
QC	Quarter-Chord line
RANS	Reynolds-Averaged Navier-Stokes
SB	Straight Blade
SQP	Sequential Quadratic Programming
TC	Tightly Coupled
TE	Trailing Edge
UL	Upstream Lean

Symbols

Symbol	Definition	Unit
C_P	Power coefficient ($C_P = P/(\rho_\infty n^3 D^5)$)	[-]
C_Q	Torque coefficient ($C_Q = Q/(\rho_\infty n^2 D^5)$)	[-]
C_T	Thrust coefficient ($C_T = T/(\rho_\infty n^2 D^4)$)	[-]
C_d	Sectional drag coefficient	[-]
C_l	Sectional lift coefficient	[-]
C_m	Sectional moment coefficient	[-]
C_p	Sectional pressure coefficient	[-]
C_q	Sectional torque coefficient	[-]
C_t	Sectional thrust coefficient	[-]
C_x	Sectional tangential force coefficient	[-]
C_z	Sectional axial force coefficient	[-]
D	Drag	[kg m s^{-2}]
D	Propeller diameter	[m]
E_k	Kinetic energy	[kg m^2 s^{-2}]
F	Prandtl tip-loss and root-loss factor	[-]
$\mathbf{F}$	Integrated force	[kg m s^{-2}]
F_{crit}	Tsai-Wu failure index	[-]
FA	Face alignment	[m]
FA^*	Normalized face alignment	[-]
J	Advance ratio	[-]
$\mathbf{K}$	Stiffness matrix	

Symbol	Definition	Unit
L	Lift	[kg m s^{-2}]
M	Mach number	[-]
M	Root bending moment	[kg m^2 s^{-2}]
$\mathbf{M}$	Integrated bending moment	[kg m^2 s^{-2}]
$\mathbf{M}$	Mass matrix	[kg]
MCA	Mid-chord alignment	[m]
N_b	Number of propeller blades	[-]
P	Power	[kg m^2 s^{-3}]
P_C	Power coefficient ($P_C = P/(\rho_\infty V_\infty^3 D^2)$)	[-]
Q	Torque	[kg m^2 s^{-2}]
Q_C	Torque coefficient ($Q_C = Q/(\rho_\infty V_\infty^2 D^3)$)	[-]
QCA	Quarter-chord alignment	[m]
QCA^*	Normalized quarter-chord alignment	[-]
R	Propeller tip radius	[m]
$\mathbf{R}$	Residual vector for aeroelastic calculations	
$\mathbf{R_{BEM}}$	Residual vector for BEM calculations	
$\boldsymbol{\mathcal{R}}$	Rotation matrix	[-]
Re	Reynolds number	[-]
S	Blade element planform area	[m^2]
T	Thrust	[kg m s^{-2}]
$\boldsymbol{\mathcal{T}}$	Transformation matrix	[-]
T_C	Thrust coefficient ($T_C = T/\rho_\infty V_\infty^2 D^2$))	[-]
V	Velocity	[m s^{-1}]
V_∞	Freestream velocity	[m s^{-1}]
Y	Blade span (undeformed blade)	[m]
Y_D	Blade span (deformed blade)	[m]
a	Axial induction factor	[-]
a'	Tangential induction factor	[-]
c	Local chord length	[m]
c_{air}	Speed of sound	[m s^{-1}]
$\mathbf{f}$	Forces and moments acting on structural node	
$\tilde{\mathbf{f}}$	Force acting on eccentric node	[kg m s^{-2}]
l	Blade element length	[m]
$\mathbf{m}$	Moment acting on structural node	[kg m^2 s^{-2}]
$\dot{m}$	Mass flow rate	[kg s^{-1}]
$\tilde{\mathbf{m}}$	Moment acting on eccentric node	[kg m^2 s^{-2}]
n	Propeller rotational speed	[s^{-1}]
$\mathbf{p}$	Momentum	[kg m s^{-1}]
$\mathbf{p}$	Structural deformation vector	[m, rad]
r	Propeller blade radial coordinate	[m]
$\mathbf{r}$	Radial vector	[m]
r'	Radial auxiliary variable	[m]
t	Time	[s]
x	Global x-coordinate	[m]
y	Global y-coordinate	[m]
z	Global z-coordinate	[m]
Λ	Sweep angle	[rad]
Ψ	Lean angle	[rad]
Ω	Angular velocity	[rad s^{-1}]
$\boldsymbol{\Omega}$	Rotor speed matrix	[rad s^{-1}]
α	Local angle of attack	[rad]
β	Blade twist angle	[rad]

Symbol	Definition	Unit
$\beta_{0.7R}$	Collective pitch angle	[rad]
γ	Lean angle (gradient-based)	[rad]
ϵ_P	Principal strain	[-]
ϵ_S	Shear strain	[-]
η	Propulsive efficiency	[-]
η	Sectional propulsor efficiency	[-]
η_i	Sectional induced efficiency	[-]
η_P	Propulsor efficiency	[-]
η_p	Sectional profile efficiency	[-]
θ	Blade pitch angle	[rad]
ξ	Sweep angle (gradient-based)	[rad]
ρ_∞	Ambient air density	[kg m^{-3}]
ζ	Angular auxiliary variable	[rad]
σ	Blade solidity	[-]
φ	Local flow angle	[rad]
ω	Rotor speed	[rad s^{-1}]

Subscripts

Subscript	Definition
∞	Freestream flow quantity
0	Incompressible quantity
a	Quantity related to aerodynamic loads
c	Quantity related to centrifugal loads
e	Quantity related to eccentric loads
eff	Effective quantity corrected for sweep or lean
root	Quantity at the blade root
s	Quantity related to internal structure
tip	Quantity at the blade tip

Superscripts

Superscript	Definition
BE	Quantity in Blade Element theory
M	Quantity in Momentum theory
flex	Quantity for flexible blade
rigid	Quantity for rigid blade
target	Target value

Contents

List of Figures

List of Tables

1

Introduction

Since the invention of jet engines, propeller-driven aircraft gradually gave way to jet aircraft, as mid-20th century aircraft design prioritized speed over efficiency [1]. To some, the use of propellers on aircraft may seem like a step back in both time and technology, but they have rapidly gained interest as sustainability is nowadays a main focus within the aviation industry. Instead of relying on fossil fuels, propellers can be powered by electric or hybrid-electric systems, which can reduce overall carbon emissions and help to minimize the environmental impact of aviation. This would be a major progression towards the net zero carbon emissions goal by 2050 [2]. Additionally, for a given thrust requirement, propellers can achieve higher propulsive efficiency than ducted fans because they can operate at larger diameters without significant nacelle drag or weight penalties.

The challenge with propeller-driven aircraft is not necessarily to enhance their propulsive efficiency, as they already offer the potential for high propulsive efficiency compared to jet engines, but to reduce noise production while maintaining this high efficiency. Especially around residential areas, noise pollution has become a more recognized problem resulting in tighter restrictions. Unlike commonly used turbofan engines, which have a nacelle to absorb acoustic energy using acoustic liners on their internal wall and chevrons at the trailing edge of the engine nozzle to reduce jet noise, propellers lack a casing for noise mitigation. As a result, reducing propeller noise relies heavily on optimization of both blade geometry and operational conditions. Recent propeller designs therefore feature complex geometries with sweep and lean to ensure both optimal aerodynamic and acoustic performance. Introducing sweep, for example, can reduce noise by inducing an acoustic phase shift along the blade span, leading to destructive interference in the noise signal [3]. Moreover, blade sweep lowers the effective Mach number, reducing aerodynamic losses due to shock wave formation and thereby improving the overall efficiency of the propeller [4].

While sweep offers aerodynamic and aeroacoustic benefits, it also introduces structural challenges that may negatively affect aerodynamic and structural performance [5, 6]. In particular, swept propeller blades experience increased bending moments and torsional loads which may lead to higher stresses and larger deformations. This effect can be mitigated by adding lean [6], which redistributes the loads along the span and can help to reduce the bending moments at the root. Therefore, sweep and lean should be viewed as complementary design features, where lean is used to counterbalance the unfavourable structural effects of sweep while still benefitting from the aeroacoustic advantages. Despite this, preliminary design studies often neglect the influence of lean, and focus mainly on sweep as the dominant geometric parameter. Such simplifications can lead to incomplete assessments of the propeller's aero-structural behaviour and may overlook valuable blade designs. Considering both sweep and lean together is therefore important to achieve realistic and well-balanced propeller blade designs.

This study investigates the combined effects of sweep and lean on both the aerodynamic performance and structural response of propeller blades. The objective is therefore to develop a low-fidelity aerodynamic model for blades featuring sweep and lean, couple it to a structural model, and analyse the aeroelastic behaviour of flexible blade designs. To accomplish this, the TU Delft aeroelastic analysis

tool developed by Rotundo et al. [7] is extended to enable analysis of arbitrary blade geometries. The extended framework is then applied to assess how curvature of propeller blades affects aerodynamic performance and structural behaviour, thereby providing insights into the aero-structural trade-offs associated with sweep and lean.

This chapter starts with a discussion on propulsive efficiency of propellers. Then, an overview of state-of-the-art research on sweep and lean is provided in section 1.2. It examines the latest advancements and applications of swept propellers designed for both improving the aerodynamic performance and reducing noise. Due to its importance for the performance evaluation of swept propeller blades, structural modelling is addressed in section 1.3. Next, section 1.4 identifies the existing gaps in current research and outlines the primary objectives of this study. The section also defines the research questions of this work to establish a clear framework for the subsequent chapters. Finally, the research outline is discussed in section 1.5.

1.1. Propeller Efficiency

It was stated without proof that the potential propulsive efficiency of propellers is higher than that of jet engines. A strong indication for this claim can be found in the current trend of modern turbofan engine development toward ever-higher bypass ratios, see Figure 1.1, which is defined as the ratio of the mass flow bypassing the engine core to the mass flow passing through it. In today's ultra-high bypass ratio engines, a large portion of the incoming air does not pass through the combustion chamber but instead flows around it, effectively mimicking the working principle of a propeller. The higher the bypass ratio, however, the larger the engine nacelle diameter must be, which in turn increases both the engine's drag and weight, potentially negating the efficiency gains from the increased bypass ratio [8]. To overcome these limitations, propeller-driven aircraft are often considered an alternative.

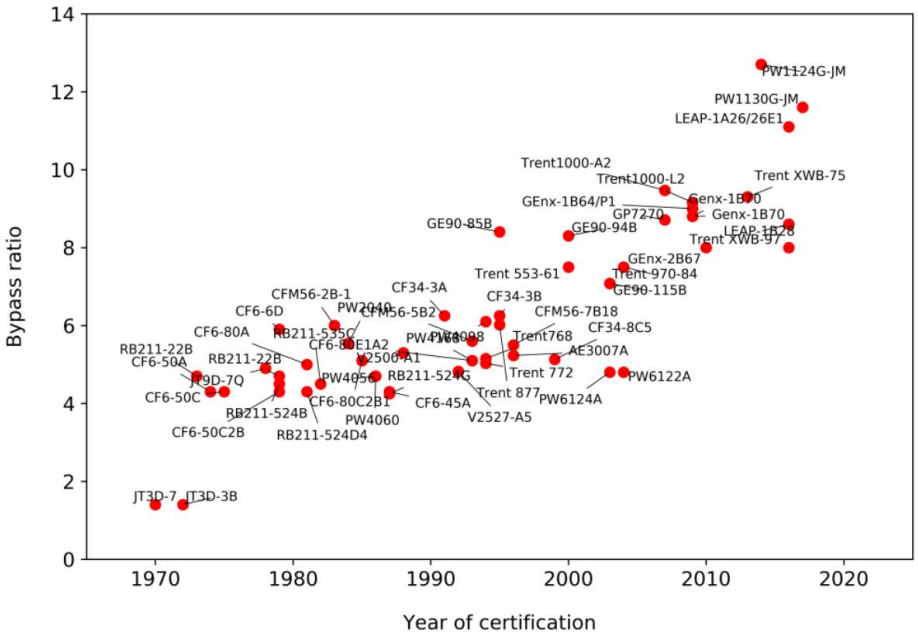

Figure 1.1: Bypass ratio trend of the past few decades [9].

To really understand the high efficiency potential of propellers, the governing equations should be examined. As with any force, thrust can be described by Newton's second law of motion, namely as the time derivative of momentum. Furthermore, the momentum gain of the aircraft is equal and opposite to the added momentum to the airflow, which implies that the thrust is proportional to mass flow through the propeller disk times the resulting change in velocity [10].

$$T = \frac{dp}{dt} = \dot{m}\Delta V \tag{1.1}$$

The propulsive efficiency is then defined as as the ratio of useful power output to the rate of kinetic energy added to the flow [10].

$$\eta = \frac{TV_\infty}{\Delta \dot{E}_k} = \frac{1}{1 + \frac{\Delta V}{2V_\infty}} \tag{1.2}$$

These expressions clearly illustrate why propellers are so efficient at propelling aircraft. To achieve the highest possible efficiency, $\Delta V/2V_\infty$ must be minimized. This means that ΔV, which is the velocity induced by the propeller, should be as small as possible. However, staying airborne requires a certain amount of thrust. So, according to Equation 1.1, a large mass flow is required, which explains the trend toward increasing bypass ratios observed over the past few decades. Unlike turbofan engines and ducted fans, propellers can satisfy these requirements because their diameter can be increased without significantly increasing weight and drag. As a result, propellers are capable of achieving higher propulsive efficiencies.

1.2. Review on Swept Propeller Blades

Already back in 1985, Miller et al. [3] developed a design tool to optimize propeller blade twist, chord and sweep distributions with respect to both fuel efficiency and noise levels. To predict the aerodynamic performance, a vortex lattice method was used within the optimization scheme. Even at that time, it was concluded that increasing the sweep angle had a big impact on the noise level reduction, while the aerodynamic performance was little affected.

In 2021, Geng et al. [11] developed a low-fidelity geometric optimization method using BEM theory that accounted for sweep. This model was used to optimize the sweep distribution of a rigid propeller blade for noise reduction while maintaining the aerodynamic efficiency. Sweep was modelled by the mid-chord alignment (MCA), represented by the mid-chord line of the blade in the plane of rotation. Using the dimensionless parameter MCA/R, the sweep distribution was compared between the optimized propeller blade and the original blade, see Figure 1.2. Lean, however, was not accounted for in this study.

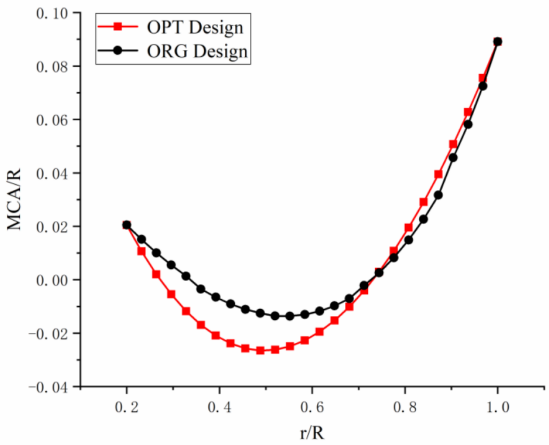

Figure 1.2: Mid-chord alignment distribution of the optimized (OPT) and the original (ORG) propeller blade [11].

The results indicate that the point of maximum sweep distribution has shifted radially inward. Furthermore, close to the root of the blade, the forward sweep has increased, while the tip remains backward-swept. In the end, due to this modified sweep distribution, the noise was reduced by 2.9 dB. Later, Geng et al. [12] also performed a multi-fidelity optimization by combining low-fidelity BEM theory with high-fidelity CFD simulations. Again, a noise reduction could be achieved by optimizing the blade sweep distribution, showing the importance of sweep for propeller design.

In that same year, Keil [13] studied the impact of blade sweep on aerodynamic and acoustic performance through a sensitivity study using 1000 swept propeller designs. Importantly, the study found

that, due to a favourable radial blade loading distribution, the most efficient configuration features a moderately forward-swept mid-segment and a backward-swept tip. It was further recommended to include a structural model for a more realistic evaluation of the propeller performance.

To highlight the importance and potential of propeller-driven aircraft once more, the IRON project is discussed. This initiative is part of the Clean Sky 2 program, which is a public-private partnership co-funded by the European Union that aims to improve the sustainability of European aviation [14]. IRON focuses on designing highly advanced propellers to reduce noise without affecting the aerodynamic performance [15]. Its goal was to reduce the near-field noise during cruise by 6 dB compared to a baseline design. Therefore, five propeller concepts were developed by IRON partners, but only two were selected for testing against the baseline in DNW's High-Speed Tunnel, see Figure 1.3. Both optimized propeller designs feature sweep and lean, but their exact distributions have not been made public. Although the 6 dB target was not reached, test data showed a noise reduction of approximately 5 dB at the measurement location and an estimated 5.5 dB at the position of aircraft fuselage [15].

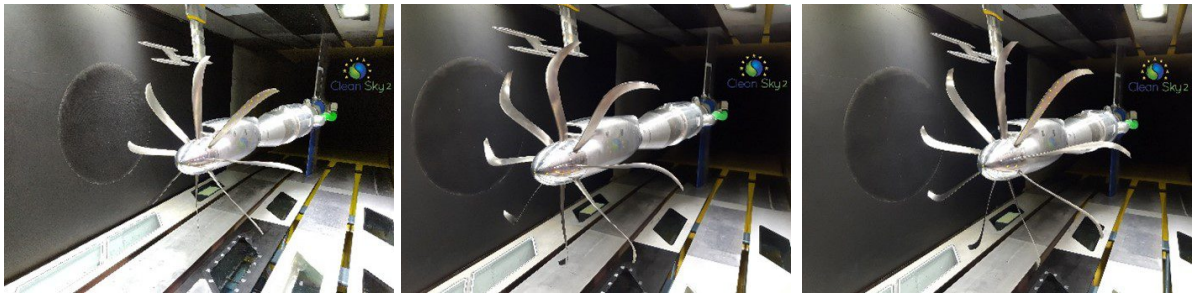

(a) Baseline propeller by Dowty Propellers.

(b) Propeller design by Cenaero.

(c) Propeller design by GE AAT Deutschland.

Figure 1.3: IRON propellers in the DNW High-Speed Tunnel [15].

Margalida et al. [16] developed a low-fidelity geometric optimization tool that integrates aerodynamics, aeroacoustics, and structural behaviour to design quiet and efficient propeller blades. Using this tool, TU Delft's reference propeller *TUD-XPROP* was first optimized for its aerodynamic performance by minimizing the energy consumption irrespective of the noise performance, and after for noise under a constrained power requirement. The study showed that although the performance curves may be offset, aerodynamic and acoustic trends were captured accurately, confirming the reliability of low-fidelity models for trend prediction. Despite sweep and lean were not optimized in this study, a version of this tool was later used to design a new propeller for TU Delft, called *TUD-XPROP-*Λ, which features increased sweep compared to *TUD-XPROP* [4]. These blades, however, do not include any lean. As both propellers will be used in this work, a side-by-side comparison is presented in Figure 1.4.

(a) *TUD-XPROP* [17].

(b) *TUD-XPROP-*Λ [4].

Figure 1.4: TU Delft reference propellers.

Following the research of Margalida et al. [16], Prud'homme van Reine [4] recently conducted wind tunnel tests on both *TUD-XPROP* and *TUD-XPROP-*Λ, commonly referred to as *XPROP* and *XPROP-*Λ, in the TU Delft's Low-Turbulence Tunnel, to study the impact of sweep on propeller performance experimentally. Even though the sweep distribution of *XPROP-*Λ was not optimized for aerodynamic performance, the results showed that its effect on the overall performance was limited. A comparison between their geometries is shown in Figure 1.5.

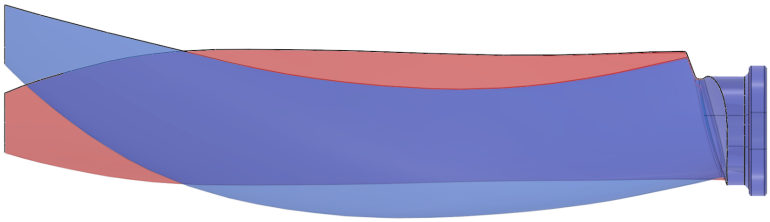

Figure 1.5: Comparison between the *XPROP* (red) and *XPROP-*Λ (blue) blade geometries [4].

In 2024, Thielen [6] published his work on the impact of structural deformations on the aerodynamic and acoustic performance of swept propellers. To this end, a parametric study was conducted by varying the sweep distribution of a baseline propeller, after which the aerodynamic, acoustic, and structural responses were analysed to reveal their interdependencies. The study showed that swept blades experience significant bending and torsional deformations. Centrifugal loads tend to straighten the blades, which causes both in-plane and out-plane bending due to their coupling, reducing the effective amount of sweep while introducing lean. Aerodynamic forces, on the other hand, were found to be the main cause of torsional deformations. Finally, Thielen [6] concluded that elasticity plays a critical role in the performance evaluation of highly swept propellers and suggested that introducing lean could help mitigate torsional deformations.

1.3. Structural Modelling

Given the importance of structural modelling for swept blades, some relevant research on this topic is reviewed. In 2014, Sodja et al. [5] developed a numerical model to predict the aerodynamic performance of flexible propeller blades with arbitrary blade axis geometry, meaning arbitrary sweep and lean distributions. Therefore, an extended BEM model was coupled to a structural solver, and blade axis geometry optimization was included as, for flexible blades, sweep and lean have a significant impact on the performance [5]. To validate the model, three blade designs were manufactured and tested experimentally, see Figure 1.6.

Figure 1.6: Forward-swept blade (FB), straight blade (SB) and backward-swept blade (BB) used for experimental investigation [5].

The study showed that the blade axis geometry has a large impact on its deformation. Backward-swept propeller blades were found to exhibit the most favourable deformation characteristics with varying advance ratio in terms of aerodynamic performance. In addition, Sodja et al. [5] concluded that propeller flexibility can enlarge the efficiency envelope significantly compared to rigid blades.

Möhren et al. [18] developed an aeroelastic model by coupling a BEM model to a Timoshenko beam model to predict the behaviour of flexible propellers. The study examined the influence of elasticity and blade sweep on aerodynamic performance, showing that both the structural properties and sweep significantly affect the performance due to torsion and bending. Composite propellers, in particular, were highlighted for their ability to provide design flexibility in tailoring structural characteristics.

To this end, Rotundo et al. [19] developed an aeroelastic optimization tool for structural tailoring of propeller blades with fixed geometry [7]. Similar to Möhren et al. [18], a BEM model was coupled to a Timoshenko model. Instead of iteratively computing aerodynamic and centrifugal loads along with the resulting structural deformation, the coupling was performed using gradients of these loads with respect to blade deformation. The tool was applied to a dual-role propeller to determine the optimal structure that minimizes the total energy consumption for a flight mission, including propulsive conditions during climb and cruise and regenerative conditions during descent. It was found that structural optimization of the flexible blade resulted in a better performance than the rigid blade for all test cases. The developed model, however, is limited to straight blades without significant sweep or lean.

1.4. Research Objectives

The presented state-of-the-art research, such as that by Geng et al. [11] and Bown et al. [15] showed the importance of blade sweep in designing future-proof propellers. Additionally Thielen [6], Möhren et al. [18] and Sodja et al. [5] have shown that structural modelling is essential when evaluating swept propeller blades. Lastly, Rotundo et al. [19] demonstrated the potential of aeroelastic tailoring to improve propeller blade performance.

Most of these studies, however, did not consider blade lean. Lean is expected to positively affect structural performance of swept blades [6], but its inclusion can also impact the aerodynamic performance due to changing blade deformations [5]. This gap in the current research motivates the work presented in this thesis.

In this study, TU Delft's aeroelastic tool developed by Rotundo et al. [19] will be extended to enable analysis of flexible propeller blades featuring both sweep and lean. The objective is to develop an aerodynamic model for swept and leaned propeller blades, to extend the tight coupling between the aerodynamic and structural model for computationally efficient aeroelastic analysis of such curved blade geometries, and to use this framework to study the effects of sweep and lean on the aerodynamic performance and structural behaviour of flexible propeller blades, with particular focus on the impact of introducing lean to swept blades. This research will therefore focus on the development of a low-fidelity, robust, and computationally efficient preliminary design tool. To achieve this objective, the following research questions have been formulated which will be examined in this report:

1. *How can the geometry and aerodynamics of propeller blades with sweep and lean be modelled?*
   (a) *How should sweep and lean be defined?*
   (b) *How can blade element momentum theory be extended to account for sweep and lean when predicting aerodynamic performance trends of swept propellers operating at low Mach numbers?*
2. *How can the aerodynamic and structural model be tightly coupled for propeller blades with sweep and lean?*
   (a) *Which aerodynamic sensitivities are required for tight aeroelastic coupling?*
   (b) *How can the required aerodynamic sensitivities be computed analytically?*
   (c) *How do the derived analytical sensitivities compare with numerically computed sensitivities?*

3. *What is the effect of combining sweep and lean on the aerodynamic performance and structural response of an isolated propeller?*
   (a) *How does the aerodynamic performance of flexible blades featuring sweep and lean compare to that of rigid blade designs?*
   (b) *What is the effect of sweep and lean on the aerodynamic performance of flexible blades compared to a straight blade?*
   (c) *How does lean influence the structural response of swept blades?*

The findings will facilitate aeroelastic analysis for swept and leaned propeller blades, paving the way for future advancements in preliminary aeroelastic design methods. Ultimately, this work will contribute to the development of highly efficient next-generation propellers, while ensuring manufacturability and practical applicability to aviation propulsion systems.

1.5. Research Outline

This work builds mainly upon the research of Rotundo et al. [19] by extending the model, hereafter referred to as *PROTEUS*, to include blade sweep and lean. Therefore, a precise understanding of the underlying geometric definitions is required, as addressed in chapter 2. This chapter provides two definitions for representing sweep and lean, along with two approaches to specify the blade's airfoil sections used in the aerodynamic model. The aerodynamic model itself is presented in chapter 3, which outlines the motivation for BEM theory and the mathematical details of its implementation. Since classical BEM models do not account for sweep and lean, correction factors are introduced to capture these effects. Finally, the extended BEM model is validated against experimental data from Prud'homme van Reine [4] for the *XPROP* and *XPROP*-Λ propellers.

Once the aerodynamic model is validated, the tight aeroelastic coupling is developed in chapter 4. This requires the gradients of the aerodynamic loads with respect to the blade deformation. Given the importance of computational efficiency in the preliminary design stage, these gradients are derived analytically and then validated against numerical calculations to ensure accuracy. The implementation of the tight aeroelastic coupling is verified by comparison with a loose coupling, and the computational times of both couplings are compared to highlight the efficiency of the tight coupling.

With the aeroelastic model fully developed, a parametric study of sweep and lean is conducted in chapter 5. To reduce the number of variables, these distributions are parametrized using Bézier curves. The study begins with a comparison between the aerodynamic performance of rigid and flexible blades to show the impact of structural deformation on the aerodynamic efficiency. It then proceeds to a more detailed analysis of flexible blades, investigating how variations in sweep and lean affect both aerodynamic performance and structural behaviour. The aerodynamic analysis examines the change in propulsor efficiency of the curved blades relative to that of a straight blade, which demonstrates how sweep and lean distributions can enhance overall performance. For the structural analysis, blade stresses and root bending moments are evaluated, showing how geometric tailoring can reduce stress levels and improve structural integrity. In addition, the effect of thrust on structural behaviour is examined to study how aerodynamic loading affects the results.

Finally, the conclusions of this work are presented in chapter 6, while its limitations and the recommendations for future work are outlined in chapter 7.

2

Geometric Modelling

This chapter provides a description how the geometry of a swept and leaned propeller blade is modelled. It defines the three-dimensional shape of the blade, including the sweep, lean, and twist distributions along the span, as well as the reference axes used. Additionally, the distinction between the aerodynamic grid and structural grid is explained.

2.1. Geometric Parameters

The geometry of a propeller blade is characterized by several key parameters that together describe its three-dimensional structure. In case of a straight blade propeller, the most fundamental geometric parameters are the chord, twist and airfoil shape distributions, and the diameter. Since these parameters define the blade's three-dimensional geometry, they also govern its aerodynamic performance.

The chord distribution affects the aerodynamic performance as variations in chord length affect the loading distribution of the propeller blade. The twist distribution controls the inflow angle of the airflow along the blade span and therefore has a significant impact on the aerodynamic forces as well. Note that the pitch angle is the sum of the local twist angle and the collective blade pitch, which, in this work, is defined as the angle between chord line at 70% of the quarter-chord line and the plane of rotation [20].

$$\theta(r) = \beta(r) + \beta_{0.7R} \tag{2.1}$$

The airfoil shape determines the cross-sectional lift-to-drag ratio, which has a strong impact on the aerodynamic efficiency. Finally, the diameter sets the overall propeller size and therefore its thrust capability. All of these quantities are typically specified as spanwise distributions, which allows them to vary along the blade length in order to achieve an optimal balance between thrust, efficiency, and structural requirements, while remaining within the imposed design constraints.

For swept and leaned propeller blades, however, two additional parameters are required to fully describe the geometry. Typically, sweep and lean are defined in terms of alignments, as in the study by Geng et al. [11]. These alignments represent offsets of the propeller's reference line relative to the global spanwise coordinate axis. In this work, the global coordinate system is defined such that the z-axis is aligned with the propeller's axis of rotation, meaning that the entire blade rotates around the z-axis during flight. The y-axis is oriented in spanwise direction of the blade, such that it aligns with the pitch axis of the blade. Lastly, the x-axis is defined perpendicular to both the y- and z-axis, and positive toward the trailing edge of the blade. Furthermore, the quarter-chord line is chosen as reference line, because it approximately coincides with the airfoil's aerodynamic centre [21], which makes it a natural reference line for evaluation of the aerodynamic loads.

The sweep alignment is defined as the offset of the quarter-chord line from the global y-axis in x-direction, as illustrated in Figure 2.1, while lean corresponds to the offset in the z-direction. In other words, sweep represents the tangential displacement and lean the axial displacement. These offsets are referred to as the quarter-chord alignment (QCA) and the face alignment (FA), respectively, and

are also specified as spanwise distributions along the blade. The QCA and FA effectively describe the x- and z-coordinates of the quarter-chord line, which provides a straightforward and convenient three-dimensional representation of the blade's reference line.

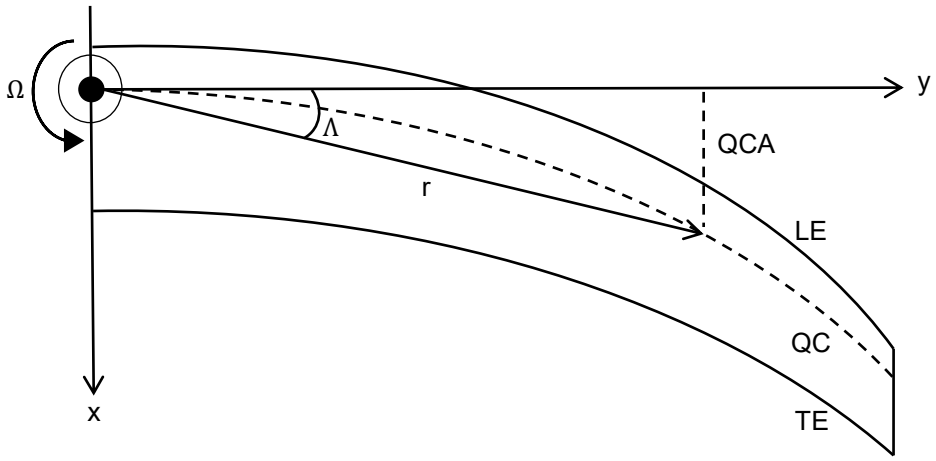

Figure 2.1: Quarter-chord alignment and sweep angle for a backward swept propeller blade.

Instead of specifying sweep and lean as geometric offsets, it is sometimes more convenient to express them as angles. As illustrated in Figure 2.1, the sweep angle is defined as the angle between the global y-axis and the vector pointing towards the quarter-chord line projected onto the xy-plane. Similarly, the lean angle is defined as the angle between the global y-axis and the vector to the quarter-chord line within the yz-plane.

$$\Lambda \coloneqq \arctan\left(\frac{QCA}{y}\right) \tag{2.2}$$

$$\Psi \coloneqq \arctan\left(\frac{FA}{y}\right) \tag{2.3}$$

2.2. Geometry Definition

The geometry of a propeller blade can be defined in several ways. For straight blades, airfoil sections are typically taken as cross-sections perpendicular to the blade axis, meaning they are all aligned and parallel to each other. This approach, however, cannot be directly applied to swept blades. Because the blade axis is curved, the airfoil sections cannot simultaneously be aligned with each other and perpendicular to the axis. Nevertheless, one of the two conditions can still hold. The first approach, in which all airfoil sections are kept perpendicular to the pitch axis and thus remain parallel to each other, as illustrated in Figure 2.2, is referred to in this work as the parallel airfoil description. The second approach defines the airfoil sections perpendicular to a chosen blade axis, also called the formation line [22]. This requires a rotated airfoil orientation to follow the curved blade axis, as shown in Figure 2.3, and is therefore referred to as the rotated airfoil description.

Swept propeller blades described by parallel airfoils have all their considered airfoil sections aligned with the global xz-plane, see Figure 2.2. Although this makes their geometry description somewhat similar to that of a straight blade, the key difference is that due to the curved quarter-chord line, the effective inflow direction experienced by the blade due to rotation is different. Consequently, this description requires a correction for the rotational velocity component.

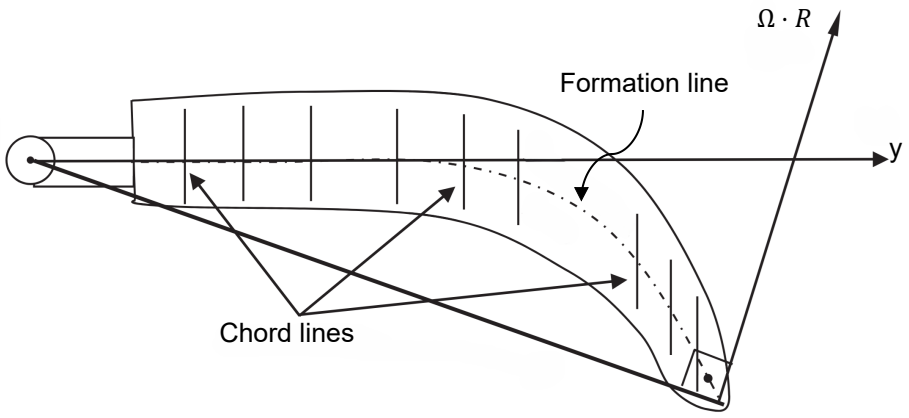

Figure 2.2: Swept propeller blade with parallel airfoil sections (adapted from [22]).

As mentioned already, the rotated airfoil description does not have airfoil sections that are parallel to each other. Instead, the airfoils are oriented perpendicular to the blade's formation line, see Figure 2.3. In section 2.1, the geometric parameters are defined with respect to the quarter-chord line, effectively making it the formation line.

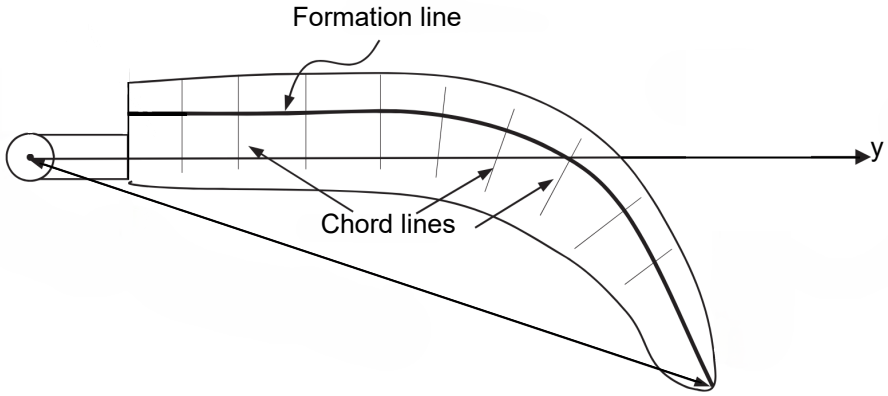

Figure 2.3: Swept propeller blade with rotated airfoil sections (adapted from [22]).

Due to the airfoil's rotation, using only Equation 2.2 and Equation 2.3 is no longer sufficient to construct the blade geometry. Since the airfoils must be oriented perpendicular to the quarter-chord line, the gradients of the QCA and FA with respect to their spanwise position are required to determine their correct orientation. The local angles that correspond to these gradients are given by Equation 2.4 and Equation 2.5. So, for the rotated airfoil description, the angles Λ and Ψ are required to construct the quarter-chord line in three-dimensional space, while the angles γ and ξ ensure that each airfoil section is correctly oriented perpendicular to this line. Note that all four angles can be expressed in terms of the quarter-chord alignment and face alignment.

$$\gamma_i = \arctan\left(\frac{QCA_{i+1} - QCA_i}{y_{i+1} - y_i}\right) \tag{2.4}$$

$$\xi_i = \arctan\left(\frac{FA_{i+1} - FA_i}{y_{i+1} - y_i}\right) \tag{2.5}$$

To construct the three-dimensional propeller blade shape, rotation matrices can be used to adjust the airfoil orientation of each blade element according to the prescribed twist, sweep, and lean distributions. Twist is applied as a rotation around the y-axis, while sweep and lean are applied as rotations around the z-axis and x-axis, respectively [22].

$$\boldsymbol{\mathcal{R}_\beta} = \begin{bmatrix} \cos(\beta) & 0 & \sin(\beta) \\ 0 & 1 & 0 \\ -\sin(\beta) & 0 & \cos(\beta) \end{bmatrix} \tag{2.6}$$

$$\boldsymbol{\mathcal{R}_\gamma} = \begin{bmatrix} \cos(\gamma) & -\sin(\gamma) & 0 \\ \sin(\gamma) & \cos(\gamma) & 0 \\ 0 & 0 & 1 \end{bmatrix} \tag{2.7}$$

$$\boldsymbol{\mathcal{R}_\xi} = \begin{bmatrix} 1 & 0 & 0 \\ 0 & \cos(\xi) & -\sin(\xi) \\ 0 & \sin(\xi) & \cos(\xi) \end{bmatrix} \tag{2.8}$$

Finally, the total transformation matrix, which ensures the correct perpendicular orientation of the airfoils along the entire quarter-chord line, is obtained by multiplying the individual rotation matrices. Since rotation matrices are non-commutative, the multiplication order can impact the resulting orientation significantly. Therefore, it is essential to apply them consistently in the same order to avoid unintended deviations.

$$\boldsymbol{\mathcal{T}} = \boldsymbol{\mathcal{R}_\beta} \cdot \boldsymbol{\mathcal{R}_\gamma} \cdot \boldsymbol{\mathcal{R}_\xi} \tag{2.9}$$

In this work, the parallel airfoil description was selected for two reasons. The first and most important reason is that it enabled straightforward validation of the aerodynamic model developed in chapter 3. Experimental performance data is available for the *XPROP* and *XPROP-*Λ propeller blade geometries, see Appendix A, including lift and drag polars for its airfoil sections taken parallel to each other. Using the rotated airfoil description would have required generating new airfoil polars, because the blade cross-sections perpendicular to the quarter-chord line can deviate significantly from those parallel to each other for blades with steep sweep or lean gradients. This would have introduced significant additional complexity and effort, which could not be accommodated within the limited time frame of this project. Second, the rotated airfoil description causes the aerodynamic planform area to overlap when considering propeller blades with steep sweep or lean gradients. A highly curved quarter-chord line causes large rotations of the perpendicular airfoil sections, which may result in overlap when the discretization of the aerodynamic grid is fine, see section 2.3. This complicates both the geometric representation of the blade as well as the aerodynamic modelling. Together, these considerations made the parallel airfoil description the most practical choice for the objectives of this work.

2.3. Aerodynamic and Structural Discretization

Finally, the blade geometry in *PROTEUS* is discretized into two separate grids: the aerodynamic grid and the structural grid. Their distinction is important, as they serve fundamentally different purposes within the aeroelastic framework.

As the name suggests, the aerodynamic grid is used to resolve the aerodynamic loading acting on the blade. It defines the discrete locations along the quarter-chord line at which aerodynamic forces and moments are evaluated, based on the blade's airfoil geometry and local flow conditions. The loads computed at these points can be integrated along the blade span to determine the overall aerodynamic performance of the propeller.

In contrast, the structural grid represents the discretization of the blade for structural analysis. To establish this grid, a reference line which is called the structural axis, must be defined. For convenience, the structural axis is taken as the quarter-chord line in this work, although in principle any other line could equally be selected without loss of generality. Consequently, the structural axis is aligned with the aerodynamic axis. However, because the aerodynamic and structural grids serve different purposes, they are discretized independently, meaning that their nodes do not coincide.

The blade structure is then modelled using linear Timoshenko beam elements, where each element is defined by two end nodes and assumes uniform properties along its length [23]. Each node has six

degrees of freedom, three translational and three rotational, while an additional eight internal degrees of freedom describe deformations at any point along the element [24]. This results in a total of twenty degrees of freedom per beam element. Since loads can only be applied at the nodes and not within the interior of a beam element [23], this work focuses on the twelve degrees of freedom associated with these nodes. These degrees of freedom are defined relative to the local coordinate system of the structural axis. For each blade element, this local system is oriented such that the y-axis follows the spanwise direction tangential to the structural axis, the x-axis aligns with the local chord line pointing toward the blade's trailing edge, and the z-axis is perpendicular to the other two axes, pointing downward [23]. This static structural model allows the structural grid to capture both the deformation and load transfer characteristics of the blade, in contrast to the aerodynamic grid, which only captures the aerodynamic forces acting on its nodes. For a more detailed discussion on the structural modelling of *PROTEUS*, the reader is referred to [24].

3

Aerodynamic Modelling

This chapter provides an overview for aerodynamic modelling of propeller blades. First, the basic expressions to express propeller performance are provided. Then, the selection procedure for the aerodynamic model used in this study is discussed in section 3.2. Finally, the selected aerodynamic model is explained in more detail and validated against experimental data.

3.1. Propeller Performance Theory

The fundamental purpose of an aircraft propeller is to generate thrust by acceleration of air, effectively converting rotational kinetic energy into translational kinetic energy. This process relies on aerodynamic principles that are largely analogous to those of aircraft wings. For a propeller cross-section, the underlying velocities and blade loading of these aerodynamic principles are illustrated in Figure 3.1.

As a propeller rotates, the pressure difference across the airfoil generates lift and drag. These forces can be decomposed into thrust and a component of aerodynamic force contributing to torque, which act parallel and tangential to the propeller's axis of rotation, respectively. Thrust produces the forward motion of the aircraft, whereas torque represents the rotational moment required to generate this thrust [25]. Additionally, Figure 3.1 highlights the induced axial and tangential velocities resulting from the flow acceleration. Due to this acceleration, the axial velocity increases and can no longer be described solely by the freestream velocity. Similarly, the tangential velocity decreases, causing it to deviate from the purely rotational velocity [25]. To capture these effects, so-called induction factors are introduced, which are essential parameters for evaluation of the aerodynamic blade loading and performance.

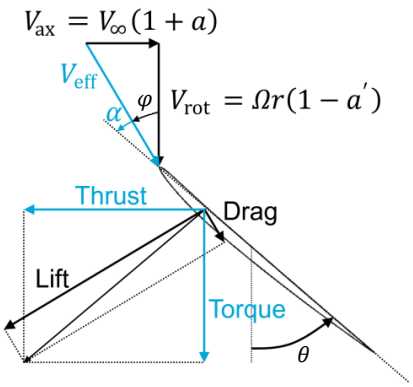

Figure 3.1: Velocities and blade loading of a swept propeller blade cross-section (adapted from [25]).

The performance of a propeller is often expressed in non-dimensional numbers, which serve as a powerful tool for comparing the performance of propellers across different sizes and operating conditions.

Commonly used non-dimensional numbers are the thrust coefficient C_T, power coefficient C_P and torque coefficient C_Q, which relate thrust, power and torque to the propeller's size and rotational speed [26].

$$C_T = \frac{T}{\rho_\infty n^2 D^4} \tag{3.1}$$

$$C_P = \frac{P}{\rho_\infty n^3 D^5} \tag{3.2}$$

$$C_Q = \frac{Q}{\rho_\infty n^2 D^5} \tag{3.3}$$

Alternatively, thrust, power, and torque can be normalized using the freestream velocity instead of the rotational speed, producing the coefficients T_C, P_C and Q_C, which are directly related to the disk loading. Thus, using this normalization, propellers that operate under the same inflow conditions and disk loading T/D^2 will have the same T_C, even when their rotational speeds differ.

$$T_C = \frac{T}{\rho_\infty V_\infty^2 D^2} \tag{3.4}$$

$$P_C = \frac{P}{\rho_\infty V_\infty^3 D^2} \tag{3.5}$$

$$Q_C = \frac{Q}{\rho_\infty V_\infty^2 D^3} \tag{3.6}$$

Likewise, the operating condition of a propeller is typically expressed in terms of the non-dimensional advance ratio, which relates the forward speed of the aircraft to the propeller's rotational speed at the blade tip. Put differently, it represents the forward distance travelled during one revolution of the propeller, normalized by its diameter.

$$J = \frac{V_\infty}{nD} \tag{3.7}$$

Finally, the propulsor efficiency is defined as the ratio of the generated thrust power to the total power of the propeller, which can be expressed in terms of the thrust and power coefficients, see Equation 3.8. This differs from the propulsive efficiency defined in Equation 1.2, as the propulsor efficiency includes losses at the rotor, like drag, while the propulsive efficiency accounts only for losses associated with the axial acceleration of the flow behind the propeller [4]. Maximizing the propulsor efficiency is crucial to achieve the most fuel-efficient operation under given propulsive conditions.

$$\eta_P = \frac{V_\infty T}{P} = \frac{J C_T}{C_P} \tag{3.8}$$

3.2. Review on Blade Element Momentum Models

Aerodynamic modelling is important for the aeroelastic analysis of a propeller design, because its accuracy has significant impact on the overall outcome of the study [27]. It depends on the accuracy required, computational resources available, and the stage of design, what fidelity level of aerodynamic modelling is applied. Low-fidelity models, based on simplified theoretical approaches [28], offer rapid assessments but they lack the precision required for final design evaluations. High-fidelity models on the other hand, use advanced numerical techniques and require significant computational power to capture detailed fluid dynamics. This makes them suitable for final design evaluation, but less practical for high-iteration preliminary design studies.

Blade element (BE) models are the most widely used low-fidelity aerodynamic models due to their simplicity and reasonable accuracy. In brief, BE theory divides the rotor blades into spanwise elements where the aerodynamic loads are computed for each segment based on local flow angles and induced velocities. The required lift and drag polars typically rely on empirical data. However, since the induced velocity is generally unknown in BE models, they must be coupled with an additional aerodynamic model to supply this information [28]. Therefore, BE models alone cannot fully provide the aerodynamic loading.

Blade element models are often coupled with momentum theory, also called actuator disk theory, which assumes that a propeller can be described by an infinitely thin disk divided into concentric annuli [29]. This rotor disk inserts momentum into the flow which causes a pressure jump that is related to the induced velocity. Unsurprisingly, the combination of the blade element model with momentum theory is called blade element momentum (BEM) theory. BEM theory iteratively couples the two approaches to determine the induced velocity and subsequently calculates the forces, moments, and power generated by the rotor. Since the wake is not resolved in BEM theory, tip-loss factors are applied for the results to be more accurate [30].

Ismail et al. [31] compared BEM theory and lifting-line theory (LLT) for a small wind turbine, which can be considered as a large propeller operating under negative thrust, using two different rotor airfoils: *Gottingen GO 398* and *Joukowski J 0021*. Their analysis assessed both aerodynamic performance and computational efficiency. The power coefficient varied by 4.4% and 6.3% between the two methods for the wind turbines with the *Gottingen GO 398* airfoil and the *Joukowski J 0021* airfoil, respectively. BEM theory overpredicted the aerodynamic performance compared to LLT due to the neglected wake effects. Although LLT required less iterations to reach convergence, its computational time was significantly higher. For the turbine with the *Gottingen GO 398* airfoil, the computational times of the simulations were 149.32 s for BEM theory and 1007.7 s for LLT, while for the *Joukowski J 0021* airfoil, they were 17.31 s and 580.3 s, respectively. This study therefore highlights the efficiency advantage of BEM theory over LLT, as it offers significantly lower computational costs while it maintains comparable performance accuracy.

Since the focus of this study is on propeller analysis during the preliminary design phase, minimizing computational cost is crucial. Aeroelastic procedures typically require many iterations to find convergence, making it crucial to minimize the computational time of the aerodynamic analysis during each iteration. Since BEM theory offers a significantly lower computational time compared to LLT while it maintains reasonable accuracy, it is the preferred aerodynamic model for this study. However, classical BEM theory, as often used for performance calculations of straight propeller blades, does not inherently account for sweep and lean. Therefore, several attempts have been made in the past to extend classical BEM theory to accurately model swept propeller blades.

In 2008, Rosen et al. [32] developed an extended BEM model by adding a radial velocity term to account for radial velocity variations enabling sweep modelling. Similar as in chapter 2, the local sweep angle was defined with respect to the quarter-chord line of the blade. Burger [33] implemented this extended BEM theory and validated the model for three randomly swept blade designs, as shown in Figure 3.2. It was concluded that the alignment between BEM and CFD is reasonable for Design 1 and Design 3. Design 2, however, shows larger discrepancies due to its lean which was not accounted for.

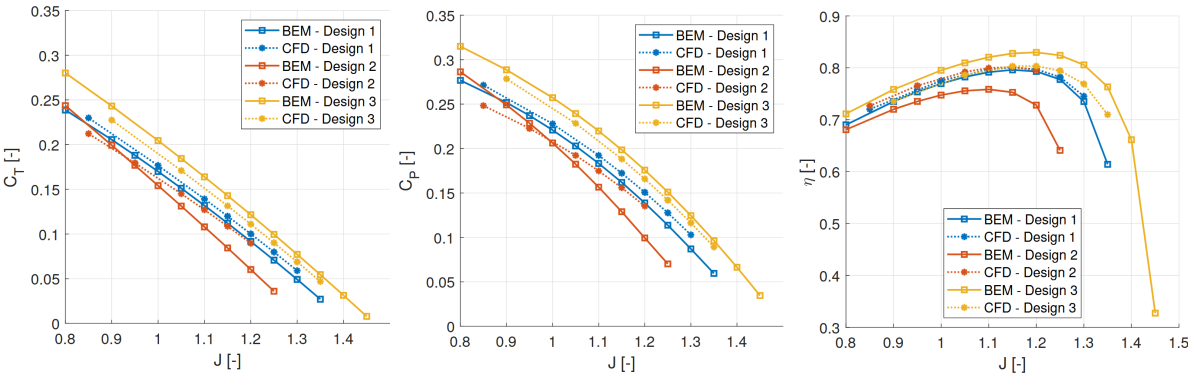

(a) Thrust coefficient. **(b)** Power coefficient. **(c)** Efficiency.

Figure 3.2: Comparison between extended BEM theory by Rosen et al. [32] and RANS CFD for three randomly swept rigid blade designs [33].

Geng et al. [11] also developed an aerodynamic model that accounts for sweep, by extending the BEM model from Liu et al. [34]. Instead of defining the sweep relative to the quarter-chord line, the mid-

chord line was used as the reference, as this is the input required by the noise model of Hanson [35] used for predicting the far-field noise emissions from the propeller. This extended BEM model was validated through experiments for a six-bladed propeller with a maximum sweep angle of $MCA/R \approx 0.09$, see Figure 1.2. The results are presented in Figure 3.3. Since only high advance ratio values were considered during their optimization procedure, Geng et al. [11] concluded that their BEM theory was sufficiently accurate.

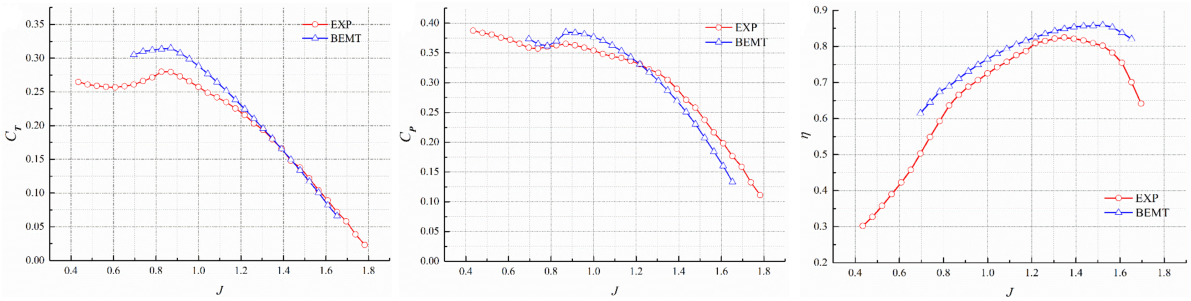

(a) Thrust coefficient. **(b)** Power coefficient. **(c)** Efficiency.

Figure 3.3: Comparison between extended BEM theory of Geng et al. [11] and experimental measurements.

The two previous methods only accounted for in-plane sweep angles, relative to the plane of rotation. As discussed previously, Sodja et al. [5] developed a BEM model capable of handling arbitrary geometries, including lean. The three propeller blade geometries shown in Figure 1.6 were experimentally tested and the results were compared with the predictions from the extended BEM model in Figure 3.4. Although there are noticeable differences between the model predictions and the experimental measurements, the overall trends remain similar.

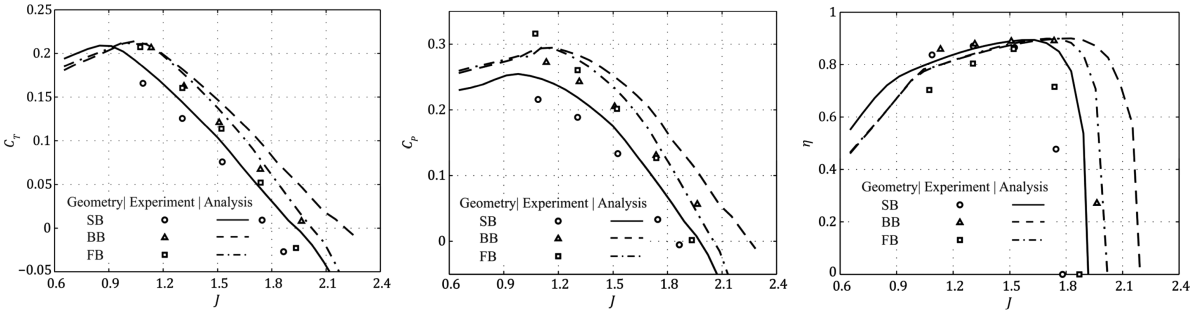

(a) Thrust coefficient. **(b)** Power coefficient. **(c)** Efficiency.

Figure 3.4: Comparison between extended BEM theory of Sodja et al. [5] and experimental test results for three flexible propeller blades.

Finally, Bergmann et al. [36] examined various sweep corrections for blade element models and compared the results with RANS CFD simulations. Initially, the models were tested for an unswept blade to assess the capabilities, followed by an evaluation of swept blades. From this analysis, two noteworthy conclusions were reached. First, when evaluating swept propeller blades with BE theory, it is essential to correct the local tangential velocity to account for the changed inflow direction at the blade element. Second, the results showed good agreement with RANS CFD simulations for sweep offsets of up to 25% of the blade span.

To conclude, reasonable agreement for BEM with sweep was found in studies like [33, 11, 5], where each of these aerodynamic models has been validated using either experimental test results or high-fidelity CFD simulations. These models typically overpredict the aerodynamic performance of swept propeller blades due to the neglected wake effects, but their predictions generally exhibit similar trends

to experimental results and CFD simulations. Additionally, Bergmann et al. [36] showed that if sweep corrections are taken into account by the model, reasonable results can be generated for sweep offsets of up to 25% of the blade span. Due to this balance between accuracy and low computational cost, the extended BEM model is selected for the aerodynamic analysis in the optimization framework of this study.

3.3. Blade Element Momentum Theory

The BEM model used in this work is based on the model developed by Adkins et al. [37]. The mathematical formulation underlying this model will be summarized briefly, but for a more detailed explanation, the reader is referred to the Master's thesis of Rotundo [23]. Additionally, the model is extended to account for the effects of blade sweep and lean.

Momentum theory models the propeller as an infinitely thin disk that generates thrust by adding momentum to the flow, resulting in an increase in total pressure and flow velocity. According to the principle of conservation of mass, the cross-sectional area of the streamtube must decrease accordingly, see Figure 3.5. In this figure, the velocity increase induced by the propeller is expressed in terms of the non-dimensional induction factor.

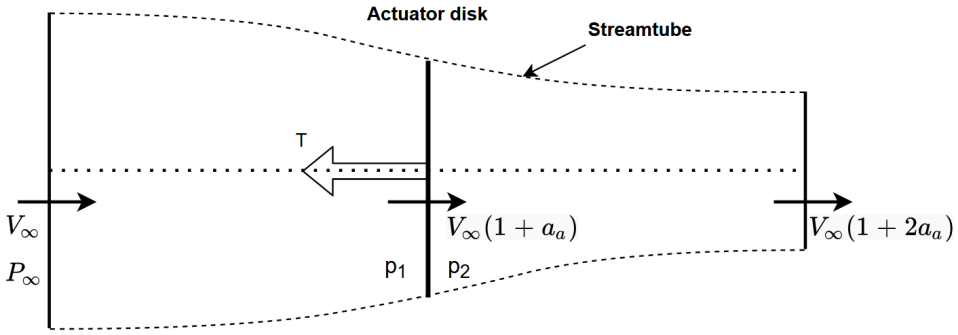

Figure 3.5: The streamtube of a propeller as modelled by Momentum theory [20].

By applying the principle of conservation of momentum, the thrust force acting on the flow can be related to the change in momentum and, consequently, the change in velocity [37].

$$C_t^M(r) = 4a(1+a) \tag{3.9}$$

Similarly, an expression for the torque coefficient can be derived.

$$C_q^M(r) = 4a'(1+a)\frac{\omega r}{V_\infty} \tag{3.10}$$

Note that these expressions depend on the radius as the induction factor varies radially along the blade span. To account for this variation, the propeller disk is divided into a finite number of annular sections. The coefficients are then computed individually for each annulus, which allows for a more accurate computation of the aerodynamic loads.

In order to compensate the momentum losses at the tip and the root of the propeller blade due to the local reduction in circulation, a tip-loss and root-loss factor are applied to the thrust and torque coefficient. Several loss factors have been proposed in literature [38], but the expressions selected for this work are those from Prandtl, as these offer a reasonable level of accuracy at low computational cost [23].

$$F_{\text{tip}} = \frac{2}{\pi}\arccos\left(\exp\left(-\frac{N_b}{2}\cdot\frac{r_{tip}-r}{r|\sin\varphi|}\right)\right) \tag{3.11}$$

$$F_{\text{root}} = \frac{2}{\pi}\arccos\left(\exp\left(-\frac{N_b}{2}\cdot\frac{r-r_{root}}{r_{root}|\sin\varphi|}\right)\right) \tag{3.12}$$

$$F = F_{\text{tip}} \cdot F_{\text{root}} \tag{3.13}$$

Lastly, a correction is applied for large negative axial induction factors, as developed by Buhl [39], to correct for the non-physical flow reversal that occurs in the propeller wake for axial induction factors of -0.5 and below [23]. Since these negative induction factors correspond to negative thrust, the correction is only applied when the propeller operates under negative thrust conditions. The final expressions of the thrust and torque coefficient in momentum theory are given by Equation 3.14 and Equation 3.15.

$$C_t^M(r) = \begin{cases} 4a(1+a)F, & \text{if } a \geq -0.326 \\ (1.39(1+a) - 1.816)F, & \text{otherwise} \end{cases} \tag{3.14}$$

$$C_q^M(r) = 4a'(1+a)\frac{\omega r}{V_\infty}F \tag{3.15}$$

These expressions for the coefficients, however, do not provide sufficient information to assess propeller performance, as the axial and tangential induction factors remain unknown. To address this, Blade Element theory is used to close the aerodynamic model. Similar to Momentum theory, an expression for the thrust and torque coefficient can be derived within the framework of Blade Element theory.

Again, the propeller blades are divided into several elements along the blade span. The difference is that for each element, the thrust and torque acting on the blade are now related to the lift and drag forces through decomposition of these forces into normal and tangential forces acting on the blade with respect to the plane of rotation. This decomposition, represented by the two-dimensional rotation matrix, can be derived from Figure 3.1 and is given below.

$$\begin{bmatrix} C_z \\ C_x \end{bmatrix} = \begin{bmatrix} \cos(\varphi) & -\sin(\varphi) \\ \sin(\varphi) & \cos(\varphi) \end{bmatrix} \cdot \begin{bmatrix} C_l(\alpha, Re) \\ C_d(\alpha, Re) \end{bmatrix} \tag{3.16}$$

The thrust and torque coefficient for Blade Element theory are then expressed in terms of these force coefficients, the blade solidity and the local flow velocity [37]. Note that the sectional lift and drag coefficients in Equation 3.16 are computed using empirical polar data depending on the angle of attack and the Reynolds number.

$$C_t^{BE}(r) = C_z\sigma(r)\left(\frac{V}{V_\infty}\right)^2 \tag{3.17}$$

$$C_q^{BE}(r) = C_x\sigma(r)\left(\frac{V}{V_\infty}\right)^2 \tag{3.18}$$

$$\sigma(r) = \frac{N_b c}{2\pi r} \tag{3.19}$$

In these expressions, the local flow velocity over the blade can be expressed in terms of the induction factors and the radial coordinate.

$$V = \sqrt{(V_\infty(1+a))^2 + (\omega r(1-a'))^2} \tag{3.20}$$

Finally, the BEM model is solved based on the assumption that the global forces of momentum theory match the local forces acting on the blades as found by blade element theory. In other words, the thrust force and torque that act on each annulus in momentum theory must equal the combined thrust and torque of all elements of blade element theory within that annulus. Therefore, the BEM model is solved iteratively by minimization of the residual vector as defined below. The aerodynamic loads and performance can then be computed using the equations stated in section 3.1.

$$\mathbf{R_{BEM}} = \begin{bmatrix} C_t^{BE} \\ C_q^{BE} \end{bmatrix} - \begin{bmatrix} C_t^M \\ C_q^M \end{bmatrix} \tag{3.21}$$

When using this BEM model, several underlying assumptions must be considered [40]. The fluid is assumed to be incompressible, inviscid, and isentropic, while the propeller is modelled as an infinitesimally thin disk divided into multiple annular sections. Momentum analysis of each annulus is one-dimensional, with momentum losses at the root and tip accounted for using the Prandtl root-loss and

tip-loss factors, respectively. Axial and tangential velocities are considered uniformly distributed across each annular section, meaning that the thrust force acting on the flow is also uniformly distributed. It is further assumed that the global forces acting on the disk match the local forces acting on the blades. The aerodynamic loads for each blade element are based on two-dimensional airfoil properties, and interactions between adjacent blade elements are neglected.

3.3.1. Compressibility Effects

An aerodynamic correction is applied to the BEM model to account for compressibility effects, which become important as the flow velocity reaches transonic speeds. In this operating regime, the pressure difference over the blade increases which results in a higher lift [41]. Below the critical Mach number, the change in drag remains small because it is dominated by friction in the subsonic flow regime [41]. However, when reaching transonic speeds, the pressure drag might increase due to its dependence on the pressure difference over the blade.

To capture these effects, the Prandtl-Glauert compressibility correction could be applied, as shown in Equation 3.22 [42], which can be used to scale the lift coefficient and the pressure drag coefficient. Alternatively, compressibility effects could be included through airfoil polar data of the lift and drag coefficients. In this case, no compressibility correction is applied to the expression for lift and drag coefficients of the BEM model directly. Instead, an airfoil polar database is used that accounts for the Mach number of the flow over the airfoil.

$$C_p = \frac{C_{p,0}}{\sqrt{1 - M^2}} \tag{3.22}$$

Since Mach dependent polar data is not available, the Prandtl-Glauert correction is used in this work. Furthermore, the available polar data does not discriminate friction drag and pressure drag, but only provides the total drag coefficient. Therefore, the compressibility correction is applied to the lift coefficient only.

3.3.2. Sweep Correction

Since momentum theory is one-dimensional, it does not account for the effects of sweep and lean. Likewise, blade element theory neglects these effects because it treats each blade element independently, assuming two-dimensional flow around them. To incorporate sweep and lean, correction factors are therefore applied within the blade element framework.

As illustrated in Figure 2.2, the blade elements of a swept propeller are no longer positioned in the same way as those of a straight blade. While the elements remain aligned with the incoming freestream flow along the span, a geometric offset shifts each element, in case of sweep, in x-direction. This offset causes the rotation vector to be no longer oriented perpendicular to the chord line, which affects the effective rotational velocity experienced by the airfoil. Figure 3.6 shows that only the component of the rotational velocity that is aligned with the chord line contributes to the relative flow experienced by the airfoil section. As a result, the tangential velocity component of Equation 3.20 is reduced by a factor of $\cos\Lambda$. The axial component, however, remains unaffected because sweep does not affect the inflow in this direction.

The resulting expression for the sweep corrected local flow velocity over each blade element is provided below.

$$V = \sqrt{(V_\infty(1+a))^2 + (\omega r(1-a')\cos\Lambda)^2} \tag{3.23}$$

The lift and drag coefficients are then obtained by evaluating the available polar data using the Reynolds number and by applying the compressibility correction based on the Mach number, both computed from the corrected flow velocity, see Equation 3.24 and Equation 3.25. Note that this correction is crucial because the aerodynamic characteristics of the airfoil are only valid when the velocity component parallel to its chord line is used. If the reduction in effective tangential velocity is not considered, the predicted lift and drag will fail to accurately represent the true aerodynamic loading on the blade section.

$$Re = \frac{\rho_\infty c V}{\mu} \tag{3.24}$$

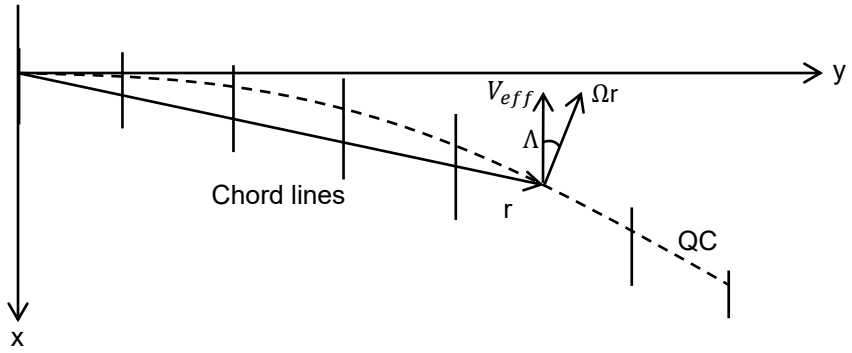

Figure 3.6: Effective rotational velocity experienced by the airfoil.

$$M = \frac{V}{c_{air}} \tag{3.25}$$

Additionally, the local flow angle, defined as the angle between the axial and tangential velocity component, is expressed as a function of the sweep angle.

$$\varphi = \arctan\left(\frac{V_\infty(1+a)}{\omega r(1-a')\cos\Lambda}\right) \tag{3.26}$$

These corrected values of the lift and drag coefficients, as well as the local flow angle, are then used in Equation 3.16 to compute the modified axial and tangential force coefficients. Finally, the thrust coefficient can be computed by substitution of these expressions into Equation 3.17. The torque, however, must not be computed along the chord line but perpendicular to the rotation vector [36]. Therefore, the torque coefficient is multiplied by $\cos\Lambda$. These coefficients are provided as input to the residual vector as defined in Equation 3.21 to iteratively solve the BEM model.

$$C_q^{BE}(r) = C_x\sigma(r)\left(\frac{V}{V_\infty}\right)^2\cos\Lambda \tag{3.27}$$

Lastly, the aerodynamic loads acting on each propeller blade section can be computed using BE theory.

$$\begin{bmatrix}\tilde{\mathbf{f}}_\mathbf{a}\\ \tilde{\mathbf{m}}_\mathbf{a}\end{bmatrix} = q_\infty S\begin{bmatrix}C_x & 0 & C_z & 0 & C_m c & 0\end{bmatrix}^T\left(\frac{V}{V_\infty}\right)^2 \tag{3.28}$$

This extended BEM model does not apply a direct correction for lean because, unlike sweep, the orientation of the airfoil does not depend on variations in lean. As a result, the local velocity over each blade element remains unaffected, and no explicit lean correction is required. However, this does not mean that lean has no impact on the aerodynamic performance at all.

Recall that, in this work, the QCA and FA are defined as the x- and z-coordinates of the quarter-chord line, respectively. Consider a blade that features only lean, so no sweep, at a zero pitch angle, see the top-left propeller cross-section in Figure 3.7. When this blade is pitched, the rotation transforms the quarter-chord line's z-coordinate (FA) into the x-coordinate (QCA). In other words, pitch converts lean into sweep. As illustrated by Figure 3.7, pitching the blade to 45° reduces the FA while increasing the QCA such that the two become equal. When the blade is pitched to 90°, the initial lean disappears entirely, and the quarter-chord line's z-coordinate is fully rotated into the x-coordinate, resulting in pure sweep. By being geometrically transformed into sweep under pitched conditions, the initial lean indirectly affects the blade loading through the sweep correction in Equation 3.23. Thus, although lean itself does not require a direct correction in the BEM model, it can still affect the blade's aerodynamic performance. Similarly, blade pitch can convert sweep into lean. This highlights that lean and sweep

are not independent under blade orientations, and their combined effects must be understood when interpreting the aerodynamic predictions of the model.

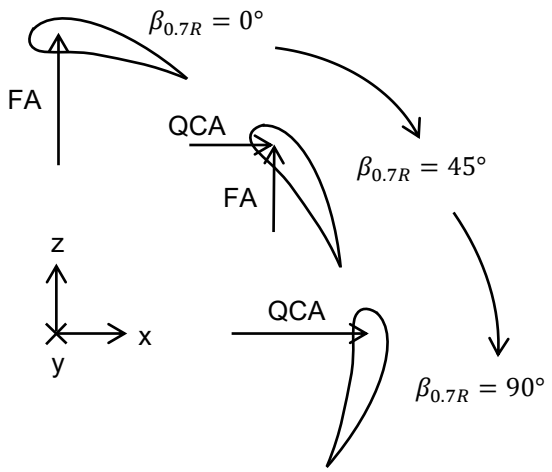

Figure 3.7: Effect of pitch on the quarter-chord alignment and face alignment.

Lastly, it should be noted that aerodynamic interaction effects between neighbouring blade elements are still neglected in this extended BEM model, meaning that sweep and lean only affect the individual blade elements. However, for propeller blades with significant curvature, this assumption becomes invalid. At large lean angles, the leading edge vortices move over the downstream neighbouring blade elements and therefore affect the aerodynamic loading. Similarly, for highly swept propeller blades, these vortices can impact the loading of adjacent elements [20]. Also, sweep induces a more pronounced spanwise flow, directed parallel to the quarter-chord line, compared to an unswept propeller. These effects could potentially be accounted for by adding additional sweep and lean correction factors based on their respective gradients as shown in Equation 2.4 and Equation 2.5. This is further supported by the research of Bergmann et al. [36]. For a more detailed discussion on alternative sweep and lean corrections, see Appendix B. Additionally, the model becomes less reliable near the blade root and tip, where three-dimensional effects dominate and invalidate the underlying two-dimensional assumptions of BEM theory. Although the Prandtl tip- and root-loss factors are applied to compensate the momentum losses in these regions, they do not account directly for the geometric influences of sweep and lean. Moreover, previous studies have indicated that Prandtl's formulation may not be the most appropriate correction for swept rotors [43]. In contrast, the mid-span region is only weakly affected by these three-dimensional tip and root effects, which makes this region more suitable for the two-dimensional analysis of the extended BEM model.

3.4. Validation of Aerodynamic Model

Finally, the extended BEM model is validated to assess its accuracy in predicting the aerodynamic behaviour of the propeller blades. For this purpose, two blade geometries are considered: the six-bladed *XPROP* (Figure 1.4a) and *XPROP*-Λ (Figure 1.4b), the latter being a modified version of *XPROP* with an increased amount of sweep. As mentioned in section 1.2, Prud'homme van Reine [4] conducted wind tunnel tests on both propellers, and his measurement data are used for validation. Further details on both propeller geometries are provided in Appendix A.

The experimental measurements were obtained at a freestream Mach number of $M = 0.12$ and collective pitch angles of 30° and 45°. For $\beta_{0.7R} = 30°$, the advance ratio ranges approximately from 0.8 to 1.3, while for $\beta_{0.7R} = 45°$, it varies roughly between 1.4 and 2.3. These operating conditions were also applied for validating the extended BEM model because validation across multiple pitch angles and sweep configurations not only increases credibility but also allows the model's sensitivity to pitch and sweep to be evaluated. For further details on the experimental methodology and the associated confidence intervals of the measurement data, the reader is referred to [4].

In the BE theory calculations, airfoil polar data from Rotundo [23] were used. These polars were generated numerically using *RFOIL* for angles of attack ranging from -24° to 24° with increments of 3°. The relatively large increment was chosen to limit the dataset size and thus computational time. Rotundo [23] showed, by comparison with aerodynamic results obtained using 0.1° increments, that the larger 3° increment has no significant impact on the predicted aerodynamic performance. When generating airfoil polar data, *RFOIL* incorporates rotational effects of the propeller by accounting for centrifugal forces and the resulting Coriolis effects. These forces establish a favourable pressure gradient that delays stall and therefore increases lift, particularly near stall conditions occurring at high angles of attack [44]. Furthermore, the transition from laminar to turbulent flow is modelled by the e^N-method using a critical amplification factor of $N = 4.5$, although *RFOIL* neglects the effect of rotation on this transition location [23]. Finally, for the BEM calculations, the aerodynamic model used 100 spanwise nodes which were all distributed using cosine spacing to achieve higher resolution near the blade ends. Also, central differencing was used in the numerical scheme to update the induction factors during the minimization of the residual vector, as given by Equation 3.21.

Figure 3.8 compares the BEM predictions with the experimental measurements, showing the thrust and power coefficients, and the efficiency, as defined by Equation 3.1, Equation 3.2 and Equation 3.8, respectively. As expected from the discussion in section 3.2, the BEM model tends to overestimate the aerodynamic performance. In fact, as reported in Table 3.1, BEM overestimates the propulsor efficiency by up to 0.091, equivalent to an error of 11.8%, while the corresponding advance ratio exhibits a discrepancy of 0.34, representing a misprediction of 19.3%. This discrepancy may arise because the BEM model assumes two-dimensional behaviour for the airfoil profile performance, neglecting three-dimensional aerodynamic effects such as tip vorticity and spanwise flow, which limits its ability to accurately represent reality. Second, the transition of the airflow from laminar to turbulent in the experiments is a process that, despite using the e^N-method, may not be captured accurately within the polar data due to the neglected impact of rotational effects. This could lead to inaccurate predictions of the lift and drag of the blade sections. Especially at a pitch angle of 45°, where the angle of attack is high, rotational effects become more pronounced, which may explain the larger discrepancies observed at 45° compared to 30°. Furthermore, whenever laminar separation occurs on the blade in the experiment, a strong three-dimensional flow field develops, which is not captured by the BEM model. Together, these factors can cause the BEM model predictions to exceed the experimentally measured performance.

Table 3.1: Comparison between BEM predictions and experimental measurements of the maximum propulsive efficiency and the corresponding advance ratio for *XPROP* and *XPROP*-Λ.

$\beta_{0.7R}$	**Propeller**	**Method**	η_P	$\Delta\eta_P$	$\Delta\eta_P$ (%)	J	ΔJ	ΔJ (%)
30°	XPROP	BEM	0.829	0.085	11.4	1.21	0.14	13.1
		Exp.	0.744			1.07		
	XPROP-Λ	BEM	0.830	0.079	10.6	1.21	0.13	11.9
		Exp.	0.751			1.08		
45°	XPROP	BEM	0.857	0.089	11.6	2.08	0.31	17.6
		Exp.	0.768			1.77		
	XPROP-Λ	BEM	0.858	0.091	11.8	2.08	0.34	19.3
		Exp.	0.767			1.74		

The differences in thrust and power coefficients, as well as in efficiency, between the BEM model predictions and the experimental measurements are shown in Figure 3.9. Percentage differences are omitted, since they become less meaningful when baseline values approach zero.

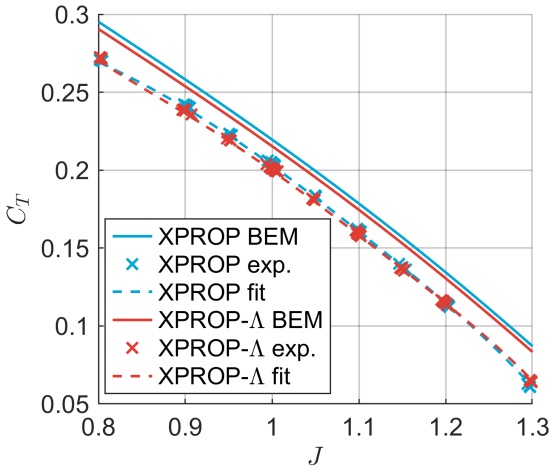

(a) Thrust coefficient at $\beta_{0.7R} = 30°$.

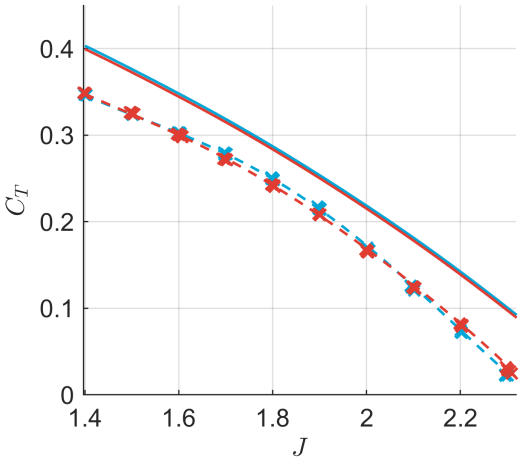

(b) Thrust coefficient at $\beta_{0.7R} = 45°$.

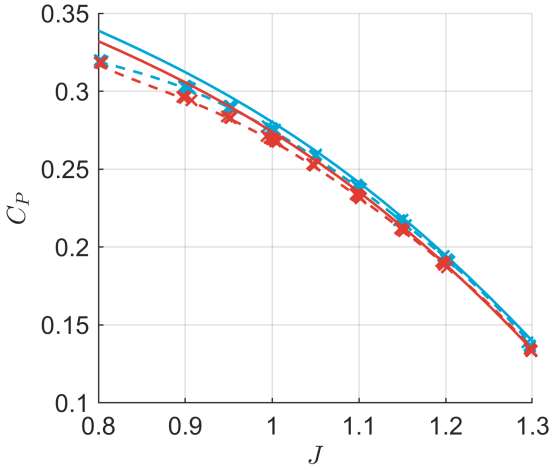

(c) Power coefficient at $\beta_{0.7R} = 30°$.

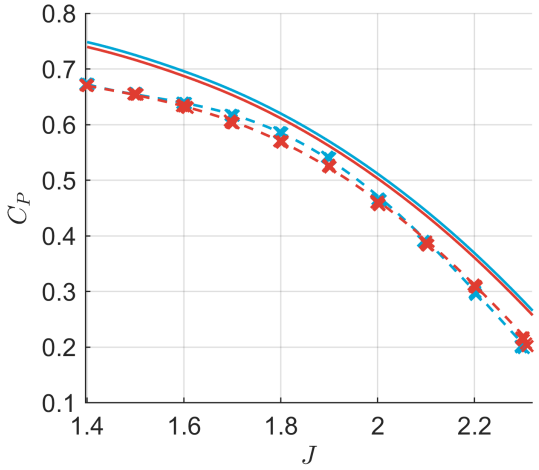

(d) Power coefficient at $\beta_{0.7R} = 45°$.

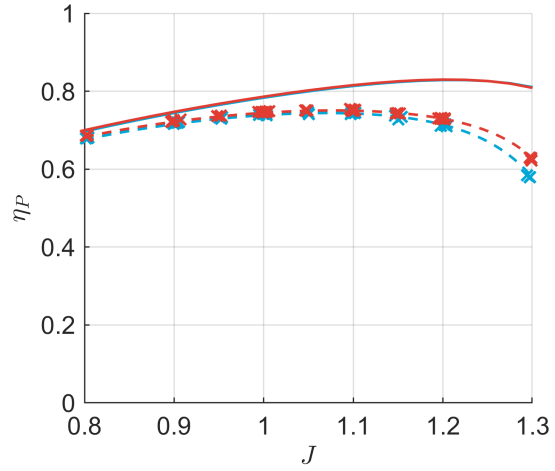

(e) Efficiency at $\beta_{0.7R} = 30°$.

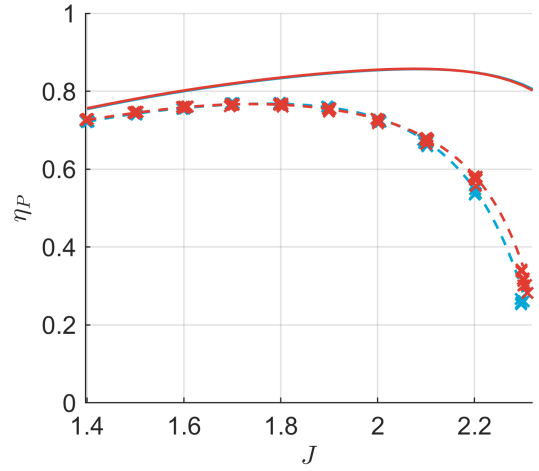

(f) Efficiency at $\beta_{0.7R} = 45°$.

Figure 3.8: Aerodynamic performance of *XPROP* and *XPROP*-Λ at $M = 0.12$, comparing the extended BEM model with experimental data, including a third-order polynomial fit to the experimental data points from [4].

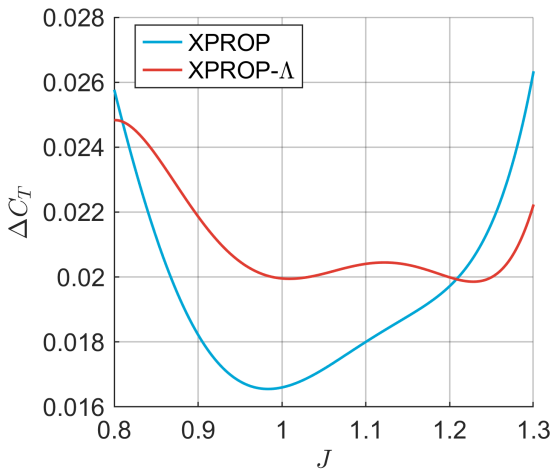

(a) Difference in thrust coefficient at $\beta_{0.7R} = 30°$.

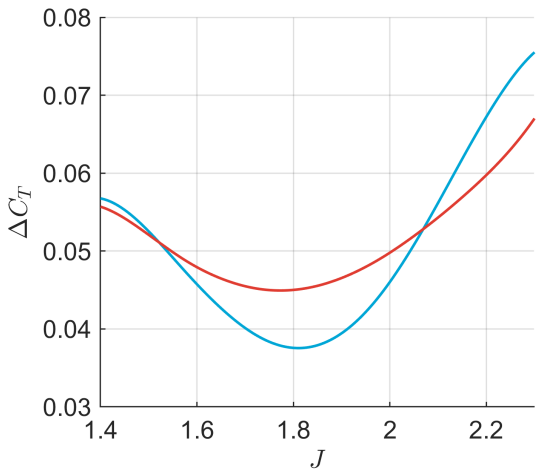

(b) Difference in thrust coefficient at $\beta_{0.7R} = 45°$.

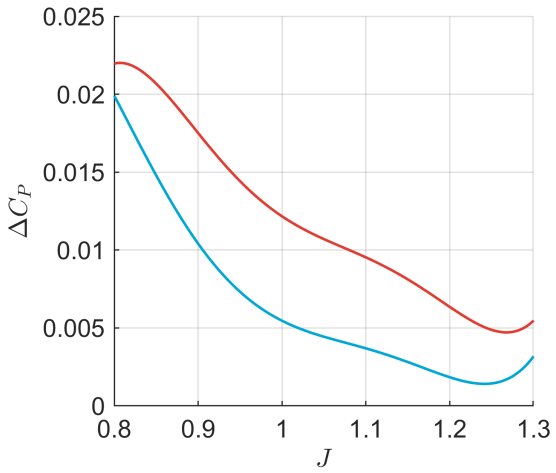

(c) Difference in power coefficient at $\beta_{0.7R} = 30°$.

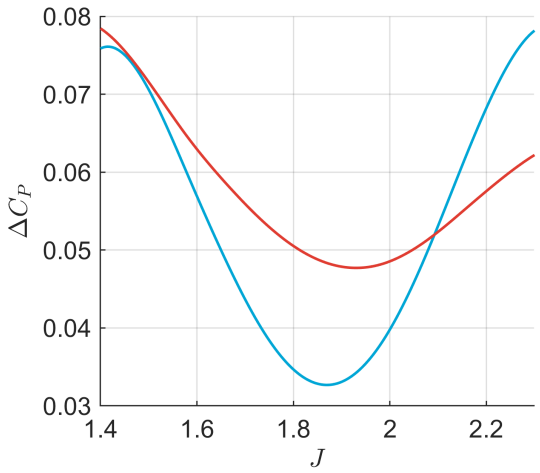

(d) Difference in power coefficient at $\beta_{0.7R} = 45°$.

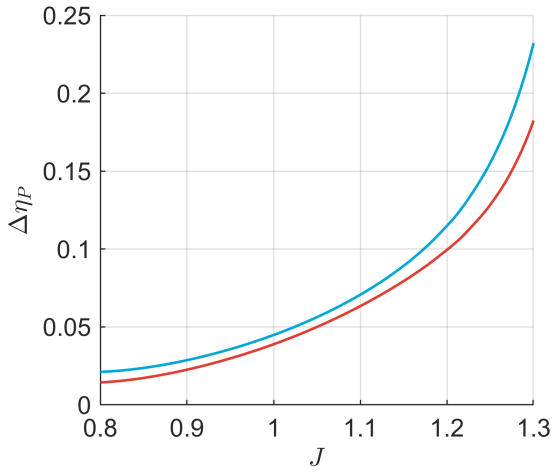

(e) Difference in efficiency at $\beta_{0.7R} = 30°$.

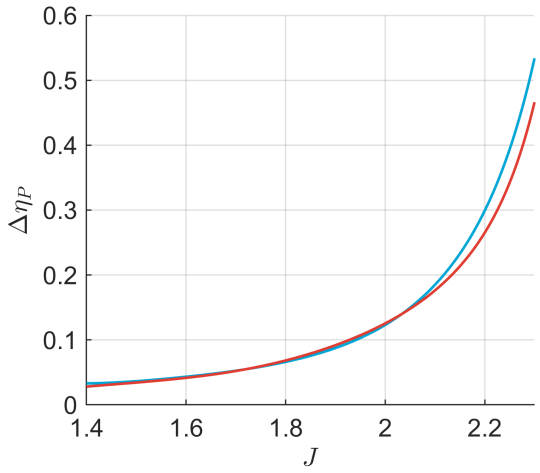

(f) Difference in efficiency at $\beta_{0.7R} = 45°$.

Figure 3.9: Aerodynamic performance difference between the predictions of BEM and the experimental measurements for *XPROP* and *XPROP-*Λ.

The results in Figure 3.9 clearly show once again that the BEM model consistently overestimates the aerodynamic performance, as all differences are positive. Notably, the trends for *XPROP* and *XPROP*-Λ are quite similar for all performance metrics. In the mid-range of the advance ratios, between $J = 0.9$ and 1.2 for 30° pitch and between $J = 1.6$ and 2.0 for 45° pitch, the discrepancies in thrust coefficient are smallest. At 30° pitch, the differences range from 0.017 to 0.020 for *XPROP* and from 0.020 to 0.021 for *XPROP*-Λ, while at 45° pitch they range from 0.038 to 0.046 and from 0.045 to 0.050 for *XPROP* and *XPROP*-Λ, respectively. This suggests that, for these pitch angles, the model provides its most reliable thrust predictions within these advance ratio ranges. Furthermore, within these ranges, the offset for *XPROP*-Λ is greater than that for *XPROP* in both thrust and power coefficients, indicating that the BEM model tends to overestimate the performance of the swept blade more than that of the straight blade. The difference in power coefficient steadily decreases with increasing J at 30° pitch, whereas at 45° pitch it reaches its minimum between $J = 1.6$ and 2.0, with minimum values of 0.033 for *XPROP* and 0.048 for *XPROP*-Λ. The difference in efficiency, however, diverges with increasing J for both blade configurations and pitch angles.

The effect of sweep on aerodynamic performance is small, as shown by the close agreement between the performance curves of *XPROP* and *XPROP*-Λ in Figure 3.8 for both the experimental measurements and the predictions by BEM. This is highlighted in Figure 3.10, which shows the difference in aerodynamic performance between *XPROP* and *XPROP*-Λ for both methods. When interpreting these results, it should be noted that at a 45° pitch angle, the blade orientation is such that sweep effectively translates into an equal amount of lean. These results therefore indicate that the influence of lean on the aerodynamic performance is also limited.

In the mid-range of $J = 0.9$ to $J = 1.2$, where the BEM model most accurately predicts thrust at 30° pitch, the difference in thrust coefficient between *XPROP* and *XPROP*-Λ ranges from -0.0044 to -0.0039 for BEM and from -0.0037 to -0.0024 for the experiments. Similarly, at 45° pitch and $J = 1.6$ to 2.0, ΔC_T ranges from -0.0036 to -0.0034 for BEM and from -0.0076 to -0.0022 for the experiments. These negative values indicate that the thrust coefficient decreases with increasing sweep, while their small magnitudes show that the sensitivity of thrust to sweep is small. Similarly, the effect of sweep on the power coefficient is negative for both the BEM predictions and the experimental results at these mid-range advance ratios. At 30° pitch, ΔC_P ranges from -0.0065 to -0.0058 for BEM and from -0.0072 to -0.0045 for the experiments, while at 45°, the ranges are -0.0086 to -0.0084 and -0.0161 to -0.0060 for BEM and the experiments, respectively. Overall, the BEM model accurately predicts the sign of the aerodynamic performance change between *XPROP* and *XPROP*-Λ, indicating that the sensitivity to sweep is well captured in direction, though its magnitude differs.

Although the absolute values of thrust and power are overestimated, the validation demonstrates that the extended BEM model successfully reproduces the performance trends of thrust and power at a 30° pitch angle, including the effects of sweep, within the mid-range advance ratio of $J = 0.9$ to 1.2. This accuracy decreases at the higher pitch setting of 45°, probably due to stronger three-dimensional aerodynamic effects. The results indicate that, for sweep and lean sensitivity studies focused on propeller performance in terms of thrust and efficiency, the model provides sufficient fidelity at 30° pitch, with these trends well captured, as shown in Figure 3.10a and Figure 3.10e. However, the accuracy of the model decreases at 45° pitch. Accordingly, the extended BEM model can be applied to parametric studies aimed at identifying design trends, though it is less suitable for detailed design optimization. This aerodynamic model can therefore provide valuable insights into the aerodynamic effects of geometric and operational changes even when absolute values are offset.

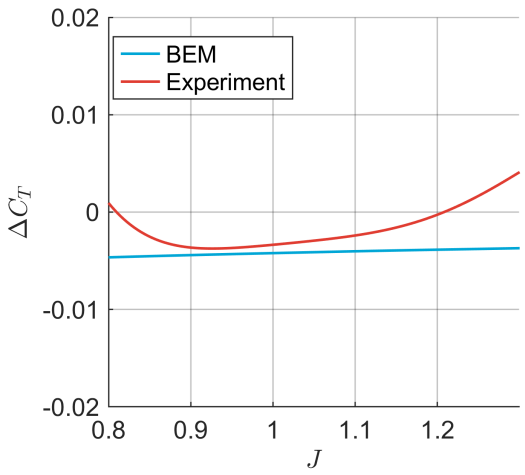

(a) Difference in thrust coefficient at $\beta_{0.7R} = 30°$.

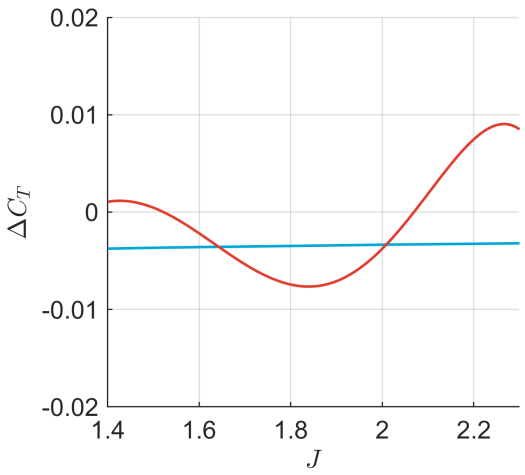

(b) Difference in thrust coefficient at $\beta_{0.7R} = 45°$.

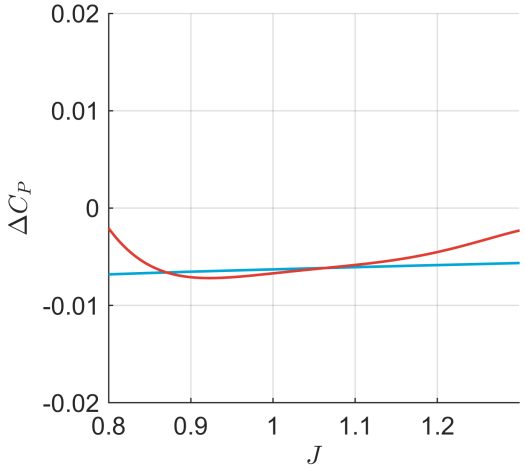

(c) Difference in power coefficient at $\beta_{0.7R} = 30°$.

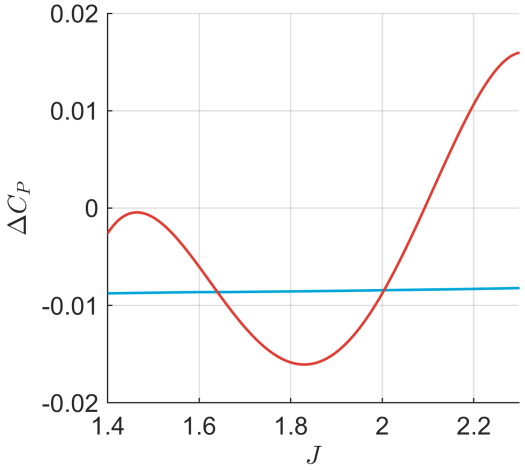

(d) Difference in power coefficient at $\beta_{0.7R} = 45°$.

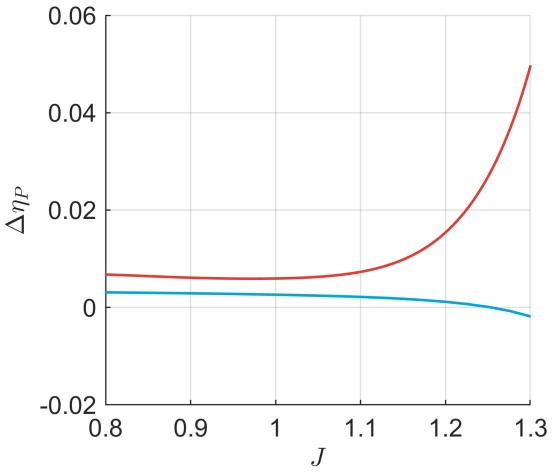

(e) Difference in efficiency at $\beta_{0.7R} = 30°$.

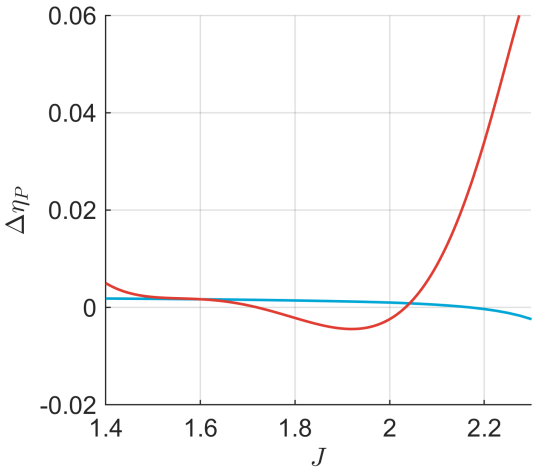

(f) Difference in efficiency at $\beta_{0.7R} = 45°$.

Figure 3.10: Aerodynamic performance difference between *XPROP* and *XPROP-*Λ as predicted by BEM and observed experimentally.

4

Aeroelastic Coupling

This chapter presents an overview of the aeroelastic coupling used in this project. It starts with a mathematical explanation of how this coupling works. Next, analytical expressions of the aerodynamic sensitivities are developed and validated by comparison with numerical calculations in section 4.2 and section 4.3, respectively. Finally, in section 4.4, verification of the aeroelastic coupling is performed.

4.1. Aeroelastic Coupling

To perform static aeroelastic analysis on the propeller blade, the external forces and moments that act on the blade must be in equilibrium with its internal forces and moments. The external forces include the aerodynamic, centrifugal and other eccentric forces, like gravity, while the structural forces are considered to be internal. Although the aerodynamic forces could be regarded as eccentric forces, since they are not evaluated on the structural nodes, they are evaluated separately for convenience. However, when the internal forces are not in equilibrium with the external forces, the blade deforms. This deformation changes the blade geometry, which in turn affects both the internal and external forces. To account for this interdependence, the internal and external forces are coupled by a residual vector, see Equation 4.1, whose minimization ensures equilibrium is reached. In other words, the coupling guarantees that the structural forces balance the sum of the aerodynamic, centrifugal and eccentric forces, and that all forces are resolved consistently with their dependence on the structural deformations.

$$\mathbf{R}(\mathbf{p}) = \mathbf{f_s}(\mathbf{p}) - (\mathbf{f_a}(\mathbf{p}) + \mathbf{f_c}(\mathbf{p}) + \mathbf{f_e}(\mathbf{p})) \tag{4.1}$$

To find this equilibrium, an iterative scheme is employed, in which the blade deformation is updated using the Newton-Raphson method.

$$\mathbf{p_{i+1}} = \mathbf{p_i} - \left(\frac{\partial \mathbf{R}}{\partial \mathbf{p}}(\mathbf{p_i})\right)^{-1} \cdot \mathbf{R}(\mathbf{p_i}) \tag{4.2}$$

This could be solved by a loosely coupled method that iteratively computes the aerodynamic loads and the resulting structural deformation, as applied by Thielen [6]. However, Rotundo [23] developed a tightly coupled method that incorporates also the gradients of the forces, which increased the robustness and convergence rate significantly compared to the loose coupling, while keeping excellent agreement with the loosely coupled method. Within this approach, the residual vector is expressed in terms of the gradients with respect to the deformations of the blade for both the internal and external forces.

$$-\mathbf{R}(\mathbf{p_i}) = \left(\frac{\partial \mathbf{f_s}}{\partial \mathbf{p}} - \frac{\partial \mathbf{f_a}}{\partial \mathbf{p}} - \frac{\partial \mathbf{f_c}}{\partial \mathbf{p}} - \frac{\partial \mathbf{f_e}}{\partial \mathbf{p}}\right)\Bigg|_{\mathbf{p_i}} (\mathbf{p_{i+1}} - \mathbf{p_i}) =: (\mathbf{K_s} - \mathbf{K_a} - \mathbf{K_c} - \mathbf{K_e}) \cdot (\mathbf{p_{i+1}} - \mathbf{p_i}) \tag{4.3}$$

Because of its computational efficiency, the gradient-based coupling is also applied in this work. According to Equation 4.3, updating the blade deformation requires the structural, aerodynamic, centrifugal,

and external stiffness matrices. For each stiffness matrix, it is necessary to verify whether the current computation method in *PROTEUS* is applicable to blade geometries with sweep and lean.

Since the structural computations in *PROTEUS* can accommodate arbitrary three-dimensional blade geometries, the calculation of the structural stiffness matrix is compatible with generic geometries [45]. The analysis of the structural stiffness matrix should therefore perform equally well for swept and leaned blades as it does for straight blades. Furthermore, gravity is not considered in this study, as its effect on propeller blades is minimal compared to fixed wings due to their considerably lower mass. As no other external forces are applied, the external stiffness matrix is not utilized.

4.1.1. Centrifugal Loads

The original model of *PROTEUS* was developed for fixed wings only, meaning that the effect of centrifugal force was not included. Rotundo et al. [19] extended the model for propeller blades by including the centrifugal force and its derivative with respect to blade deformation.

$$\mathbf{f_c}(\mathbf{p}) = -\mathbf{M} \cdot \mathbf{\Omega} \cdot \mathbf{\Omega} \cdot (\mathbf{r} + \mathbf{p}) \tag{4.4}$$

$$\frac{d\mathbf{f_c}}{d\mathbf{p}} = -\mathbf{M} \cdot \mathbf{\Omega} \cdot \mathbf{\Omega} =: \mathbf{K_c} \tag{4.5}$$

For the twelve degrees of freedom of each beam element, the squared rotor speed matrix is given below. Note that its values for rotational degrees of freedom are all zero, meaning that these do not contribute to the centrifugal force [19].

$$\mathbf{\Omega} \cdot \mathbf{\Omega} = \begin{bmatrix} \boldsymbol{\omega}^2 & \mathbf{0_{3x3}} & \mathbf{0_{3x3}} & \mathbf{0_{3x3}} \\ \mathbf{0_{3x3}} & \mathbf{0_{3x3}} & \mathbf{0_{3x3}} & \mathbf{0_{3x3}} \\ \mathbf{0_{3x3}} & \mathbf{0_{3x3}} & \boldsymbol{\omega}^2 & \mathbf{0_{3x3}} \\ \mathbf{0_{3x3}} & \mathbf{0_{3x3}} & \mathbf{0_{3x3}} & \mathbf{0_{3x3}} \end{bmatrix} \quad \text{where} \quad \boldsymbol{\omega}^2 = \begin{bmatrix} -\omega^2 & 0 & 0 \\ 0 & -\omega^2 & 0 \\ 0 & 0 & 0 \end{bmatrix} \tag{4.6}$$

Since the definition of the rotor speed matrix is independent of blade geometry parameters, it remains unchanged when sweep or lean is introduced. The mass matrix does depend on blade geometry, but its existing formulation in *PROTEUS* is already applicable to arbitrary three-dimensional shapes. Therefore, no adjustments are required for the computation of the centrifugal loads.

PROTEUS contains two types of mass matrices. The consistent mass matrix integrates the mass over the volume of the beam, thereby accounting for mass variations within the beam element. This produces non-zero off-diagonal matrix terms resulting in mass coupling between (neighbouring) degrees of freedom of the nodes. On the other hand, the lumped mass matrix assumes that the beam element mass is concentrated at its nodes, with the mass evenly distributed among the two nodes, resulting in a diagonal matrix without any mass coupling [23]. Although the consistent mass matrix offers higher fidelity, it increases computational cost due to the added complexity in the coupled equations of motion. The lumped mass matrix, however, reduces computational effort while maintaining sufficient accuracy for most engineering applications. For these reasons, the lumped mass matrix is adopted in this work.

4.1.2. Aerodynamic Loads

In contrast to the centrifugal loads, it is easier to evaluate the aerodynamic loads on the aerodynamic grid instead of the structural grid, because that is where the aerodynamic quantities are known [23]. However, Equation 4.1 and Equation 4.3 require the aerodynamic loads and their derivatives with respect to blade deformation to be evaluated on the structural grid. In his dissertation, Werter [24] developed a method to transform eccentric loads to nodal loads. This method can also be applied to map the aerodynamic loads from the aerodynamic grid to the structural grid, as shown in Equation 4.7. For a more detailed mathematical explanation of the $\mathbf{H^T B_e^T}$ mapping, the reader is referred to [24].

$$\mathbf{f_a} = \mathbf{H^T B_e^T} \begin{bmatrix} \tilde{\mathbf{f}}_\mathbf{a} \\ \tilde{\mathbf{m}}_\mathbf{a} \end{bmatrix} \tag{4.7}$$

This equation shows that taking the variation of the aerodynamic loads results in three contributions to the aerodynamic stiffness matrix, see Equation 4.8. Werter [24] showed that this could be expressed

as the sum of the geometric moment stiffness $\mathbf{K_h}$, the geometric rotation stiffness $\mathbf{K_g}$ and the material stiffness $\mathbf{K_m}$, each multiplied by the variation in blade deformation.

$$\delta\mathbf{f_a} = \delta\mathbf{H^T}\mathbf{B_e^T}\begin{bmatrix}\tilde{\mathbf{f}}_\mathbf{a}\\ \tilde{\mathbf{m}}_\mathbf{a}\end{bmatrix} + \mathbf{H^T}\delta\mathbf{B_e^T}\begin{bmatrix}\tilde{\mathbf{f}}_\mathbf{a}\\ \tilde{\mathbf{m}}_\mathbf{a}\end{bmatrix} + \mathbf{H^T}\mathbf{B_e^T}\delta\begin{bmatrix}\tilde{\mathbf{f}}_\mathbf{a}\\ \tilde{\mathbf{m}}_\mathbf{a}\end{bmatrix} =: (\mathbf{K_h} + \mathbf{K_g} + \mathbf{K_m})\delta\mathbf{p} \tag{4.8}$$

Since $\mathbf{K_h}$ and $\mathbf{K_g}$ are only dependent on the aerodynamic loads and not on their variation, these stiffness matrices do not require any adjustments in *PROTEUS* to account for sweep and lean. Thus, when extending the aeroelastic model to include sweep and lean, extension of the aerodynamic model itself is sufficient for these terms. The material stiffness matrix, on the other hand, does depend on the variation of the aerodynamic loads. Therefore, it requires revision when using the extended BEM model. Rotundo [23] showed that the material stiffness matrix can be expressed in terms of gradients of the aerodynamic loads with respect to the structural degrees of freedom directly.

$$\mathbf{K_m} = \mathbf{H^T}\mathbf{B_e^T} \cdot \frac{d}{d\mathbf{p}}\begin{bmatrix}\tilde{\mathbf{f}}_\mathbf{a}\\ \tilde{\mathbf{m}}_\mathbf{a}\end{bmatrix} \cdot \mathbf{B_e}\mathbf{H} \tag{4.9}$$

A structural node contains both three translational and rotational degrees of freedom, meaning that the derivative of the aerodynamic loads with respect to the blade deformation can be written in terms of these six degrees of freedom. Rotundo [23] assumed in his work that the aerodynamic loads depend only on the twist angle β. Due to the more general blade geometries considered here, this assumption is not made. It is assumed, however, that the loads are independent of the axial position z, making the corresponding aerodynamic sensitivities zero, as shown in Equation 4.10.

$$\begin{aligned}\frac{d}{d\mathbf{p_a}}\begin{bmatrix}\tilde{\mathbf{f}}_\mathbf{a}\\ \tilde{\mathbf{m}}_\mathbf{a}\end{bmatrix} &= \begin{bmatrix}\frac{d}{dx}\tilde{\mathbf{f}}_\mathbf{a} & \frac{d}{dy}\tilde{\mathbf{f}}_\mathbf{a} & \frac{d}{dz}\tilde{\mathbf{f}}_\mathbf{a} & \frac{d}{d\Lambda}\tilde{\mathbf{f}}_\mathbf{a} & \frac{d}{d\beta}\tilde{\mathbf{f}}_\mathbf{a} & \frac{d}{d\Psi}\tilde{\mathbf{f}}_\mathbf{a}\\ \frac{d}{dx}\tilde{\mathbf{m}}_\mathbf{a} & \frac{d}{dy}\tilde{\mathbf{m}}_\mathbf{a} & \frac{d}{dz}\tilde{\mathbf{m}}_\mathbf{a} & \frac{d}{d\Lambda}\tilde{\mathbf{m}}_\mathbf{a} & \frac{d}{d\beta}\tilde{\mathbf{m}}_\mathbf{a} & \frac{d}{d\Psi}\tilde{\mathbf{m}}_\mathbf{a}\end{bmatrix}\\ &= \begin{bmatrix}\frac{d}{dx}\tilde{\mathbf{f}}_\mathbf{a} & \frac{d}{dy}\tilde{\mathbf{f}}_\mathbf{a} & 0 & \frac{d}{d\Lambda}\tilde{\mathbf{f}}_\mathbf{a} & \frac{d}{d\beta}\tilde{\mathbf{f}}_\mathbf{a} & \frac{d}{d\Psi}\tilde{\mathbf{f}}_\mathbf{a}\\ \frac{d}{dx}\tilde{\mathbf{m}}_\mathbf{a} & \frac{d}{dy}\tilde{\mathbf{m}}_\mathbf{a} & 0 & \frac{d}{d\Lambda}\tilde{\mathbf{m}}_\mathbf{a} & \frac{d}{d\beta}\tilde{\mathbf{m}}_\mathbf{a} & \frac{d}{d\Psi}\tilde{\mathbf{m}}_\mathbf{a}\end{bmatrix}\end{aligned} \tag{4.10}$$

In the next section, analytical expressions for the aerodynamic sensitivities with respect to the deformations in these remaining five structural degrees of freedom will be derived, and the results will be compared against numerical calculations to assess their accuracy in section 4.3.

4.2. Aerodynamic Sensitivities

The derivatives in Equation 4.10 can be evaluated either analytically or numerically, using the extended BEM model described in section 3.3. The numerical approach may seem more straightforward to implement, as it relies on finite difference approximations. However, the analytical approach is computationally faster and could provide more insight into the dependencies of the aerodynamic loads on the blade deformation parameters.

In the following subsections, the sensitivity expressions for each degree of freedom will be presented. First, the analytical expressions for the sensitivity with respect to twist deformation will be derived in detail. The sensitivities with respect to sweep and lean are then derived using a similar approach, and therefore only the new derivatives are presented. Finally, the two remaining sensitivities of the aerodynamic loads with respect to blade deformations in the translational degrees of freedom, x and y, are addressed.

4.2.1. Sensitivities to Twist Deformation

The sensitivity with respect to twist deformation is expected to be the largest compared to other structural degrees of freedom, because it directly affects the blade's local angle of attack. Therefore, the analytical expressions of these sensitivities were also derived by Rotundo et al. [19]. However, this was done for a BEM model without sweep and lean corrections. Here, the derivation is shown for the extended BEM model from section 3.3.

The first step is to take the derivative of the aerodynamic loads, see Equation 3.28, with respect to the twist angle.

$$\begin{aligned}\frac{d}{d\beta}\begin{bmatrix}\tilde{\mathbf{f}}_\mathbf{a}\\ \tilde{\mathbf{m}}_\mathbf{a}\end{bmatrix} &= q_\infty S\begin{bmatrix}C_{x_\beta} & 0 & C_{z_\beta} & 0 & C_{m_\beta}c & 0\end{bmatrix}^T\left(\frac{V}{V_\infty}\right)^2\\ &+ q_\infty S\begin{bmatrix}C_x & 0 & C_z & 0 & C_m c & 0\end{bmatrix}^T\frac{2V}{V_\infty^2}\frac{dV}{d\beta}\\ &+ q_\infty\frac{dS}{d\beta}\begin{bmatrix}C_x & 0 & C_z & 0 & C_m c & 0\end{bmatrix}^T\left(\frac{V}{V_\infty}\right)^2\end{aligned} \tag{4.11}$$

The first terms that appear in this equation are the derivatives of the tangential and axial force coefficients. These can be rewritten in terms of the lift and drag coefficients using Equation 3.16. Since the lift and drag coefficients, but also the moment coefficient in Equation 4.11 above, are dependent on the angle of attack, the chain rule is applied. Furthermore, the derivatives of these coefficients with respect to the angle of attack can be obtained numerically using available polar data.

$$\begin{bmatrix}C_{l_\beta}\\ C_{d_\beta}\\ C_{m_\beta}\end{bmatrix} = \begin{bmatrix}C_{l_\alpha}\\ C_{d_\alpha}\\ C_{m_\alpha}\end{bmatrix}\frac{d\alpha}{d\beta} \tag{4.12}$$

$$\Rightarrow \begin{bmatrix}C_{z_\beta}\\ C_{x_\beta}\end{bmatrix} = \begin{bmatrix}\cos\varphi & -\sin\varphi\\ \sin\varphi & \cos\varphi\end{bmatrix}\begin{bmatrix}C_{l_\alpha}\\ C_{d_\alpha}\end{bmatrix}\frac{d\alpha}{d\beta} + \begin{bmatrix}-\sin\varphi & -\cos\varphi\\ \cos\varphi & -\sin\varphi\end{bmatrix}\begin{bmatrix}C_l\\ C_d\end{bmatrix}\frac{d\varphi}{d\beta} \tag{4.13}$$

Note that the angle of attack and the flow angle are related as shown in Figure 3.1, from which the following relationship becomes evident.

$$\frac{d\alpha}{d\beta} = \frac{d(\beta-\varphi)}{d\beta} = 1 - \frac{d\varphi}{d\beta} \tag{4.14}$$

Besides $d\varphi/d\beta$, the derivative of the resultant velocity is required in the second line of Equation 4.11. Using Equation 3.26 and Equation 3.23, respectively, these two derivatives are both expressed in terms of $da/d\beta$, $da'/d\beta$, $d\Lambda/d\beta$ and $dr/d\beta$.

$$\frac{d\varphi}{d\beta} = \sin\varphi\cos\varphi\left(\frac{1}{1-a}\frac{da}{d\beta} + \frac{1}{1-a'}\frac{da'}{d\beta} + \tan\Lambda\frac{d\Lambda}{d\beta} - \frac{1}{r}\frac{dr}{d\beta}\right) \tag{4.15}$$

$$\frac{dV}{d\beta} = \frac{1}{V}\left(V_\infty^2(1+a)\frac{da}{d\beta} - (\omega r)^2(1-a')^2\cos^2\Lambda\left(\frac{1}{1-a'}\frac{da'}{d\beta} + \frac{1}{r}\frac{dr}{d\beta} - \tan\Lambda\frac{d\Lambda}{d\beta}\right)\right) \tag{4.16}$$

Geometric Sensitivities to Twist Deformation

Some of the required derivatives in the sensitivity equations above depend solely on geometric parameters and therefore they do not depend directly on the load case settings. These sensitivities are hereafter referred to as *geometric sensitivities*. In the derivation of the sensitivities to twist deformation, these geometric sensitivities are $dS/d\beta$, $d\Lambda/d\beta$ and $dr/d\beta$. Since they cannot be solved for within the BEM model itself, they are obtained by varying the blade geometry and analysing the resulting changes.

First of all, it is assumed that the planform area does not depend on twist as both the chord length and the length of the quarter-chord line do not change due to twist.

$$\frac{dS}{d\beta} = 0 \tag{4.17}$$

The sensitivity of the sweep angle with respect to deformations of twist is derived using the definition of the sweep angle, given by Equation 2.2.

$$\frac{d\Lambda}{d\beta} = \frac{1}{\left(1+\tan^2\Lambda\right)y}\frac{dQCA}{d\beta} \tag{4.18}$$

The variation of the quarter-chord alignment with twist is still unknown. To determine $dQCA/d\beta$, two temporary parameters are introduced. First, r' is defined as the distance between the global y-axis and the blade's quarter-chord point of the airfoil section under consideration, see Figure 4.1. Since both the QCA and FA distributions are defined relative to the y-axis, its magnitude can be expressed in terms of these quantities. Second, an angle ζ is defined as the angle between the global x-axis and r'.

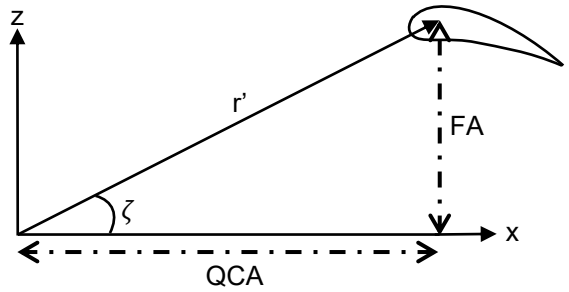

Figure 4.1: Illustration of ζ and r'.

From their definition, it follows that both parameters can be expressed solely in terms of QCA and FA.

$$r' \coloneqq \sqrt{x_{QC}^2 + z_{QC}^2} = \sqrt{QCA^2 + FA^2} \tag{4.19}$$

$$\tan\zeta \coloneqq \frac{FA}{QCA} \tag{4.20}$$

Obviously, for a rotation around the y-axis, which is what the twist deformation in the global coordinate system represents, $dr'/d\beta = 0$ and $d\zeta/d\beta = -1$.

$$\frac{dr'^2}{d\beta} = 2QCA\frac{dQCA}{d\beta} + 2FA\frac{dFA}{d\beta} = 0 \tag{4.21}$$

$$\frac{d\zeta}{d\beta} = \frac{1}{1+\left(\frac{FA}{QCA}\right)^2}\left(\frac{1}{QCA}\frac{dFA}{d\beta} - \frac{FA}{QCA^2}\frac{dQCA}{d\beta}\right) = -1 \tag{4.22}$$

Equation 4.21 and Equation 4.22 can now be solved for their two unknowns.

$$\Rightarrow \frac{dQCA}{d\beta} = FA \tag{4.23}$$

$$\Rightarrow \frac{dFA}{d\beta} = -QCA \tag{4.24}$$

Finally, Equation 4.18 can be expressed in terms of FA.

$$\frac{d\Lambda}{d\beta} = \frac{FA}{y\left(1+\tan^2\Lambda\right)} \tag{4.25}$$

The last geometric sensitivity that must be derived for the twist is $dr/d\beta$. In this context, r is defined as the distance from the axis of rotation to the quarter-chord line of the blade. From this definition, the analytical expression for $dr/d\beta$ can be derived using Equation 4.23. Here, it should be noted that $dy/d\beta = 0$ as a rotation around the y-axis does not change the y-coordinate itself.

$$\frac{dr}{d\beta} = \frac{d}{d\beta}\left(\sqrt{QCA^2 + y^2}\right) = \frac{QCA}{r}\frac{dQCA}{d\beta} = \frac{QCA \cdot FA}{r} \tag{4.26}$$

Sensitivity of Induction Factors to Twist Deformation

Finally, a numerical scheme is applied to compute the sensitivities of the induction factors, $da/d\beta$ and $da'/d\beta$, providing the last sensitivities required to determine the sensitivity of the aerodynamic loads of Equation 4.11. This is achieved by iteratively evaluating the derivatives of the thrust and torque coefficients from both momentum theory and blade element theory. This method was developed by Rotundo [23] but it will be reviewed here, as the original model has been both improved and extended to account for curved blades.

The thrust and torque coefficients in blade element theory are given by Equation 3.17 and Equation 3.27, respectively. These expressions are used to determine their differentials with respect to twist deformation.

$$\frac{d}{d\beta}C_t^{\mathsf{BE}} = C_{z_\beta}\sigma\left(\frac{V}{V_\infty}\right)^2 + C_z\sigma\frac{2V}{V_\infty^2}\frac{dV}{d\beta} + C_z\left(\frac{V}{V_\infty}\right)^2\frac{d\sigma}{d\beta} \tag{4.27}$$

$$\frac{d}{d\beta}C_q^{\mathsf{BE}} = C_{x_\beta}\sigma\left(\frac{V}{V_\infty}\right)^2\cos\Lambda + C_x\sigma\frac{2V}{V_\infty^2}\frac{dV}{d\beta}\cos\Lambda + C_x\left(\frac{V}{V_\infty}\right)^2\cos\Lambda\frac{d\sigma}{d\beta} - C_x\sigma\left(\frac{V}{V_\infty}\right)^2\sin\Lambda\frac{d\Lambda}{d\beta} \tag{4.28}$$

In Equation 4.27 and Equation 4.28, the sensitivity of the blade solidity appears. In contrast to straight blades, this term must be accounted for when analysing curved blades because $dr/d\beta$ is non-zero whenever both the quarter-chord alignment and face alignment are non-zero. To derive the sensitivity of the blade solidity, its definition in Equation 3.19 is used.

$$\frac{d\sigma}{d\beta} = \frac{-\sigma}{r}\frac{dr}{d\beta} \tag{4.29}$$

Similarly, the differentials of the thrust and torque coefficients with respect to twist deformation in momentum theory are derived using Equation 3.14 and Equation 3.15, respectively.

$$\frac{d}{d\beta}C_t^{\mathsf{M}} = \begin{cases} 4(1+2a)F\frac{da}{d\beta} + 4a(1+a)\frac{dF}{d\beta}, & \text{if } a \geq -0.326 \\ 1.39F\frac{da}{d\beta} + (1.39(1+a) - 1.816)\frac{dF}{d\beta}, & \text{otherwise} \end{cases} \tag{4.30}$$

$$\frac{d}{d\beta}C_q^{\mathsf{M}} = 4(1+a)\frac{wr}{V_\infty}F\frac{da'}{d\beta} + 4a'\frac{wr}{V_\infty}F\frac{da}{d\beta} + 4a'(1+a)\frac{wr}{V_\infty}\frac{dF}{d\beta} + 4a'(1+a)\frac{\omega}{V_\infty}F\frac{dr}{d\beta} \tag{4.31}$$

In these expressions, the sensitivity of the Prandtl loss factor with respect to twist deformation $\frac{dF}{d\beta}$ appears. Recall that this can be written as the product of the tip-loss factor and the root-loss factor. According to Equation 3.11 and Equation 3.12, both factors depend solely on r and φ. Therefore, the differential $dF/d\beta$ can be decomposed into partial derivatives with respect to these parameters. Furthermore, using these equations, the partial derivatives of F_{tip} and F_{root} with respect to the inflow angle can be obtained directly.

$$\frac{dF}{d\beta} = \left(\frac{\partial F_{\mathsf{tip}}}{\partial\varphi}F_{\mathsf{root}} + F_{\mathsf{tip}}\frac{\partial F_{\mathsf{root}}}{\partial\varphi}\right)\frac{\partial\varphi}{\partial\beta} + \left(\frac{\partial F_{\mathsf{tip}}}{\partial r}F_{\mathsf{root}} + F_{\mathsf{tip}}\frac{\partial F_{\mathsf{root}}}{\partial r}\right)\frac{\partial r}{\partial\beta} \tag{4.32}$$

$$\frac{\partial F_{\mathsf{tip}}}{\partial\varphi} = -\frac{N_b\left(r_{\mathsf{tip}} - r\right)}{\pi r|\sin\varphi|}\frac{\cos\varphi}{\sin\varphi}\frac{1}{\sqrt{\exp\left(\frac{N_b\left(r_{\mathsf{tip}}-r\right)}{r|\sin\varphi|}\right) - 1}} \tag{4.33}$$

$$\frac{\partial F_{\mathsf{root}}}{\partial\varphi} = -\frac{N_b\left(r - r_{\mathsf{root}}\right)}{\pi r|\sin\varphi|}\frac{\cos\varphi}{\sin\varphi}\frac{1}{\sqrt{\exp\left(\frac{N_b\left(r-r_{\mathsf{root}}\right)}{r_{\mathsf{root}}|\sin\varphi|}\right) - 1}} \tag{4.34}$$

To investigate the behaviour of these derivatives near the blade ends, the limits are evaluated as r approaches r_{tip} from below ($r \to r_{\mathsf{tip}}^-$) in Equation 4.33 and r approaches r_{root} from above ($r \to r_{\mathsf{root}}^+$) in Equation 4.34. In both cases, the resulting limit is indeterminate because both the numerator and denominator reach zero. Therefore, l'Hôpital's rule is applied to evaluate this limit.

$$\lim_{u\to 0^+}\frac{u}{\sqrt{e^u - 1}} = \lim_{u\to 0^+}\frac{1}{\frac{d}{du}\left(\sqrt{e^u - 1}\right)} = \lim_{u\to 0^+}\frac{2\sqrt{e^u - 1}}{e^u} = 0 \tag{4.35}$$

As a result, $\partial F_{\text{tip}}/\partial\varphi$ and $\partial F_{\text{root}}/\partial\varphi$ approach zero at the blade tip and root, respectively. Since F_{tip} and F_{root} also vanish at these locations, the inflow angle derivatives in Equation 4.32 vanish at the blade ends.

The radial derivatives, on the other hand, require more careful consideration. Similarly, these partial derivatives can be obtained using Equation 3.11 and Equation 3.12.

$$\frac{\partial F_{\text{tip}}}{\partial r} = -\frac{N_b}{\pi|\sin\varphi|}\frac{1}{\sqrt{\exp\left(\frac{N_b\left(r_{\text{tip}}-r\right)}{r|\sin\varphi|}\right)-1}}\cdot\frac{r_{\text{tip}}-r\frac{dr_{\text{tip}}}{dr}}{r^2} \tag{4.36}$$

$$\frac{\partial F_{\text{root}}}{\partial r} = -\frac{N_b}{\pi|\sin\varphi|}\frac{1}{\sqrt{\exp\left(\frac{N_b\left(r-r_{\text{root}}\right)}{r_{\text{root}}|\sin\varphi|}\right)-1}}\cdot\frac{r\frac{dr_{\text{root}}}{dr}-r_{\text{root}}}{r_{\text{root}}^2} \tag{4.37}$$

Thus, the behaviour at the blade tip and root now depends on the radial derivatives of their respective radii, dr_{tip}/dr and dr_{root}/dr. For example, if $dr_{\text{tip}}/dr = dr_{\text{root}}/dr = 0$, the numerators in Equation 4.36 and Equation 4.37 are constant, causing the derivatives to diverge at the corresponding locations. However, if $dr_{\text{tip}}/dr = dr_{\text{root}}/dr = 1$, the same limit can be evaluated as in Equation 4.35, leading to vanishing $\partial F_{\text{tip}}/\partial r$ and $\partial F_{\text{root}}/\partial r$ at the blade tip and root, respectively.

Unfortunately, an analytical expression for dr_{tip}/dr and dr_{root}/dr could not be determined. For the pitch sensitivities, however, the radial contribution in Equation 4.32 is assumed to be negligible, because the derivative of the flow angle $d\varphi/d\beta$ is expected to dominate $dr/d\beta$ by several orders of magnitude. This assumption is later proven to be correct in section 4.3 by comparison with numerically computed sensitivities, see Figure 4.4e and Figure 4.6e.

Consequently, an exact evaluation of dr_{tip}/dr and dr_{root}/dr is not required.

$$\frac{dF}{d\beta} \approx \left(\frac{\partial F_{\text{root}}}{\partial\varphi}F_{\text{tip}} + F_{\text{root}}\frac{\partial F_{\text{tip}}}{\partial\varphi}\right)\frac{\partial\varphi}{\partial\beta} \tag{4.38}$$

Finally, the twist sensitivity model is closed by a residual vector that equates the derivatives of both the thrust and torque coefficients from Blade Element theory and Momentum theory.

$$\mathbf{R_{BEM}} = \begin{bmatrix} \frac{dC_t^{\text{BE}}}{d\beta} - \frac{dC_t^{\text{M}}}{d\beta} & \frac{dC_q^{\text{BE}}}{d\beta} - \frac{dC_q^{\text{M}}}{d\beta} \end{bmatrix}^T := 0 \tag{4.39}$$

This residual vector is minimized, to solve for the differentials $da/d\beta$ and $da'/d\beta$, using the Newton-Raphson method with the iteration scheme as shown below.

$$\begin{bmatrix} \frac{da}{d\beta} \\ \frac{da'}{d\beta} \end{bmatrix}_{i+1} = \begin{bmatrix} \frac{da}{d\beta} \\ \frac{da'}{d\beta} \end{bmatrix}_{i} - \begin{bmatrix} \frac{\partial R_1}{\partial(\frac{da}{d\beta})} & \frac{\partial R_1}{\partial(\frac{da'}{d\beta})} \\ \frac{\partial R_2}{\partial(\frac{da}{d\beta})} & \frac{\partial R_2}{\partial(\frac{da'}{d\beta})} \end{bmatrix}_{i}^{-1} \cdot \mathbf{R_{BEM}} \tag{4.40}$$

4.2.2. Sensitivities to Sweep Deformation

The expressions for the sweep sensitivities are largely similar as those derived for twist in subsection 4.2.1, with the primary difference being the replacement of $d/d\beta$ by $d/d\Lambda$. Similarly, the methodology for solving the sensitivity model using the iterative numerical scheme remains the same and will not be repeated here. However, the geometric sensitivities associated with sweep deformations are different and will be explicitly derived. Note that during these derivations, it is assumed that the orientation of airfoil sections remain unchanged under blade deformations. In other words, it is assumed that the airfoil sections remain parallel to the incoming flow, even when the blade is rotated around the z-axis. For small deformation angles, this approximation is considered reasonable.

When applying the same derivation for sweep as was conducted for twist, three geometric sensitivities appear: $dS/d\Lambda$, $d\beta/d\Lambda$ and $dr/d\Lambda$. Similar to the case of twist, it is assumed that the planform area

does not depend on sweep, since neither the chord length nor the length of the quarter-chord line changes due to such a deflection. Additionally, it is assumed that the sensitivity of the twist angle with respect to sweep deformation is zero, because the orientation of the chord line relative to the global xz-plane is unaltered.

$$\frac{dS}{d\Lambda} = 0 \tag{4.41}$$

$$\frac{d\beta}{d\Lambda} = 0 \tag{4.42}$$

The only remaining sensitivity is therefore that of the radial displacement $dr/d\Lambda$, which represents the radial shift of the blade sections due to sweep. In this differential, the radius r is defined as the distance to the z-axis. Since a rotation around the z-axis does not affect the distance to it, it can be concluded that also this sensitivity vanishes.

$$\frac{dr}{d\Lambda} = 0 \tag{4.43}$$

Note that the issue with the unknown radial derivative of the Prandtl loss factor, as explained in subsection 4.2.1, is avoided because $\partial F/\partial r$ is now multiplied by $dr/d\Lambda$, which equals zero.

4.2.3. Sensitivities to Lean Deformation

Also the sensitivities to lean deformations are derived analogously to those for twist. The resulting geometric lean sensitivities are $dS/d\Psi$, $d\beta/d\Psi$, $dr/d\Psi$ and $d\Lambda/d\Psi$. Consistent with the earlier assumptions, the sensitivities of the planform area and twist are taken as zero.

$$\frac{dS}{d\Psi} = 0 \tag{4.44}$$

$$\frac{d\beta}{d\Psi} = 0 \tag{4.45}$$

In order to compute $dr/d\Psi$, the radius is once more defined as the distance to the rotation axis.

$$\frac{dr}{d\Psi} = \frac{d}{d\Psi}\sqrt{x^2+y^2} = \frac{1}{2r}\left(2x\frac{dx}{d\Psi} + 2y\frac{dy}{d\Psi}\right) = \frac{y}{r}\frac{dy}{d\Psi} \tag{4.46}$$

Similar to the derivations of $dQCA/d\beta$ and $dFA/d\beta$, two temporary parameters r' and ζ are introduced to determine $dy/d\Psi$ and $dFA/d\Psi$, but these are now defined slightly different. Again, r' is defined as the distance from the blade's quarter-chord point to the deformation axis, which is now the global x-axis, while ζ represents the angle between the global y-axis and r'. In this case, however, $d\zeta/d\Psi = 1$.

$$r' := \sqrt{y^2 + FA^2} \tag{4.47}$$

$$\tan\zeta := \frac{FA}{y} \tag{4.48}$$

From these two definitions, the variations of the quarter-chord's y- and z-coordinate with respect to lean deformation can be determined.

$$\frac{dy}{d\Psi} = -FA \tag{4.49}$$

$$\frac{dFA}{d\Psi} = y \tag{4.50}$$

Substitution of $dy/d\Psi$ into Equation 4.46 yields the final expression for $dr/d\Psi$.

$$\frac{dr}{d\Psi} = \frac{-y \cdot FA}{r} \tag{4.51}$$

Since this derivative is non-zero for blades with lean, the unknown radial derivative of the Prandtl loss factor may result in an increased error. Nevertheless, it is assumed that the impact of this effect remains negligible.

Lastly, using the definition of the sweep angle given by Equation 2.2, the analytical expression for the sensitivity $d\Lambda/d\Psi$ can be derived.

$$\frac{d\Lambda}{d\Psi} = \frac{-QCA}{y^2\left(1+\left(\frac{QCA}{y}\right)^2\right)}\frac{dy}{d\Psi} = \frac{QCA \cdot FA}{y^2+QCA^2} \tag{4.52}$$

4.2.4. Sensitivities to Radial Deformation

The two remaining sensitivities of the aerodynamic loads with respect to blade deformations are those in the translational degrees of freedom. Instead of computing the derivatives directly with respect to x and y, they can be expressed in terms of the radial deformations [23].

$$r = \sqrt{x^2+y^2} \Rightarrow \begin{cases} \dfrac{d}{dx} = \dfrac{x}{r}\dfrac{d}{dr} \\ \dfrac{d}{dy} = \dfrac{y}{r}\dfrac{d}{dr} \end{cases} \tag{4.53}$$

$$\begin{aligned} \Rightarrow \frac{d}{dx}\begin{bmatrix}\tilde{\mathbf{f}}_\mathbf{a} \\ \tilde{\mathbf{m}}_\mathbf{a}\end{bmatrix} &= \frac{q_\infty x}{r}\frac{dS}{dr}\begin{bmatrix}C_x & 0 & C_z & 0 & C_m c & 0\end{bmatrix}^T\left(\frac{V}{V_\infty}\right)^2 \\ &+ \frac{q_\infty x S}{r}\begin{bmatrix}C_{x_r} & 0 & C_{z_r} & 0 & C_{m_r} c & 0\end{bmatrix}^T\left(\frac{V}{V_\infty}\right)^2 \\ &+ \frac{q_\infty x S}{r}\begin{bmatrix}C_x & 0 & C_z & 0 & C_m c & 0\end{bmatrix}^T\frac{2V}{V_\infty^2}\frac{dV}{dr} \end{aligned} \tag{4.54}$$

$$\begin{aligned} \Rightarrow \frac{d}{dy}\begin{bmatrix}\tilde{\mathbf{f}}_\mathbf{a} \\ \tilde{\mathbf{m}}_\mathbf{a}\end{bmatrix} &= \frac{q_\infty y}{r}\frac{dS}{dr}\begin{bmatrix}C_x & 0 & C_z & 0 & C_m c & 0\end{bmatrix}^T\left(\frac{V}{V_\infty}\right)^2 \\ &+ \frac{q_\infty y S}{r}\begin{bmatrix}C_{x_r} & 0 & C_{z_r} & 0 & C_{m_r} c & 0\end{bmatrix}^T\left(\frac{V}{V_\infty}\right)^2 \\ &+ \frac{q_\infty y S}{r}\begin{bmatrix}C_x & 0 & C_z & 0 & C_m c & 0\end{bmatrix}^T\frac{2V}{V_\infty^2}\frac{dV}{dr} \end{aligned} \tag{4.55}$$

The derivatives in Equation 4.54 and Equation 4.55 are obtained analogously to the twist sensitivities as well. Even in this derivation, the partial derivative of the Prandtl loss factor with respect to r is neglected as it could not be determined exactly.

$$\frac{dF}{dr} = \frac{\partial F}{\partial r} + \frac{\partial F}{\partial \varphi}\frac{\partial \varphi}{\partial r} \approx \frac{\partial F}{\partial \varphi}\frac{\partial \varphi}{\partial r} \tag{4.56}$$

The resulting geometric sensitivities that appear are $d\beta/dr$, $d\Lambda/dr$ and dS/dr. First of all, it is assumed that twist remains constant with variations in radius because a radial displacement of the blade sections should not change the angular orientation of the chord line. Therefore, the local twist distribution is preserved.

$$\frac{d\beta}{dr} = 0 \tag{4.57}$$

The expression for $d\Lambda/dr$ is derived analytically from the definition of the sweep angle. Since Λ depends on both the x- and y-coordinate of the quarter-chord line, the chain rule is applied, leading to zero sensitivity.

$$\frac{d\Lambda}{dr} = \left(\frac{x}{r}\frac{d}{dx} + \frac{y}{r}\frac{d}{dy}\right)\arctan\left(\frac{QCA}{y}\right) = 0 \tag{4.58}$$

Note that in this derivation, $dQCA/dx = 1$ because QCA is simply the x-coordinate of the quarter-chord line.

Finally, the variation of the planform area with respect to radial deformation must be determined. In contrast to the other degrees of freedom, dS/dr does not vanish, as stretching the blade directly increases its planform area. To account for this effect, the area increase is taken to be proportional to the local chord length multiplied by the span of the blade section and divided by the total blade span. Any change in chord length due to blade stretching, which could be captured through Poisson's ratio, is neglected in this work.

$$\frac{dS}{dr} = \frac{c\Delta r}{r_{\text{tip}} - r_{\text{root}}} \tag{4.59}$$

4.3. Validation of Aerodynamic Sensitivities

To validate the analytical sensitivity expressions, the results are compared with numerical calculations under the following operating conditions: advance ratios ranging from 0.6 to 1.5, a fixed collective pitch angle of $\beta_{0.7R} = 20°$, and an incoming velocity of 30 m/s at sea level. For the numerical differentiation, central differencing is applied with a small perturbations of $\Delta\beta = 10^{-7}$ degrees, $\Delta\Lambda = 10^{-7}$ degrees, $\Delta\Psi = 10^{-7}$ degrees, and $\Delta r = 10^{-7}$ m, to evaluate the sensitivities with respect to twist, sweep, lean and radial deformation, respectively. Similarly, the lift and drag curve slopes used in Equation 4.13 are obtained by perturbing the angle of attack with a step size of $\Delta\alpha = 10^{-7}$ degrees. These small perturbations ensure numerical accuracy while minimizing truncation errors [23]. Furthermore, 50 spanwise cosine-spaced elements were used for the aerodynamic analysis. To assess the robustness and applicability of the derived sensitivities for different blade designs, both the baseline *XPROP* geometry and its swept configuration *XPROP*-Λ are analysed.

The model for computing the aerodynamic sensitivities with respect to twist deformation, developed in subsection 4.2.1, has not only been extended to account for propeller blades with sweep and lean, but also improved compared to the original model by Rotundo [23]. Before discussing the aerodynamic sensitivity results for curved blades, these improvements are shown. To ensure a fair comparison, the analyses are performed for a completely straight version of the *XPROP* propeller blade, with $QCA = 0$ mm and $FA = 0$ mm along the span, which removes the effect of the geometric sensitivities. Figure 4.2 presents the comparison between analytical and numerical results for $dC_x/d\beta$ obtained with the original model, while Figure 4.3 shows the corresponding results for the improved version. These results are obtained using the same numerical settings as described above. The figures illustrate the spanwise distributions of the sensitivities for three advance ratios, $J = 0.6$, 0.9 and 1.5. Additionally, the absolute difference between the analytical and numerical sensitivity is shown, emphasizing the critical regions in advance ratio and spanwise position where the largest discrepancies occur. Comparisons between the original and improved models for other sensitivities with respect to twist deformation, as well as mathematical details on the specific improvements, are provided in Appendix C.

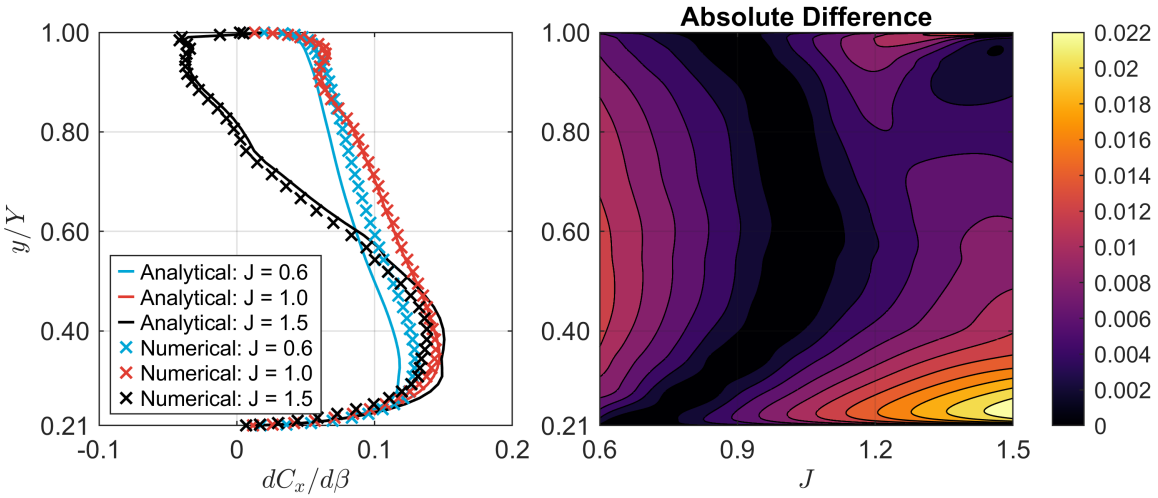

Figure 4.2: Comparison between analytically and numerically computed $dC_x/d\beta$ using the original model of Rotundo [23] for the modified *XPROP* propeller at $\beta_{0.7R} = 20°$ and $V_\infty = 30$ m/s.

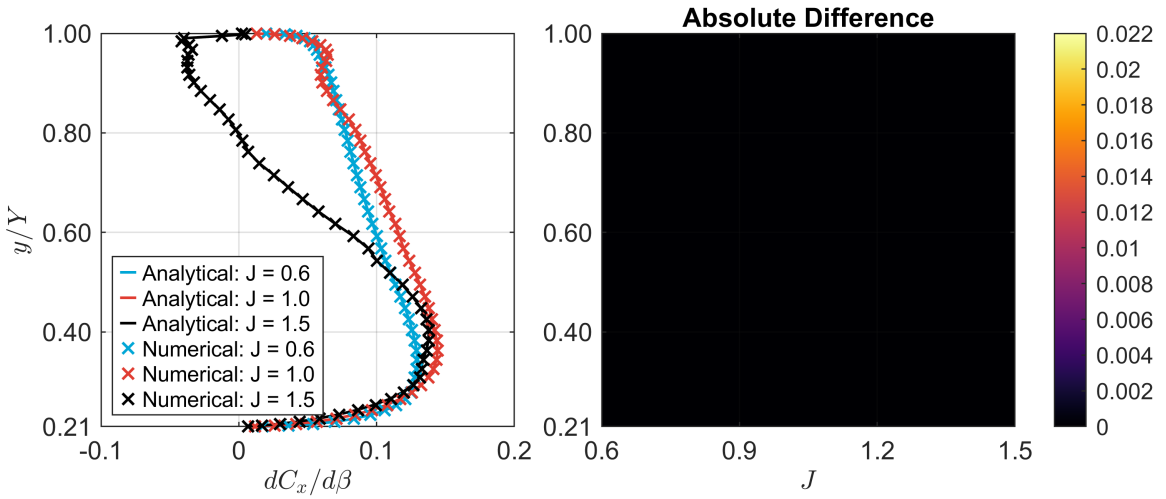

Figure 4.3: Comparison between analytically and numerically computed $dC_x/d\beta$ using the model developed in subsection 4.2.1 for the modified *XPROP* propeller at $\beta_{0.7R} = 20°$ and $V_\infty = 30$ m/s.

The figures clearly show that, across the entire range of J and along the full blade span, the discrepancies between analytical and numerical results are reduced. The absolute differences in Figure 4.3 are substantially smaller than those in Figure 4.2, with the maximum error reduced by more than an order of magnitude. These results confirm that the adjustments introduced in this work are a significant improvement. Beyond increasing the accuracy of the sensitivities, the refinements are also expected to increase the efficiency and robustness of the aeroelastic analysis by enabling faster and more stable convergence of the tightly coupled procedure.

Figures Figure 4.4 to Figure 4.7 present the comparison between the analytical and numerical results for the twist sensitivities using the model developed in subsection 4.2.1. Figure 4.4 shows the sensitivities for *XPROP* that directly appear in Equation 4.11, except for $dS/d\beta$. The corresponding geometric twist sensitivities, which are particularly relevant when analysing curved blades, are shown separately in Figure 4.5. Similarly, Figure 4.6 and Figure 4.7 show the (geometric) twist sensitivities for *XPROP*-Λ. Since the geometric sensitivities are independent of the advance ratio, only one representative curve is shown. Similar comparisons for the sweep, lean and radial sensitivities are presented in Appendix D.

The figures show a good overall agreement between the analytically and numerically computed twist sensitivities. All trends are captured accurately, as the plots show maximum absolute differences that are roughly two orders of magnitude smaller than the sensitivities themselves. Most importantly, the terms $dC_x/d\beta$, $dC_z/d\beta$, $dC_m/d\beta$ and $dV/d\beta$, which appear directly in Equation 4.11, closely match the numerical results. In the end, these sensitivities directly determine the accuracy of the aerodynamic stiffness matrix, making their reliable prediction of primary importance. Although the maximum error does increase from *XPROP* to *XPROP*-Λ, the sensitivities remain reasonably accurate, showing the robustness of the twist sensitivities to sweep. Possibly, the results could have been further improved, as it is assumed in Equation 4.12 that the polar data only depends on the angle of attack, while it also depends on the velocity through the Reynolds number. Incorporating this velocity dependency in the analytical sensitivities might reduce the observed deviations.

In general, the largest errors in twist sensitivities are observed at the root for *XPROP*, while they appear at the tip for *XPROP*-Λ. Although the results for $dF/d\beta$ confirm that the assumption in Equation 4.38 is sufficiently accurate, including a more precise sensitivity of the Prandtl loss factor, by development of dr_{rip}/dr and dr_{root}/dr, might potentially increase the overall accuracy at the blade ends. The expected impact, however, is limited, because $dr/d\beta$ is much smaller than $d\varphi/d\beta$. Regarding the structural deformations, the small error at the root for *XPROP* is unlikely to have a large impact on the predicted deformation, since the dynamic pressure is low in these regions, resulting in small load variations [19]. In contrast, the largest errors occur at the blade tip for *XPROP*-Λ, where the dynamic pressure is high. This could lead to a more noticeable impact on the structural deformation.

Also the geometric sensitivities $d\Lambda/d\beta$ and $dr/d\beta$ show negligible differences, even for the swept blade design. The results for $dS/d\beta$ are noisy, but since their magnitude is small for both *XPROP* and *XPROP*-Λ, it is reasonable to assume them to be zero. All in all, the results indicate that the analytical expressions accurately predict twist sensitivities and that these predictions are robust for varying blade designs.

The analytically computed sensitivities to sweep, lean and radial deformation show good agreement with those computed numerically as well, see Appendix D. Unlike the twist sensitivities, the largest discrepancies are located more towards the blade tip for both *XPROP* and *XPROP*-Λ, which could impact the structural deformation prediction of the model. Nevertheless, all sensitivities predictions are acceptable, confirming their robustness to different blade geometries. Even the analytical predictions for $dF/d\Psi$ and dF/dr closely match the numerical results, confirming the assumption that the radial effect is indeed negligible. Lastly, all geometric sensitivities predicted to vanish show indeed no dependency in the numerical computations, although $dr/d\Lambda$, $dS/d\Lambda$ and $dS/d\Psi$ exhibit some low-magnitude noise, supporting the validity of these assumptions. Furthermore, $dr/d\Psi$, $d\Lambda/d\Psi$ and dS/dr are predicted with high accuracy, which ensures that these geometric sensitivities can be applied with confidence. Because the absolute error of dS/dr follows the same trend as the sensitivity itself, it is likely due to a constant fractional offset, possibly caused by neglecting changes in chord length. Nevertheless, the magnitude of this error remains relatively small.

It should be noted that the magnitudes of the sweep and lean sensitivities are smaller than those of twist, while the radial sensitivities are significantly larger. However, these results must be interpreted with care, as the variation of a given quantity not only depends on the sensitivity magnitude but also on the magnitude of the corresponding deformation. Since the deformations in the rotational degrees of freedom are expected to be of the same order of magnitude, the sensitivity magnitude itself determines whether the effect is significant and must be accounted for, or whether it can be considered negligible. The deformations in the translational degrees of freedom, however, are expected to be very small (as later confirmed in Figure 4.8a and Figure 4.9a, where the deformations remain below 0.1% of the blade span), which reduces their overall influence despite the larger sensitivities. Given that all sensitivities are predicted with reasonable accuracy, none are neglected in the subsequent analysis of this work.

Finally, to demonstrate that the computational cost of the analytical sensitivities is lower than that of the numerical approach, the two methods are compared for each degree of freedom, see Table 4.1. The reported computational times correspond to the evaluation of the sensitivities for advance ratios ranging from 0.6 to 1.5 with 0.1 increments. The corresponding numerical computational cost is evaluated for the same set of sensitivities and load cases.

Table 4.1: Comparison of the computational cost required for evaluation of the analytical and numerical sensitivities, computed on an *AMD Ryzen 5 5500U* processor using multithreading in *MATLAB* across 6 cores.

Propeller	Method	t_β [s]	t_Λ [s]	t_Ψ [s]	t_r [s]
XPROP	Numerical	6.753	6.750	6.959	3.728
	Analytical	0.397	0.383	0.388	0.374
	Reduction (%)	94.1	94.3	94.4	90.0
XPROP-Λ	Numerical	6.598	6.656	6.542	4.093
	Analytical	0.388	0.373	0.373	0.254
	Reduction (%)	94.1	94.4	94.3	93.8

These results show that the analytical method comes indeed with a much lower computational cost than the numerical approach. With a reduction in computational time of at least 90%, this could have a significant impact on the overall efficiency of the aeroelastic analysis, depending on the number of iterations during which these sensitivities are applied, which in turn is influenced by the accuracy of the sensitivities themselves through Equation 4.2.

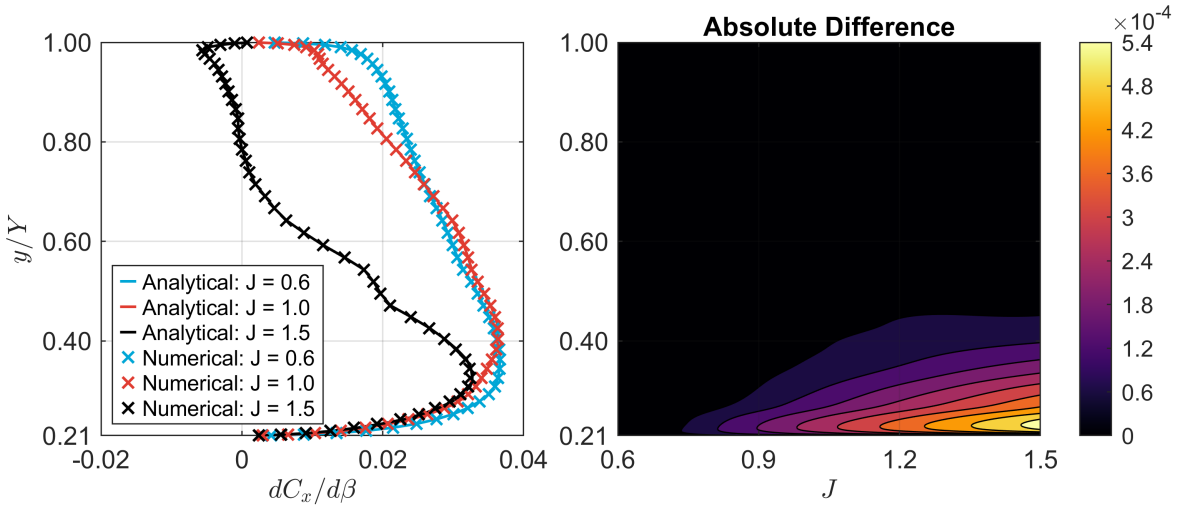

(a) Spanwise distribution of $dC_x/d\beta$.

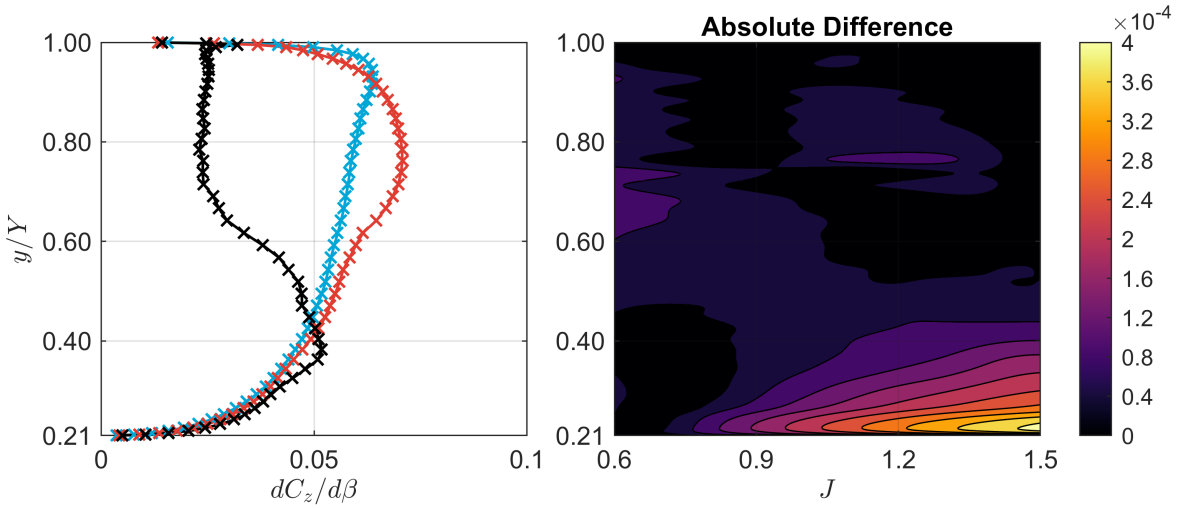

(b) Spanwise distribution of $dC_z/d\beta$.

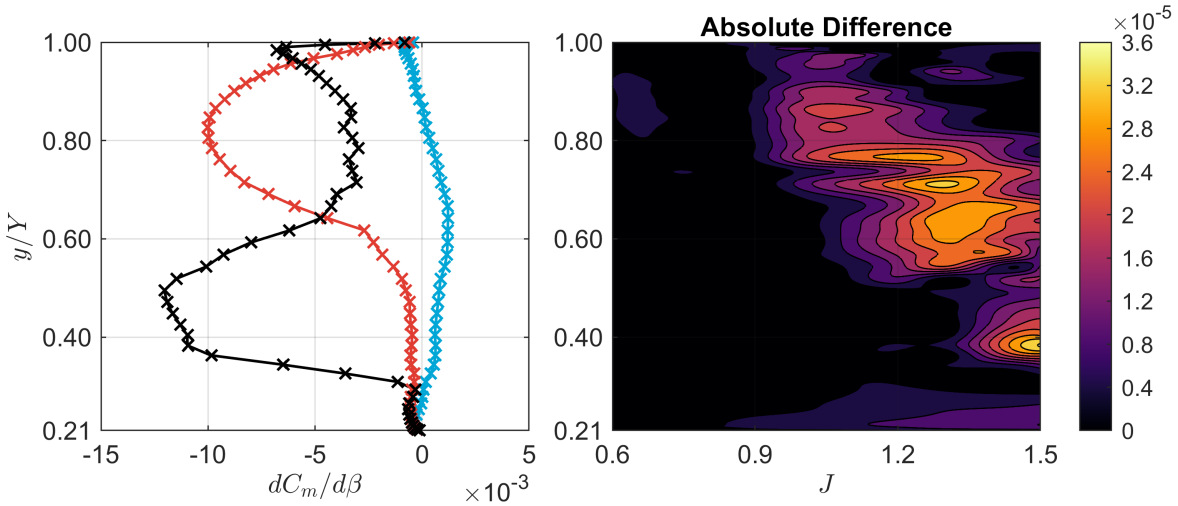

(c) Spanwise distribution of $dC_m/d\beta$.

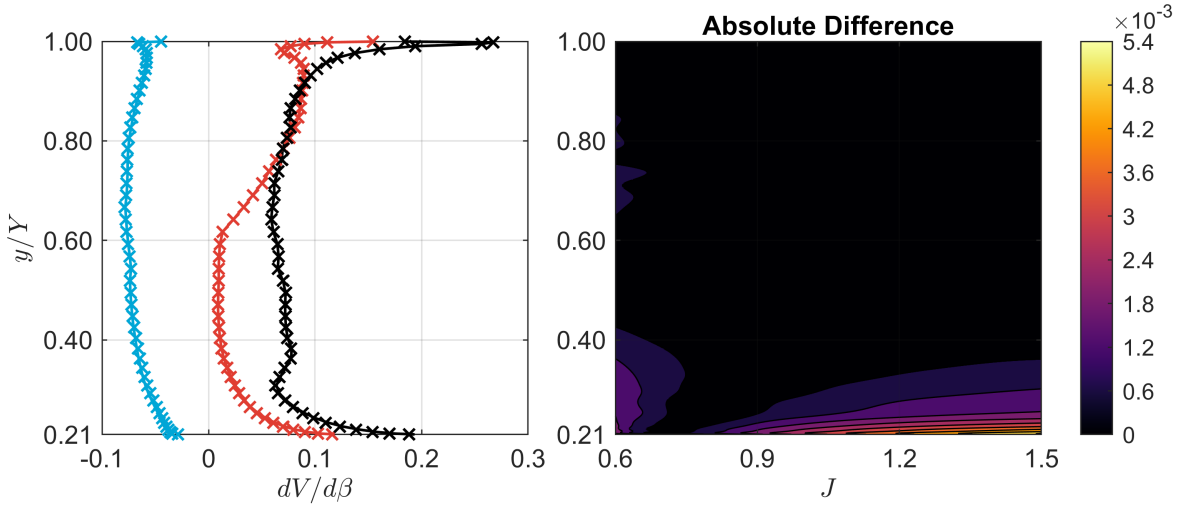

(d) Spanwise distribution of $dV/d\beta$.

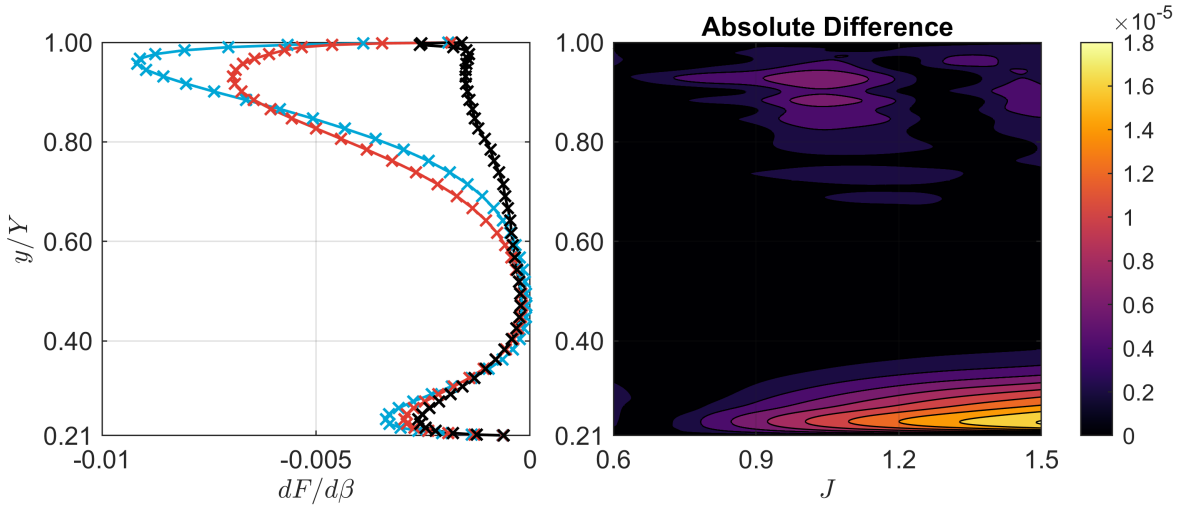

(e) Spanwise distribution of $dF/d\beta$.

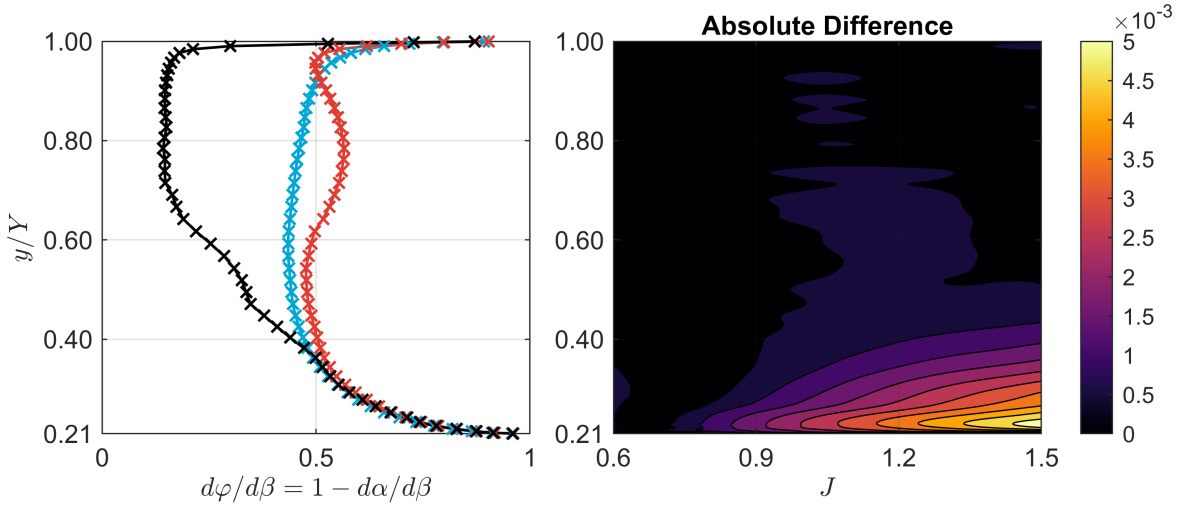

(f) Spanwise distribution of $d\varphi/d\beta$.

Figure 4.4: Comparison between the analytically and numerically computed twist sensitivities for the *XPROP* propeller at $\beta_{0.7R} = 20°$ and $V_\infty = 30$ m/s.

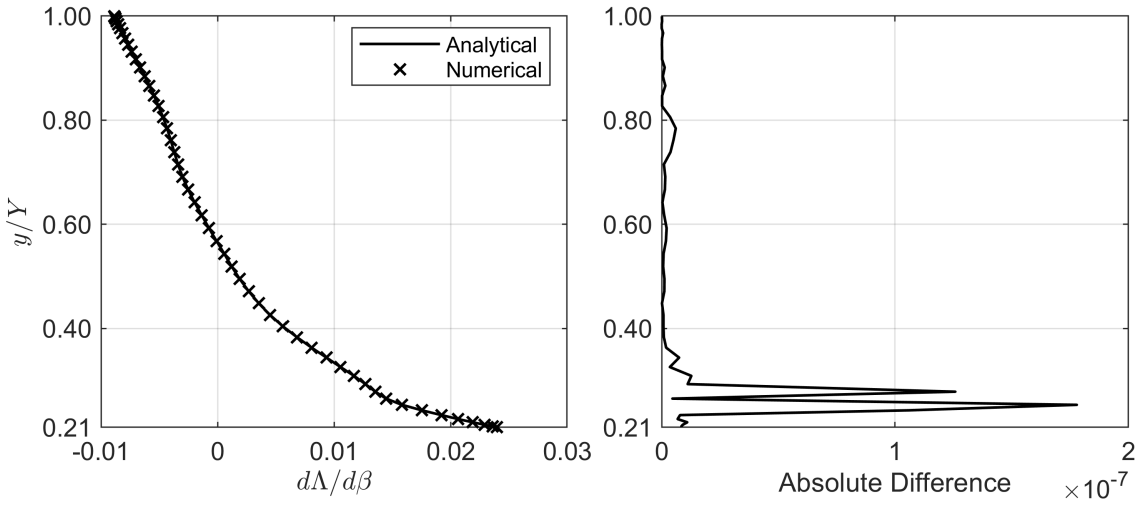

(a) Spanwise distribution of $d\Lambda/d\beta$.

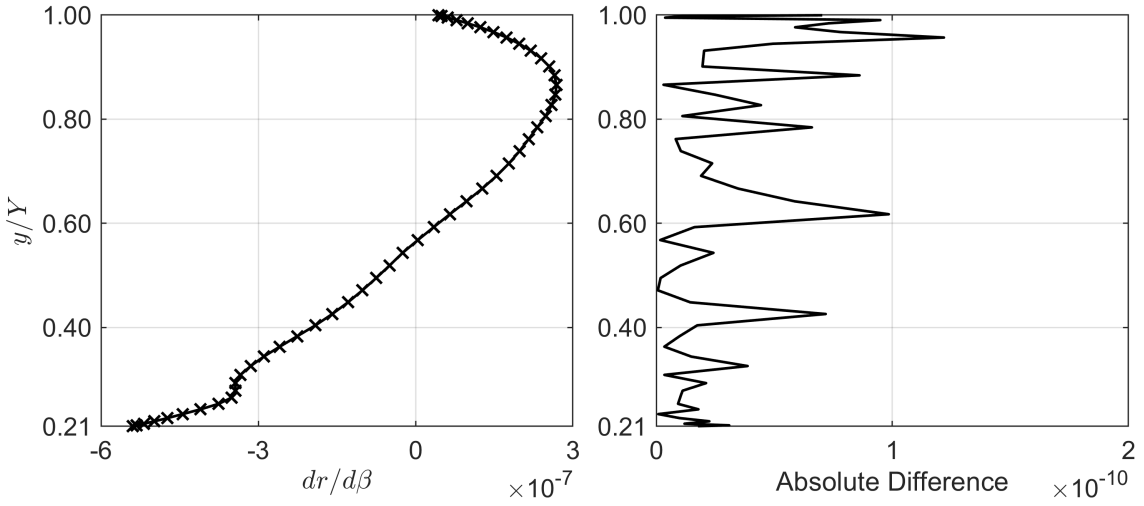

(b) Spanwise distribution of $dr/d\beta$.

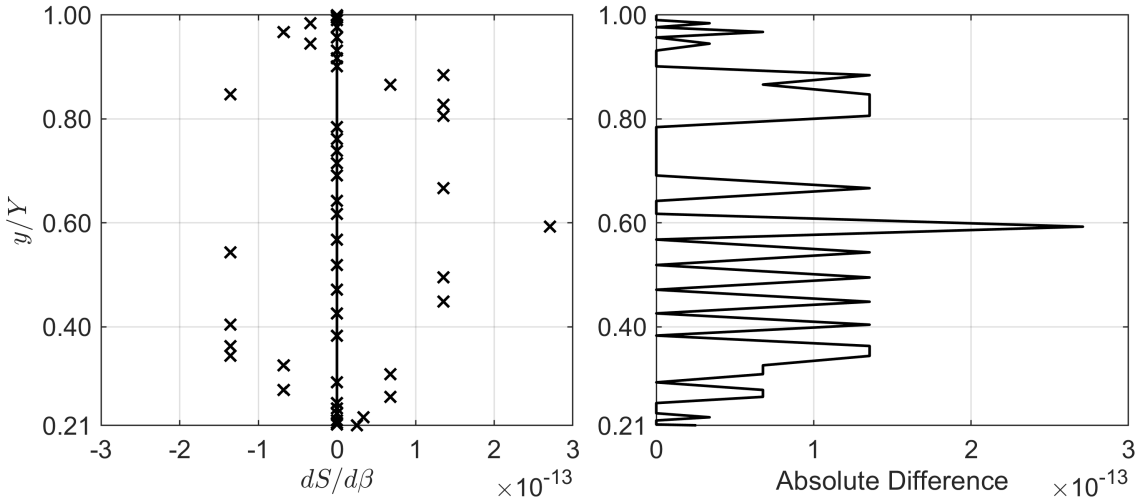

(c) Spanwise distribution of $dS/d\beta$.

Figure 4.5: Comparison between the analytically and numerically computed geometric twist sensitivities for the *XPROP* propeller at $\beta_{0.7R} = 20°$ and $V_\infty = 30$ m/s.

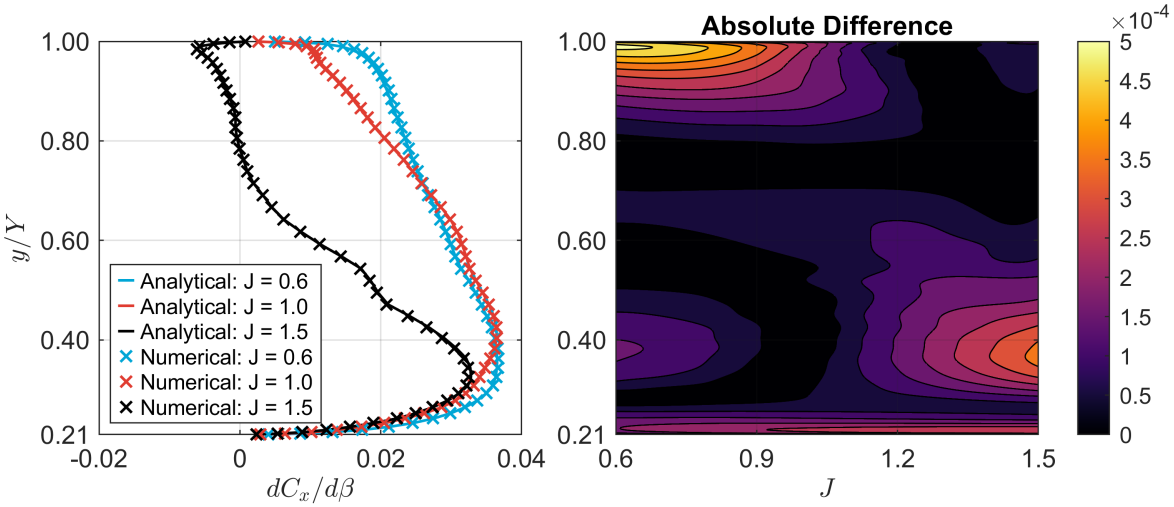

(a) Spanwise distribution of $dC_x/d\beta$.

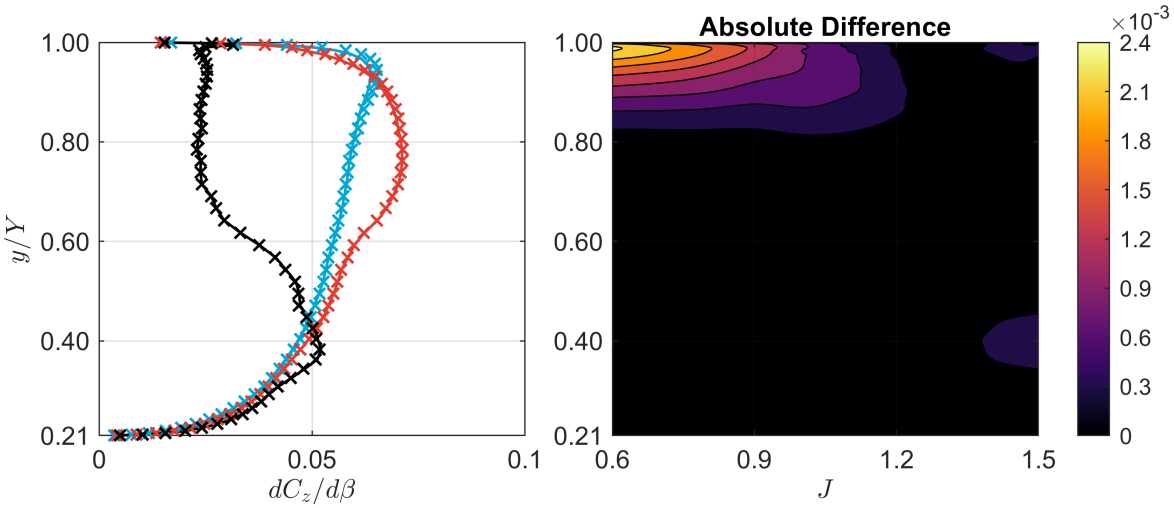

(b) Spanwise distribution of $dC_z/d\beta$.

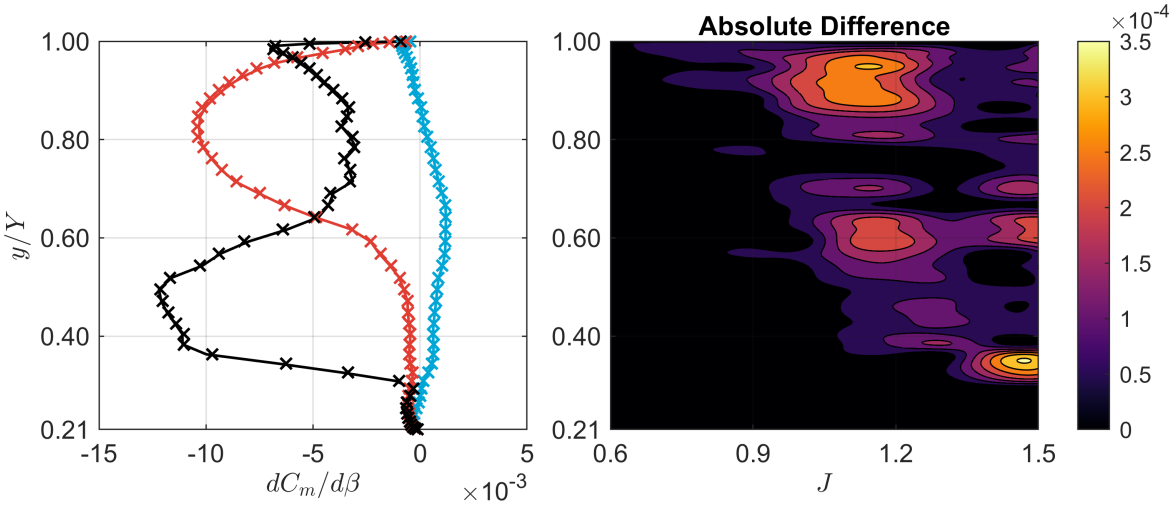

(c) Spanwise distribution of $dC_m/d\beta$.

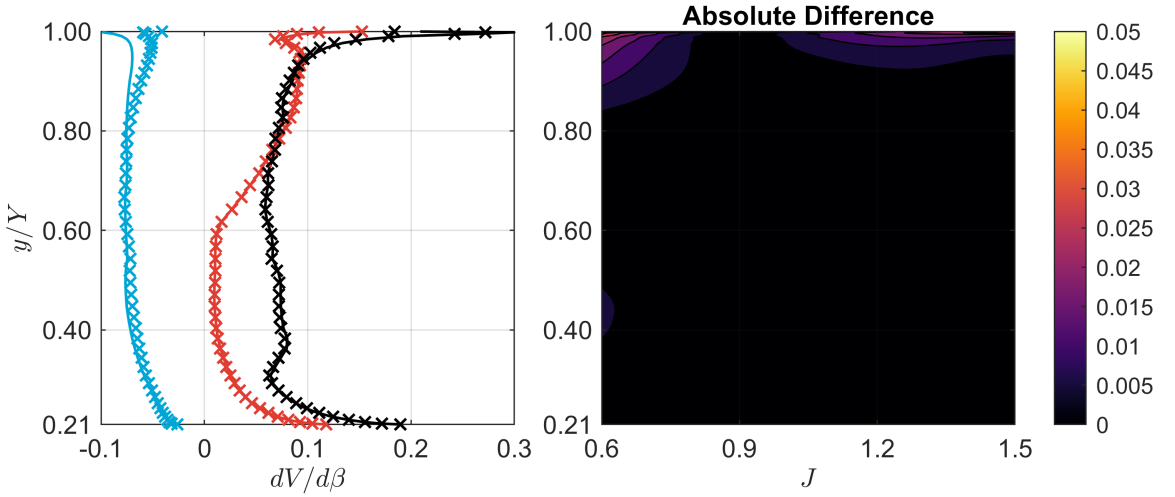

(d) Spanwise distribution of $dV/d\beta$.

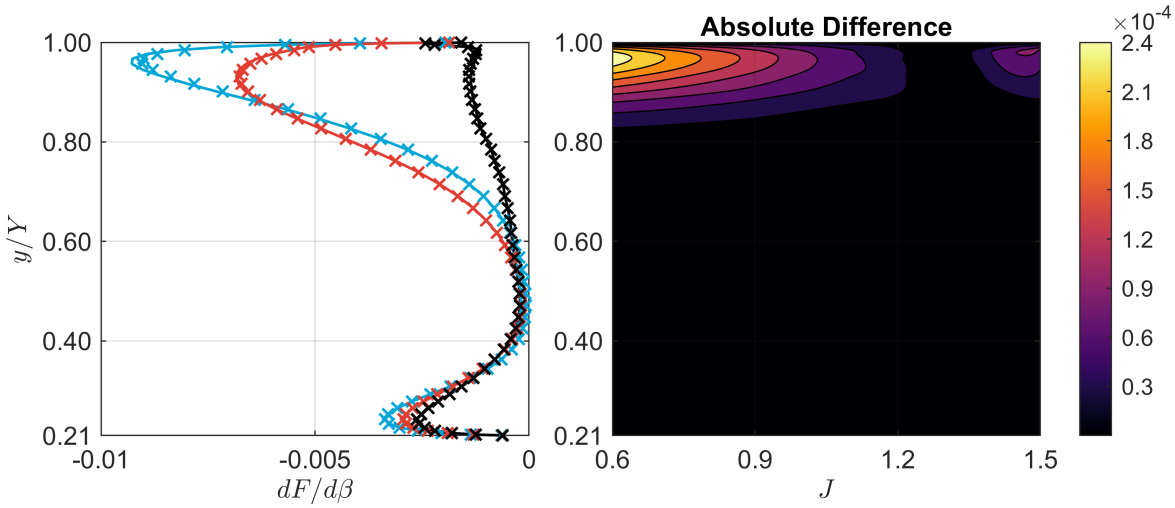

(e) Spanwise distribution of $dF/d\beta$.

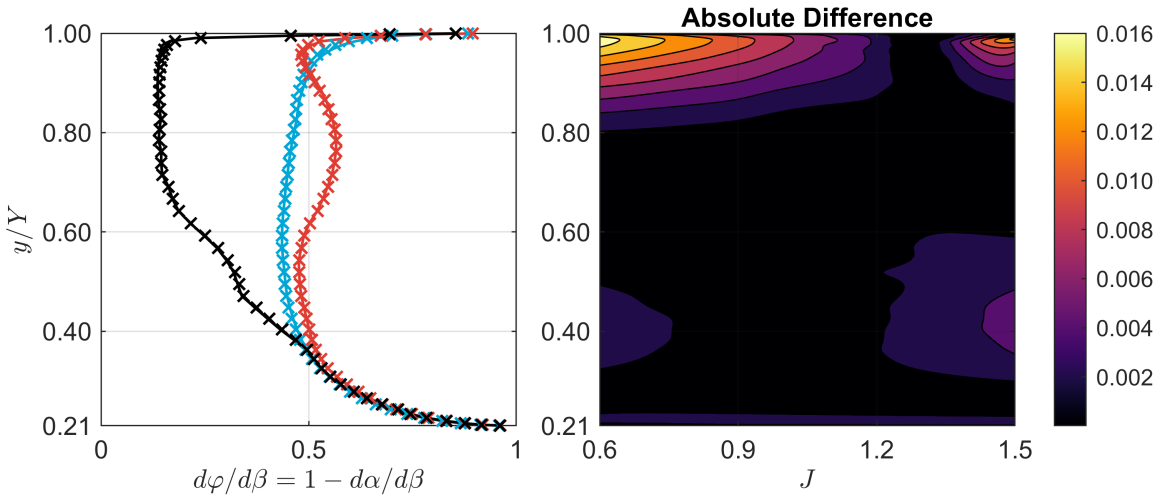

(f) Spanwise distribution of $d\varphi/d\beta$.

Figure 4.6: Comparison between the analytically and numerically computed twist sensitivities for the *XPROP*-Λ propeller at $\beta_{0.7R} = 20°$ and $V_\infty = 30$ m/s.

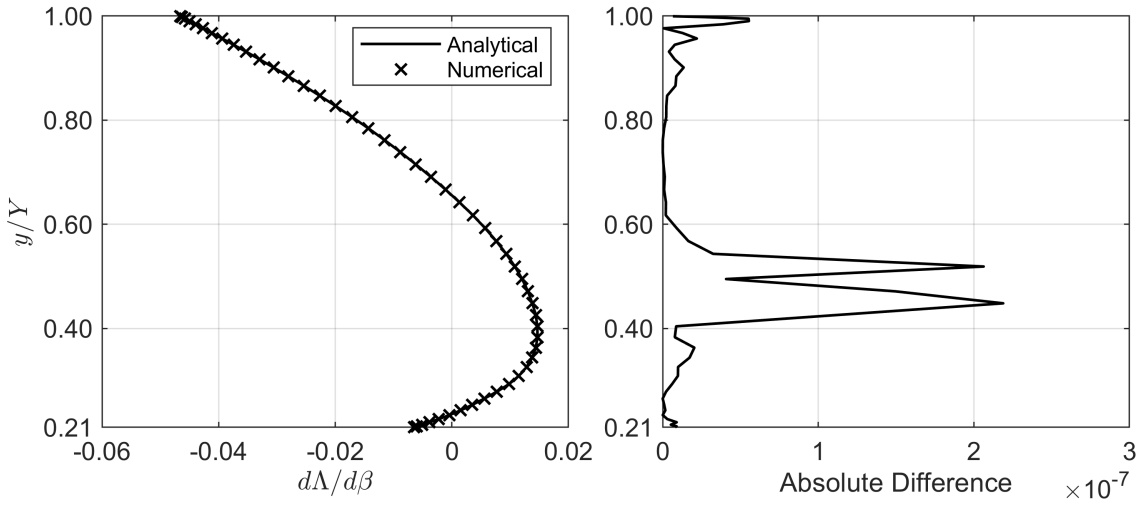

(a) Spanwise distribution of $d\Lambda/d\beta$.

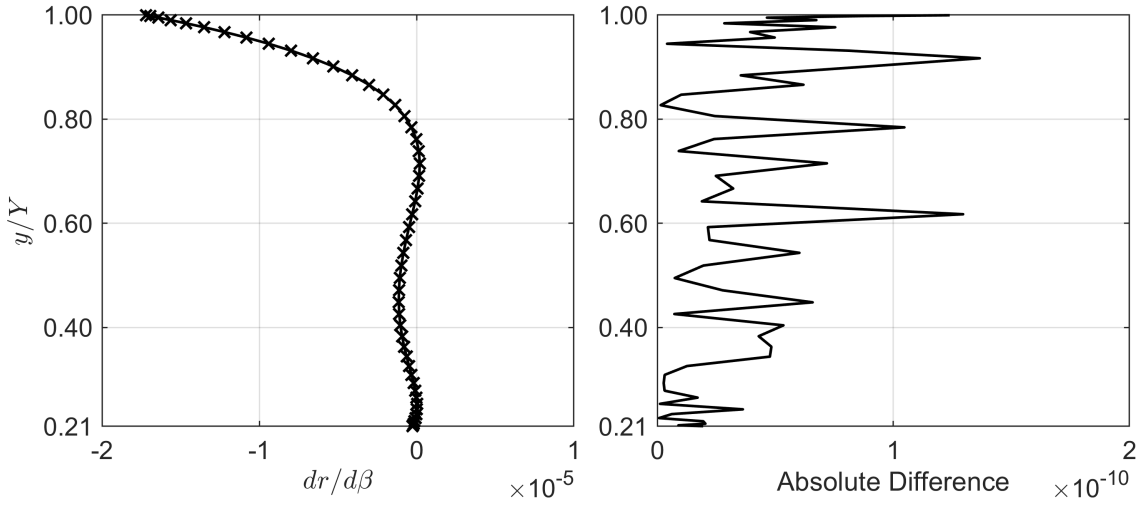

(b) Spanwise distribution of $dr/d\beta$.

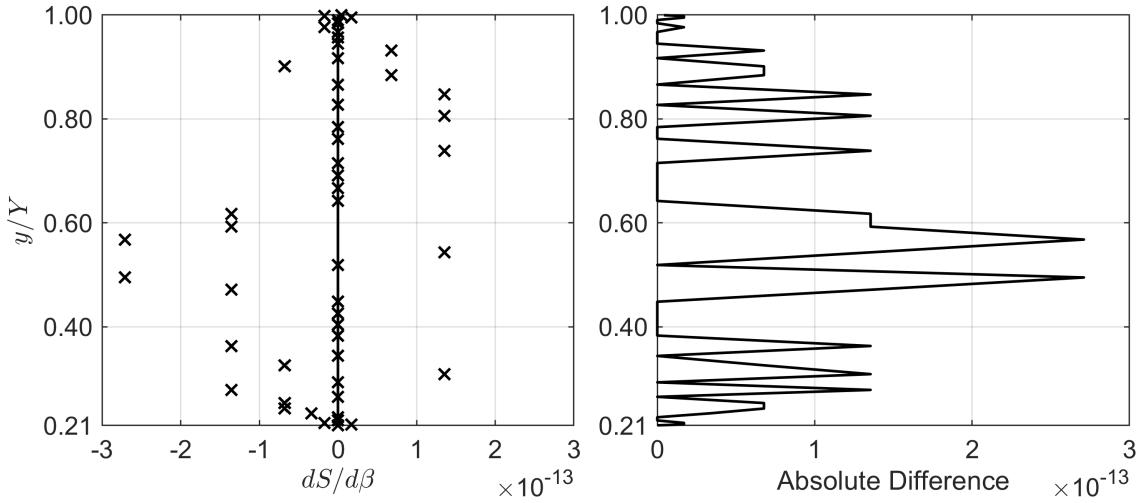

(c) Spanwise distribution of $dS/d\beta$.

Figure 4.7: Comparison between the analytically and numerically computed geometric twist sensitivities for the *XPROP*-Λ propeller at $\beta_{0.7R} = 20°$ and $V_\infty = 30$ m/s.

4.4. Verification of Aeroelastic Coupling

Now that the analytical expressions of the aerodynamic sensitivities have been derived and validated, the next step is to verify their correct implementation within the aeroelastic coupling framework. This step is crucial to ensure that the tightly coupled model converges to the correct blade deformation under prescribed load conditions. Therefore, the results of the tightly coupled (TC) model are compared with those from a loosely coupled (LC) model. This loosely coupled model operates as follows: in each iteration, the aerodynamic and centrifugal forces are first computed for the current blade geometry. These loads are then applied to the structural grid to obtain the corresponding blade deformation. The updated geometry is subsequently used to recompute the aerodynamic and centrifugal forces, which in turn produce a new deformation. This cycle is repeated until the differences in deformation between successive iterations fall below a specified tolerance, at which point the solution is considered converged to a static equilibrium [23]. As discussed in section 4.1, the tightly coupled model differs in that the blade geometry is updated based on the sensitivities of the aerodynamic and centrifugal loads. If both models converge to the same blade geometry, it can be concluded that the tight coupling has been implemented correctly. Finally, the aerodynamic performance can be evaluated to assess whether potential differences in geometry have a measurable effect on the predicted loads and propulsive efficiency.

To test the coupling under variations in sweep, both *XPROP* and *XPROP-*Λ are analysed. Especially the latter requires attention, as its twist sensitivities, which are expected to have the largest contribution, showed relatively large errors at the blade tip. This could have a significant impact on the structural deformation predicted by the tightly coupled aeroelastic model due to the high dynamic pressure in this region. Therefore, it must be tested whether this model also predicts the same structural deformation as the loosely coupled model for swept blades.

The comparison between the two couplings is performed for both positive thrust (load case 1) and negative thrust (load case 2). It should be noted that the aerodynamic model has not been validated for the negative thrust load case. However, the test still allows verification of the coupling implementation, as both coupling approaches rely on the same aerodynamic model.

Table 4.2: Operating conditions for verification of the aeroelastic coupling.

Load case	Advance ratio [-]	Pitch angle [deg.]	Velocity [m/s]	Altitude [m]
1	1.0	30	30	0
2	2.0	30	60	0

Since the analysis is aeroelastic, also the structural settings are of interest. However, as variations in structural properties are not studied in this work, the same properties are used as by Rotundo [23]. For completeness, these properties are briefly summarized below.

The top and bottom skin of the propeller, as well as its spars, are each modelled by a single laminate. These laminates are symmetric and consist of *AS4/APC2* composites with a thickness of 0.75 mm. The front and rear spar are positioned at 2% and 90% of the chord length along the blade span, respectively. The ply angles are defined by the laminate stacking sequence given in Equation 4.60.

$$\mathcal{S} = \{0^\circ \quad 15^\circ \quad 30^\circ \quad 30^\circ \quad 45^\circ \quad 45^\circ \quad 60^\circ \quad 60^\circ \quad 75^\circ \quad 90^\circ\}_S \tag{4.60}$$

For the numerical computations, the structural model is discretized into 35 linearly spaced elements, while the aerodynamic model consists of 100 elements using a cosine spacing. Furthermore, each blade cross-section is modelled with 100 shell elements. A convergence tolerance of 10^{-4} is used, meaning that the maximum element-wise difference in deformation between successive iterations must be less than 0.01% for the solution to be considered converged.

Figure 4.8 and Figure 4.9 show the comparison of the predicted deformation between the tightly and loosely coupled method for *XPROP* and *XPROP-*Λ, respectively. Additionally, the aerodynamic performance of the deformed blades is compared between the two couplings in Table 4.3.

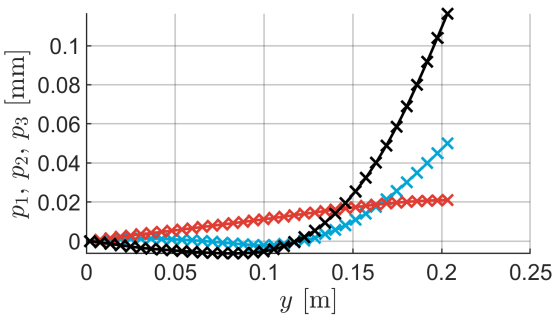

(a) Translational deformations for load case 1.

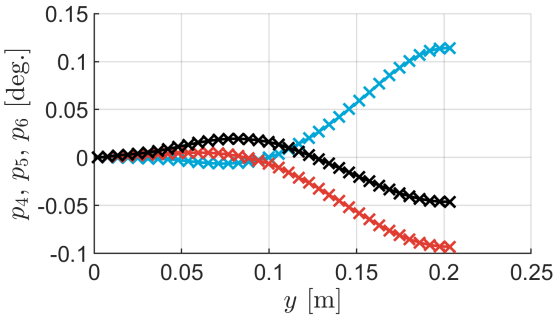

(b) Rotational deformations for load case 1.

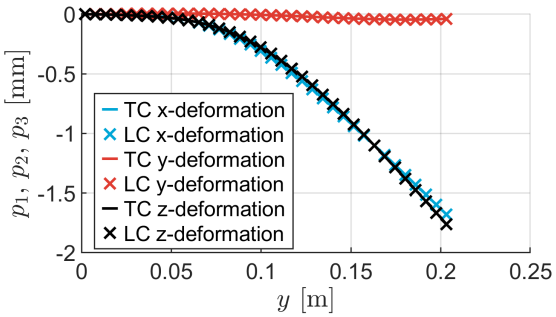

(c) Translational deformations for load case 2.

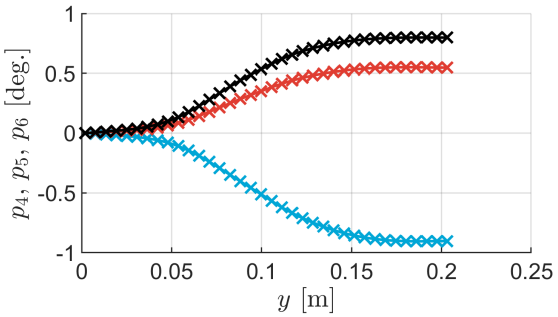

(d) Rotational deformations for load case 2.

Figure 4.8: Comparison of the blade deformation between the tightly and loosely coupled models for the *XPROP* propeller.

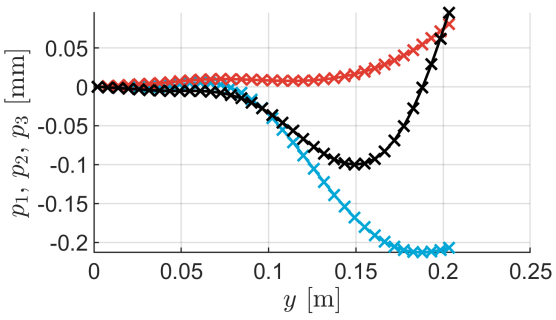

(a) Translational deformations for load case 1.

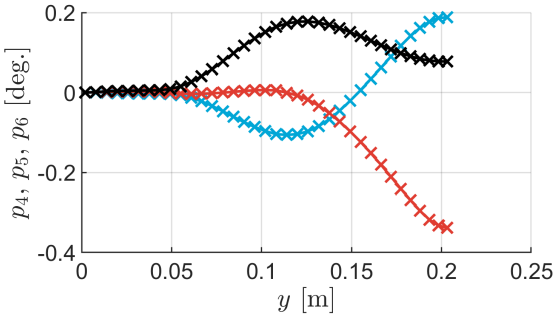

(b) Rotational deformations for load case 1.

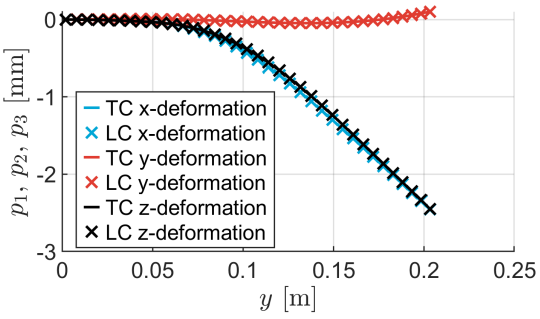

(c) Translational deformations for load case 2.

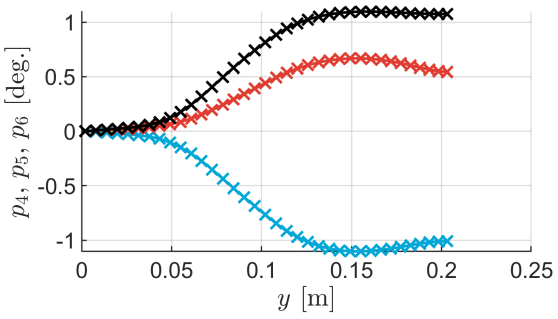

(d) Rotational deformations for load case 2.

Figure 4.9: Comparison of the blade deformation between the tightly and loosely coupled models for the *XPROP*-Λ propeller.

Table 4.3: Comparison of the aerodynamic performance between the tightly and loosely coupled models.

Propeller	Load case	Coupling	C_T	C_P	C_Q	η_P
XPROP	1	Tight	0.213	0.273	0.043	0.782
		Loose	0.213	0.273	0.043	0.782
	2	Tight	-0.300	-0.391	-0.062	N/A
		Loose	-0.300	-0.391	-0.062	N/A
XPROP-Λ	1	Tight	0.208	0.265	0.042	0.785
		Loose	0.208	0.265	0.042	0.785
	2	Tight	-0.298	-0.389	-0.062	N/A
		Loose	-0.298	-0.389	-0.062	N/A

The results indicate that the tightly and loosely coupled models match closely, with differences remaining below 0.001% for both load cases and propeller geometries. The deformations in all degrees of freedom are predicted very similarly by both models, yielding nearly identical aerodynamic performance of the propeller. Therefore, it can be concluded that the tight coupling has been implemented correctly and that it can be used with confidence. Moreover, the small errors observed in the analytical sensitivities from section 4.2 do not result in noticeable differences in blade deformation, providing further validation of the tightly coupled method.

Lastly, the computational cost required for the loosely and tightly coupled method is compared in Table 4.4 for the propeller blades and load cases considered in this section. It is observed that the tightly coupled method consistently reduces the computational time by up to 40.5%, confirming its efficiency advantage. This reduction can have a significant impact on the overall computational cost, particularly when multiple iterations of the static aeroelastic analysis are involved, as is often the case during optimization studies.

Table 4.4: Comparison of the computational cost required for evaluation of the tightly and loosely coupled models, computed on an *AMD Ryzen 5 5500U* processor using multithreading in *MATLAB* across 6 cores.

Propeller	Load case	Coupling	Computational time [s]	Reduction (%)
XPROP	1	Tight	5.825	27.8
		Loose	8.066	
	2	Tight	6.707	34.5
		Loose	10.24	
XPROP-Λ	1	Tight	4.859	40.5
		Loose	8.171	
	2	Tight	7.549	33.8
		Loose	11.40	

5

Sweep and Lean Parameter Study

The primary objective of this chapter is to examine the influence of sweep and lean on the aerodynamic performance and structural behaviour of propeller blades. To this end, a parameter study is conducted in which the quarter-chord alignment and face alignment are parametrically varied using Bézier curves. The aerodynamic efficiency and structural integrity are examined across a range of sweep and lean configurations, thereby providing deeper insight into the aeroelastic behavioural trends of advanced propeller geometries. Beyond offering insights into the effects of sweep and lean, this study also demonstrates the capabilities of the developed aeroelastic framework.

A parameter study is deliberately chosen as a first step rather than a design study since road parametric explorations offer general insights into how sweep and lean affect blade loading, efficiency, and stresses, which are essential before pursuing any targeted optimization. A follow-up design study, however, would require extensive additional development and computational effort that falls outside the time constraints of this project. The results presented here therefore lay the foundation for future design studies using the developed aeroelastic framework.

5.1. Parameter Space Selection

To systematically investigate the effects of sweep and lean, it is necessary to define a manageable and representative parameter space for the blade geometry. Manually prescribing their distributions across the blade span would not only be time-consuming but could also lead to discontinuities in these spanwise distributions. To overcome this, the QCA and FA are parametrized using Bézier curves, as introduced in Appendix E. Such parametric curves allow the blade geometry to be defined by a small number of control points, which significantly reduces the number of design variables, while the distributions remain smooth and continuous.

To demonstrate this, the QCA distribution of *XPROP*-Λ is approximated using a quadratic Bézier curve, see Figure 5.1. The result shows that the Bézier parametrization indeed reduces the number of variables significantly as only three control points are required, resulting in six parameters, instead of 25 radial variables. The optimal coordinates of these control points are determined using the SQP algorithm, with a maximum error of approximately $\Delta QCA/Y \approx 0.001$ for the reference distribution from Appendix A. The resulting coordinates are listed in Table 5.1.

In this parameter study, the control points of *XPROP*-Λ are used as a reference to define the parameter space of the quarter-chord alignment. Since the propeller includes a hub where the blade is clamped, the blade is assumed to be fixed up to a spanwise position of $y/Y = 0.195$. Accordingly, the coefficients are updated, as shown by the baseline in Table 5.1, to enforce zero sweep at the hub while the remainder of the distribution adjusts automatically. This shows the flexibility and effectiveness of using Bézier curves. In reality, the *XPROP* hub radius is located at $y/Y = 0.21$. However, for convenience, $y/Y = 0.195$ is used as the hub radius, corresponding to $y = 39.62$ mm based on the dimensions listed in Table A.1. While the exact value of $y/Y = 0.21$ would be required for an accurate comparison with *XPROP*, the small difference has no meaningful impact on the conclusions of the parameter study.

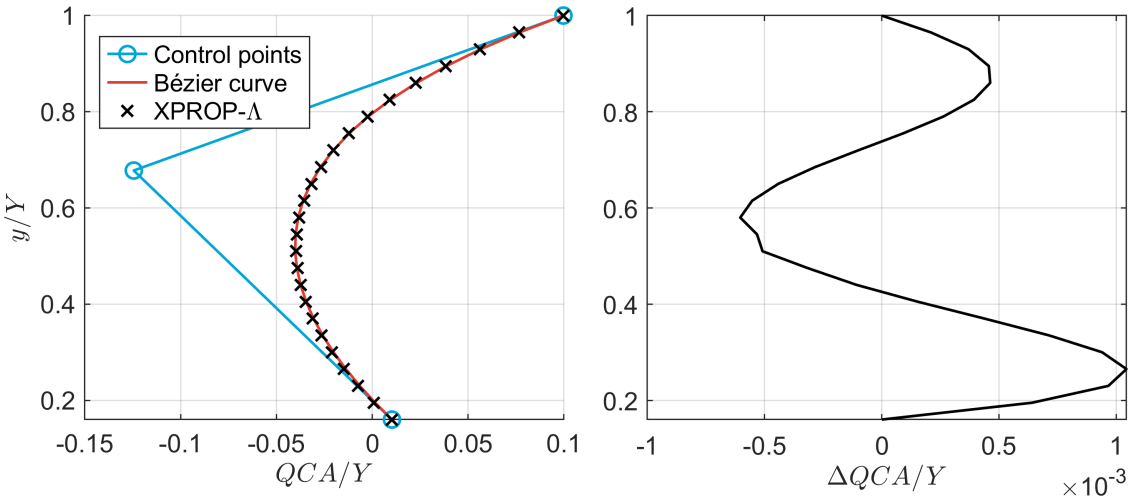

Figure 5.1: Quadratic Bézier approximation of the QCA distribution for *XPROP-*Λ.

Table 5.1: Control point coordinates of the Bézier approximation for the QCA distribution of *XPROP-*Λ, and of the baseline QCA distribution used in this parameter study.

Control point	XPROP-Λ		Baseline	
	$\boldsymbol{QCA/Y}$	$\boldsymbol{y/Y}$	$\boldsymbol{QCA/Y}$	$\boldsymbol{y/Y}$
1	0.010	0.160	0.000	0.195
2	-0.125	0.678	-0.115	0.696
3	0.100	1.000	0.100	1.000

Various sweep distributions are generated by scaling the baseline QCA/Y distribution provided in Table 5.1. This is a convenient method to vary the radial distribution as only a single scaling variable is required. Since the tip of propeller blades is typically backward-swept, the scaling is varied such that the resulting QCA at the tip ranges between $QCA_{\text{tip}}/Y =$ -0.1 and $QCA_{\text{tip}}/Y =$ 0.2, as shown in Figure 5.2a. For convenience, QCA^* is defined as QCA_{tip}/Y in the subsequent analysis.

A slightly different approach is applied to change the lean of the blade. Instead of scaling an existing distribution, entirely new distributions are defined. The lean distribution is assumed to be less complex, as only fully upstream or fully downstream lean configurations are considered. The chosen control point coordinates for the FA distribution are shown in Table 5.2, where FA^* denotes the non-dimensional face alignment at the blade tip, $FA^* := FA_{\text{tip}}/Y$. These control points are selected such that the rate of change of FA increases progressively toward the tip. The range of FA^* is slightly wider than that of QCA^*, varying from -0.2 to 0.2, but it has the same maximum offset. Representative spanwise distributions of FA that cover the entire parameter space are shown in Figure 5.2b.

Table 5.2: Control point coordinates for the FA distributions.

Control point	$\boldsymbol{FA/Y}$	$\boldsymbol{y/Y}$
1	0	0.195
2	0	0.500
3	FA^*	1

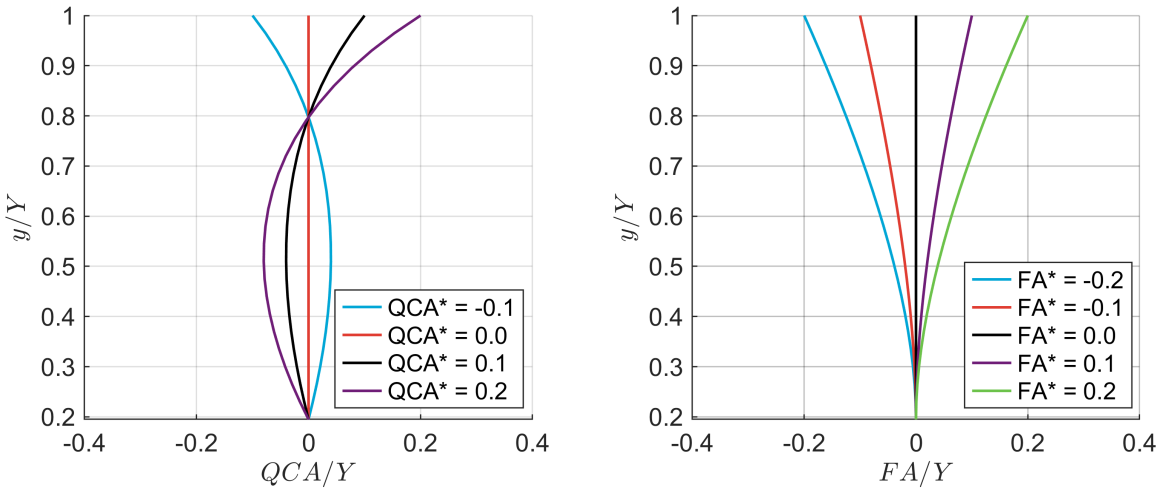

(a) Spanwise QCA distributions.

(b) Spanwise FA distributions.

Figure 5.2: QCA and FA distributions of the analysed blade configurations.

Note that, by convention, positive QCA values correspond to backward sweep, whereas a positive FA represents upstream lean, i.e., in the direction of thrust. Furthermore, Figure 5.2 shows that the selected parameter space for sweep and lean is limited, not only because arbitrarily complex distributions are avoided, but also due to the imposed limits on the minimum and maximum values of the quarter-chord alignment and face alignment at the blade tip. However, in reality the magnitudes of the sweep and lean offsets are restricted by the constrained propeller diameter, as their relative contributions to the diameter vary across different pitch settings. Hence, the selected ranges should represent a subset of practical configurations.

In the following sections, a comparative study between the aerodynamic performance of rigid and flexible propeller blades is conducted first, followed by a more detailed analysis focusing on flexible blades only.

5.2. Impact of Blade Flexibility on Performance

The aerodynamic performance of rigid and flexible propeller blades is compared to evaluate the impact of structural flexibility on the performance across a range of blade geometries. To isolate the effects of sweep and lean, the blade construction procedure first applies the pitch setting, after which sweep and lean are applied through prescribed offsets of the quarter-chord line. It should be noted that this approach results in slightly different blade geometries for each pitch setting. However, reversing this order would change the sweep and lean offsets during pitch rotation, as illustrated in Figure 3.7.

Five blade designs are selected for this efficiency analysis. To study the effect of lean, three unswept blades with $QCA^* = 0$ and tip lean offsets of FA^* -0.2, $FA^* = 0$ and $FA^* = 0.2$ are selected. Similarly, to study the effect of sweep, blades with zero lean ($FA^* = 0$) and sweep factors of QCA^* = -0.1, 0, and 0.1 are analysed. Together, these cases define five distinct blade geometries. These blades are analysed at a freestream Mach number of $M = 0.12$, for three pitch settings of 30°, 35° and 45°. Furthermore, the aerodynamic calculations were performed using 75 cosine-spaced elements. The flexible blade has the same structural properties as those in section 4.4, except for the number of structural nodes, which is increased to 50 to improve numerical accuracy. The comparison of aerodynamic efficiency between the rigid and flexible blades is shown in Figure 5.3, where the propulsor efficiency is plotted against the thrust coefficient T_C, allowing for a direct comparison of the peak efficiency between rigid and flexible blades as well as across the different blade designs.

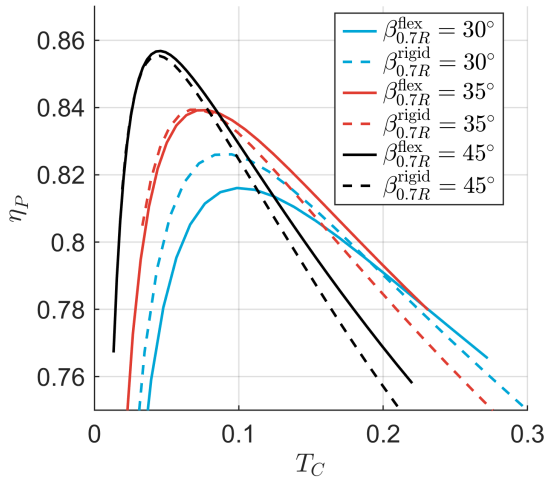

(a) $QCA^* = 0$ and $FA^* = -0.2$.

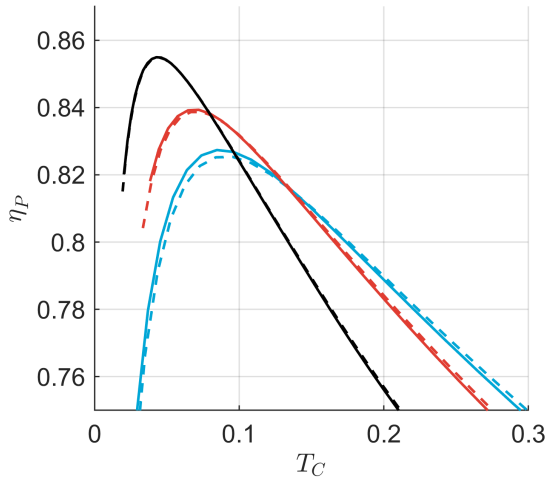

(b) $QCA^* = 0.0$ and $FA^* = 0.2$.

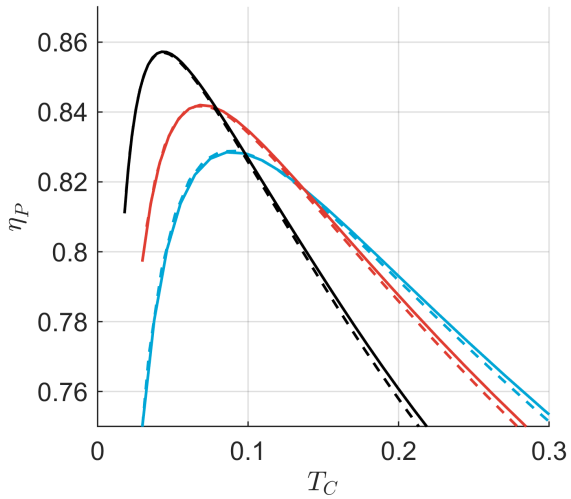

(c) $QCA^* = 0$ and $FA^* = 0$.

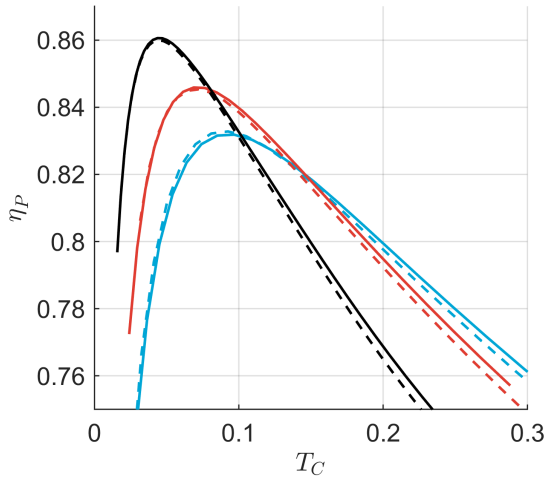

(d) $QCA^* = -0.1$ and $FA^* = 0$.

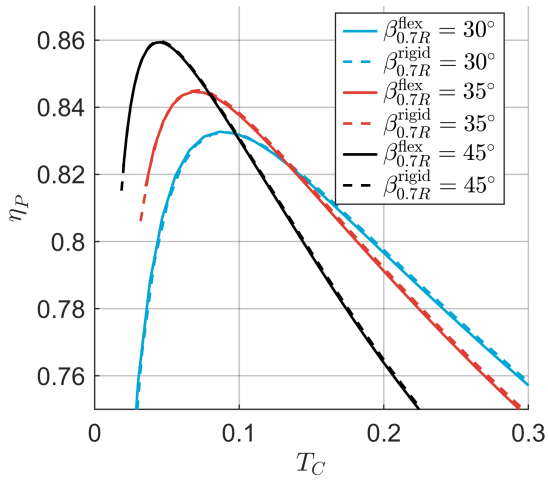

(e) $QCA^* = 0.1$ and $FA^* = 0$.

Figure 5.3: Comparison of propulsor efficiency between rigid and flexible blades.

The differences in peak aerodynamic performance between the rigid and flexible blades are generally small, typically below 0.003. An exception occurs for the blade with $QCA^* = 0$ and $FA^* = -0.2$ at $\beta_{0.7R} = 30°$, where the peak efficiency decreases from 0.826 to 0.816 between the rigid and the flexible blade, while the corresponding thrust coefficient increases from 0.09 to 0.10. Among the geometries considered, positive sweep and negative lean tend to produce slightly more noticeable deviations than negative sweep or positive lean, while for the straight blade, the peak efficiencies are almost identical at all pitch settings. Furthermore, the sensitivity to flexibility does depend on the pitch setting, in particular for the blade with $QCA^* = 0$ and $FA^* = -0.2$.

For most blades configurations and pitch settings in Figure 5.3, flexibility appears to have only a small impact on peak aerodynamic efficiency. However, this does not imply that flexibility has no aerodynamic impact at all. In fact, it has a noticeable effect on both thrust and power. This is shown in Figure 5.4, which presents the thrust and power coefficient curves at 30° pitch for two blades without lean and $QCA^* = -0.1$ and $QCA^* = 0.1$, whose efficiency curves are shown in Figure 5.3d and Figure 5.3e, respectively. Since the curves for the flexible blade are shifted noticeably compared to those of the rigid blade, this indicates that flexibility affects the achievable thrust and required power at the given advance ratios. This effect on thrust and power is observed for all five blades across all three pitch settings.

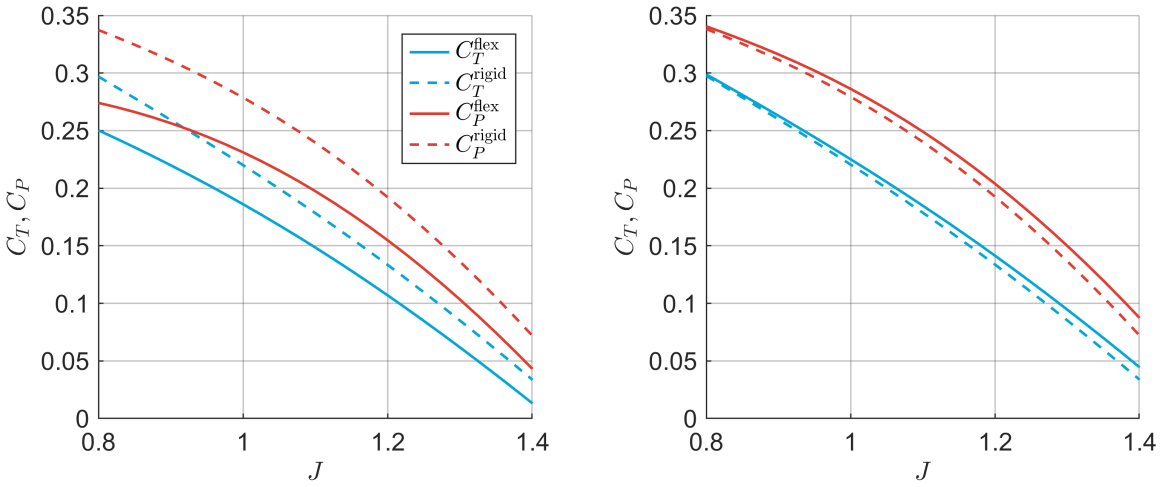

(a) $QCA^* = -0.1$ and $FA^* = 0$.

(b) $QCA^* = 0.1$ and $FA^* = 0$.

Figure 5.4: Thrust and power coefficient comparison between the rigid and flexible blade at $\beta_{0.7R} = 30°$.

Thus, compared to the rigid blade, it can be concluded the impact of structural flexibility on peak aerodynamic efficiency is limited. Although structural flexibility can introduce torsional and translational deformations that affect the local pitch angle and the spanwise loading distribution, causing changes in both the generated thrust and required power, these aeroelastic effects are not strong enough to significantly change the peak aerodynamic efficiency. Furthermore, as also concluded in section 3.4, the effect of sweep and lean on the rigid blade at a given pitch setting is also limited.

Finally, the observation that the peak efficiency of the lower pitch setting lies within the efficiency curve of the higher pitch setting, whereas in practice the peak efficiencies typically appear sequentially, can likely be explained by two factors. First, as noted earlier, the QCA and FA offsets are applied after the pitch setting, which means that different blades are being compared across the pitch settings. Second, the discrepancy may be attributed to the limitations of the BEM model. As shown in Figure 3.8, the BEM model predicts a shifted peak efficiency and different slopes in the efficiency curves compared to the experimental data. These altered slopes can cause the by BEM predicted η_P–T_C curves to stretch laterally, offering an explanation why sequential peak efficiencies typically appear in practice but not in the BEM results.

5.3. Aerodynamic Performance of Flexible Blades

In this section, the aerodynamic performance of flexible blades is examined throughout the parameter space by comparing each configuration to the straight blade. The aim is to understand how variations in sweep and lean affect the aerodynamic efficiency when blade flexibility is considered.

5.3.1. Aerodynamic Efficiency

To assess the aerodynamic performance of flexible propeller blades, the aeroelastic analysis is performed at constant thrust coefficient T_C, which ensures each propeller is compared under the same loading condition T/D^2. This removes the effect of rotor diameter and isolates efficiency differences between blade shapes, allowing a fair comparison of their aerodynamic effectiveness. The operating conditions are set to $M = 0.12$ and $J = 1$, while the blade pitch is adjusted as needed to reach the target thrust coefficient. The pitch setting is updated according to Equation 5.1, using the aerodynamic sensitivities from section 4.2. Each blade is constructed at a zero-pitch setting, meaning that sweep and lean are defined at zero pitch before the pitch setting is subsequently modified. This approach follows the construction method used for *XPROP*-Λ [4]. So, unlike the results in section 5.2, the sweep and lean values discussed in this section refer to their values at the zero-pitch configuration.

$$\Delta\beta_{0.7R} = \frac{T_C^{\text{target}} - T_C}{dT_C/d\beta} \tag{5.1}$$

The structural discretization and properties are identical to those described in section 5.2. Furthermore, a target thrust coefficient of $T_C^{\text{target}} = 0.230$ with a tolerance of 0.001 is prescribed. Using these settings, all blade geometries were evaluated successfully and their final thrust coefficients were within tolerance. The resulting difference in propulsor efficiency with respect to the straight blade across the parameter space is presented in Figure 5.5.

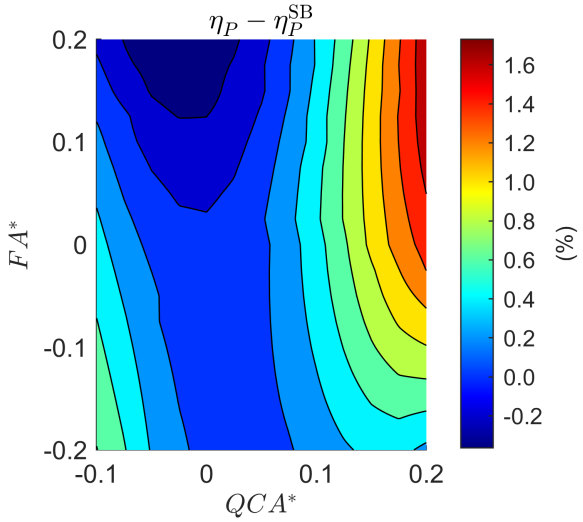

Figure 5.5: Propulsor efficiency compared to that of the straight blade.

The results indicate that the propulsor efficiency of a flexible swept and leaned blade can increase up to 1.7% relative to the flexible straight blade. Backward sweep combined with positive lean yields the largest improvement, while negative lean produces smaller gains. For blades with moderate backward or forward sweep, whether the efficiency exceeds that of the straight blade depends on the amount of lean, with large positive lean leading to a reduction in efficiency. Note that these trends only hold within this parameter study, where sweep, lean and pitch are varied while all other geometric parameters and operating conditions remain fixed. In a design study, where geometric and structural parameters as well as operating conditions can be adjusted, the efficiency trends could differ substantially.

The observed variations in propulsor efficiency arise from changes in the spanwise aerodynamic loading distribution. Geometric changes, along with variations in induced velocities, change the inflow

angle, which affects the orientation of the lift and drag forces relative to the propeller disk. This, in turn, changes how these forces are decomposed into thrust and torque components, ultimately affecting the overall efficiency. To illustrate this, the sectional thrust and torque distributions, as well as their ratio, are analysed for five representative blades. The selected blades include the straight blade (SB) and the four corner configurations of the parameter space, as listed in Table 5.3, characterized by forward sweep (FS), backward sweep (BS), downstream lean (DL) and upstream lean (UL). The results, as shown in Figure 5.6, clearly demonstrate that the spanwise distributions of the aerodynamic loading vary with blade geometry, affecting the corresponding ratio of thrust to torque. In these figures, Y_D refers to the span of the deformed blade tip, which may differ from that of the undeformed configuration due to blade stretching caused by centrifugal stiffening.

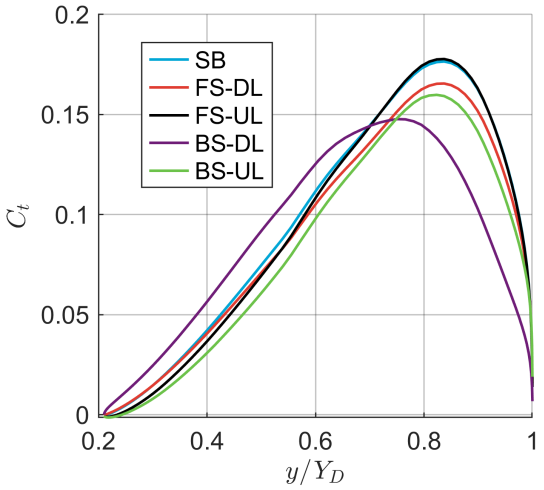

(a) Sectional thrust coefficient.

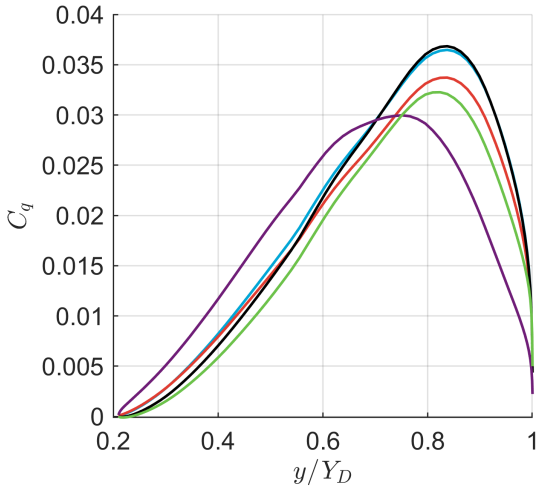

(b) Sectional torque coefficient.

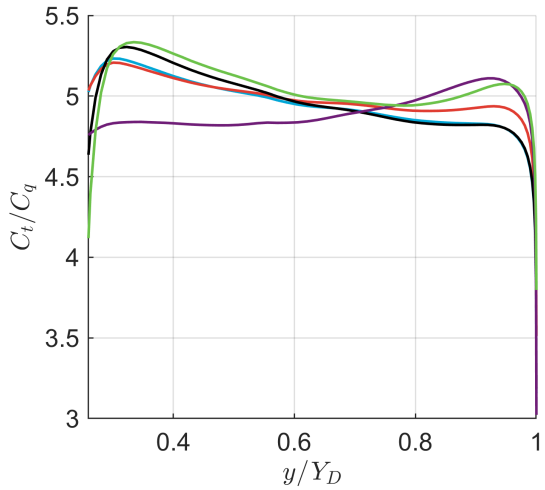

(c) Ratio of thrust coefficient to torque coefficient.

Figure 5.6: Spanwise distributions of the thrust and torque coefficients and their ratio for the blades defined in Table 5.3.

Table 5.3: Selected blades for further aerodynamic analysis.

Blade	QCA^*	FA^*
SB	0	0
FS-DL	-0.1	-0.2
FS-UL	-0.1	0.2
BS-DL	0.2	-0.2
BS-UL	0.2	0.2

The BS-DL blade in particular exhibits a loading distribution that differs considerably from the other four blades. Since the aerodynamic loads are highly sensitive to torsional deformation, which effectively corresponds to changes in local pitch, it is natural to examine these torsional deformations of each blade more closely. This comparison is presented in Figure 5.7, where the torsional deformation is denoted by p_5, together with the resulting pitch distributions.

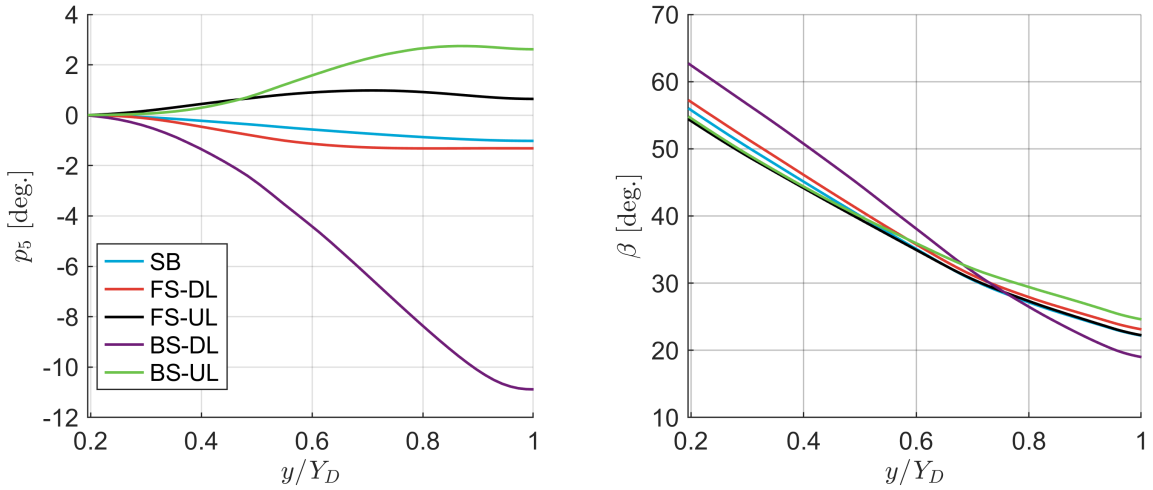

(a) Torsional deformation distribution.

(b) Pitch distribution.

Figure 5.7: Comparison of the torsional deformation and the resulting pitch distributions for the blades defined in Table 5.3.

Compared to the other blades, the BS-DL blade exhibits a pronounced negative torsional deformation, as shown in Figure 5.7a. Therefore, its washout is larger, which means that a higher twist angle is required at the root to compensate for the lower thrust generation near the tip in order to achieve the same overall T_C. In other words, the BS-DL blade twists so strongly that, compared to the other blades, the inboard section must generated considerably more thrust, while the outboard region becomes aerodynamically less effective. As a result, the thrust and torque coefficient distributions for BS-DL are shifted inboard, as shown in Figure 5.6. This behaviour is confirmed by the twist distribution in Figure 5.7b, where BS-DL shows the highest twist angle near the root and the lowest twist angle toward the tip.

To show that these variations in loading distribution indeed result in the efficiency trends observed in Figure 5.5, the sectional propulsor efficiency is introduced. This quantity can be decomposed into the induced efficiency and profile efficiency, which allows the losses due to profile drag to be decoupled from those associated with the induced axial and swirl velocities. The sectional induced, profile and the resulting propulsor efficiency, are defined in Equation 5.2, Equation 5.3 and Equation 5.4, respectively [46].

$$\eta_i = \frac{1 - a'}{1 + a} \tag{5.2}$$

$$\eta_p = \frac{1 - \tan\varphi \frac{C_d}{C_l}}{1 + \frac{1}{\tan\varphi} \frac{C_d}{C_l}} \tag{5.3}$$

$$\eta = \eta_i \eta_p \tag{5.4}$$

Increases in either induced or profile efficiency along the span yield higher sectional propulsor efficiency, and therefore overall propulsor efficiency. Since the aerodynamic loads are largest near the blade tip, this part of the span contributes most to the total propulsor efficiency. The spanwise distributions of the induced, profile and sectional propulsor efficiency for the five selected blades from Table 5.3 are analysed independently and presented in Figure 5.8.

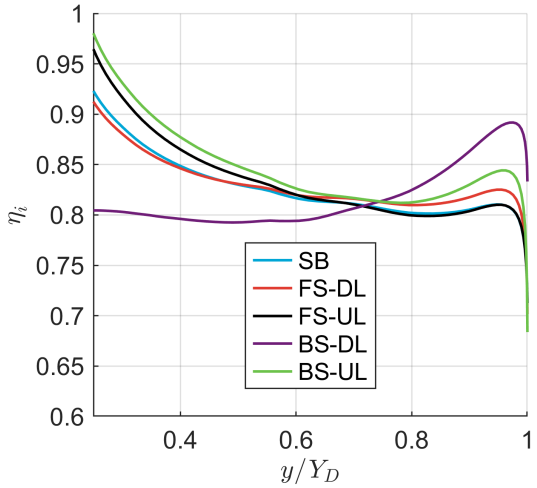

(a) Induced efficiency.

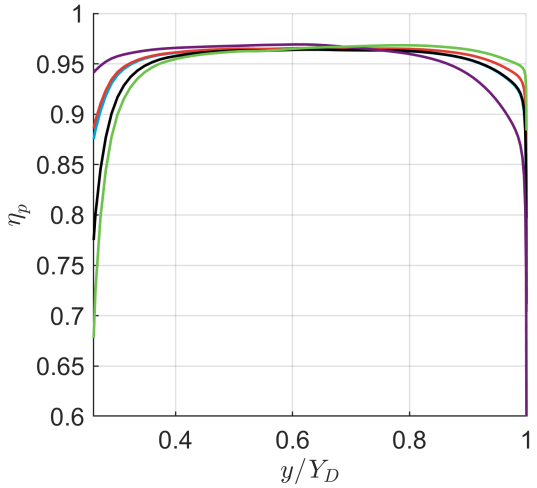

(b) Profile efficiency.

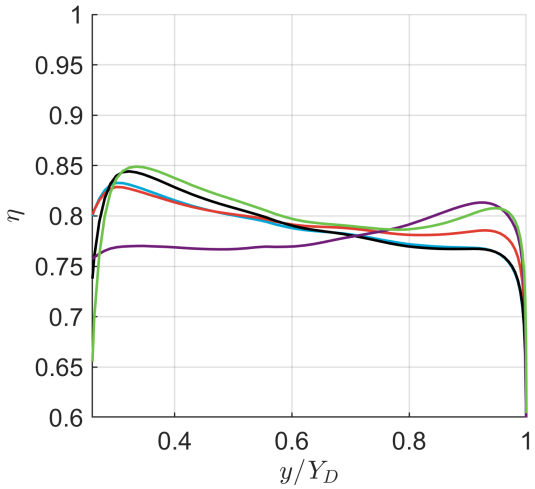

(c) Sectional propulsor efficiency.

Figure 5.8: Spanwise distributions of the sectional induced, profile and propulsor efficiencies for the blades defined in Table 5.3.

This figure shows that the distributions of both the induced efficiency and profile efficiency vary with blade geometry. The induced efficiency exhibits significant variation among the blades across the entire span, which indicates that the geometric variations strongly influence the axial and swirl induced

velocities. Differences in profile efficiency are most pronounced near the blade root and tip. This implies that changes in blade shape primarily affect how the sectional lift and drag contribute to thrust and torque in these regions. Furthermore, the trends observed at the blade tip for the induced and profile efficiency do not follow the same pattern, meaning that the two mechanisms do not reinforce each other in a straightforward way. As a result, the differences in sectional propulsor efficiency arise from the combined impact of these two components. However, based on the trends of the sectional propulsor efficiency, the effects of induced efficiency appear to dominate those of profile efficiency, as their variations align more closely. Thus, the differences in sectional propulsor efficiency, and therefore in overall propulsor efficiency are primarily driven by variations in losses associated with the induced velocities. Moreover, the sectional propulsor efficiency closely aligns with the C_t/C_q distributions shown in Figure 5.6c, confirming that the observed efficiency trends are indeed driven by changes in the spanwise loading distribution.

According to Figure 5.8c, the BS-DL and BS-UL blades achieve the highest sectional propulsor efficiencies near the tip. Between $y/Y_D = 0.8$ and y/Y_D = 1, BS-DL performs slightly better than BS-UL, while BS-UL outperforms BS-DL in the inner sections of the blade. Although the root region contributes less to the overall propulsor efficiency, the higher efficiency of BS-UL in this region more than compensates for this. As a result, BS-UL achieves the highest overall propulsor efficiency, as shown in Figure 5.5. Similarly, the FS-DL blade achieves a lower sectional propulsor efficiency near the tip than BS-DL, but its higher performance at the root offsets this, yielding a higher overall propulsor efficiency as well. The remaining FS-UL and SB blades show the lowest sectional propulsor efficiencies near the tip and, consequently, the lowest overall efficiencies among the five blades. These two blades have very similar spanwise distributions, with SB performing slightly better near the tip and root, but slightly worse in between. Their overall propulsor efficiencies are therefore nearly identical, with SB exceeding FS-UL by only 0.05, according to Figure 5.5.

5.3.2. Limitations of Efficiency Comparison at Constant Thrust Coefficient

An efficiency increase of 1.7% may appear significant, but it is important to consider how reliable this result is given the fidelity of the aerodynamic model. The BEM model used in this study is not fully accurate for highly curved blades, since it tends to overestimate the propulsor efficiency. However, this overestimation is of a similar magnitude for the straight blade, as shown by Figure 3.9e and Figure 3.9f. Consequently, while the absolute efficiency values may be too optimistic, the relative performance differences between blades remain meaningful. The model is therefore expected to reliably capture relative efficiency changes and trends caused by variations in sweep and lean, offering valuable insight into the impact of geometry on aerodynamic performance. Furthermore, it was found that the BEM model provides more accurate predictions at a pitch angle of 30° than at 45°. As shown in Figure 5.9a, maintaining a constant thrust coefficient of $T_C = 0.23$ causes the collective pitch to vary between 28° and 38°. Moreover, torsional deformation reduces the effective pitch angle at the reference location, indicating that the BEM model is likely to perform even more accurately under these deformed conditions. This should keep the operating conditions within a favourable range where the predictions of BEM are most reliable.

To enable meaningful comparisons between different geometries, the operating conditions must be defined consistently. For blades with sweep and lean, however, the pitch angle can change the propeller diameter and, consequently, the aerodynamic and structural loading distributions. For comparison of the aerodynamic performance, a constant thrust coefficient T_C is applied by adjustment of the pitch setting. By fixing T_C, each propeller is compared under the same loading condition T/D^2, regardless of its diameter. The propulsor efficiency, given in Equation 3.8, can also be expressed in terms of T_C [25].

$$\eta_P = \frac{J^3 T_C}{C_P} \tag{5.5}$$

Since T_C and J are fixed, the efficiency depends solely on C_P, which can be rewritten in terms of the torque coefficient C_Q.

$$\eta_P = \frac{J^3 T_C}{2\pi C_Q} \tag{5.6}$$

Torque depends directly on the lever arm of each blade element, making the radial position, defined as

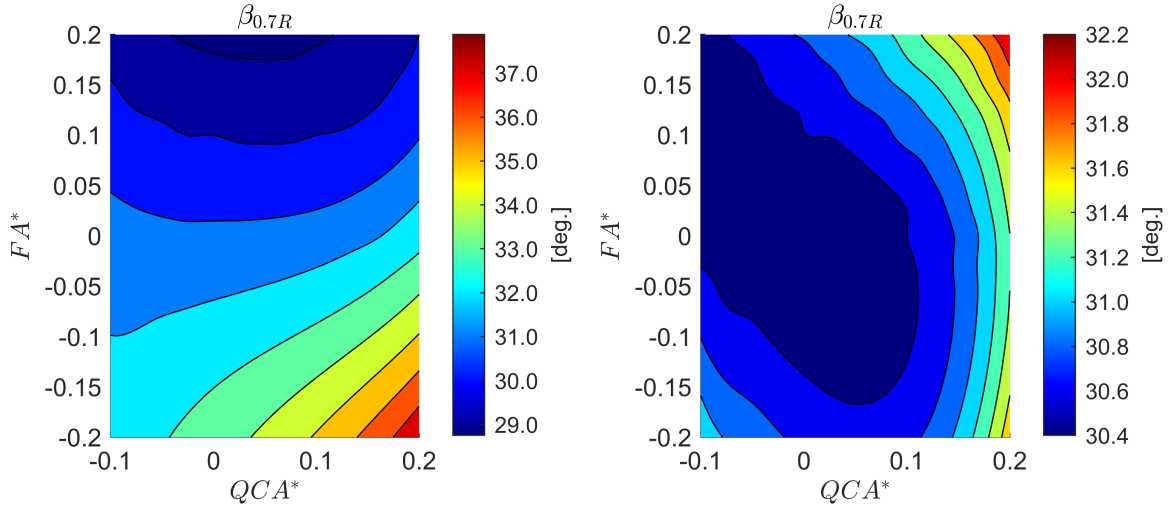

(a) Pitch angle without torsional deformation. **(b)** Pitch angle including torsional deformation.

Figure 5.9: Comparison of the blade collective pitch angles at reference location for a thrust coefficient of $T_C = 0.23$, showing the effect of torsional deformation.

the distance from the rotation axis to the blade element in the global xy-plane, critical in determining the overall propeller performance. The propeller disk area, that is the projected area swept by the rotating blades perpendicular to the rotation axis, is therefore important as it is related to the radial position of the blade tip. At zero pitch, blades with different sweep and lean distributions already have different propeller disk areas because sweep contributes to this projected area, while lean does not. However, when comparing blades at a constant thrust coefficient, the pitch angle is adjusted to trim the thrust to the target value. Applying pitch changes the projection of the quarter-chord line onto the global coordinate axes, effectively converting lean into sweep and vice versa, see Figure 3.7. As a result, when comparing blade configurations to the straight blade at a constant thrust coefficient, differences in disk area arise not only from the initial sweep and lean distributions but also from the applied pitch angle. Any variation in disk area, whether due to geometry or pitch setting, changes the radial positions of the blade elements and therefore the lever arms that determine torque, affecting the aerodynamic efficiency as described in Equation 5.6. Thus, ideally, efficiency variations should reflect only the changes in disk area caused by structural deformations.

For the blades considered in this analysis, the propeller disk radii compared to the straight blade are shown in Figure 5.10. These values correspond to the non-rotating blade geometry, meaning that centrifugal stiffening effects are not included. The figure shows that the differences in radius are small for most blade configurations. A notable increase, up to 3.6%, only occurs for highly backward-swept blades combined with upstream lean, and to a lesser extent for forward-swept blades with downstream lean, due to the smaller range of forward sweep considered. Consequently, part of the observed efficiency gain in Figure 5.5 may be attributed to the increase in disk area. Again, this is why curved propeller blades should ideally be compared at equal disk areas. However, the efficiency trends in Figure 5.5 do not directly match the trends in radius in Figure 5.10. This indicates that aeroelastic effects, in particular for blades with significant backward sweep, also contribute to the efficiency increase. A similar effect may occur for forward-swept blades, but the limited range considered here does not allow for a reliable assessment. Thus, sweep has a beneficial impact on propulsor efficiency beyond the effect of propeller disk area changes alone.

If the applied sweep and lean are increased further than in this study, a more consistent approach would be to fix the propeller diameter and scale the radial positions of the blade elements accordingly. However, scaling all blade element radii to achieve an equal propeller disk area is not straightforward, as it can be done either linearly or non-linearly, with both approaches introducing their own challenges. A linear scaling preserves the overall geometric shape but does not necessarily maintain relative aerodynamic characteristics between the blade sections, because the local flow conditions could vary, chang-

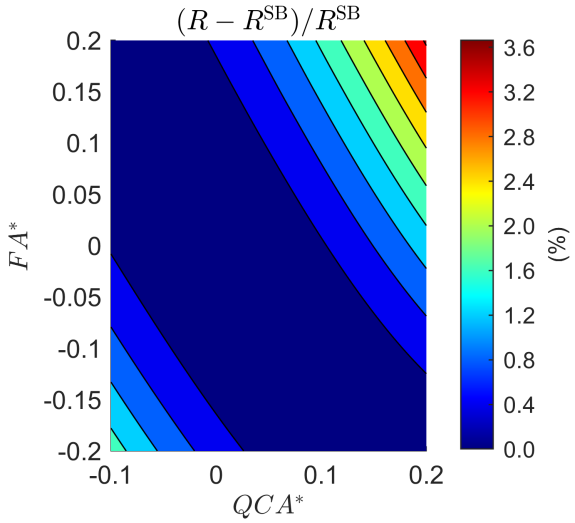

Figure 5.10: Comparison of propeller disk radius for non-rotating blades compared to the straight blade.

ing both the local Reynolds number and Mach number. Non-linear scaling could better preserve the relative aerodynamic features between the blade elements, but it could affect the overall blade geometry and therefore the structural response. Moreover, only adjusting radial positions is insufficient, as the scaling must also account for the axial coordinates to ensure geometric consistency. This scaling is beyond the scope and time constraints of this work.

Another complication is that maintaining a constant thrust coefficient requires adjusting the pitch angle, which means that each blade configuration reaches its peak efficiency at a different advance ratio. As a result, some propellers may operate near their peak efficiency while others may not. This further complicates a fair assessment of the aerodynamic performance, but this approach is the most practical approach within the current scope of this work.

Finally, it must be noted that the thrust coefficient was prescribed with a tolerance of 0.001 on a target value of 0.23, corresponding to a tolerance of roughly 0.4%. Although this small variation could influence the calculated efficiency, this effect would be randomly distributed across the parameter space and appear as noise in Figure 5.5, which is not visibly apparent.

5.4. Structural Behaviour of Flexible Blades

To compare the structural behaviour of flexible blades, focusing on blade stresses and root bending moments, a constant dimensional thrust T is applied. This choice is motivated by the fact that the structural response of the blade depends on the magnitude of the aerodynamic load. Using constant T_C would imply that both the thrust and propeller disk area may vary with the geometry, which would complicate a direct comparison of structural behaviour. However, also at constant thrust, the propeller disk area varies with sweep and lean, and therefore the lever arm used to generate torque also changes. As a result, differences in structural deformation can still be attributed to variations in the applied load, and not only to the blade's geometry. This limits the validity of the comparison. Nonetheless, this approach remains preferable to varying both thrust and disk area simultaneously, as would occur when using constant T_C.

In order to keep the dimensional thrust T constant, the pitch setting is updated according to Equation 5.7. The applied operating conditions, structural properties and grid discretization are the same as in subsection 5.3.1, while the target thrust is set to $T = 50$ N with a tolerance of 0.1 N. To provide perspective, this corresponds to $T_C = 0.15$ for the rigid *XPROP* propeller.

$$\Delta\beta_{0.7R} = \frac{T^{\text{target}} - T}{dT/d\beta} \tag{5.7}$$

5.4.1. Blade Stress

The structural stress of the composite propeller blades is evaluated using the Tsai-Wu failure criterion. This criterion provides a measure of the stress level in the composite material, where values below 1 indicate that the material has not failed [47]. This failure index F_{crit} can be evaluated across all the structural members. For all blade geometries considered in this parameter study, the maximum values on the top and bottom skin are presented in Figure 5.11, thereby providing insight into the most heavily loaded propeller blades. Similarly, the maximum values of F_{crit} for the leading edge and trailing edge spar laminates are presented Figure F.1. These are positioned as close as possible to the leading and trailing edges of the blades and, due to their small size, are expected to have a negligible effect on the deformations [23].

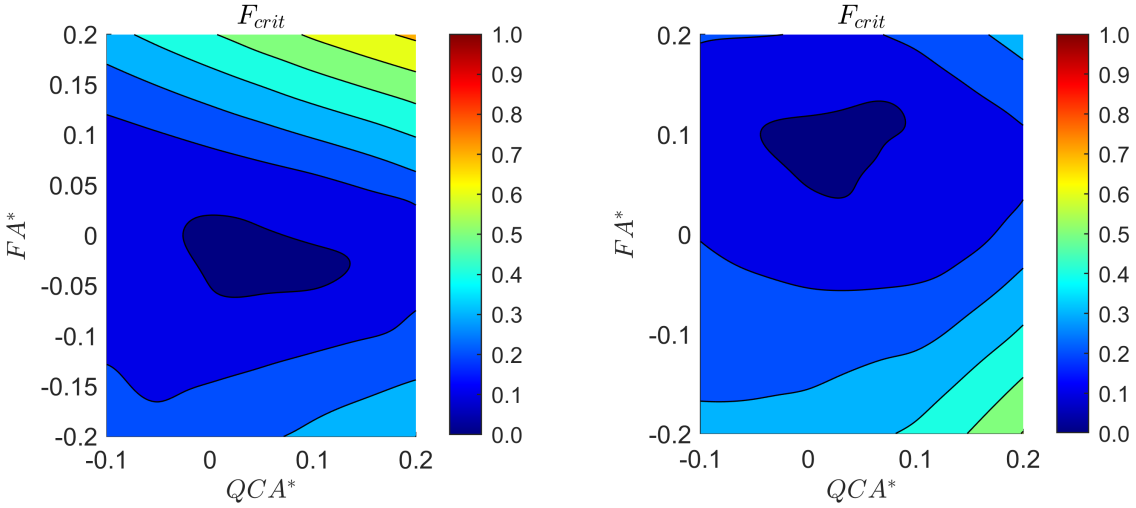

(a) Top skin. **(b)** Bottom skin.

Figure 5.11: Maximum failure index based on Tsai-Wu failure theory for the top and bottom skin laminates at a thrust of 50 N.

None of the propeller blades fail under the applied operating conditions. The top skin of the blade with $QCA^* = 0.2$ and $FA^* = 0.2$ experiences the most stress with $F_{crit} \approx 0.72$, while the bottom skin and both spars remain well below the failure threshold. However, the absolute stress values should be interpreted with caution, as they are not the primary focus of this parameter study. Only in a design study, the absolute values are important because they determine whether the structure approaches material limits and to what extent it meets specific safety requirements. In this parameter study, the trends are the primary focus, as they reveal how changes in geometry affect the blade stress. Nevertheless, the absolute values could still provide insight into whether the structure is over- or underdesigned for the given loading conditions, offering an indication of how much the geometry could be changed without risking structural failure.

For all tip lean values, applying forward sweep yields the most favourable values of the maximum failure index, while for a given sweep distribution, the optimal lean varies. These trends are explained by the principal and shear strain contours in Figure 5.12, sampled at the same locations as F_{crit}, which reveal that the top skin of the blade with $QCA^* = 0.2$ and $FA^* = 0.2$ experiences both relatively high principal and shear strains, whereas its bottom skin experiences negligible principal strain. This difference explains why the top skin approaches the failure limit more closely than the bottom skin. Additionally, for this particular blade, the Tsai-Wu failure factor is plotted across the blade surface in Figure 5.13. The maximum stress is concentrated around $y/Y_D \approx 0.35$, slightly inboard of the blade's most forward point, while the rest of the blade experiences relatively low stress levels. Given the generally low stress across the blade, it may be considered overdesigned for these specific operating conditions. Therefore, reducing the overall blade thickness could be an option to lower its weight and reduce material costs. In the region of relatively high stress, however, the local thickness should be reduced more conservatively to maintain structural integrity.

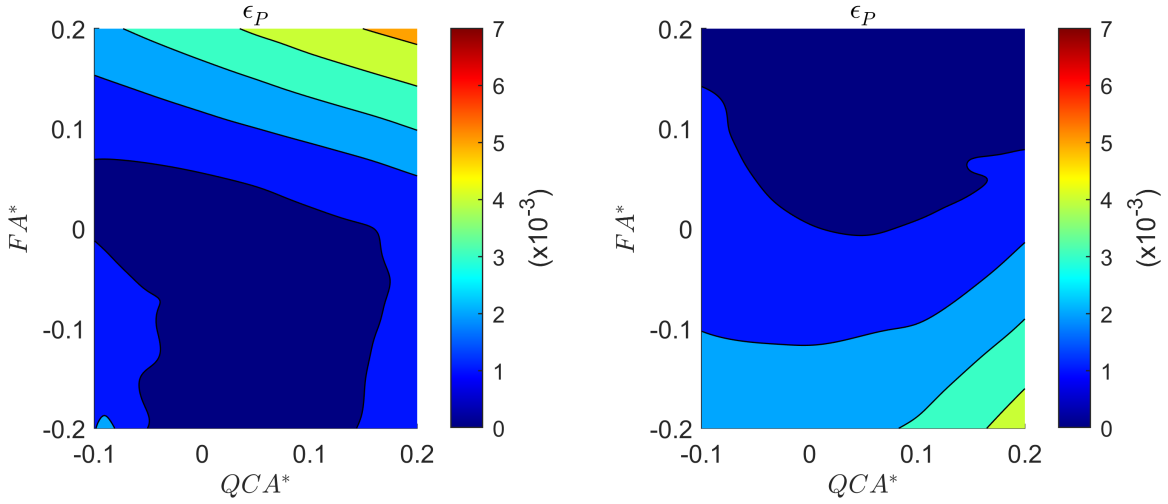

(a) Top skin principal strain.

(b) Bottom skin principal strain.

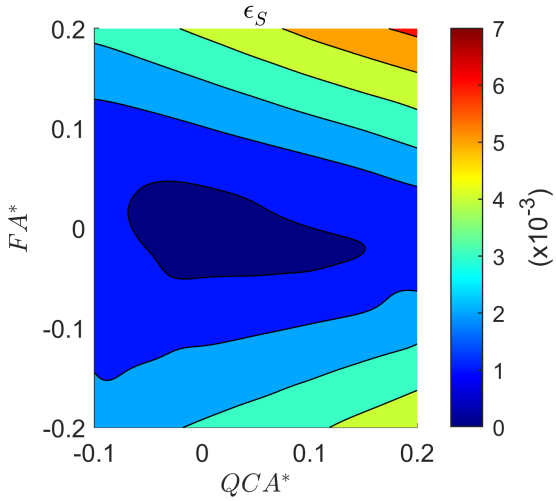

(c) Top skin shear strain.

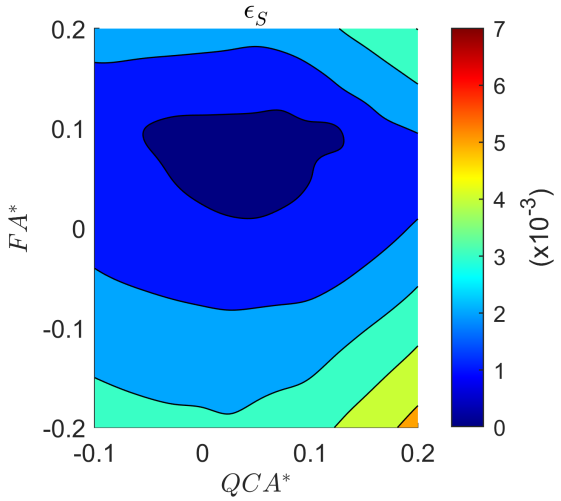

(d) Bottom skin shear strain.

Figure 5.12: Strain at the location of maximum F_{crit} at a thrust of 50 N.

The variation in the spanwise position corresponding to the maximum F_{crit} value across the parameter space is shown in Figure 5.14, where y_{crit}/Y_D denotes the normalized spanwise location of this maximum. For the top skin, blades with significant F_{crit}, characterized by positive sweep and positive lean as shown in Figure 5.11a, reach their peak value of F_{crit} at nearly the same spanwise position, around $y_{crit}/Y_D \approx 0.35$. This may be attributed to the use of scaled *XPROP*-Λ blades, which all reach their maximum forward point at the same spanwise position, as shown in Figure 5.2a. In contrast, under negative lean, substantial variations are observed for y_{crit}/Y_D. The associated F_{crit} values, however, remain sufficiently small to be of limited importance. Moreover, these variations in y_{crit}/Y_D are likely due to numerical inaccuracies in F_{crit}. Given that these values are very small across the entire blade, this could result in large fluctuations of the spanwise location corresponding to the maximum F_{crit} value between different blades. A similar pattern is observed on the bottom skin, where the regions with large variations in y_{crit}/Y_D correspond to the lowest F_{crit} values, making this effect negligible as well. Also, note that for blade configurations with sweep and lean near $QCA^* = 0.1$ and $FA^* = 0.05$, the maximum value of F_{crit} on the bottom is located within the propeller hub, although its absolute value is too small for this effect to be significant.

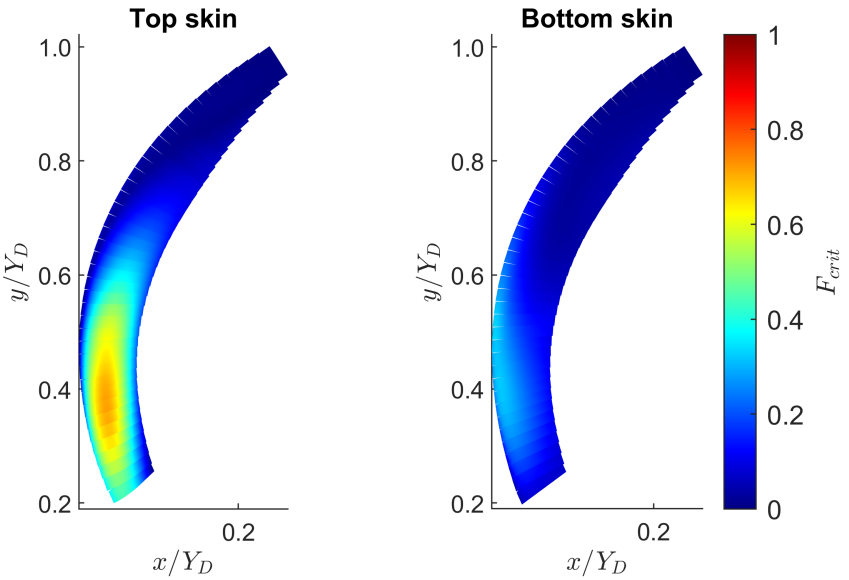

Figure 5.13: Tsai-Wu failure index across the blade for $QCA^* = 0.2$ and $FA^* = 0.2$.

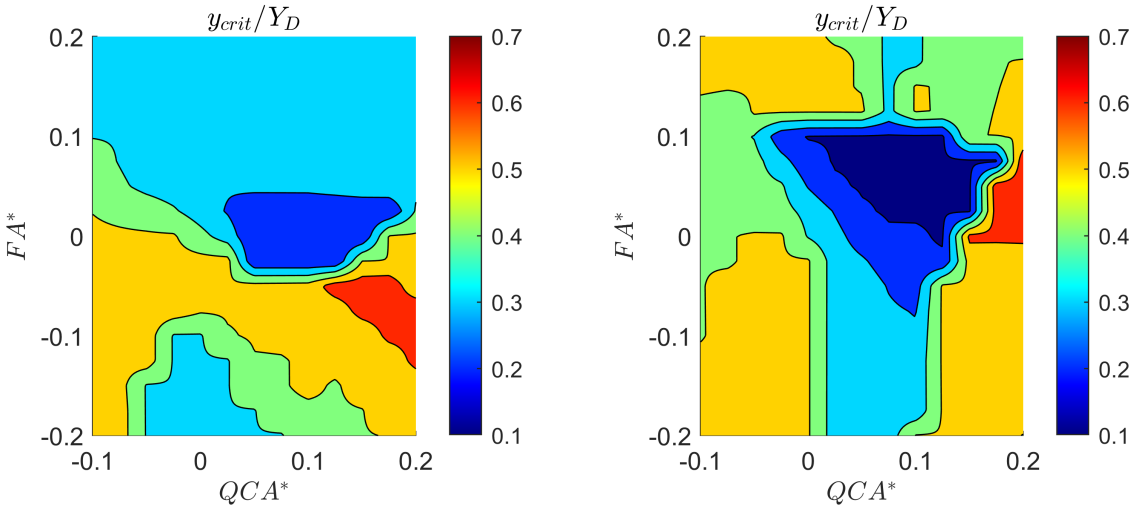

(a) Top skin.

(b) Bottom skin.

Figure 5.14: Spanwise position of maximum failure index at a thrust of 50 N.

5.4.2. Root Bending Moment

The root bending moments, that are the moments acting at the propeller hub, are presented in Figure 5.15. Here, M_x represents the moment associated with bending out of the rotational plane; M_y corresponds to the torsional moment about the pitch axis, which must be resisted by the pitch mechanism; and M_z represents the moment about an axis parallel to the propeller's rotational axis at the propeller hub. Therefore, M_z does not correspond directly to the moment that must be overcome by the engine, since it is not calculated about the actual axis of rotation. The difference in radius between the propeller hub and the axis of rotation causes both the aerodynamic and centrifugal forces to contribute differently to M_z at the hub compared to the axis of rotation. Since the blades are all straight within the hub, M_y directly represents the torsional moment that must be resisted by the pitch mechanism.

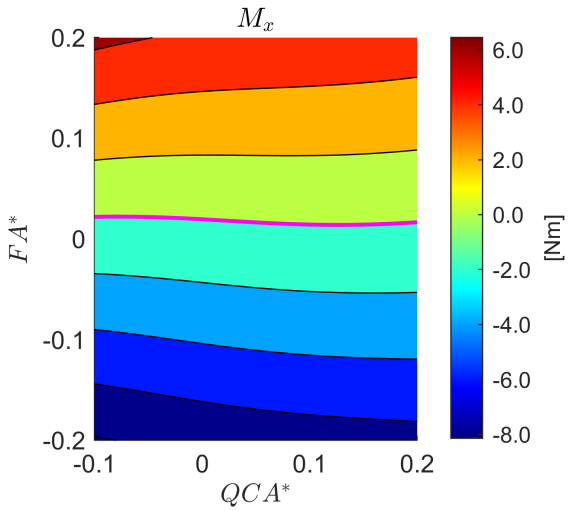

(a) Bending moment about the x-axis.

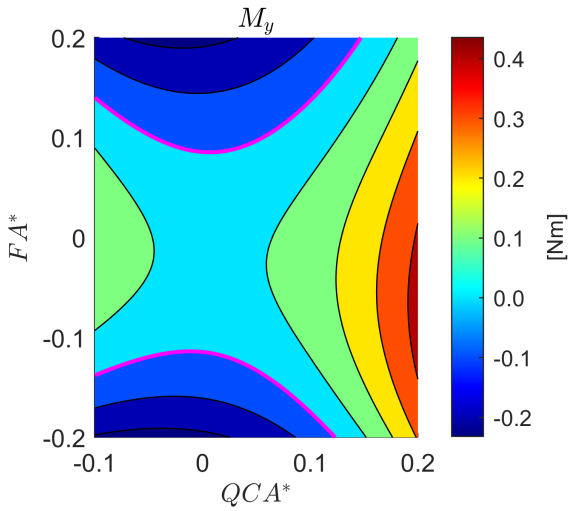

(b) Bending moment about the y-axis.

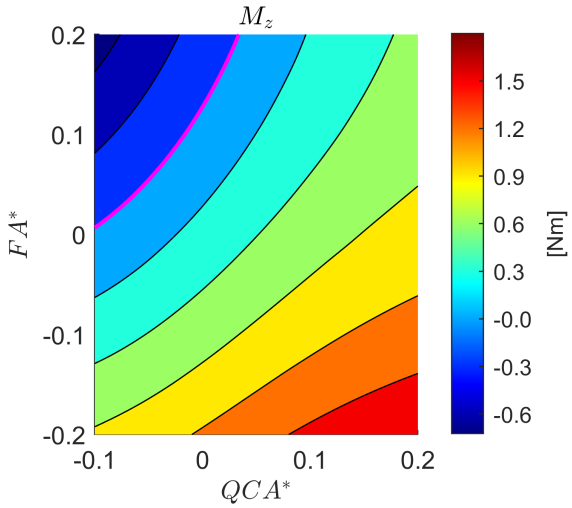

(c) Bending moment about the z-axis.

Figure 5.15: Propeller hub bending moments at a thrust of 50 N. The lines in magenta highlight the blade geometries with zero bending moment in the corresponding degree of freedom.

Figure 5.15 shows that lean has a pronounced impact on the bending moment about the x-axis, while the effect of sweep is negligible. For M_y, both sweep and lean affect the result, although the overall magnitude of M_y varies only slightly across the entire parameter space relative to M_x and M_z. This indicates that the blade geometry has little impact on the moment required by the pitch mechanism. Thus, compared to the variations observed in M_x and M_z, the variation in M_y could be considered negligible. The moment about the z-axis increases consistently with increasing sweep and decreasing lean.

The variations in the magnitude of M_x are substantially larger than those of M_y and M_z, which indicates that minimization of M_x could be an important design target. In Figure 5.15, the magenta line highlights the blades for which the bending moment about the x-axis is zero, appearing at almost constant lean values. According to Figure 5.11, blades along this $M_x = 0$ line with negative QCA^* experience low F_{crit} and correspondingly low M_z. This indicates that for these configurations, the combined effects of aerodynamic and centrifugal loading result in minimal structural demand both at the root and along the span. On the other hand, blades with large positive QCA^* along this zero M_x line experience both higher values of F_{crit} and of M_z, meaning that the structural stresses increase with positive sweep.

Two interesting blades are the straight blade and the blade with $QCA^* = 0$ and $FA^* = 0.1$, as Fig-

ure 5.15 shows that the bending moment changes sign between them in all three degrees of freedom. To clarify the trend of their root bending moments, the spanwise distributions of the integrated aerodynamic, centrifugal and resulting structural forces and moments are examined. These distributions show how the loads accumulate from tip to root and thus illustrate how geometric variations affect the spanwise blade loading and the resulting root bending moments, providing insight into why certain geometries produce a zero root bending moment. For each type of force, the integrated force is obtained by summing the nodal forces provided on the structural nodes. Although the aerodynamic loads are initially defined on the aerodynamic grid, they are mapped onto the structural grid as explained in subsection 4.1.2. At any structural node i, the integrated force is obtained by adding its nodal force to the nodal forces of all nodes located further out along the span., see Equation 5.8. In this equation, N refers to the structural node at the blade tip.

$$\mathbf{F}_i = \sum_{j=i}^{N} \mathbf{f}_j \tag{5.8}$$

Since the blade is in static equilibrium, a reaction force at the root must ensure that the sum of the structural forces becomes zero at the hub.

$$\mathbf{F}_{\text{root}} = \sum_{j=1}^{N} \mathbf{f}_{\mathbf{s}j} = \mathbf{0} \tag{5.9}$$

The spanwise distributions of the integrated aerodynamic, centrifugal and structural forces for all three degrees of freedom are shown in Figure 5.16 for the straight blade and the blade with $QCA^* = 0$ and $FA^* = 0.1$. While the structural forces in x- and z-direction are comparable in magnitude, the force is y-direction is dominant. In x-direction, both the aerodynamic and centrifugal force contribute to the structural force, whereas in the y-direction, the centrifugal force dominates. As expected for a propeller rotating about the z-axis, the centrifugal force has no z-component, so the structural force in this direction depends solely on the aerodynamic force.

These force distributions demonstrate how variations in lean change the balance of forces along the span. In x-direction, the changes in blade geometry primarily affect the centrifugal force distribution. The aerodynamic force, however, remains nearly constant in all degrees of freedom, consistent with earlier observations in this work, indicating that geometric modifications can redirect the structural forces to achieve a beneficial structural response without substantially changing the aerodynamic behaviour. As the centrifugal force has no component in the z-direction, the resulting structural force in this direction is little affected by this variation in lean between the two blades. In contrast, the centrifugal force varies in y-direction, although its effect is small compared to the absolute values, causing a change in the structural force of about 1%. Lastly, it should be noted that the integrated structural forces indeed reduce to zero at the hub, which confirms that the blade is in static equilibrium. To assess the contribution of these forces to the root bending moment, the integrated moments are examined next.

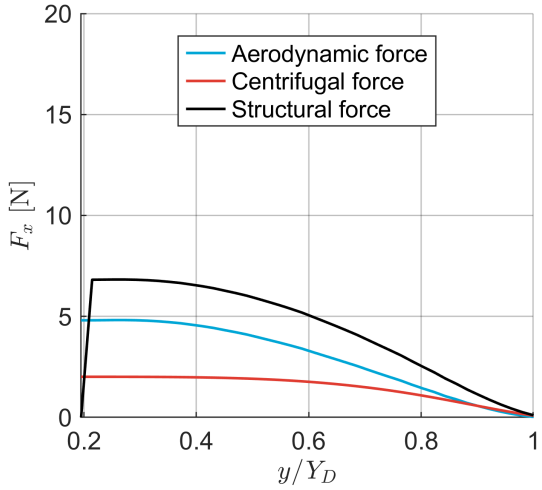

(a) Forces in x-direction for $FA^* = 0$.

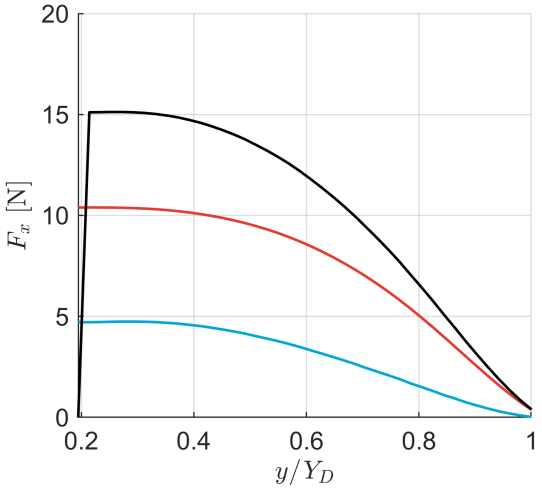

(b) Forces in x-direction for $FA^* = 0.1$.

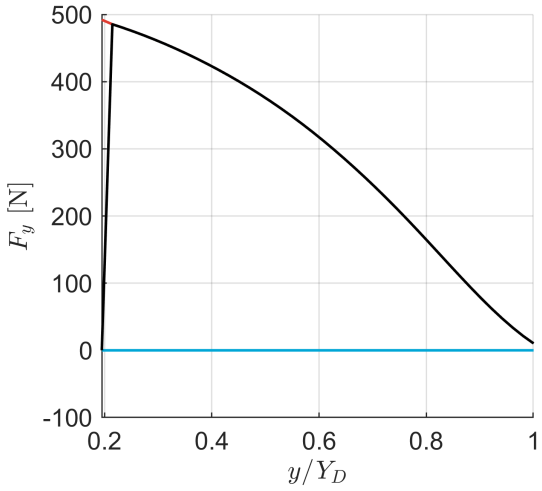

(c) Forces in y-direction for $FA^* = 0$.

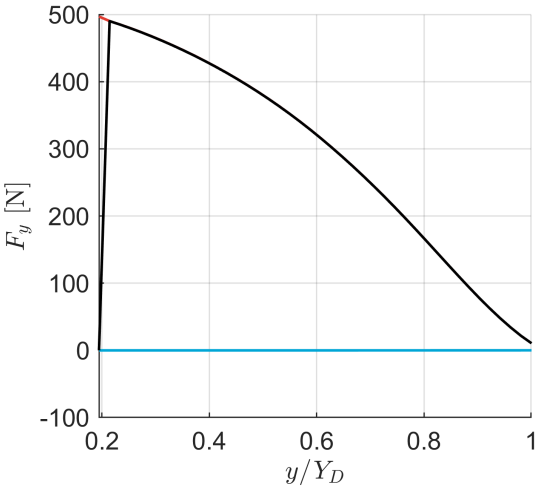

(d) Forces in y-direction for $FA^* = 0.1$.

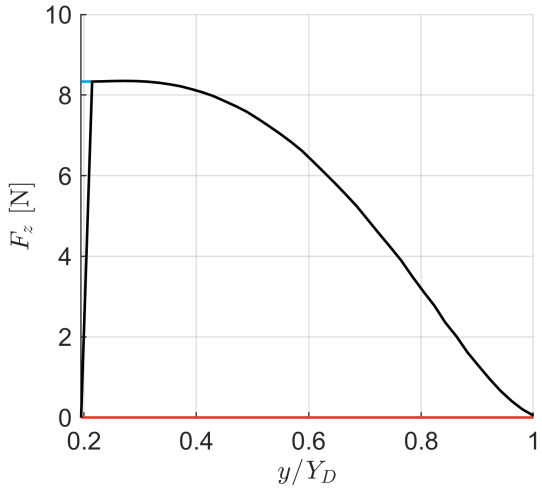

(e) Forces in z-direction for $FA^* = 0$.

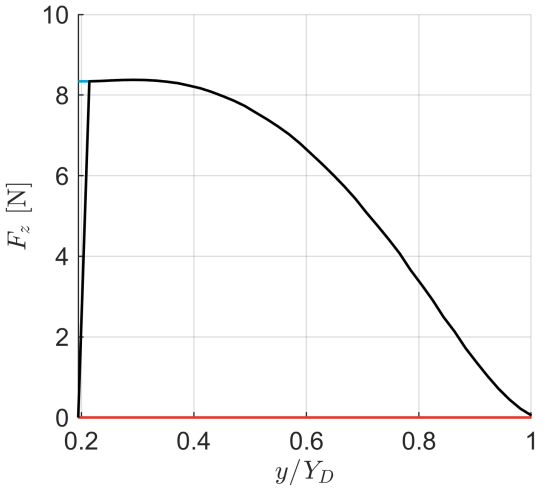

(f) Forces in z-direction for $FA^* = 0.1$.

Figure 5.16: Spanwise distributions of aerodynamic, centrifugal and structural integrated forces for two unswept blades.

The integrated moment is computed by summing the nodal moments together with the moments generated by the nodal forces [5]. These nodal moments arise because the aerodynamic and centrifugal loads do not act directly along the structural axis. The aerodynamic loads act on the aerodynamic grid, producing an aerodynamic moment when mapped onto the structural grid. Similarly, the centrifugal force acts at the cross-sectional centre of mass, which does not necessarily coincide with the structural axis, generating an additional moment. The second contribution of the integrated moment comes from the fact that each nodal force acting on a structural node further outward along the span generates a moment about the chosen reference point of integration. Therefore, at any structural node i, the integrated moment is obtained by summing its nodal moment to the nodal moments of all spanwise outward nodes, and by adding the moments produced by the nodal forces acting at those same nodes, see Equation 5.10. In this way, the integrated moment distribution captures the cumulative effect of all loads acting from the blade tip toward the reference node.

$$\mathbf{M}_i = \sum_{j=i}^{N} \mathbf{m}_j + (\mathbf{r}_j - \mathbf{r}_i) \times \mathbf{f}_j \tag{5.10}$$

As with the integrated structural force, static equilibrium requires that the integrated structural moment reduces to zero at the hub.

$$\mathbf{M}_{\text{root}} = \sum_{j=1}^{N} \mathbf{m}_{\mathbf{s}j} = \mathbf{0} \tag{5.11}$$

For the same unswept blades as in Figure 5.16, with $FA^* = 0$ and $FA^* = 0.1$, the integrated bending moments for all degrees of freedom are shown in Figure 5.17. As expected, the reaction moment at the root ensures that the integrated structural moments reach zero at the hub for both blades in all directions. The aerodynamic moment remains largely unaffected by the change in lean in all three degrees of freedom, whereas the moment due to the centrifugal force does vary in magnitude only. This variation causes the integrated structural bending moment to change sign between the two blades in all directions.

The analysis now concentrates on M_x, since minimizing this moment may be a relevant design target due to its largest variations. The aerodynamic moment in x-direction remains largely unchanged with variations in lean, so the centrifugal force component of M_x becomes the primary focus. Because M_x partially arises from the cross-product of the radius vector with the force vector, only F_y and F_z contribute. The centrifugal force, however, has no component in the z-direction, while its y-component varies only slightly. This indicates that the observed changes in M_x are primarily driven by the change in geometry, affecting both the nodal moment contributions along the span and how the centrifugal forces contribute to the integrated moment through their associated moment arms. More specifically, introducing lean affects the positions of the centres of mass relative to the structural axis, changing the moment arms of the centrifugal forces and thus affecting the magnitude, and possibly the sign, of the nodal moments. At the same time, the geometry affects the positions of the structural nodes relative to each other, changing the three-dimensional distances between the structural nodes. This affects how the nodal forces contribute to the integrated moment, again influencing both the magnitude and possibly the sign of the resulting force-induced moments. Together, these effects determine the variation of the centrifugal force component of M_x observed between the two blades.

As the centrifugal force component of M_x changes magnitude between the two blades, the integrated structural moment changes sign. As a result, the reaction at the root also switches sign, being negative for the straight blade and producing a negative root bending moment, and positive for the blade with lean, matching the trends observed in Figure 5.15. This implies that there must exist an intermediate lean distribution for which the blade experiences a zero root bending moment about the x-axis. Similarly, the spanwise distributions of the integrated moments M_y and M_z indicate that intermediate lean distributions must exist for which the blade experiences a zero root bending moment in the respective degree of freedom. As shown in Figure 5.15, some blade configurations even satisfy $M_x = 0$ and $M_z = 0$ or $M_y = 0$ and $M_z = 0$. However, no single blade configuration both satisfies $M_x = 0$ and $M_y = 0$, nor does any blade meet all three conditions simultaneously.

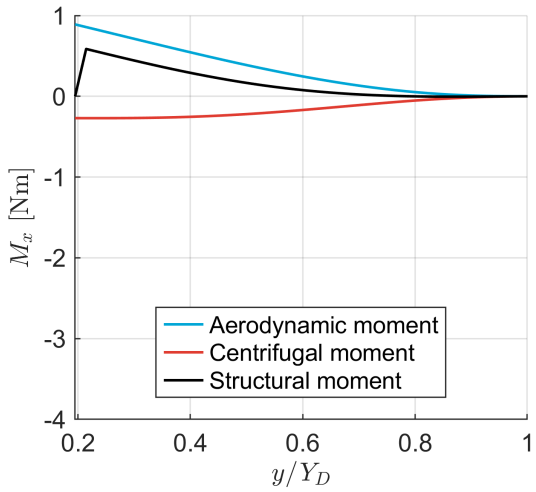

(a) Moments about the x-axis for $FA^* = 0$.

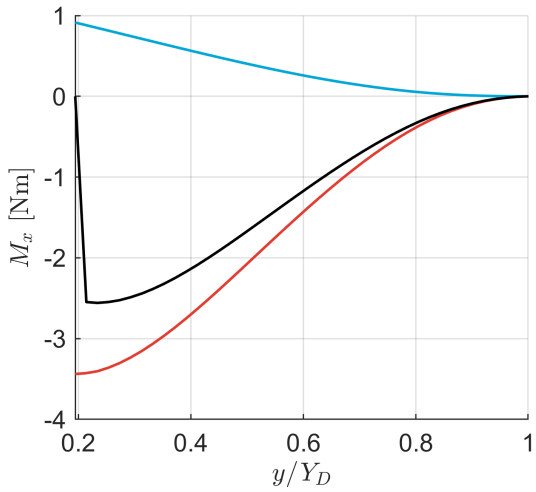

(b) Moments about the x-axis for $FA^* = 0.1$.

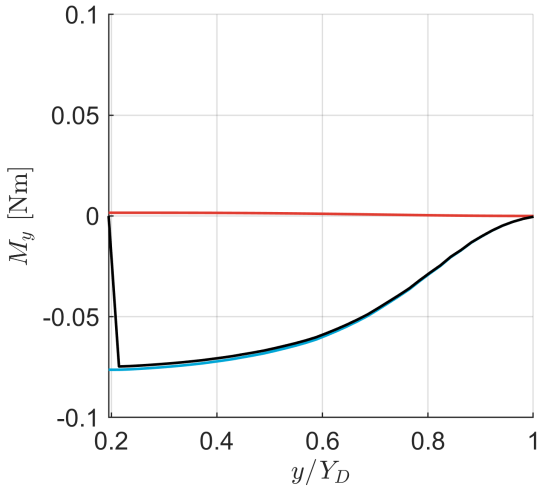

(c) Moments about the y-axis for $FA^* = 0$.

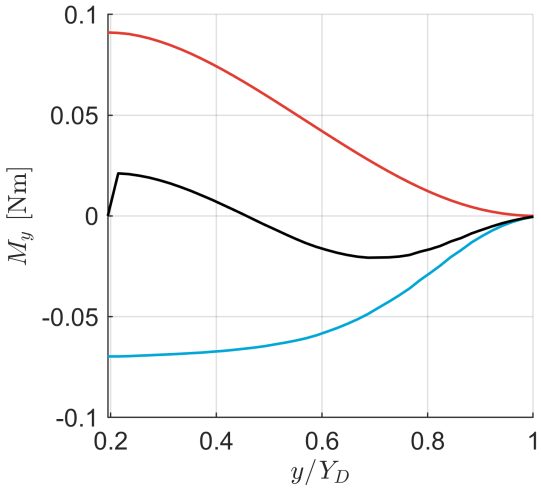

(d) Moments about the y-axis for $FA^* = 0.1$.

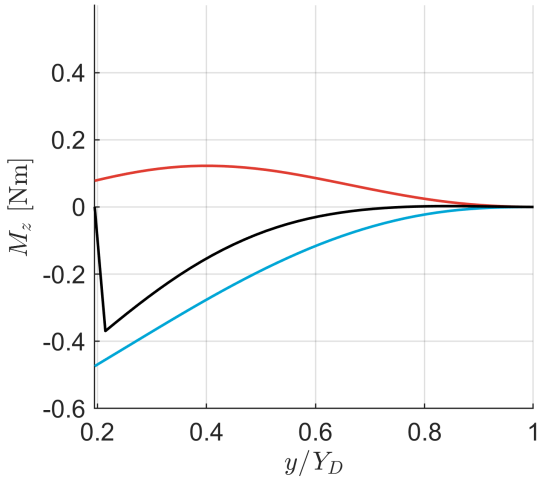

(e) Moments about the z-axis for $FA^* = 0$.

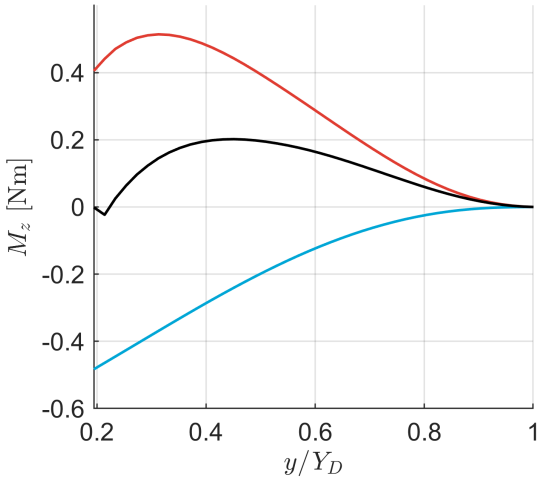

(f) Moments about the z-axis for $FA^* = 0.1$.

Figure 5.17: Spanwise distributions of aerodynamic, centrifugal and structural integrated bending moments for two unswept blades.

5.4.3. Impact of Increased Thrust Level

The effect of thrust on structural behaviour is studied by increasing thrust from 50 N to 100 N, which in practice corresponds to applying a higher pitch setting, while keeping all other parameters fixed. This change affects the blade stresses, as shown by the maximum failure index on the top and bottom skin laminates in Figure 5.18. The corresponding principal and shear strains are provided in Figure F.2.

Compared to Figure 5.11, the maximum value of F_{crit} for the top skin decreases for the blades with positive lean, suggesting a redistribution of the aerodynamic and centrifugal loads that lowers the resulting structural stress. However, this reduction is small, with $\Delta F_{crit} < 0.1$. For the bottom skin, on the other hand, the changes between the two thrust settings are negligible. As shown by Figure 5.19, the corresponding spanwise location of maximum F_{crit} on both skins remains largely unchanged between the two thrust settings. For the top skin, the blades with the highest F_{crit}, characterized by positive sweep and positive lean, show a slight outward shift in this location from $y_{crit}/Y_D = 0.35$ at the 50 N thrust setting to $y_{crit}/Y_D = 0.37$ at 100 N thrust setting, whereas for the bottom skin this difference is too small to determine. This indicates that the region of the blade most vulnerable to structural failure is largely insensitive to this change in operating condition.

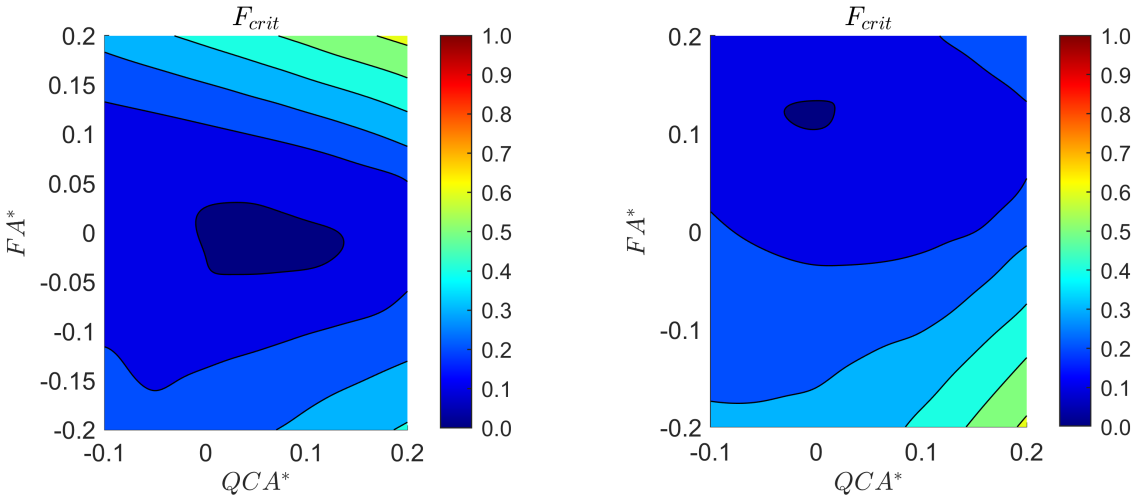

(a) Top skin. **(b)** Bottom skin.

Figure 5.18: Maximum failure index for the top and bottom skin laminates at 100 N thrust.

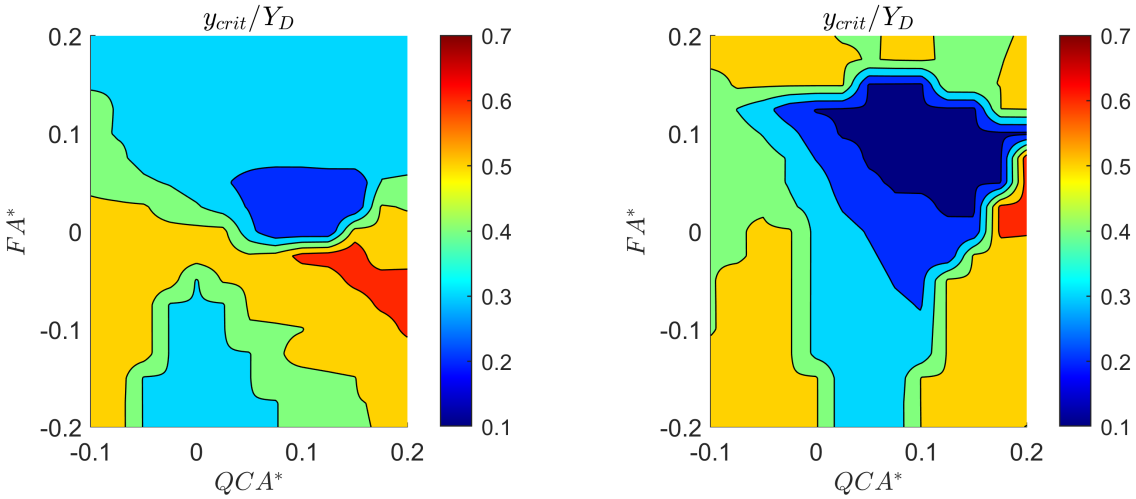

(a) Top skin. **(b)** Bottom skin.

Figure 5.19: Spanwise position of maximum failure factor at a thrust setting of 100 N.

The root bending moments for the 100 N thrust setting are presented in Figure 5.20. Overall, the trends are consistent with those observed at 50 N. The moment M_x still primarily depends on lean and remains largely insensitive to sweep. However, the magnitudes of M_x have decreased throughout the entire parameter space. As a result, the $M_x = 0$ line now occurs at higher lean values. In fact, whereas at 50 N the $M_x = 0$ line was located around $FA^* = 0.02$, it has shifted to approximately $FA^* = 0.04$ at 100 N. This means that a larger positive lean is required for the blade to achieve zero M_x under the higher thrust setting. The range of M_y has slightly increased but it remains small compared to the ranges of M_x and M_z. Therefore, M_y continuous to play a small role in structural stress at the blade root. The values of M_z have increased across the parameter space, and its overall range has also expanded, meaning that the sensitivity of M_z to sweep and lean has increased. Furthermore, a consequence of the decreased M_x is that the lines of $M_x = 0$ and $M_y = 0$ are located closer to each other at 100 N than at 50 N. However, this comes at the cost of increased M_z.

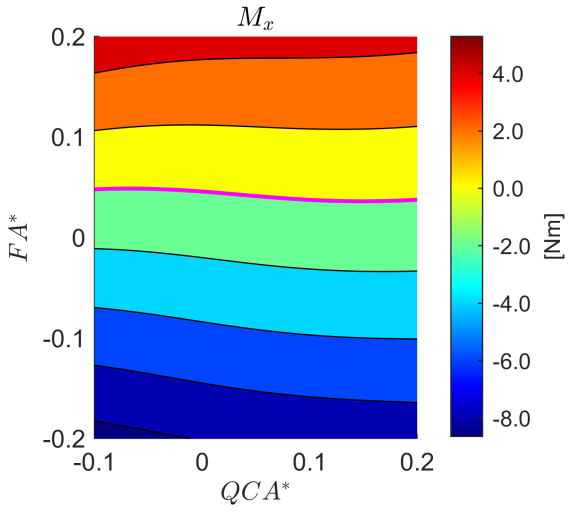

(a) Bending moment about the x-axis.

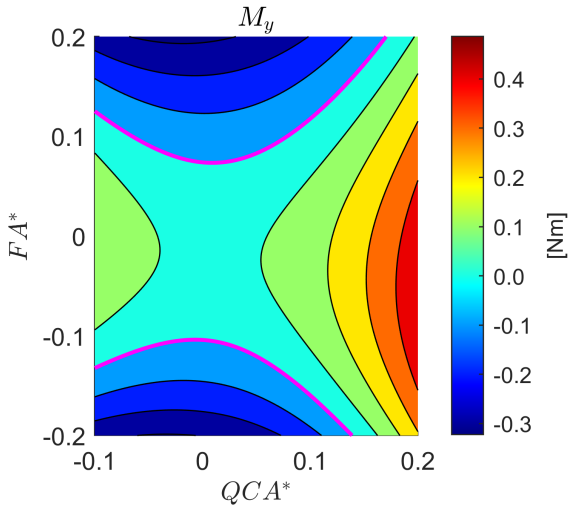

(b) Bending moment about the y-axis.

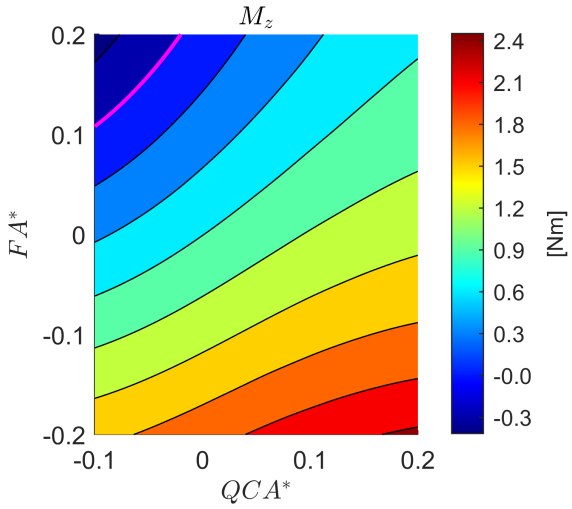

(c) Bending moment about the z-axis.

Figure 5.20: Bending moments at the propeller hub for a thrust setting of 100 N.

Similar to the 50 N thrust setting, M_x again exhibits the largest variation in magnitude across the parameter space at 100 N, compared to M_y and M_z. This implies that minimization of M_x could still be a design target. The underlying behaviour can again be analysed through the integrated forces, computed for the same unswept blades used in the 50 N study, with $FA^* = 0$ and $FA^* = 0.1$. The results are shown in Figure 5.21. As expected, in order to achieve the higher thrust setting, the integrated

aerodynamic forces in x- and z-direction have increased for both blades. In the x-direction, the force has increased from 4.8 N to 10.5 for the straight blade and from 4.7 N to 10.4 N for the leaned blade. In the z-direction, the aerodynamic force increased from 8.3 N at 50 N to 16.7 N at 100 N for both blades. Due to the two-dimensional nature of the BEM model, the aerodynamic force in y-direction remains zero for both blades at both thrust settings. The increase in pitch angle, and the resulting increase of aerodynamic loads, also affects the centrifugal force. Among its components only F_x changes significantly, increasing from 2.0 N to 3.4 N for the straight blade and from 10.4 N to 14.7 N for the leaned blade. These changes in forces result in the differences in root bending moments observed at 50 N in Figure 5.15 compared to those at 100 N in Figure 5.20.

Lastly, the integrated moments for the 100 N thrust setting are shown in Figure 5.22 for the straight blade and the leaned blade with $FA^* = 0$ and $FA^* = 0.1$. The corresponding reaction moments for both blades, and also both thrust settings, are summarized in Table 5.4. The reaction moment at the root in x-direction is lower at 100 N than at 50 N for both blades, that in y-direction remains nearly unchanged and the reaction moment in z-direction increases, consistent with the trends observed in Figure 5.20. Furthermore, also at 100 N, the reaction moment changes sign between the straight and leaned blades in all three degrees of freedom. This suggests the existence of an intermediate lean value where the reaction moment vanishes, resulting in a zero root bending moment. As in the 50 N case, this sign change is primarily driven by centrifugal loads, since the aerodynamic forces are nearly identical for the two blade configurations, as shown by the integrated force distributions in Figure 5.21.

Table 5.4: Comparison of the reaction moments at the propeller hub between the two thrust settings of 50 N and 100 N for both the straight and leaned propeller blades.

Blade	Thrust [N]	M_x [Nm]	M_y [Nm]	M_z [Nm]
Straight	50	-0.59	0.07	0.37
	100	-1.32	0.08	0.84
Leaned	50	2.55	-0.02	0.02
	100	1.69	-0.05	0.37

These results highlight that the numerical values obtained in this parameter study depend on the operating conditions, which have not been optimized in this work. Therefore, when interpreting the results, emphasis should be placed on the observed trends, as they provide insight into how variations in the design parameters affect both the structural behaviour and aerodynamic performance of the blades, allowing for informed design decisions. A comprehensive design study should thus consider multiple operating conditions across the entire mission profile to ensure both the structural behaviour and aerodynamic performance are accurately captured.

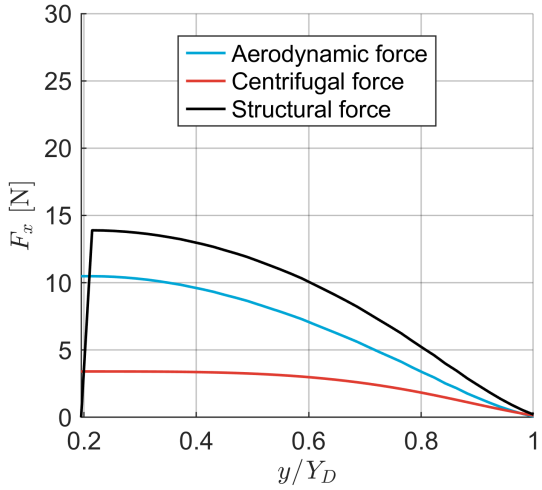

(a) Forces in x-direction for $FA^* = 0$.

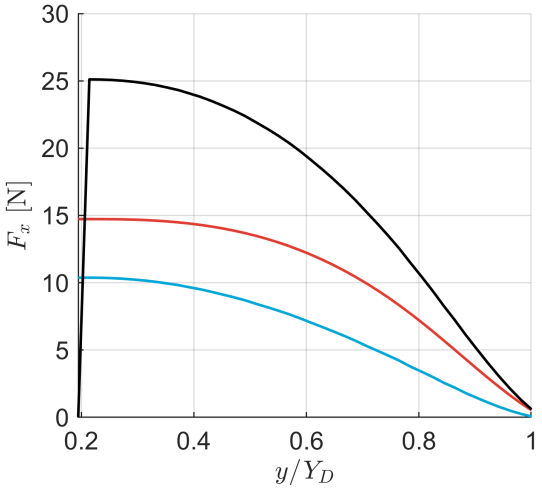

(b) Forces in x-direction for $FA^* = 0.1$.

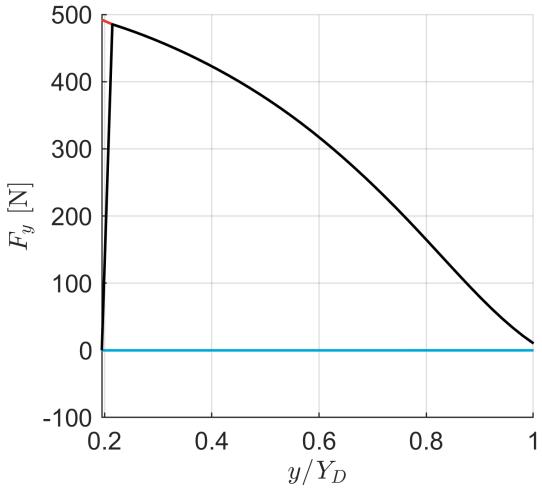

(c) Forces in y-direction for $FA^* = 0$.

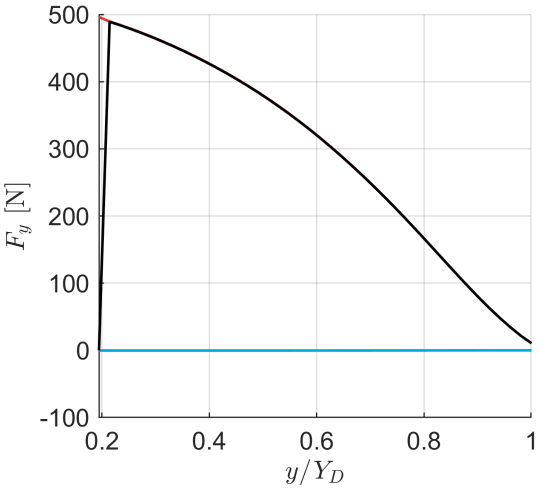

(d) Forces in y-direction for $FA^* = 0.1$.

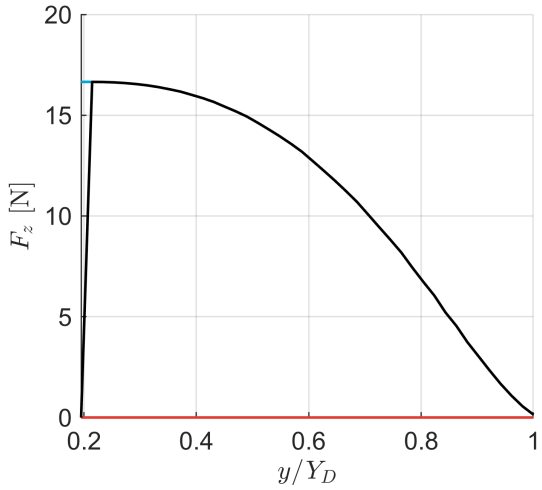

(e) Forces in z-direction for $FA^* = 0$.

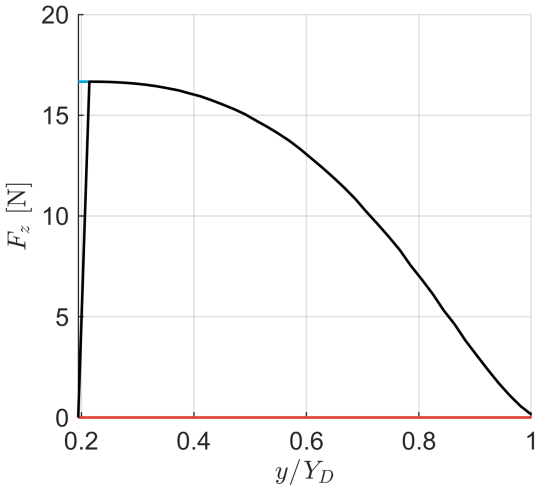

(f) Forces in z-direction for $FA^* = 0.1$.

Figure 5.21: Spanwise distributions of integrated forces for two unswept blades at a thrust setting of 100 N.

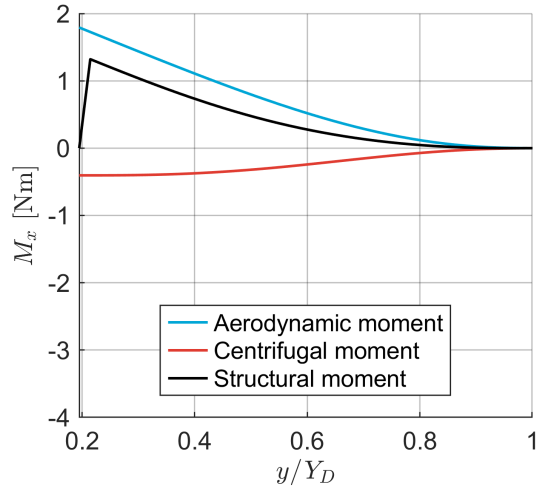

(a) Moments about the x-axis for $FA^* = 0$.

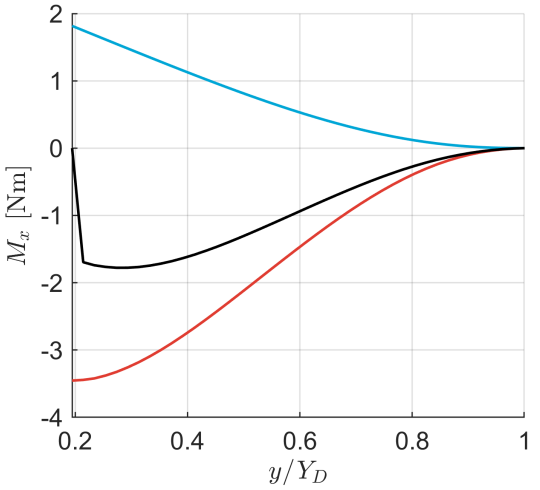

(b) Moments about the x-axis for $FA^* = 0.1$.

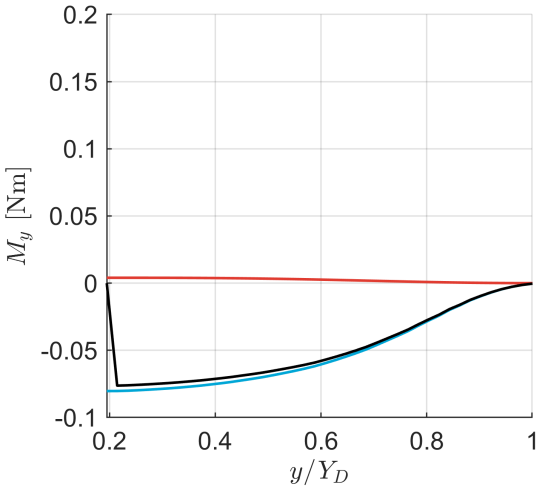

(c) Moments about the y-axis for $FA^* = 0$.

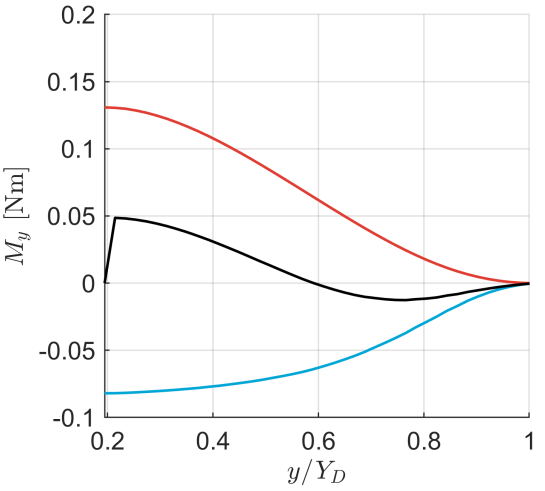

(d) Moments about the y-axis for $FA^* = 0.1$.

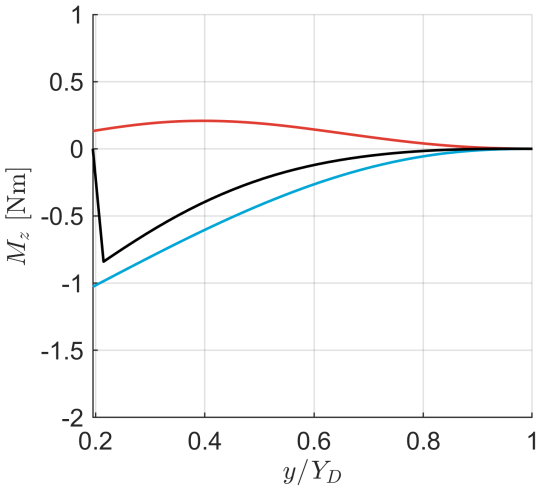

(e) Moments about the z-axis for $FA^* = 0$.

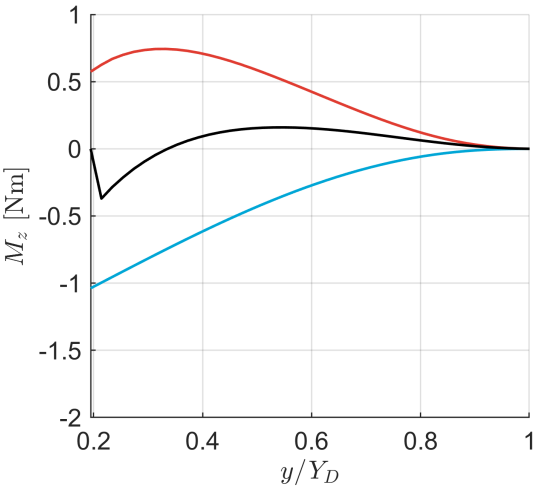

(f) Moments about the z-axis for $FA^* = 0.1$.

Figure 5.22: Spanwise distributions of aerodynamic, centrifugal and structural integrated bending moments for two unswept blades.

6

Conclusion

In this thesis, an aeroelastic analysis tool was developed for propeller blades with arbitrary sweep and lean distributions. To achieve this, an aerodynamic model capable of accounting for sweep and lean was developed and coupled to the existing structural model through a tight coupling approach. Finally, a parameter study was conducted to systematically study the effects of sweep and lean on aerodynamic performance trends and structural response.

Accordingly, the research was structured into three main parts, each addressing one of the research questions defined in chapter 1. The first research question concerns the geometric representation of a swept blade and the development of the aerodynamic model, as addressed in chapter 2 and chapter 3, respectively. The second research question focuses on the establishment of the tight aeroelastic coupling, with particular emphasis on the derivation of the analytical sensitivities, as discussed in chapter 4. The third research question focuses on the parameter study, presented in chapter 5.

The conclusions of this research, along with the corresponding answers to these research questions, are presented below. The research questions are repeated for convenience.

1. *How can the geometry and aerodynamics of propeller blades with sweep and lean be modelled?*
    a) *How should sweep and lean be defined?*
    b) *How can blade element momentum theory be extended to account for sweep and lean when predicting aerodynamic performance trends of swept propellers operating at low Mach numbers?*

To define the geometry of a swept and leaned propeller blade, the global coordinate system must be defined first. In this thesis, the coordinate system is oriented such that the y-axis and z-axis align with the pitch and rotation axes, respectively, while the x-axis is perpendicular to both and oriented positively toward the trailing edge of the blade. Sweep and lean are then defined relative to these axes.

In this work, the geometry of the swept and leaned propeller blade is defined in terms of the quarter-chord alignment QCA and the face alignment FA. These alignments represent the offsets of the quarter-chord line from the global y-axis in x- and z-direction, respectively. In other words, QCA and FA correspond directly to the x- and z-coordinates of the quarter-chord line in the global coordinate system, respectively. This quarter-chord line was chosen as the reference line because it approximately coincides with the aerodynamic centre of the airfoil.

In addition to using geometrical offsets, sweep and lean should also be defined in terms of angles. Two definitions for each parameter were mentioned. First, the sweep angle can be defined as the angle between the global y-axis and the vector pointing towards the quarter-chord line projected onto the xy-plane, while the lean angle is defined similarly using the yz-plane. The alternative definition expresses the sweep and lean angles in terms of the spanwise gradients of the associated alignments. Since the airfoil sections used to evaluate the lift and drag polars are aligned parallel to the incoming flow, these gradient-based angles are not required to determine the airfoil orientation. Additionally, they are

not applied in the sweep correction of the aerodynamic model, which accounts only for the absolute offset of the quarter-chord line and not its spanwise variation. Hence, in this work, the sweep and lean angle are defined as the angles corresponding to the quarter-chord line offsets in the global coordinate system.

As mentioned, the airfoil sections used to evaluate lift and drag polars in this work are oriented parallel to each other for two main reasons. First, this arrangement enabled straightforward validation of the aerodynamic model, as the experimental data from Prud'homme van Reine [4] contained measurements for *XPROP* and *XPROP-*Λ where the airfoil sections parallel to the freestream flow were known and the corresponding lift and drag polars were readily available. Second, aligning the sections in this way prevents overlap of adjacent blade elements, which can occur for highly curved blades due to steep gradients of the quarter-chord line, particularly when the blade is finely discretized along the span. These considerations made the use of parallel airfoil sections the most practical.

In this work, the aerodynamics are modelled using blade element momentum (BEM) theory, which does not inherently account for sweep and lean. Therefore, to enable BEM to capture the aerodynamics of curved blades, a correction factor must be applied. As in swept blades the blade elements are no longer positioned such that the rotation vector is perpendicular to the local chord line, a sweep correction must be applied to the rotational velocity. The orientation of the airfoil relative to the axial freestream velocity remains unchanged, so no correction is required for this component. Lean does not change the airfoil orientation relative to either velocity component, and thus no correction factor is needed to account for blades with lean. However, when pitching the blade, lean transforms into sweep, which indirectly affects the aerodynamic performance. Additionally, the torque coefficient must be adjusted by the sweep angle to account only for the component of torque perpendicular to the rotation vector.

Validation of the extended BEM model against the experimental data from Prud'homme van Reine [4] showed that, although the absolute values are overestimated, the BEM model accurately predicts overall aerodynamic performance trends in terms of thrust, with less accuracy for efficiency. Consistent with the measurements, the predicted effects of sweep and lean on the performance are small. The model reliably captures the sensitivity to sweep for both thrust and efficiency at 30° pitch, though this accuracy decreases at 45° pitch, likely due to stronger three-dimensional aerodynamic effects. This confirms that, despite its limited effect, the extended BEM model can reliably predict the influence of sweep. Thus, for sweep and lean sensitivity studies, the model provides sufficient fidelity at pitch angles around 30°. Accordingly, the model can be applied to parametric studies aimed at identifying design trends, but it is less suitable for detailed design optimization due to the overestimation of absolute performance.

2. *How can the aerodynamic and structural models be tightly coupled for propeller blades with sweep and lean?*
    a) *Which aerodynamic sensitivities are required for tight aeroelastic coupling?*
    b) *How can the required aerodynamic sensitivities be computed analytically?*
    c) *How do the derived analytical sensitivities compare with numerically computed sensitivities?*

The aerodynamic BEM model is tightly coupled to the structural model, meaning that the aerodynamic and centrifugal loads, along with the resulting structural deformations, are not computed iteratively. Instead, the deformations are updated based on the gradients of the aerodynamic and centrifugal loads with respect to the blade deformations. While the gradients of the centrifugal loads were already correctly included in *PROTEUS*, those of the aerodynamic loads needed refinement due to the extension of the BEM model. Since computational efficiency is essential for a preliminary design tool, it was decided to derive these gradients analytically.

A node on the structural grid is defined with three translational and three rotational degrees of freedom corresponding to the three axes of the global coordinate system. Since the aerodynamic loads are independent of the z-coordinate, the sensitivities are only required in the remaining five degrees of freedom, which include translations along x and y and rotations about the x-, y-, and z-axes. These sensitivities can be derived analytically using the methodology developed by Rotundo et al. [19], though improvements are introduced in this work to enhance their accuracy. Based on the extended BEM model, the sensitivities are further adapted to account for blades with sweep and lean. In addition,

geometrical sensitivities must be introduced, defined as sensitivities that do not depend on the operating conditions but solely on the geometry of the quarter-chord line, to predict how the geometric parameters change with translational and rotational variations of the blade. Unlike straight blades, these are non-zero for swept and leaned blades, meaning that they can impact the overall accuracy of the sensitivities. The radial derivative of the Prandtl loss factor, however, presents some difficulties, as it introduces non-zero radial derivatives of the hub and tip radii. Since this radial contribution is small, it can be safely neglected.

The aerodynamic sensitivities with respect to blade deformation in the other degrees of freedom can be derived similarly, except that the sensitivities with respect to blade deformations in the translational degrees of freedom require reformulation in terms of the radial derivative. These derivations were therefore not reproduced in this report. Only the geometric sensitivities were derived explicitly, as they cannot be obtained analogously.

To validate the analytically derived sensitivities, they were compared with numerically computed sensitivities, showing strong agreement across all degrees of freedom. While the error increases slightly between *XPROP* and *XPROP*-Λ, the results remain accurate, which demonstrates the robustness of the analytical sensitivities across different blade geometries. Despite neglecting the radial contribution of the Prandtl loss factor, the comparison with numerical results is satisfactory. The geometric sensitivities, in particular, show excellent agreement. Since the sensitivities show such strong agreement, all of them were used in the aeroelastic analysis of chapter 5.

In terms of computational efficiency, the analytical method shows significant improvement, reducing the computational cost by over 90% compared to numerical computations. For *XPROP*, this results in a 30% reduction in computational time of the aeroelastic analysis when using the tight coupling compared to the loose coupling, while for *XPROP*-Λ the reduction is even larger. At the same time, the predicted structural deformations and aerodynamic loads show excellent agreement between the two methods, confirming that the tight coupling approach can be used with confidence.

3. *What is the effect of combining sweep and lean on the aerodynamic performance and structural response of an isolated propeller?*
    a) *How does the aerodynamic performance of flexible blades featuring sweep and lean compare to that of rigid blade designs?*
    b) *What is the effect of sweep and lean on the aerodynamic performance of flexible blades compared to a straight blade?*
    c) *How does lean influence the structural response of swept blades?*

To study the effects of sweep and lean on the aerodynamic performance and structural response of a propeller blade, a parameter study was performed. Sweep was parametrized by scaling the geometry of *XPROP*-Λ, while lean was represented using a simplified distribution oriented either fully upstream or fully downstream.

The aerodynamic efficiency of five flexible blades was compared with their rigid counterparts at pitch settings of 30°, 35°, and 45°. The selected blades included the straight blade, two unswept blades with positive and negative lean, and two blades without lean featuring positive and negative sweep. Overall efficiency differences were found to be small. Backward sweep and downward lean caused noticeable deviations, but the pitch setting dictated which configuration performed better, so no consistent trend could be determined. Differences in peak aerodynamic efficiency were generally below 0.3%, except for the unswept blade with downstream lean at a pitch of 30°, where the rigid blade outperformed the flexible blade by 1%. Despite this limited effect on peak efficiency, blade flexibility does have a measurable aerodynamic impact, as it affects both the generated thrust and required power. Thus, although structural flexibility introduces torsional and translational deformations that influence the local pitch angle and spanwise loading distribution, thereby changing both the generated thrust and required power, it can be concluded that these aeroelastic effects are not strong enough to significantly change peak aerodynamic efficiency.

The aerodynamic performance of flexible blades was further examined through aeroelastic analysis at a constant thrust coefficient T_C. The results show that, within the considered parameter space and

operating conditions, the propulsor efficiency can increase by up to 1.7% compared to the flexible straight blade. Blades combining backward sweep with upward lean achieve the highest efficiency, while negative lean yields a smaller, yet positive, effect. A reduction in efficiency compared to the straight blade only occurs for blades with moderate backward or forward sweep combined with positive lean. These efficiency differences result from changes in the aerodynamic loading distribution along the blade due to the varying geometries. The observed efficiency trends can be attributed to changes in the spanwise distribution of induced and profile efficiencies, which together define the spanwise variation of sectional propulsor efficiency. Induced efficiency was found to be the dominant factor, meaning that the blade geometry primarily affects efficiency by changing the induced velocities and causing variations in the associated losses due to swirl. Part of this observed efficiency increase, however, can be attributed to the larger disk area of propellers with highly curved blades. Nevertheless, the efficiency trends do not directly match the trends in disk radius, which indicates a contribution from aeroelastic effects, in particular for backward-swept blades. To clearly isolate these aeroelastic contributions, curved blades should ideally be compared at equal disk areas. Forward sweep may offer similar benefits, but that could not be determined due to the limited range of forward sweep considered in this study.

The structural behaviour of flexible blades was assessed through aeroelastic analysis at constant dimensional thrust. Using the Tsai-Wu failure index F_{crit}, trends in blade stress could be visualized. This revealed that the top skin laminate experiences the highest stress, which increases with backward sweep and upstream lean. These trends are explained by the principal strain and shear strain, showing that higher values of one or both correspond to a higher F_{crit}. Furthermore, for geometries with significant F_{crit}, the maximum value of F_{crit} consistently occurs at nearly the same spanwise location, which was attributed to the use of scaled *XPROP*-Λ blades. Regarding the effect of lean on swept blades, both forward-swept and backward-swept blades exhibit the most favourable structural response in terms of F_{crit} when no lean is applied.

The structural response of swept blades was further analysed using root bending moments, which provide an indirect measure of blade stress at the propeller hub. The root bending moment about the x-axis, corresponding to bending out of the plane of rotation, was found to vary most across the parameter space, which could make minimization of M_x an important design target. Lean has a pronounced impact on the bending moment about the x-axis, while the effect of sweep is negligible. Therefore, applying upstream lean to a swept blade can significantly reduce the root bending moment about the x-axis. In fact, for a given blade sweep, it is even possible to apply an amount of upstream lean that results in zero M_x. Due to the small variation in M_y across the parameter space, applying lean has a negligible effect on it, while increasing lean also positively impacts M_z. Thus, lean can significantly affect the root bending moment for swept blades, although the resulting changes in blade stress, as indicated by F_{crit}, must also be considered.

These trends in root bending moments with varying geometry can be explained by the spanwise distributions of the integrated forces and moments. The analysis showed that varying lean changes the spanwise distributions of the centrifugal force and the resulting moments, while the distributions of the aerodynamic forces and moments remain nearly unchanged. Thus, changing lean affects the spanwise distribution of the centrifugal loads, which could result in a favourable bending moment at the propeller hub.

Lastly, the effect of thrust setting on the structural response was examined by doubling the thrust. This increase caused a slight decrease in maximum F_{crit} for the top skin, suggesting that the aerodynamic and centrifugal loads are redistributed in a way that lowers the resulting structural stresses, while F_{crit} for the bottom skin remained nearly unaffected. The root bending moments were also affected, with decreasing M_x and increasing M_z. Due to the negative sign of M_x, a higher lean is required for a given blade sweep to achieve zero M_x at the higher thrust setting. Meanwhile, M_y remains small compared to M_x and M_z. The trends in root bending moment could again be explained by variations in the spanwise distributions of the integrated forces and moments, which show that changes in the centrifugal load remain the primary driving factor at higher thrust. Comparison of the results between the two thrust settings highlights that the numerical values obtained in this parameter study depend on the operating conditions, which have not been optimized in this work. Therefore, when interpreting the results, emphasis should be placed on the observed trends rather than on the absolute values.

7

Recommendations

In this chapter, the limitations of this work are examined and the assumptions that may influence the accuracy of the results are discussed. In addition, recommendations for future research are provided, focusing on potential methodological improvements, extensions of the aeroelastic framework, and further studies that could enhance the understanding of sweep and lean effects on propeller performance.

Regarding the geometry of the propeller blade, the aeroelastic model assumes that the airfoil sections retain their shape and remain parallel to the freestream flow at all times. In other words, as the blade deforms under aerodynamic and centrifugal loads, the cross-sections are assumed not to undergo significant shear or twisting that would change either their shape or their orientation relative to the axial flow, apart from variations in pitch angle. This assumption is likely reasonable for small deformations but becomes less accurate as the deformations grow larger. In such cases, bending–twisting coupling can change the orientation of the airfoil section under transverse loads, while extension–shearing coupling can change the airfoil shape under axial loads. This could affect both the aerodynamic loading and the structural response. By neglecting these effects, the model may predict local deformations incorrectly, particularly near the blade root where the bending moments are large, or near the tip where the aerodynamic loading is high.

In this work, the aerodynamic model was validated only for *XPROP* and *XPROP*-Λ, whereas the parameter study considered a much larger range of sweep. Moreover, the validation was limited to blades with negligible lean. Wind tunnel testing of highly curved blades would therefore be valuable to assess whether the extended BEM model remains accurate for larger sweep and lean. Such tests could also indicate whether additional sweep and lean corrections, for example based on their local gradients, are necessary.

Another limitation concerns compressibility. Since the model applies the Prandtl–Glauert correction, results are valid only for Mach numbers up to approximately 0.7. Furthermore, the BEM model could only be validated at low Mach and Reynolds numbers due to the limited availability of experimental data. Therefore, it would be interesting to identify up to which Mach number BEM remains accurate, thus at which point accuracy degrades, and what additional sweep and lean corrections may be required under such conditions. For higher Mach numbers, rather than applying the Prandtl–Glauert correction to numerically computed airfoil polars, it may be better to use polar data from higher-fidelity numerical simulations like RANS. This approach would directly account for compressibility effects and remove the need for additional correction factors. Furthermore, RANS can better predict the transition from laminar to turbulent flow, making the e^N method unnecessary. However, BEM theory might not be adequate for conditions where three-dimensional shock wave formation occurs.

In general, BEM models are unable to capture three-dimensional aerodynamic effects because they neglect interactions between blade elements. An alternative would be to use a higher-fidelity aerodynamic model such as lifting-line theory. Prud'homme van Reine [4] conducted a comparative study of two different LLT methods against experimental performance data for the XPROP and XPROP-Λ propellers. The results showed that both LLT methods failed to accurately predict the aerodynamic

performance. In fact, switching between the two lifting-line methods had a larger impact on the performance than changing from XPROP to XPROP-Λ. In other words, the sensitivity of LLT to the chosen method is larger than the sensitivity of the aerodynamic performance to sweep. This suggests that LLT may not be sufficiently reliable for accurately predicting the performance of swept propeller blades. Therefore, replacing BEM with LLT offers little improvement. For higher aerodynamic accuracy, more advanced methods such as the vortex-lattice method could be applied. However, these come with increased computational cost, which might be undesirable during the preliminary design phase.

Although the analytical aerodynamic sensitivities showed high accuracy compared to numerically computed results, they could be further improved by extending the sensitivity of the lift, drag, and moment coefficients to account for velocity changes resulting from the structural deformation. For example, the sensitivity of these coefficients with respect to twist deformation can be expressed in terms of $dV/d\beta$.

$$\begin{bmatrix} C_{l_\beta} \\ C_{d_\beta} \\ C_{m_\beta} \end{bmatrix} = \begin{bmatrix} C_{l_\alpha} \\ C_{d_\alpha} \\ C_{m_\alpha} \end{bmatrix} \frac{d\alpha}{d\beta} + \begin{bmatrix} C_{l_{Re}} \\ C_{d_{Re}} \\ C_{m_{Re}} \end{bmatrix} \frac{\rho c}{\mu} \frac{dV}{d\beta} \tag{7.1}$$

However, the magnitudes of $C_{l_{Re}}$, $C_{d_{Re}}$ and $C_{m_{Re}}$ are expected to be much smaller than those of C_{l_α} C_{d_α} C_{m_α}, because the effect of angle of attack on the aerodynamic performance is much more significant than that of velocity change. This would therefore only have a minor impact on the analytical results. Additionally, the radial contribution of the Prandtl loss factor sensitivities could be further examined to enhance the analytical sensitivities.

In the parameter study of this work, the applied range of sweep and lean was limited. For sweep, only scaled versions of *XPROP-*Λ were considered. This simplification is reasonable, as tip sweep is typically backward to reduce both the tip Mach number and noise, while blades are often forward-swept near the root to limit the tip offset. Lean, on the other hand, was restricted to fully upward or fully downward distributions. Using the Bézier parametrization, the parameter space could be easily expanded by increasing the range of the control point coordinates or the number of control points, to allow for more complex distributions. The use of scaled *XPROP-*Λ blades may also explain the nearly constant spanwise location of maximum stress, which could be further investigated by testing sweep distributions that are not scaled versions of *XPROP-*Λ. Additionally, when performing a parameter study, scaling the propeller diameter could be considered to enable comparison of propellers of equal size.

The next step would be to perform a design study focusing on structural optimization of curved propeller blades. Geometric design variables could also be included into the optimization framework to achieve a fully aeroelastically optimized design. However, improvements to the aerodynamic model may be necessary to provide more accurate predictions, in particular for highly curved blades or blades operating at high freestream Mach numbers or pitch angles. Moreover, the present aeroelastic model is limited to static analysis, meaning that dynamic effects such as flutter are not considered. Studying these effects would be essential for a comprehensive evaluation of the blades' aerodynamic performance and structural integrity.

References

[1] P. Alves, M. Silvestre, and P. Gamboa. “Aircraft Propellers—Is There a Future?” In: *Energies* 13 (2020), p. 4157. DOI: 10.3390/en13164157.

[2] L. L. Jensen, P. A. Bonnefoy, J. I. Hileman, and J. T. Fitzgerald. “The carbon dioxide challenge facing U.S. aviation and paths to achieve net zero emissions by 2050”. In: *Progress in Aerospace Sciences* 141 (2023). DOI: 10.1016/j.paerosci.2023.100921.

[3] C. J. Miller and J. P. Sullivan. “Noise Constraints Effecting Optimal Propeller Designs”. In: SAE General Aviation Aircraft Meeting and Exposition. NASA Technical Memorandum, 1985. DOI: 10.4271/850871.

[4] K. Prud’homme van Reine. “A Comparative Study into the Effectiveness of Lifting-Line Methods for Swept Propellers”. M.Sc. Thesis. Delft University of Technology, Sept. 2025. URL: http://repository.tudelft.nl/.

[5] J. Sodja, R. Drazumeric, T. Kosel, and P. Marzocca. “Design of Flexible Propellers with Optimized Load-Distribution Characteristics”. In: *Journal of Aircraft* 51.1 (2014), pp. 117–128. DOI: 10.2514/1.C032131.

[6] Jaimy Thielen. “Effects of Elasticity on Aeroacoustic Performance of Low-Noise Swept Propellers”. M.Sc. Thesis. Delft: Delft University of Technology, May 2024. URL: http://repository.tudelft.nl/.

[7] C. D. Rotundo, J. Sodja, and T. Sinnige. “Aeroelastic tailoring of dual-role propellers”. In: Aeroelasticity & Structural Dynamics in a Fast Changing World 17 – 21 June 2024. The Hague, The Netherlands, 2024.

[8] F. Yin and A. G. Rao. “A review of gas turbine engine with inter-stage turbine burner”. In: *Progress in Aerospace Sciences* 121 (2020). DOI: 10.1016/j.paerosci.2020.100695.

[9] F. Yin. “Engine Design Trends - AE4238 Aero Engine Technology Lecture 5”. Delft, Sept. 19, 2023.

[10] J.D. Anderson. “Some Propulsion Characteristics”. In: *Aircraft Performance and Design*. 5th ed. Tata McGraw-Hill, 2012, pp. 145–188. ISBN: 978-0-07-070245-5.

[11] X. Geng, T. Hu, P. Liu, T. Sinnige, and G. Eitelberg. “Analysis of thrust-scaled acoustic emissions of aircraft propellers and their dependence on propulsive efficiency”. In: 32nd Congress of the International Council of the Aeronautical Sciences. International Council of the Aeronautical Sciences, 2021.

[12] X. Geng, P. Liu, T. Hu, Q. Qu, J. Dai, C. Lyu, Y. Ge, and R.A.D. Akkermans. “Multi-fidelity optimization of a quiet propeller based on deep deterministic policy gradient and transfer learning”. In: *Aerospace Science and Technology* 137 (2023). DOI: 10.1016/j.ast.2023.108288.

[13] T. H. Keil. “A sensitivity study on the effect of blade sweep on the trade-off between propeller efficiency and noise with panel method analysis”. M.Sc. Thesis. Delft University of Technology, Oct. 2021. URL: http://repository.tudelft.nl/.

[14] *Who we are*. Clean Aviation. URL: https://www.clean-aviation.eu/about-us/who-we-are (visited on 09/21/2025).

[15] N. W. Bown, R. Simpson, L. Baert, I. Lepot, M. Minervino, M. Barbarino, G. Mingione, D. Giacché, L. Drack, K. Lammers, R. Habing, P. Gardarein, Y. Delrieux, M. Balbo, and M. DiGiulio. “Experimental and Analytical Evaluation of Low-Noise Propeller Designs for Large Regional Aircraft”. In: *AIAA SCITECH 2024 Forum*. American Institute of Aeronautics and Astronautics, 2024. DOI: 10.2514/6.2024-2637.

[16] G. Margalida, B. della Corte, T. Sinnige, K. Knepper, B. Soemarwoto, and R. Nahuis. “Low Fidelity Multidisciplinary Methodology for Efficient and Quiet Propeller Design: Numerical Investigation and Experimental Validation”. In: *30th AIAA/CEAS Aeroacoustics Conference (2024)*. American Institute of Aeronautics and Astronautics, 2024. DOI: 10.2514/6.2024-3317.

[17] *Propeller Models*. TU Delft: Faculty of Aerospace Engineering, Flight Performance and Propulsion Department. URL: https://www.tudelft.nl/lr/organisatie/afdelingen/flow-physics-and-technology/flight-performance-propulsion/flight-performance/propeller-aerodynamics/facilities/propeller-models (visited on 08/21/2025).

[18] F. Möhren, O. Bergmann, F. Janser, and C. Braun. “On the influence of elasticity on propeller performance: a parametric study”. In: *CEAS Aeronautical Journal* 14 (2023). DOI: 10.1007/s13272-023-00649-y.

[19] C. D. Rotundo, T. Sinnige, and J. Sodja. “Aeroelastic Model for Design of Composite Propellers”. In: Proceedings of the AIAA SCITECH 2024 Forum. American Institute of Aeronautics and Astronautics, 2024. DOI: 10.2514/6.2024-2677.

[20] W. de Haan. “Impact of Blade Sweep on Aerodynamic and Aeroacoustic Performance Optimization of Isolated Propellers”. M.Sc. Thesis. Delft University of Technology, Aug. 2021. URL: http://repository.tudelft.nl/.

[21] J. D. Anderson. “Incompressible Flow over Airfoils”. In: *Fundamentals of Aerodynamics*. 6th ed. McGraw-Hill series in aeronautical and aerospace engineering. Mcgraw-Hill Education, 2017, pp. 321–422. ISBN: 978-1-259-12991-9. URL: http://lccn.loc.gov/2015040997.

[22] O. Gur. “Propeller Geometric Definition”. In: *Propeller Design*. 1st ed. American Institute of Aeronautics & Astronautics, 2024, pp. 27–37. ISBN: 978-1-62410-714-6.

[23] C. D. Rotundo. “M.Sc. Graduation Project, Flexible Composite Propeller Design for Optimized Performance in Propulsive and Regenerative Operating Conditions”. M.Sc. Thesis. Delft University of Technology, Nov. 2023. URL: http://repository.tudelft.nl/.

[24] N. P. M. Werter. “Aeroelastic Modelling and Design of Aeroelastically Tailored and Morphing Wings”. PhD thesis. Delft University of Technology, 2017. URL: http://repository.tudelft.nl/.

[25] T. Sinnige. “Propeller Propulsion Aerodynamics - AE4130 Aircraft Aerodynamics Lecture 14”. Delft, Jan. 10, 2024.

[26] Q. R. Wald. “The aerodynamics of propellers”. In: *Progress in Aerospace Sciences* 42.2 (2006), pp. 85–128. DOI: 10.1016/j.paerosci.2006.04.001.

[27] O. Bergmann, F. Götten, C. Braun, and F. Janser. “Comparison and evaluation of blade element methods against RANS simulations and test data”. In: *CEAS Aeronautical Journal* 13 (2022), pp. 535–557. DOI: 10.1007/s13272-022-00579-1.

[28] O. Gur and A. Rosen. “Comparison between blade-element models of propellers”. In: *The Aeronautical Journal* 112.1138 (2008), pp. 689–704. DOI: 10.1017/S0001924000002669.

[29] W. J. M. Rankine. “On the mechanical principles of the action of propellers”. In: *Transaction of the Institute of Naval Architects* 6 (1865).

[30] E. Branlard, K. Dixon, and M. Gaunaa. “An improved tip-loss correction based on vortex code results”. In: *Proceedings of EWEA 2012 - European Wind Energy Conference & Exhibition*. European Wind Energy Association (EWEA). European Wind Energy Association (EWEA), 2012.

[31] K. Ismail and W. Okita. “A Comprehensive Comparative Investigation of the Lifting Line Theory and Blade Element Momentum Theory Applied to Small Wind Turbines”. In: *Journal of Energy Resources Technology* 144.8 (2022). DOI: 10.1115/1.4053066.

[32] A. Rosen and O. Gur. “Novel Approach to Axisymmetric Actuator Disk Modeling”. In: *AIAA Journal* 46.11 (2008), pp. 2914–2925. DOI: 10.2514/1.37383.

[33] S. Burger. “Multi-Fidelity Aerodynamic and Aeroacoustic Sensitivity Study of Isolated Propellers”. M.Sc. Thesis. Delft University of Technology, Sept. 2020. URL: http://repository.tudelft.nl/.

[34] X. Liu and W. He. “Performance Calculation and Design of Stratospheric Propeller”. In: *IEEE Access* 5 (2017), pp. 14358–14368. DOI: 10.1109/ACCESS.2017.2725303.

[35] D. B. Hanson. “Helicoidal Surface Theory for Harmonic Noise of Propellers in the Far Field”. In: *AIAA Journal* 18.10 (1980), pp. 1213–1220. DOI: 10.2514/3.50873.

[36] O. Bergmann, F. Möhren, C. Braun, and F. Janser. “Aerodynamic Analysis of Swept Propeller with BET and RANS”. In: Deutscher Luft- und Raumfahrtkongres 2021. Publisher: Deutsche Gesellschaft für Luft- und Raumfahrt. 2021. DOI: 10.25967/550151.

[37] C. N. Adkins and R. H. Liebeck. “Design of optimum propellers”. In: *Journal of Propulsion and Power* 10.5 (1994), pp. 676–682. DOI: 10.2514/3.23779.

[38] E. Branlard. “Wind turbine tip-loss corrections”. M.Sc. Thesis. Technical University of Denmark, Sept. 2011. URL: https://backend.orbit.dtu.dk/ws/portalfiles/portal/155576829/Branlard_2011_TipLosses_MscThesis_Public.pdf.

[39] M. L. Buhl Jr. *New Empirical Relationship between Thrust Coefficient and Induction Factor for the Turbulent Windmill State*. Technical Report NREL/TP-500-36834. 2005.

[40] C. Bak. “Aerodynamic design of wind turbine rotors”. In: *Wind Energy Systems*. Elsevier, 2011, pp. 161–207. DOI: 10.1533/9780857090638.2.161.

[41] J. D. Anderson. “Aerodynamics of the Airplane: The Drag Polar”. In: *Aircraft Performance and Design*. 5th ed. Tata McGraw-Hill, 2012, pp. 51–144. ISBN: 978-0-07-070245-5.

[42] J. D. Anderson. “Subsonic Compressible Flow over Airfoils: Linear Theory”. In: *Fundamentals of Aerodynamics*. 6th ed. McGraw-Hill series in aeronautical and aerospace engineering. Mcgraw-Hill Education, 2017, pp. 739–810. ISBN: 978-1-259-12991-9. URL: http://lccn.loc.gov/2015040997.

[43] M. L. A. Gemaque, J. R. P. Vaz, and O. R. Saavedra. “Optimization of Hydrokinetic Swept Blades”. In: *Sustainability* 14.21 (2022). DOI: 10.3390/su142113968.

[44] J. Goyal, T. Sinnige, F. Avallone, and C. Ferreira. “Aerodynamic and Aeroacoustic Characteristics of an Isolated Propeller at Positive and Negative Thrust”. In: *AIAA AVIATION 2021 FORUM* (2021). DOI: 10.2514/6.2021-2187.

[45] N. P. M. Werter and R. De Breuker. “A novel dynamic aeroelastic framework for aeroelastic tailoring and structural optimisation”. In: *Composite Structures* 158 (2016), pp. 369–386. DOI: 10.1016/j.compstruct.2016.09.044.

[46] M. Drela. *QPROP Formulation*. 2006. URL: https://web.mit.edu/drela/Public/web/qprop/qprop_theory.pdf.

[47] V. Giurgiutiu. “Chapter 2 - Fundamentals of aerospace composite materials”. In: *Stress, Vibration, and Wave Analysis in Aerospace Composites*. Academic Press, 2022, pp. 29–109. ISBN: 978-0-12-813308-8. DOI: https://doi.org/10.1016/B978-0-12-813308-8.00004-1.

[48] R. Nederlof, D. Ragni, and T. Sinnige. “Experimental Investigation of the Aerodynamic Performance of a Propeller at Positive and Negative Thrust and Power”. In: *AIAA Aviation 2022 forum* (2022). DOI: 10.2514/6.2022-3893.

[49] A. Busemann. “Aerodynamischer Auftrieb bei Überschallgeschwindigkeit”. In: *Conference Proceedings Volta Congress*. 1935.

[50] B. G. Marinus. “Multidisciplinary Optimization of Aircraft Propeller Blades”. PhD thesis. University Lyon, Nov. 2011. URL: https://acoustique.ec-lyon.fr/publi/marinius_thesis.pdf.

[51] B. G. Marinus, M. Roger, R. Van Den Braembussche, and W. Bosschaerts. “Multidisciplinary Optimization of Propeller Blades: focus on the aeroacoustic results”. In: *17th AIAA/CEAS Aeroacoustics Conference (32nd AIAA Aeroacoustics Conference)*. June 2011. DOI: 10.2514/6.2011-2801.

[52] S. Baydas and B. Karakas. “Defining a curve as a Bezier curve”. In: *Journal of Taibah University for Science* 13.1 (2019), pp. 522–528. DOI: 10.1080/16583655.2019.1601913.

[53] M. H. Straathof, M. J. L. van Tooren, M. Voskuijl, and B. Koren. “Aerodynamic Shape Parameterisation and Optimisation of Novel Configurations”. In: *Proceedings of the 2008 Royal Aeronautical Society Annual Applied Aerodynamics Research Conference*. 2008. URL: https://repository.tudelft.nl/.

[54] W. de Gruijl. “The Impact of Installation Effects on Propeller Design Optimization for Aerodynamic and Aeroacoustic Performance”. M.Sc. Thesis. Delft University of Technology, May 2022. URL: http://repository.tudelft.nl/.

[55] X. Shen, H. Yang, J. Chen, X. Zhu, and Z. Du. “Aerodynamic shape optimization of non-straight small wind turbine blades”. In: *Energy Conversion and Management* 119 (2016), pp. 266–278. DOI: 10.1016/j.enconman.2016.04.008.

A

Propeller Blade Geometry

The *TUD-XPROP* propeller, often referred to as *XPROP*, is the reference propeller within the Flight Performance and Propulsion (FPP) department of TU Delft's Aerospace Engineering faculty. It is a six-bladed propeller with a diameter of 0.4064 m. Since its blades have negligible sweep and lean, they can be considered straight. The propeller is designed with a variable-pitch mechanism that allows the blades to be manually adjusted to any desired pitch setting [17], making the propeller suitable for a wide range of experimental tests.

To investigate the aerodynamic effects of sweep, the FPP department has designed a propeller called *XPROP*-Λ. This propeller shares the same geometry as *XPROP* with an increased amount of sweep, which was achieved by displacement of the blade's quarter-chord line in (negative) x-direction under zero-pitch.

The geometric layout of *XPROP* is shown in Figure A.1, and the geometric properties of both propellers are listed in Table A.1.

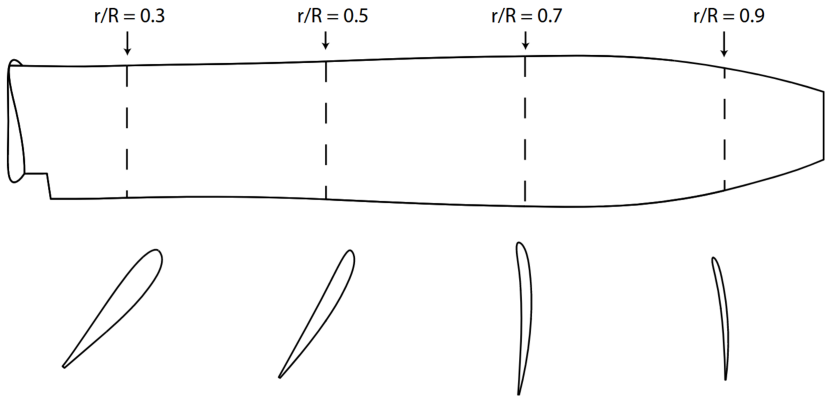

Figure A.1: Geometry layout of *XPROP* [48].

Table A.1: Geometric properties of the *XPROP* and *XPROP*-Λ propellers [48, 4].

Spanwise position	**Twist angle**	**Chord length**	FA	QCA ***XPROP***	QCA ***XPROP-*Λ**
[mm]	[deg.]	[mm]	[mm]	[mm]	[mm]
32.51	26.82	32.57	2.229	-4.409	2.086
39.62	24.83	32.10	2.041	-4.410	0.176
46.74	22.89	31.63	1.858	-4.401	-1.518
53.85	20.99	31.15	1.694	-4.416	-3.007
60.96	19.15	30.68	1.596	-4.595	-4.300
68.07	17.38	30.23	1.476	-4.714	-5.401
75.18	15.62	29.85	1.339	-4.789	-6.315
82.30	13.87	29.58	1.195	-4.841	-7.042
89.41	12.14	29.49	1.055	-4.904	-7.581
96.52	10.43	29.58	0.918	-4.987	-7.928
103.6	8.730	29.84	0.781	-5.085	-8.076
110.7	7.050	30.18	0.643	-5.197	-8.015
117.9	5.390	30.52	0.498	-5.278	-7.736
125.0	3.750	30.78	0.351	-5.351	-7.223
132.1	2.120	30.94	0.200	-5.407	-6.460
139.2	0.600	31.05	0.057	-5.453	-5.429
146.3	-0.730	31.17	-0.070	-5.498	-4.107
153.4	-1.870	31.16	-0.180	-5.522	-2.472
160.5	-2.910	30.78	-0.279	-5.480	-0.498
167.6	-3.900	29.78	-0.363	-5.323	1.846
174.8	-4.800	28.04	-0.422	-5.030	4.589
181.9	-5.670	25.52	-0.456	-4.589	7.766
189.0	-6.530	22.23	-0.458	-4.000	11.41
196.1	-7.370	18.53	-0.430	-3.326	15.57
203.2	-8.000	13.83	-0.349	-2.481	20.27

B

Alternative Sweep and Lean Corrections in BEM Modelling

The sweep correction applied to the BEM model in subsection 3.3.2 accounts for sweep effects on the rotational velocity experienced by the blade. However, this is not the only possible approach. Instead of correcting only the rotational velocity, as shown in Equation 3.23, one could also correct the total inflow velocity in accordance with simple sweep theory for fixed wings [49].

$$V = \sqrt{(V_\infty(1+a))^2 + (\omega r(1-a'))^2} \cdot \cos\Lambda \tag{B.1}$$

However, due to the geometric analogy between sweep and lean for varying pitch angles, it may be appropriate to extend this correction by including the lean angle as well.

$$V = \sqrt{(V_\infty(1+a))^2 + (\omega r(1-a'))^2} \cdot \cos\Lambda \cos\Psi \tag{B.2}$$

Alternatively, rather than applying a correction based on the angles associated with the geometric offset of the quarter-chord line, the velocity could be corrected using the angles that correspond to the local gradients of sweep and lean, as given by Equation 2.4 and Equation 2.5, respectively.

$$V = \sqrt{(V_\infty(1+a))^2 + (\omega r(1-a'))^2} \cdot \cos\gamma \cos\xi \tag{B.3}$$

These three alternative sweep and lean corrections are implemented in the BEM model described in section 3.3, and their aerodynamic performance predictions are compared against experimental data in Figure B.1, Figure B.2 and Figure B.3, respectively.

Figure B.1 and Figure B.2 show equivalent behaviour, as sweep reduces thrust and power slightly, while it leaves the efficiency approximately unchanged. This outcome is expected, as the face alignment of *XPROP* and *XPROP*-Λ is small, resulting in minor lean angles. Consequently, the lean correction has only a minimal effect on the velocity. Moreover, these results show little deviation from those in Figure 3.8. Therefore, it can be concluded that the absolute magnitudes of the QCA and FA are too small to test the effect of sweep and lean on the aerodynamic performance accurately. Larger offsets would probably result in more pronounced variations which would provide a stronger basis for validation. In contrast, Figure B.3 shows that the correction based on the local gradients of the QCA and FA, given by Equation B.3, significantly overestimates the reductions in thrust and power. In other words, it overpredicts the aerodynamic sensitivity to sweep. The change in efficiency, however, is relatively small as observed in the experimental data.

Overall, these findings suggest that the corrections based on the absolute offset of the quarter-chord line yield trends that are more consistent with the experimental data than those based on the local gradients of the quarter-chord. Given that the differences between the results in Figure 3.8, Figure B.1 and Figure B.2 are minimal, due to the small quarter-chord offsets (QCA and FA), it could not be determined which correction performs best. Since Equation 3.23 provides the most physically plausible explanation, it is the correction applied in this work.

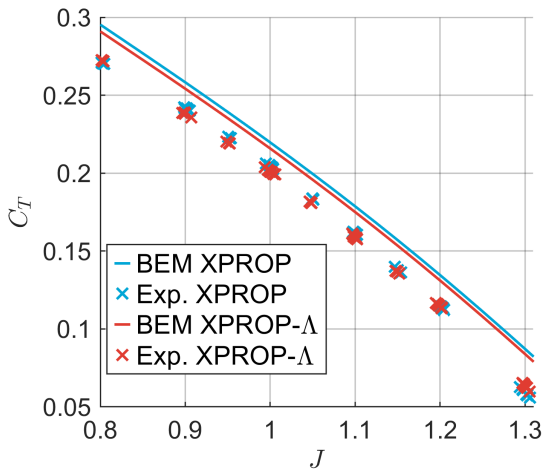

(a) Thrust coefficient at $\beta_{0.7R} = 30°$.

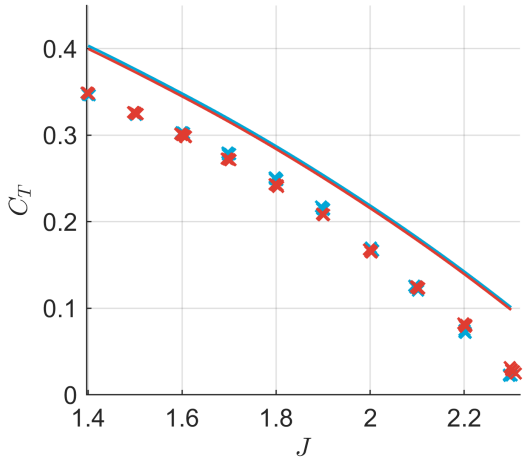

(b) Thrust coefficient at $\beta_{0.7R} = 45°$.

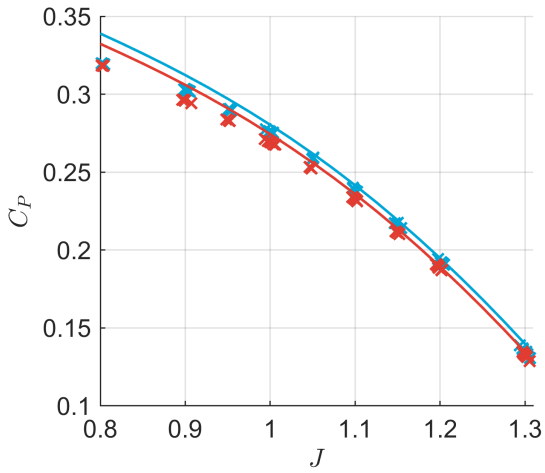

(c) Power coefficient at $\beta_{0.7R} = 30°$.

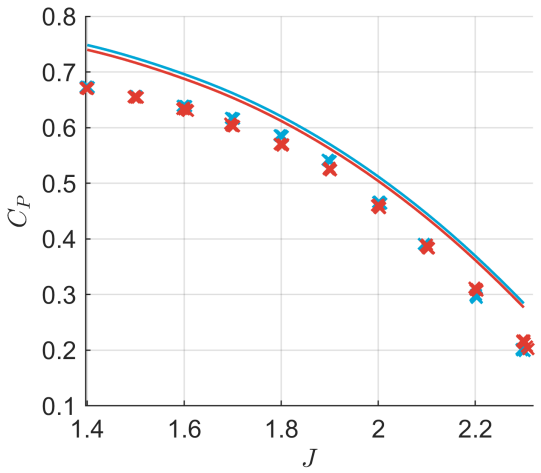

(d) Power coefficient at $\beta_{0.7R} = 45°$.

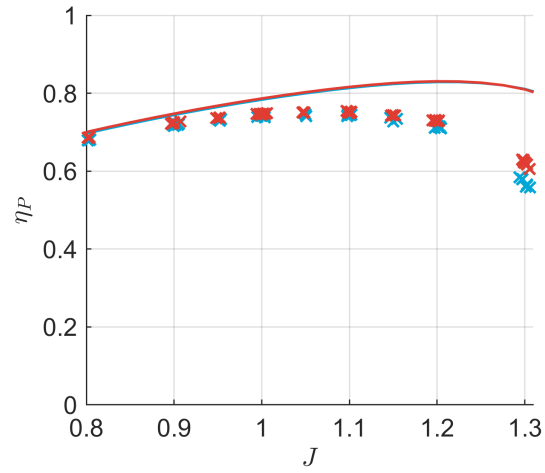

(e) Propulsive efficiency at $\beta_{0.7R} = 30°$.

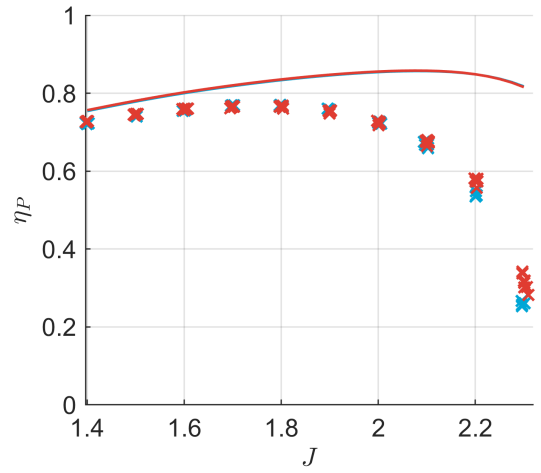

(f) Propulsive efficiency at $\beta_{0.7R} = 45°$.

Figure B.1: Aerodynamic performance plots of *XPROP* and *XPROP*-Λ at $M = 0.12$, using the sweep correction given by Equation B.1 and experimental data from [4].

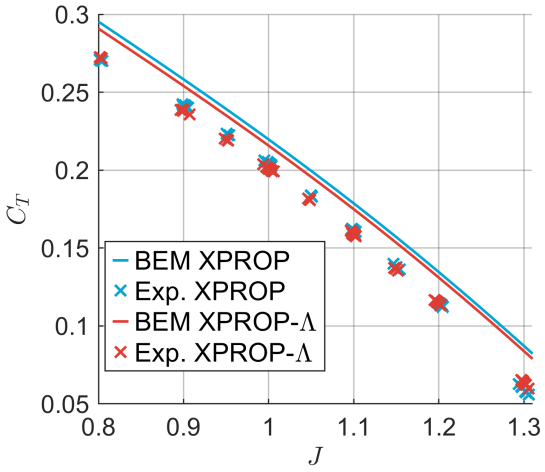

(a) Thrust coefficient at $\beta_{0.7R} = 30°$.

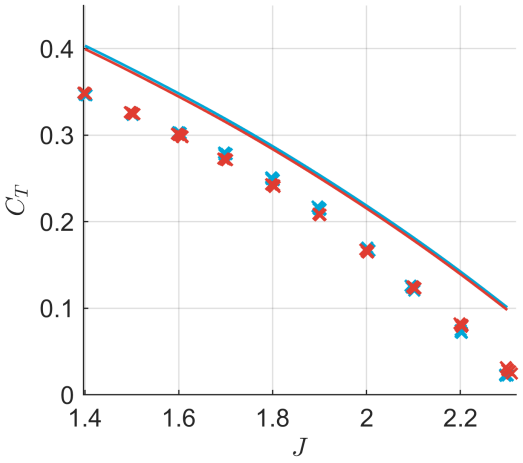

(b) Thrust coefficient at $\beta_{0.7R} = 45°$.

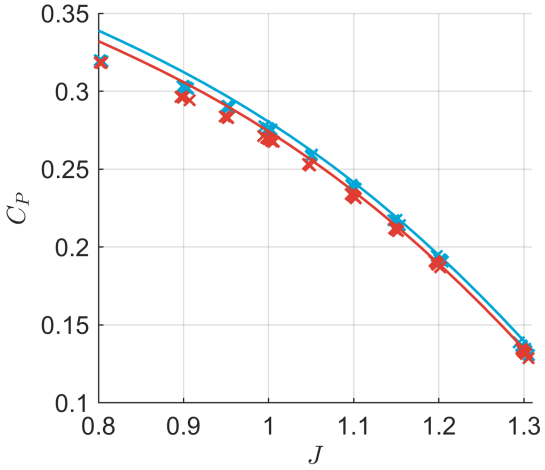

(c) Power coefficient at $\beta_{0.7R} = 30°$.

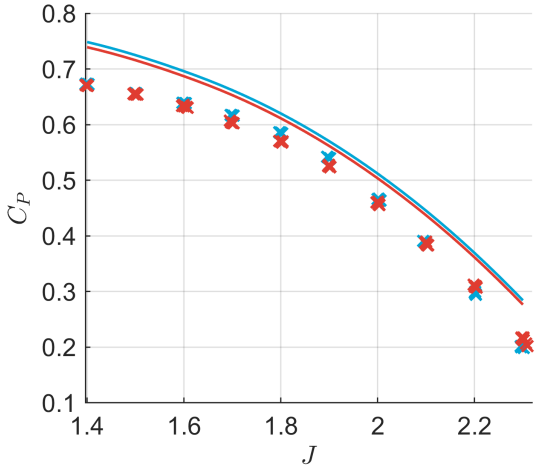

(d) Power coefficient at $\beta_{0.7R} = 45°$.

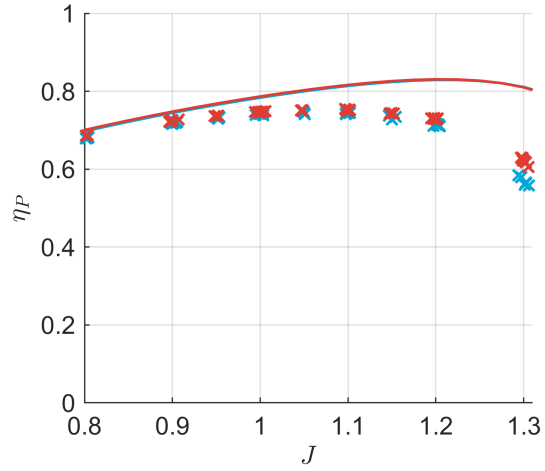

(e) Propulsive efficiency at $\beta_{0.7R} = 30°$.

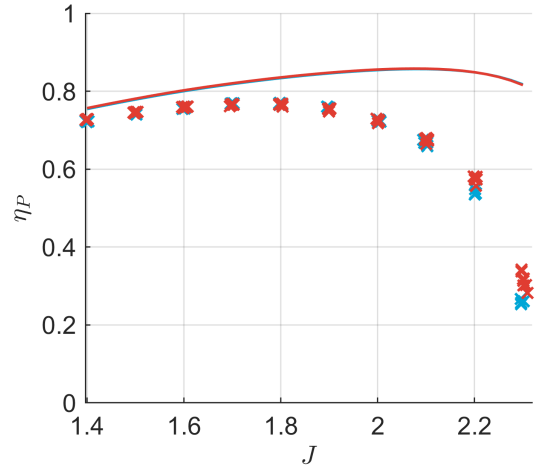

(f) Propulsive efficiency at $\beta_{0.7R} = 45°$.

Figure B.2: Aerodynamic performance plots of *XPROP* and *XPROP-*Λ at $M = 0.12$, using the sweep correction given by Equation B.2 and experimental data from [4].

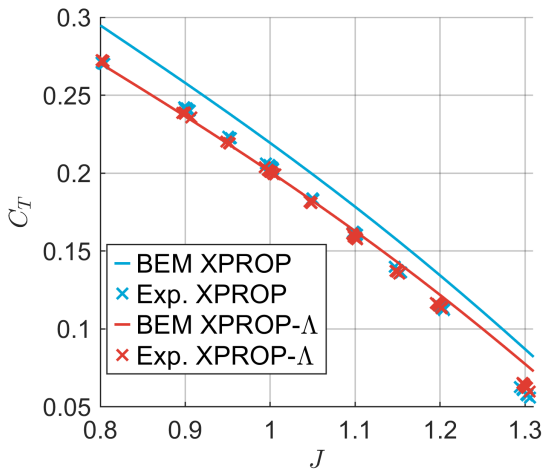

(a) Thrust coefficient at $\beta_{0.7R} = 30°$.

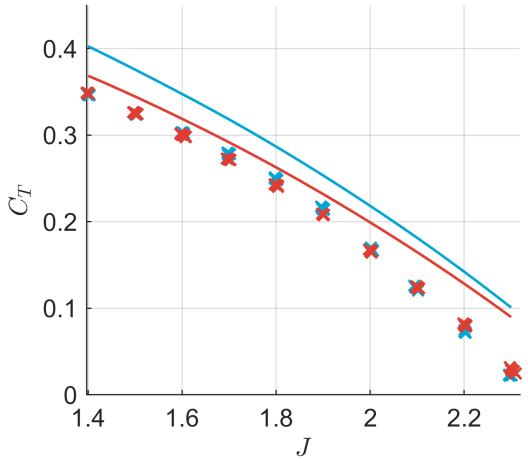

(b) Thrust coefficient at $\beta_{0.7R} = 45°$.

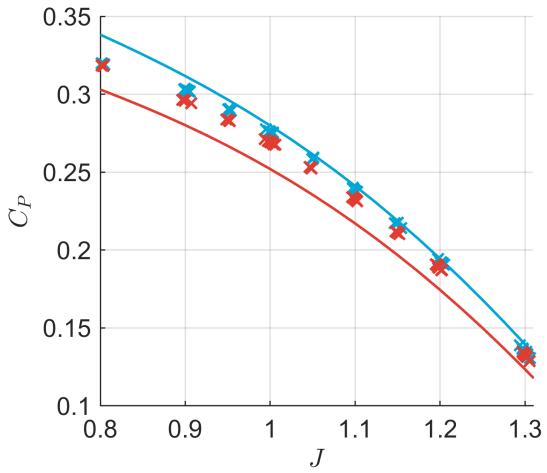

(c) Power coefficient at $\beta_{0.7R} = 30°$.

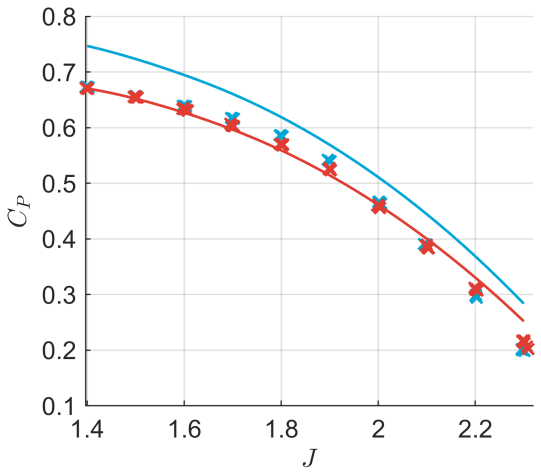

(d) Power coefficient at $\beta_{0.7R} = 45°$.

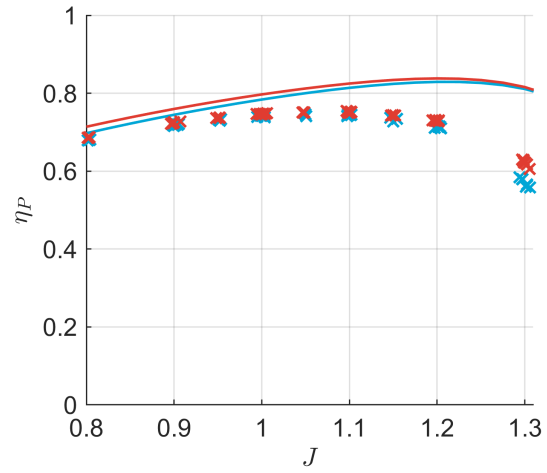

(e) Propulsive efficiency at $\beta_{0.7R} = 30°$.

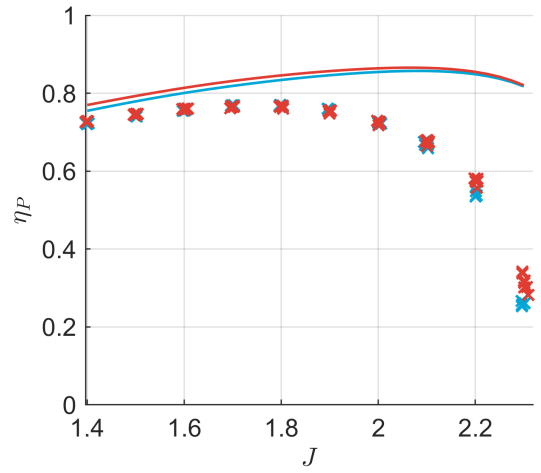

(f) Propulsive efficiency at $\beta_{0.7R} = 45°$.

Figure B.3: Aerodynamic performance plots of *XPROP* and *XPROP*-Λ at $M = 0.12$, using the sweep correction given by Equation B.3 and experimental data from [4].

C

Twist Sensitivity Model Comparison

The model for computing the aerodynamic sensitivities with respect to twist deformation, developed in subsection 4.2.1, has not only been extended to account for propeller blades with sweep and lean, but also improved compared to that in [19]. This appendix discusses these improvements, and compares the twist sensitivities predicted by both models for a straight propeller blade.

The main difference is that Rotundo [23] assumed that the axial and tangential force coefficient vary with the angle of attack only, see Equation C.1, while in this work, variations of the flow angle are also accounted for, as shown by Equation 4.13.

$$\begin{bmatrix} C_{z_\beta} \\ C_{x_\beta} \end{bmatrix} = \begin{bmatrix} \cos\varphi & -\sin\varphi \\ \sin\varphi & \cos\varphi \end{bmatrix} \begin{bmatrix} C_{l_\alpha} \\ C_{d_\alpha} \end{bmatrix} \frac{d\alpha}{d\beta} \tag{C.1}$$

Additionally, Rotundo [23] assumed that the thrust and torque coefficients in momentum theory depend only on the induction factors because this theory is one-dimensional. However, when including Prandtl's tip and root loss corrections, these coefficients also become dependent on the flow angle. Therefore, the decomposition of the twist derivative into axial and tangential induction factor components, as given by Equation C.2, is not valid.

$$\frac{dC_t^{\mathsf{M}}}{d\beta} = \frac{\partial C_t^{\mathsf{M}}}{\partial a}\frac{\partial a}{\partial \beta} + \frac{\partial C_t^{\mathsf{M}}}{\partial a'}\frac{\partial a'}{\partial \beta} \tag{C.2}$$

$$\frac{dC_q^{\mathsf{M}}}{d\beta} = \frac{\partial C_q^{\mathsf{M}}}{\partial a}\frac{\partial a}{\partial \beta} + \frac{\partial C_q^{\mathsf{M}}}{\partial a'}\frac{\partial a'}{\partial \beta} \tag{C.3}$$

These modifications to the analytical expressions yield a significant improvement in the accuracy of the sensitivity predictions for straight blades. This is demonstrated by comparing the analytical and numerical sensitivities for both models, see Figure C.1 and Figure C.2. The calculations are performed for a three-bladed *XPROP* propeller scaled by a factor of 4.5, as used in [19]. To ensure a valid comparison, the geometry is slightly adjusted by setting $QCA = 0$ mm and $FA = 0$ mm along the entire span, thereby eliminating the contribution of the geometric sensitivities. For consistency, both figures use the same colour bar scale, although this scale is unnecessarily large for the improved sensitivities. Furthermore, the figures only show $dC_x/d\beta$, $dC_z/d\beta$ and $dF/d\beta$ because these sensitivities are directly affected by the modifications. The other sensitivities, however, benefit indirectly through increased overall accuracy.

The absolute differences shown in Figure C.2 are significantly smaller than those in Figure C.1, in particular for $dC_x/d\beta$ and $dC_z/d\beta$. This confirms that the modifications introduced in this work are definitely an improvement. In addition to improving the accuracy of the sensitivity predictions, these refinements are expected to enhance the efficiency and robustness of the aeroelastic analysis through faster and more stable convergence of the tight coupling procedure.

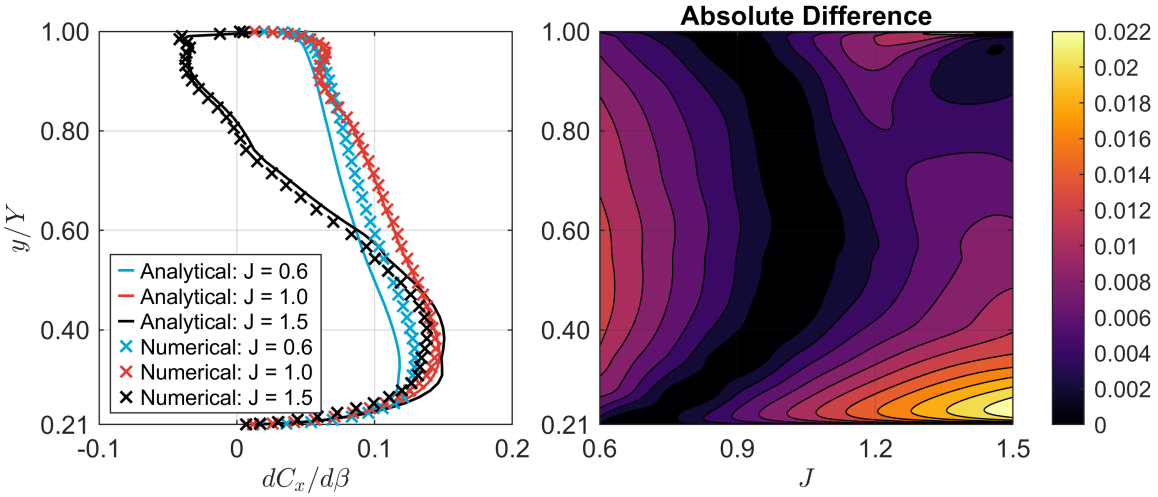

(a) Spanwise distribution of $dC_x/d\beta$.

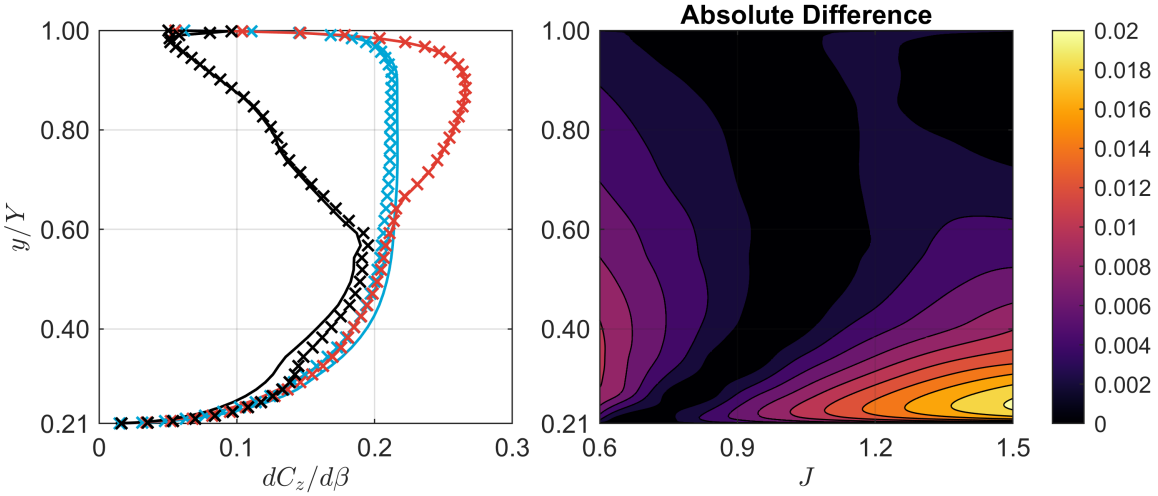

(b) Spanwise distribution of $dC_z/d\beta$.

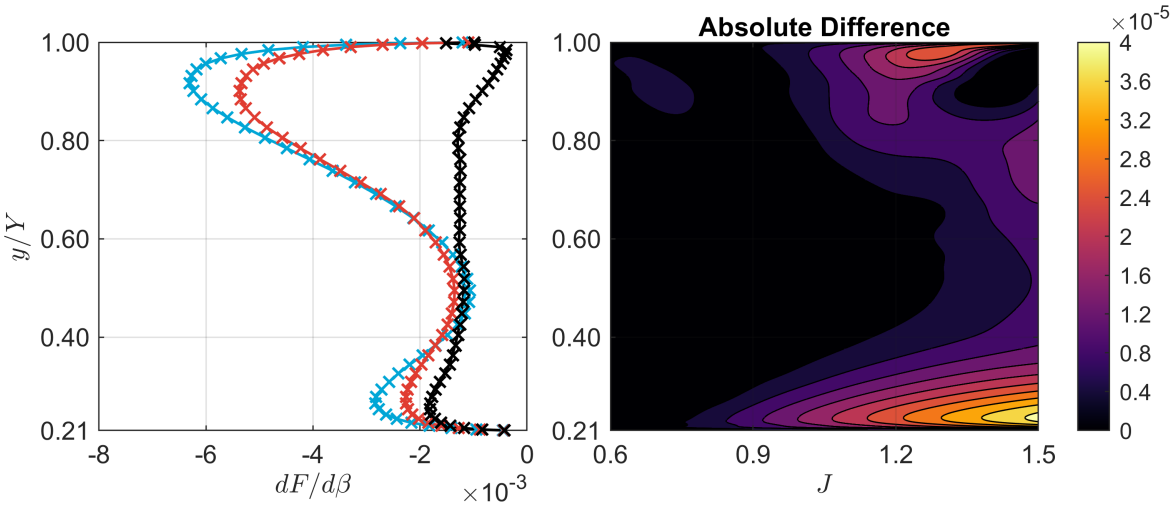

(c) Spanwise distribution of $dF/d\beta$.

Figure C.1: Comparison between analytically and numerically computed twist sensitivities using the sensitivity model developed by Rotundo [23] for the modified *XPROP* propeller at $\beta_{0.7R} = 20°$ and $V_\infty = 30$ m/s.

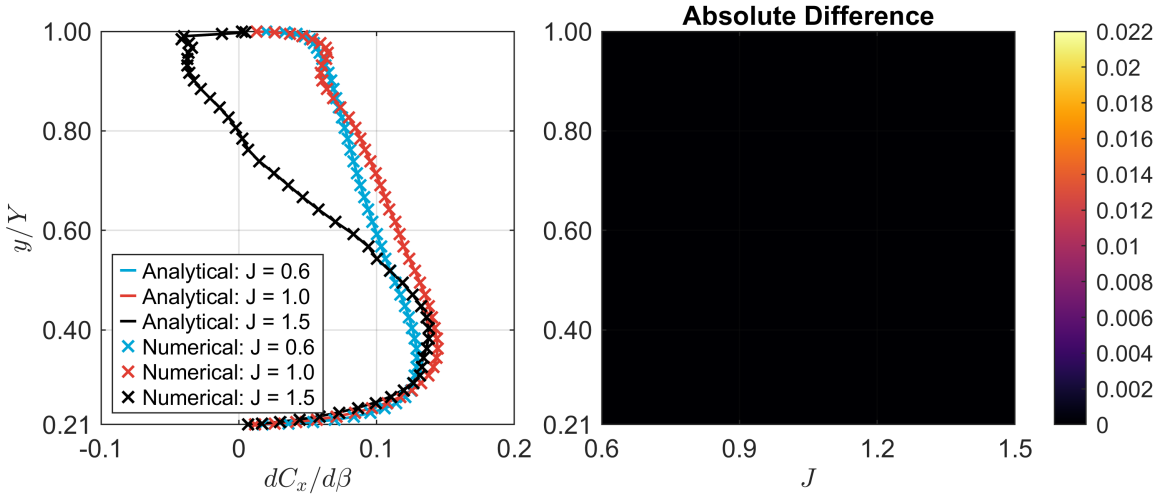

(a) Spanwise distribution of $dC_x/d\beta$.

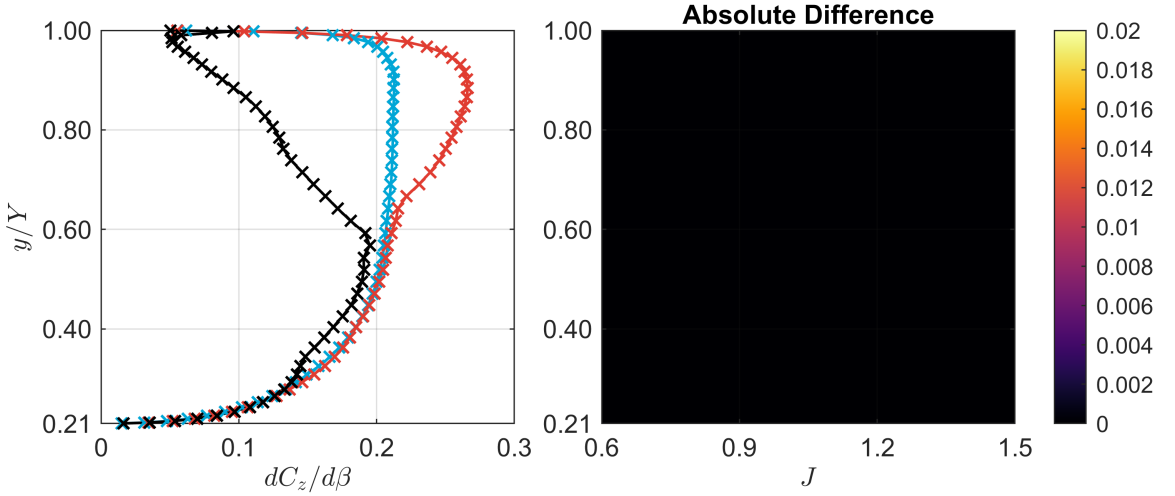

(b) Spanwise distribution of $dC_z/d\beta$.

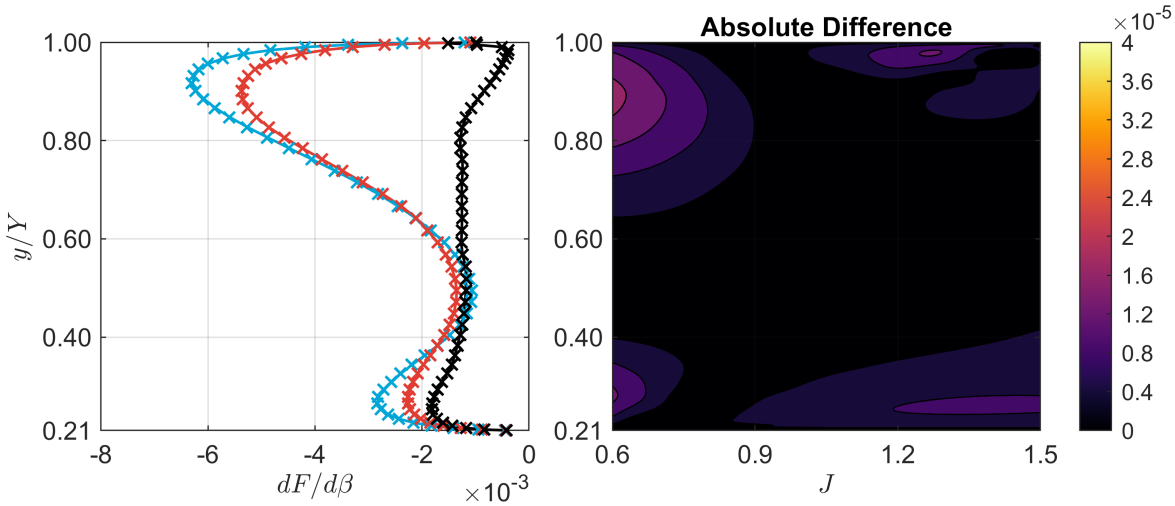

(c) Spanwise distribution of $dF/d\beta$.

Figure C.2: Comparison between analytically and numerically computed twist sensitivities obtained using the developed model in subsection 4.2.1 for the modified *XPROP* propeller at $\beta_{0.7R} = 20°$ and $V_\infty = 30$ m/s.

D

Aerodynamic Sensitivity Analysis for Sweep, Lean, and Radial Deformation

This appendix presents the aerodynamic sensitivity plots with respect to sweep, lean and radial deformation in Appendix D.1, Appendix D.2 and Appendix D.3, respectively. For all degrees of freedom, the results are structured in a consistent order for convenience. First, the sensitivities for the *XPROP* propeller are shown, followed by the corresponding geometric sensitivities. Then, those obtained for *XPROP-*Λ are presented. All plots are generated using the same load conditions and numerical settings as described in subsection 4.2.1.

D.1. Sweep Sensitivities

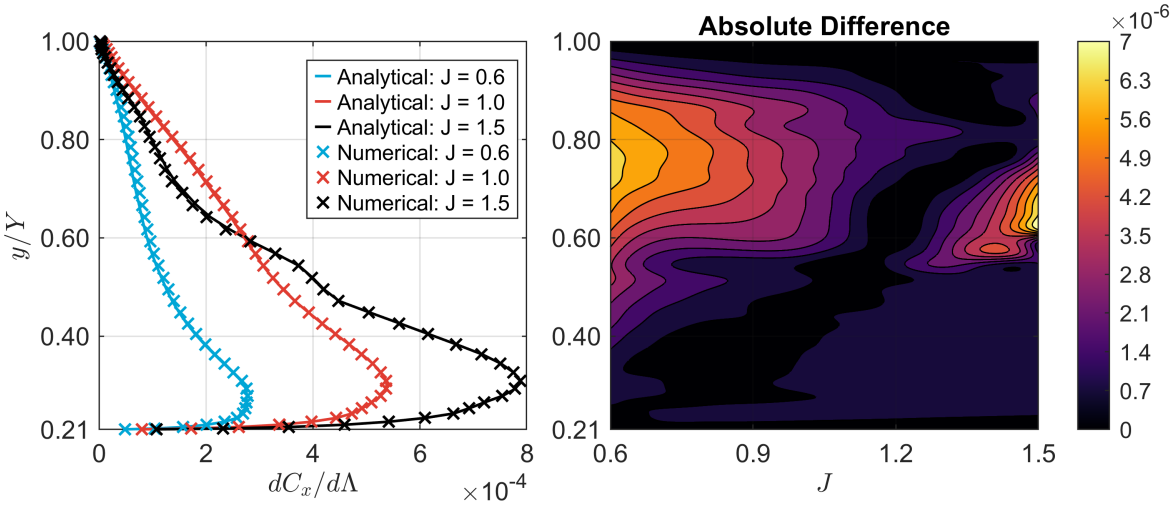

(a) Spanwise distribution of $dC_x/d\Lambda$.

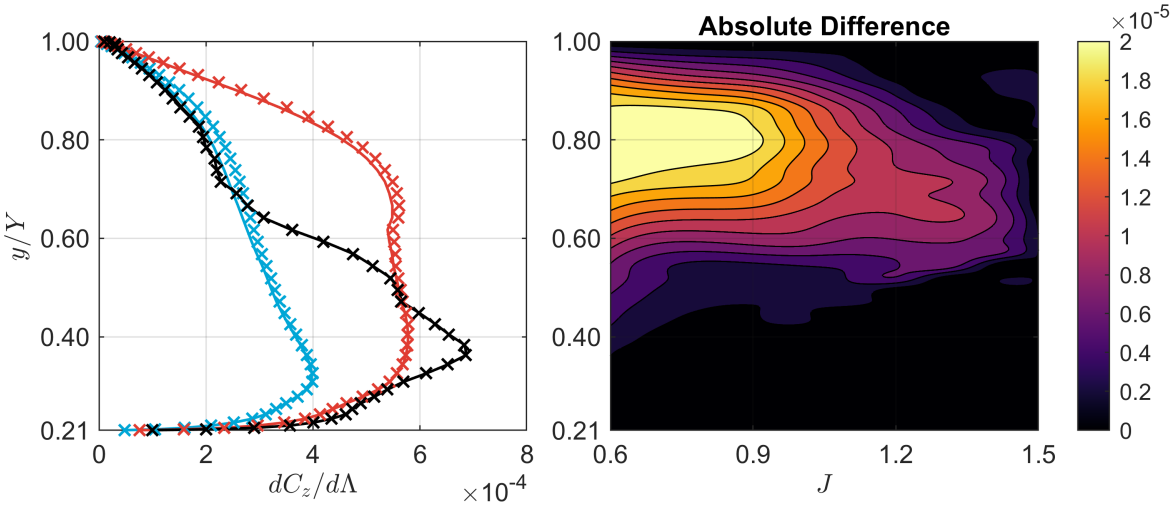

(b) Spanwise distribution of $dC_z/d\Lambda$.

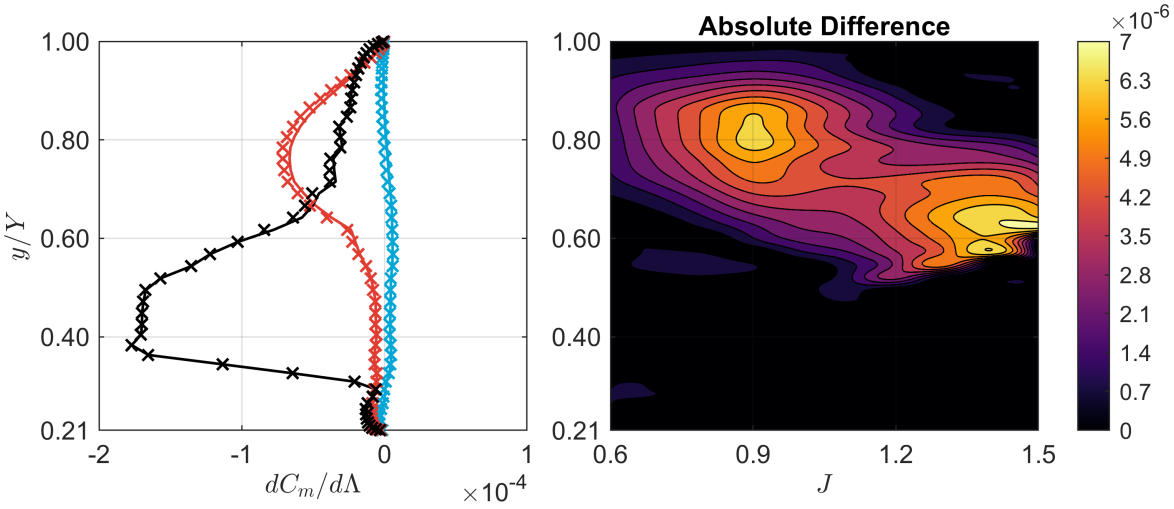

(c) Spanwise distribution of $dC_m/d\Lambda$.

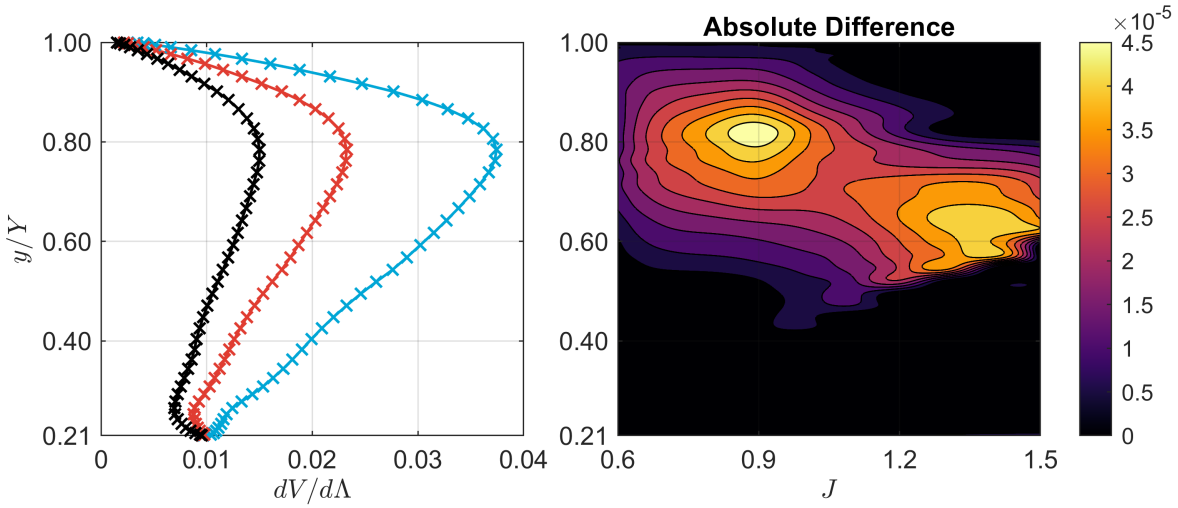

(d) Spanwise distribution of $dV/d\Lambda$.

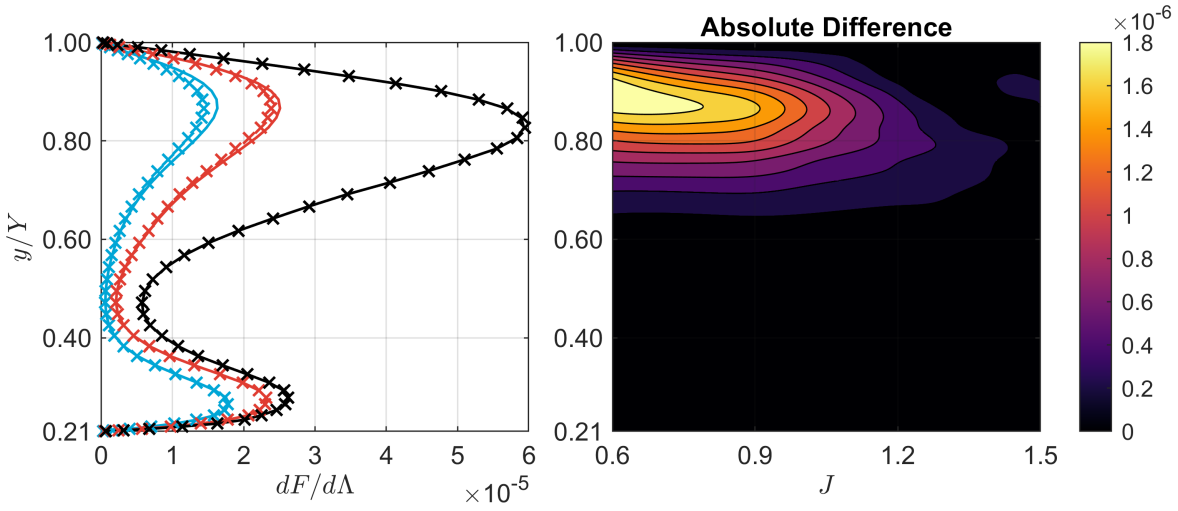

(e) Spanwise distribution of $dF/d\Lambda$.

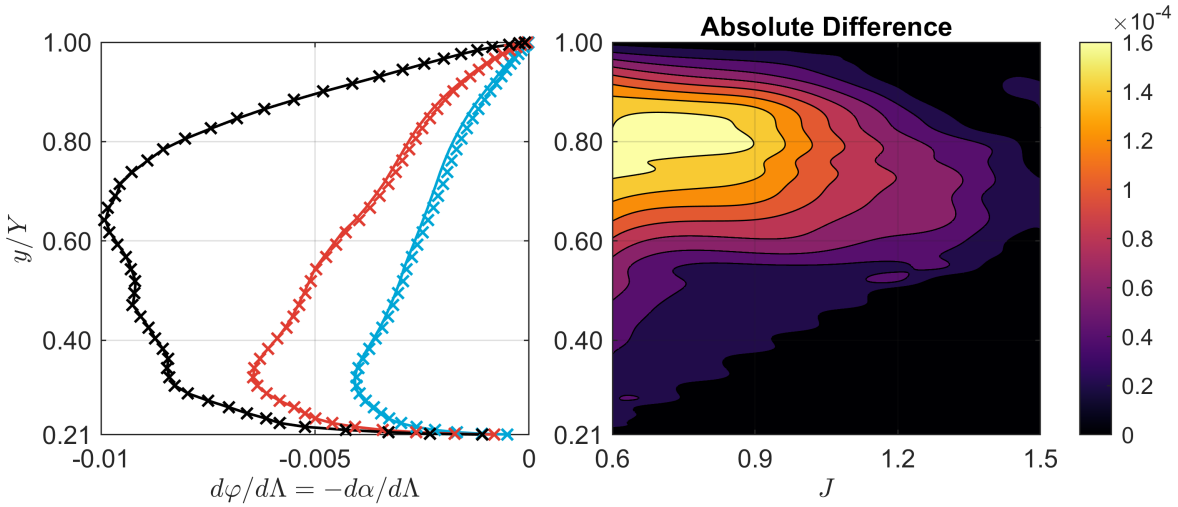

(f) Spanwise distribution of $d\varphi/d\Lambda$.

Figure D.1: Comparison between the analytically and numerically computed sweep sensitivities for the *XPROP* propeller at $\beta_{0.7R} = 20°$ and $V_\infty = 30$ m/s.

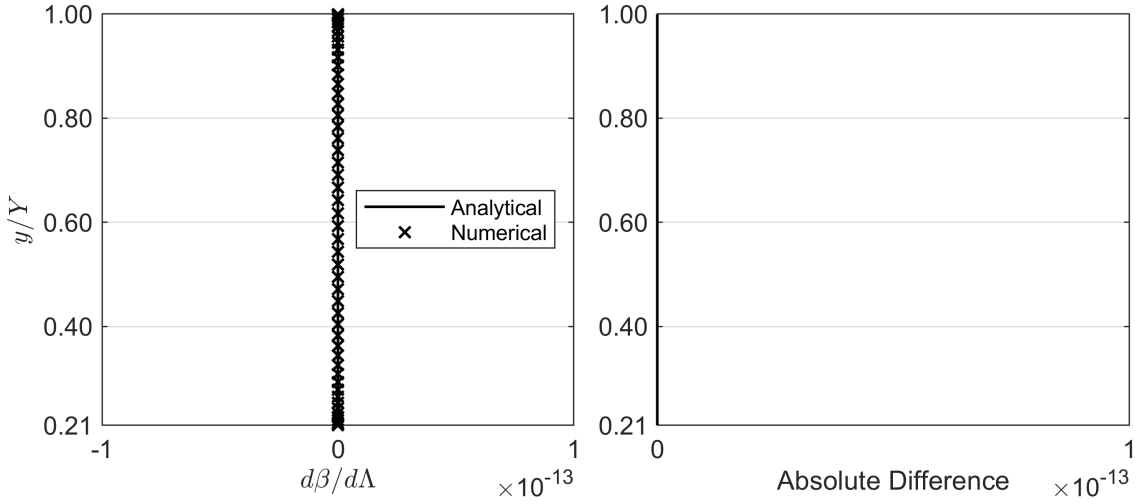

(a) Spanwise distribution of $d\beta/d\Lambda$.

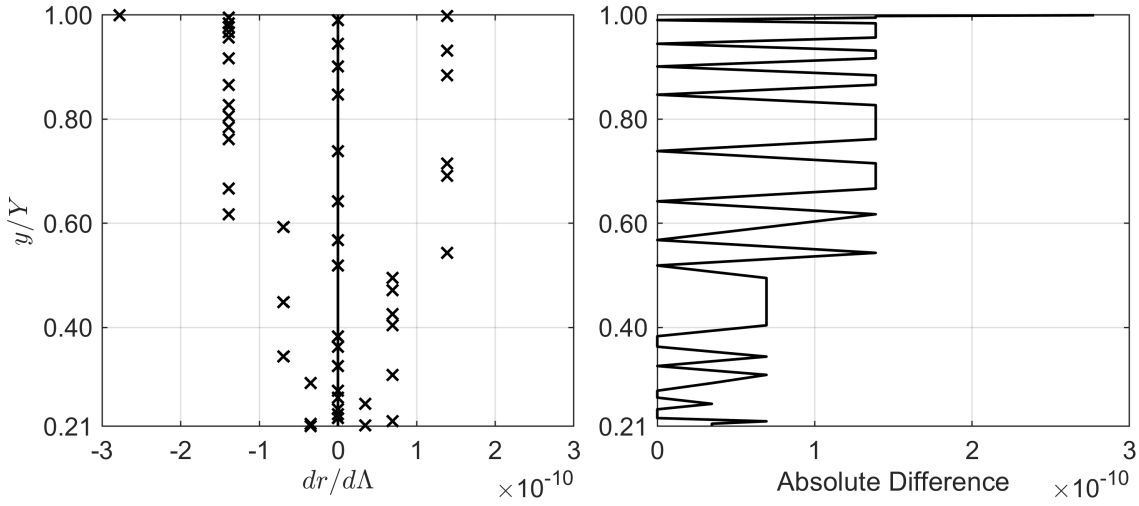

(b) Spanwise distribution of $dr/d\Lambda$.

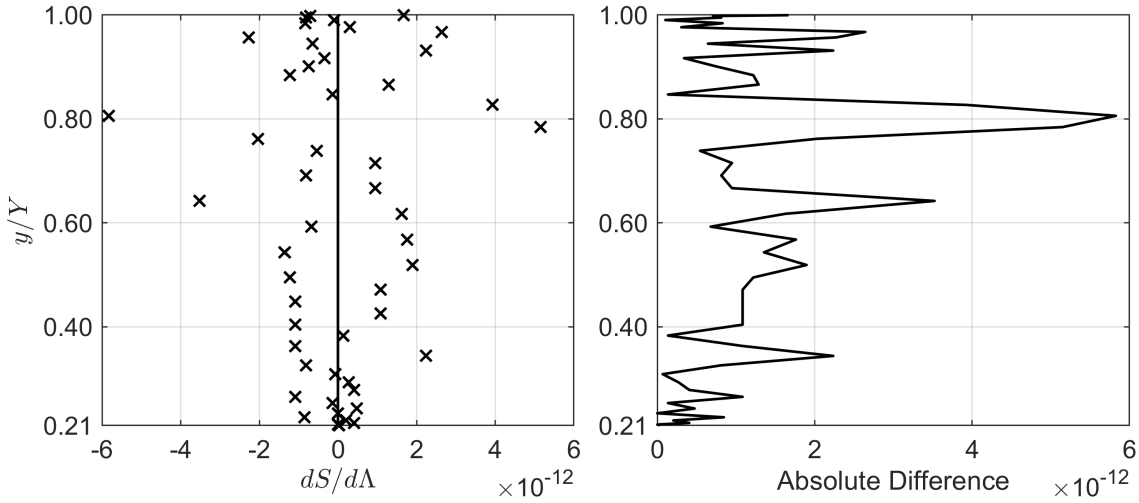

(c) Spanwise distribution of $dS/d\Lambda$.

Figure D.2: Comparison between the analytically and numerically computed geometric sweep sensitivities for the *XPROP* propeller at $\beta_{0.7R} = 20°$ and $V_\infty = 30$ m/s.

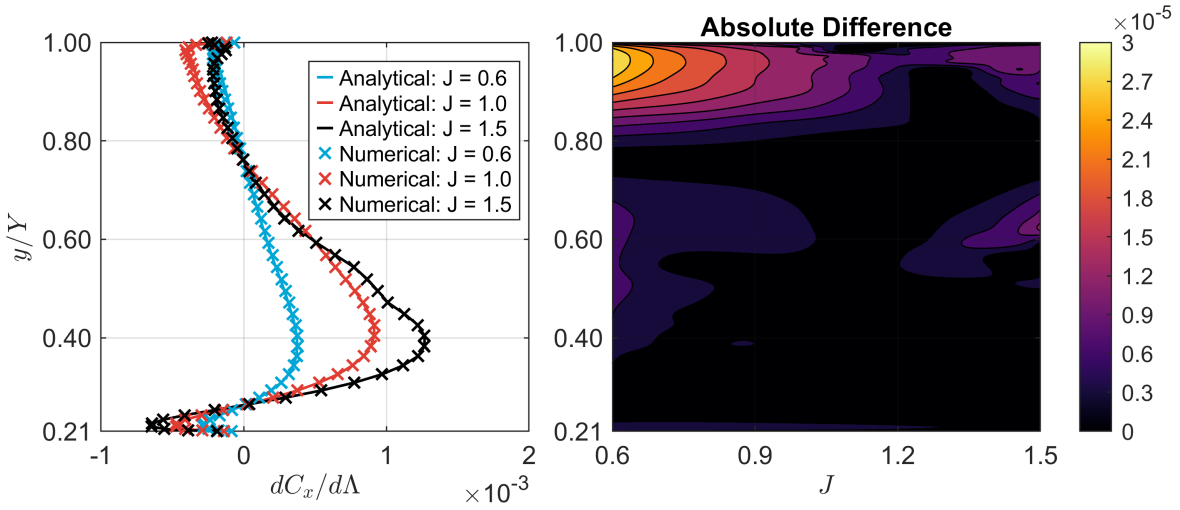

(a) Spanwise distribution of $dC_x/d\Lambda$.

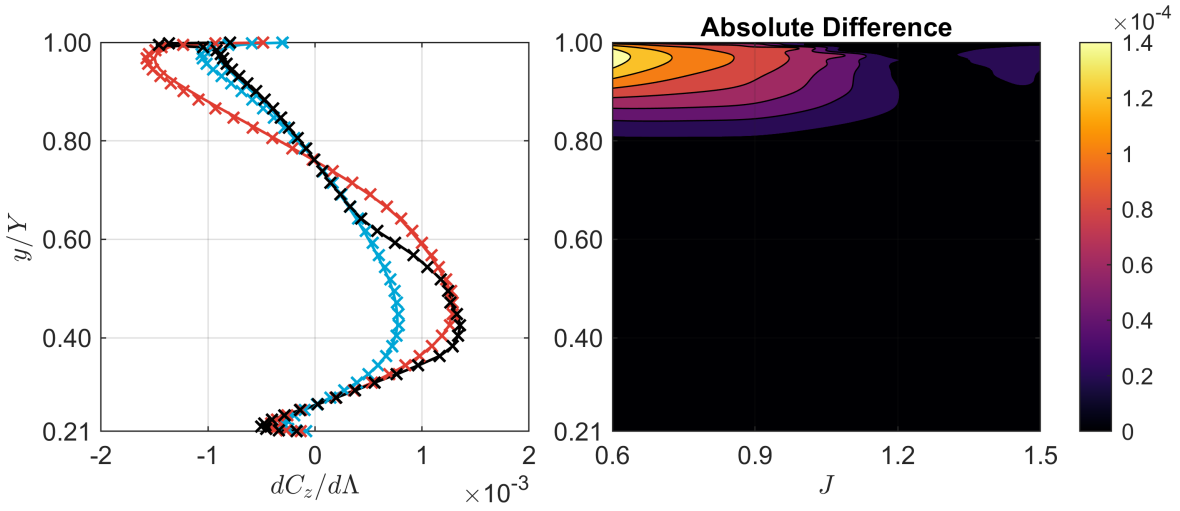

(b) Spanwise distribution of $dC_z/d\Lambda$.

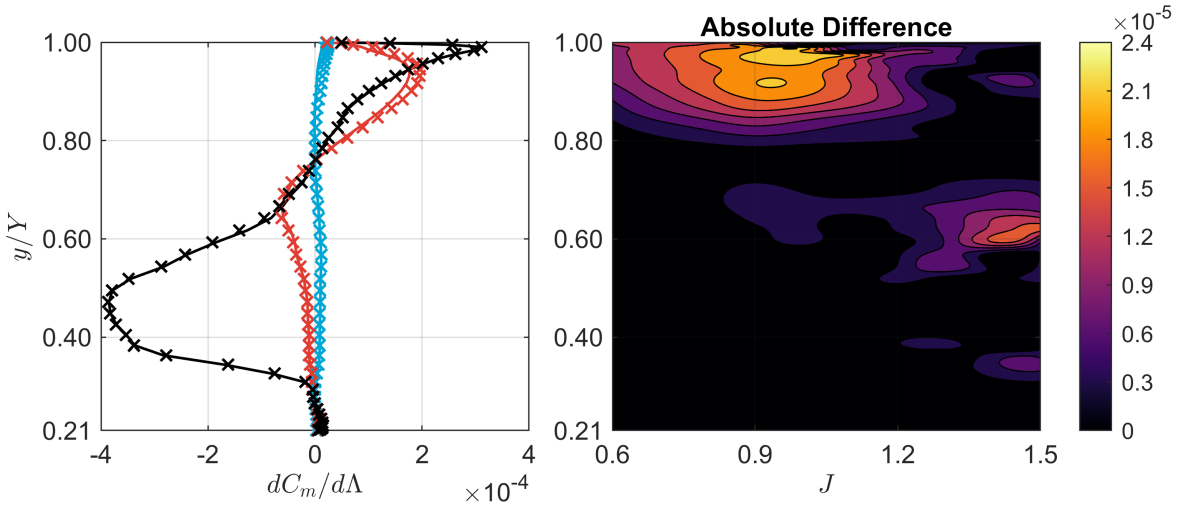

(c) Spanwise distribution of $dC_m/d\Lambda$.

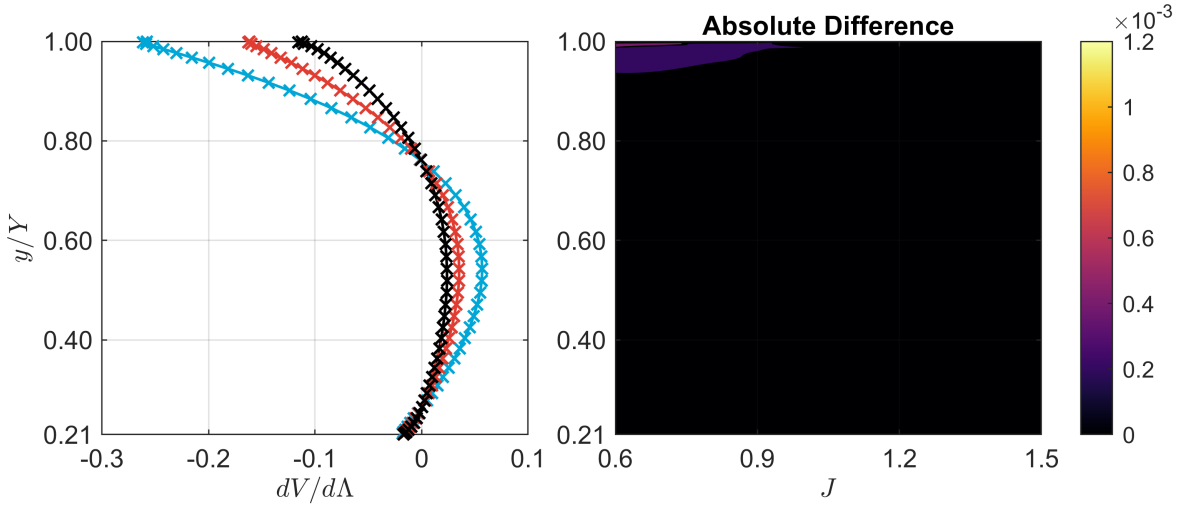

(d) Spanwise distribution of $dV/d\Lambda$.

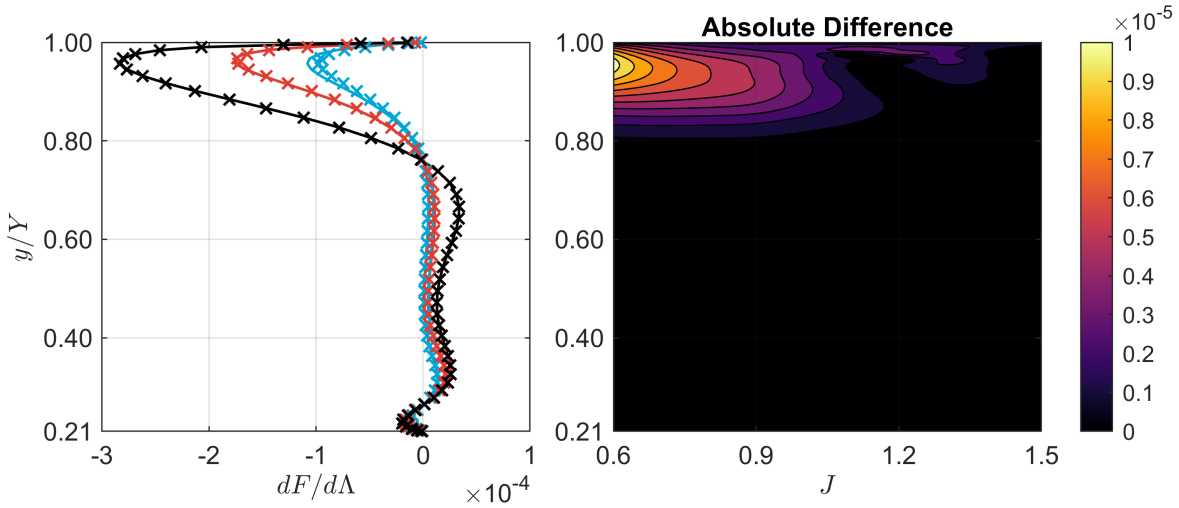

(e) Spanwise distribution of $dF/d\Lambda$.

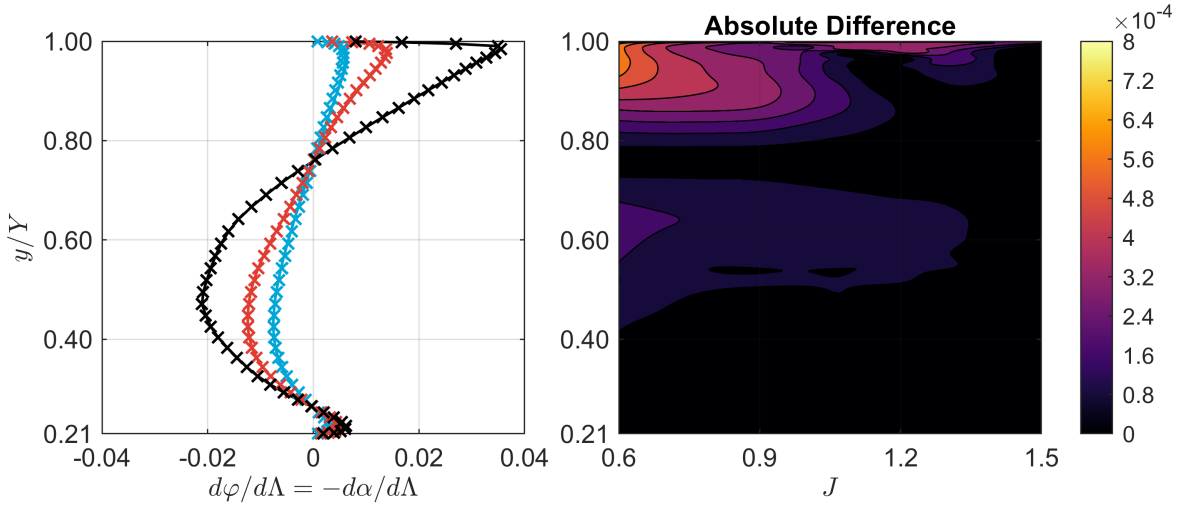

(f) Spanwise distribution of $d\varphi/d\Lambda$.

Figure D.3: Comparison between the analytically and numerically computed sweep sensitivities for the *XPROP*-Λ propeller at $\beta_{0.7R} = 20°$ and $V_\infty = 30$ m/s.

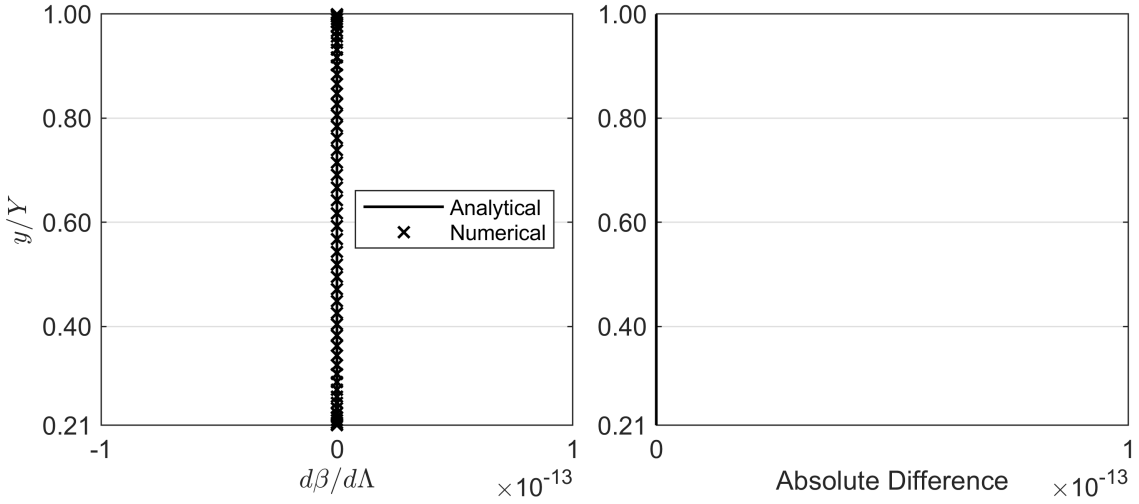

(a) Spanwise distribution of $d\beta/d\Lambda$.

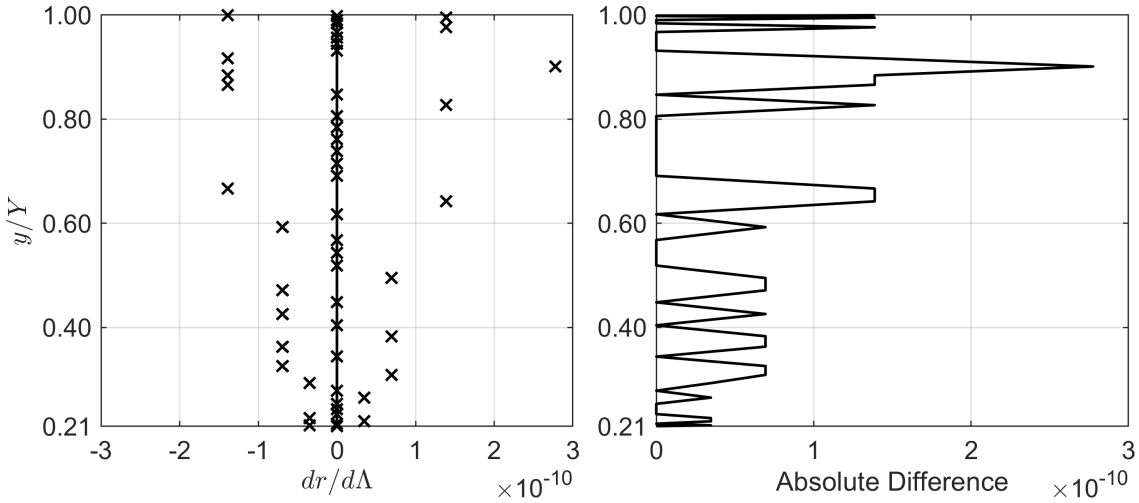

(b) Spanwise distribution of $dr/d\Lambda$.

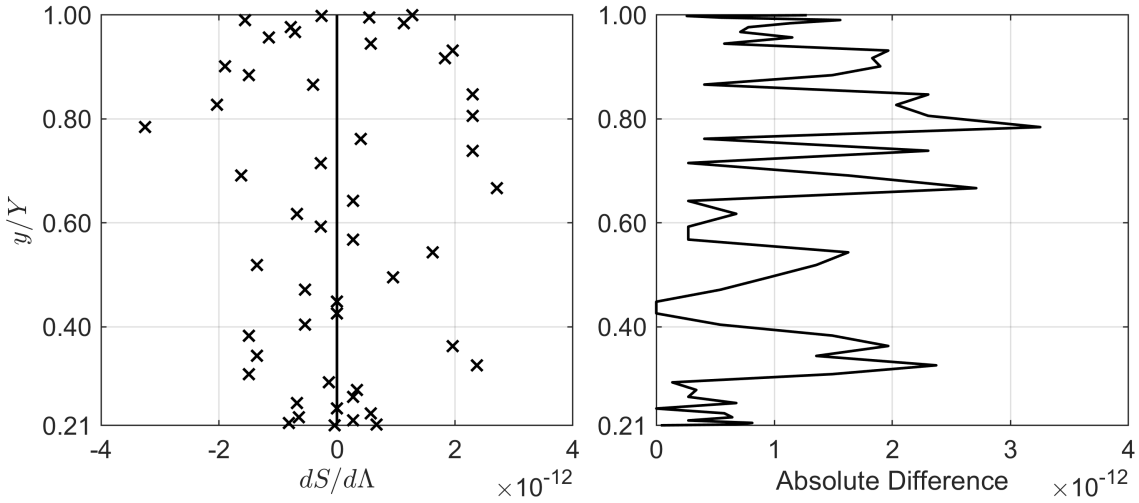

(c) Spanwise distribution of $dS/d\Lambda$.

Figure D.4: Comparison between the analytically and numerically computed geometric sweep sensitivities for the *XPROP*-Λ propeller at $\beta_{0.7R} = 20°$ and $V_\infty = 30$ m/s.

D.2. Lean Sensitivities

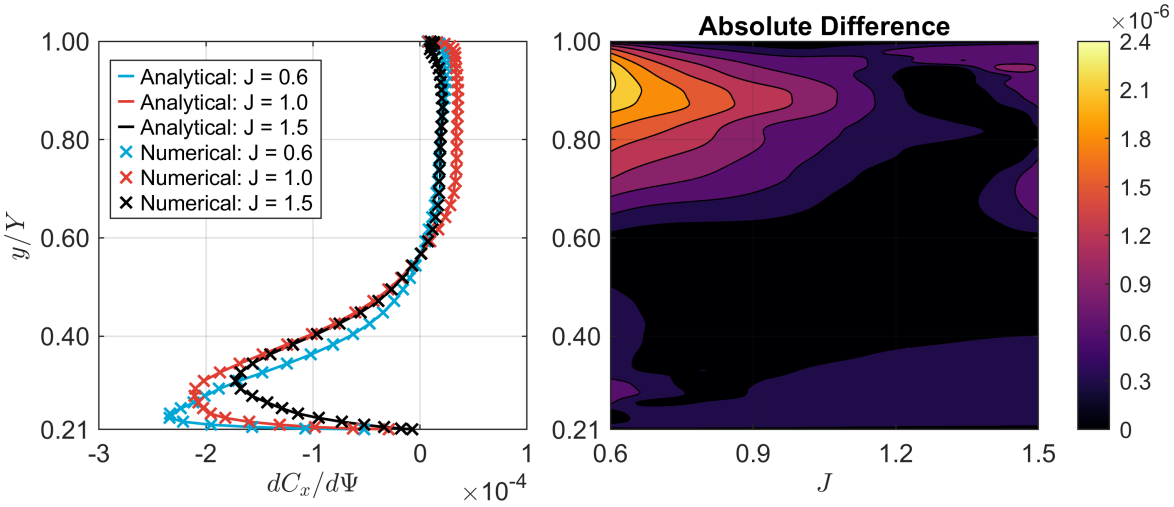

(a) Spanwise distribution of $dC_x/d\Psi$.

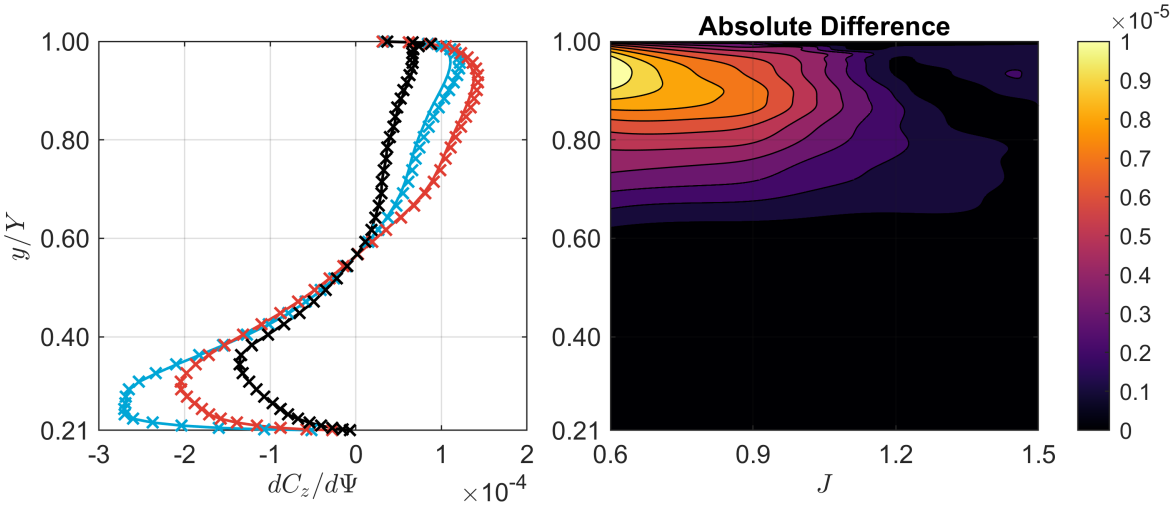

(b) Spanwise distribution of $dC_z/d\Psi$.

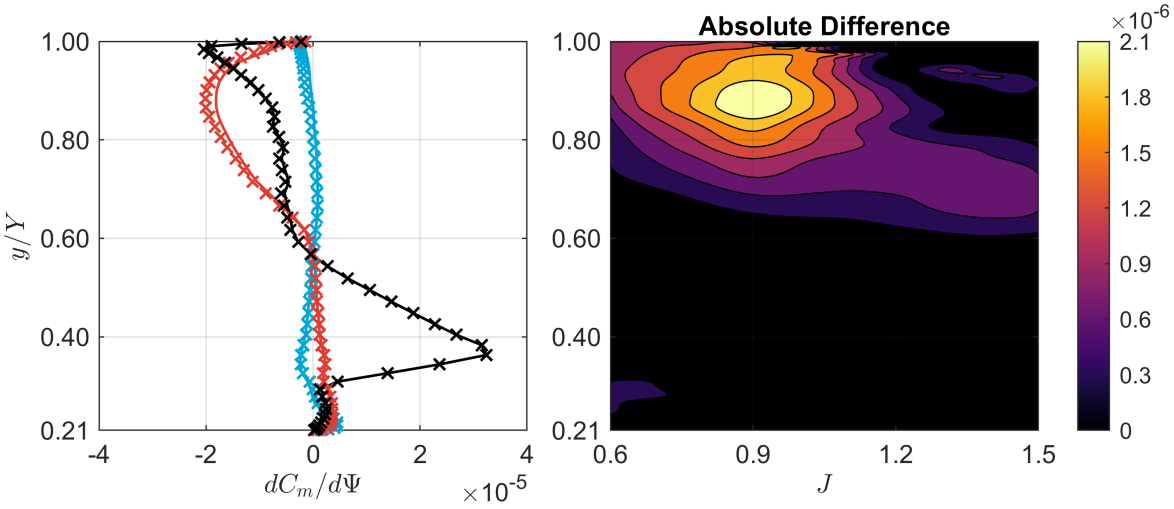

(c) Spanwise distribution of $dC_m/d\Psi$.

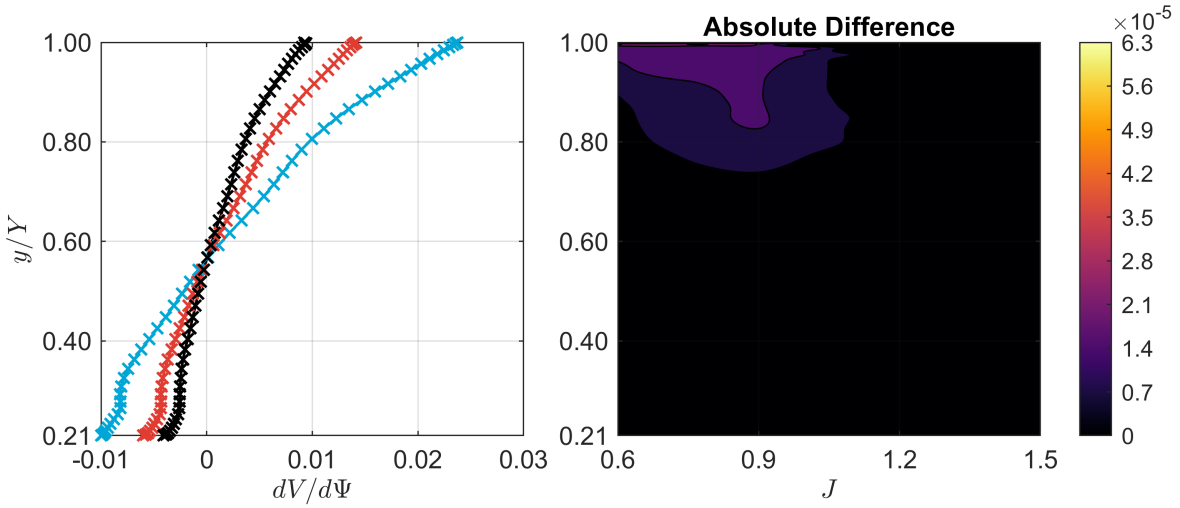

(d) Spanwise distribution of $dV/d\Psi$.

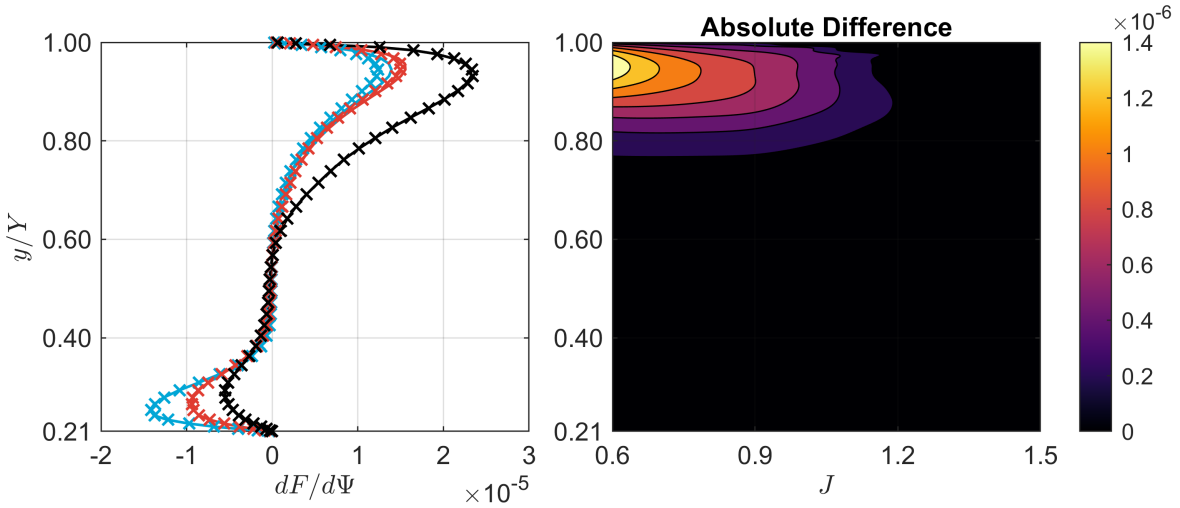

(e) Spanwise distribution of $dF/d\Psi$.

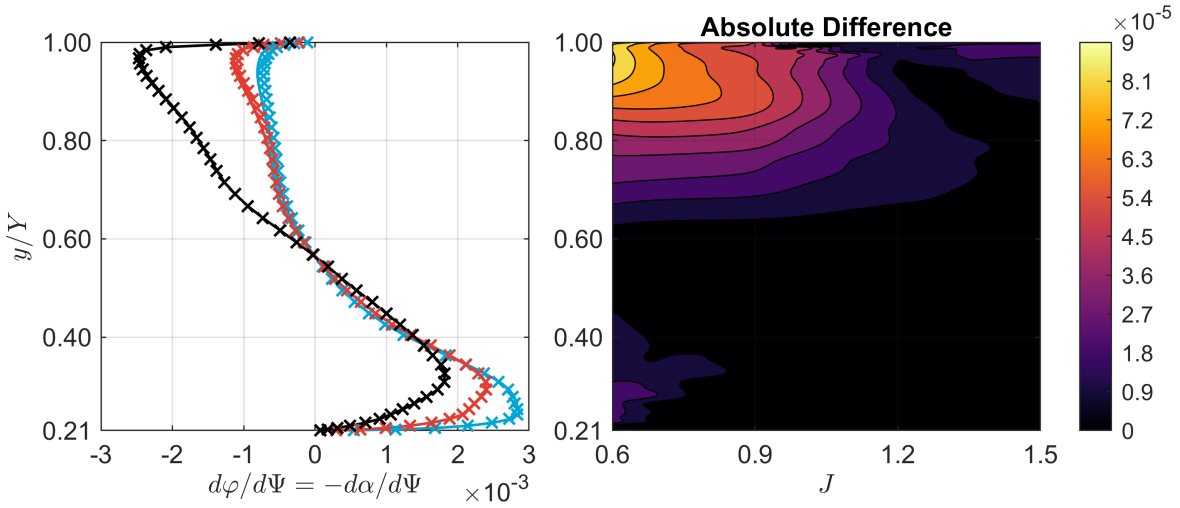

(f) Spanwise distribution of $d\varphi/d\Psi$.

Figure D.5: Comparison between the analytically and numerically computed lean sensitivities for the *XPROP* propeller at $\beta_{0.7R} = 20°$ and $V_\infty = 30$ m/s.

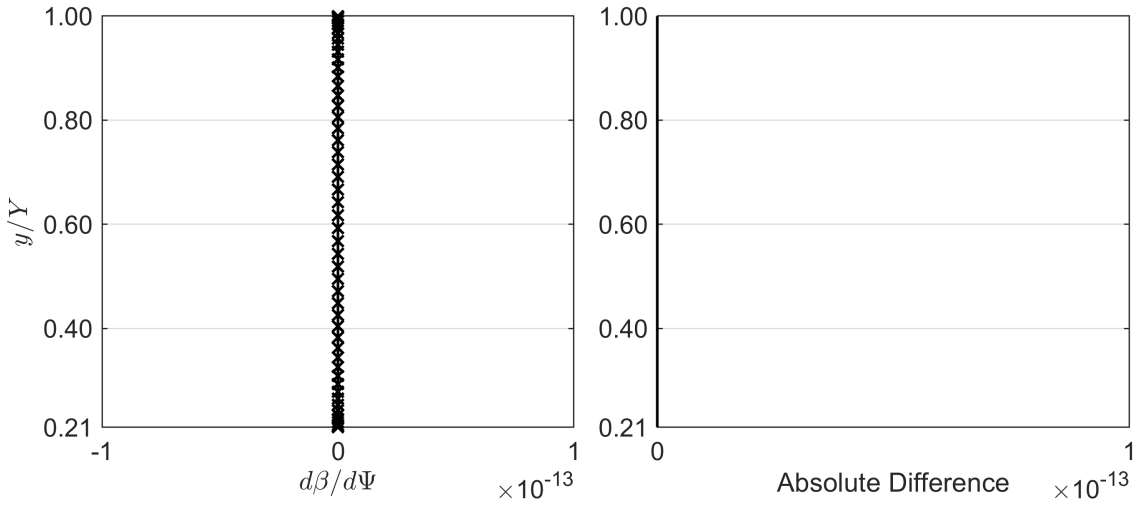

(a) Spanwise distribution of $d\beta/d\Psi$.

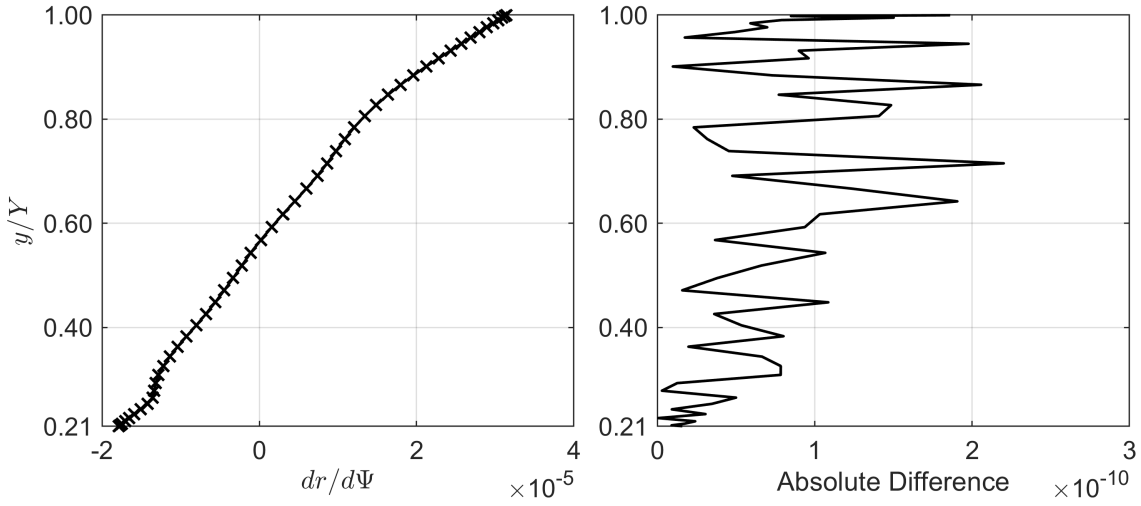

(b) Spanwise distribution of $dr/d\Psi$.

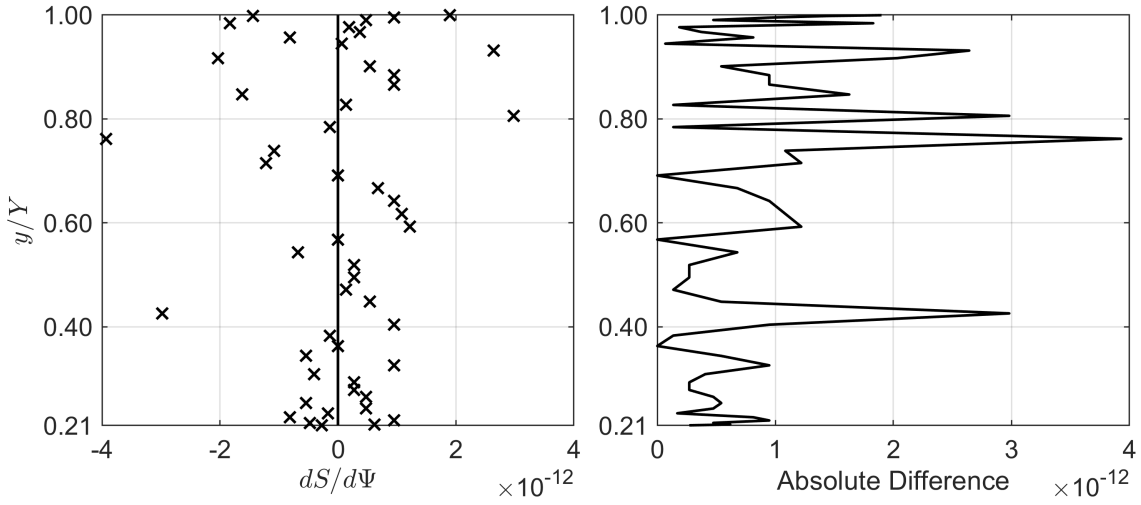

(c) Spanwise distribution of $dS/d\Psi$.

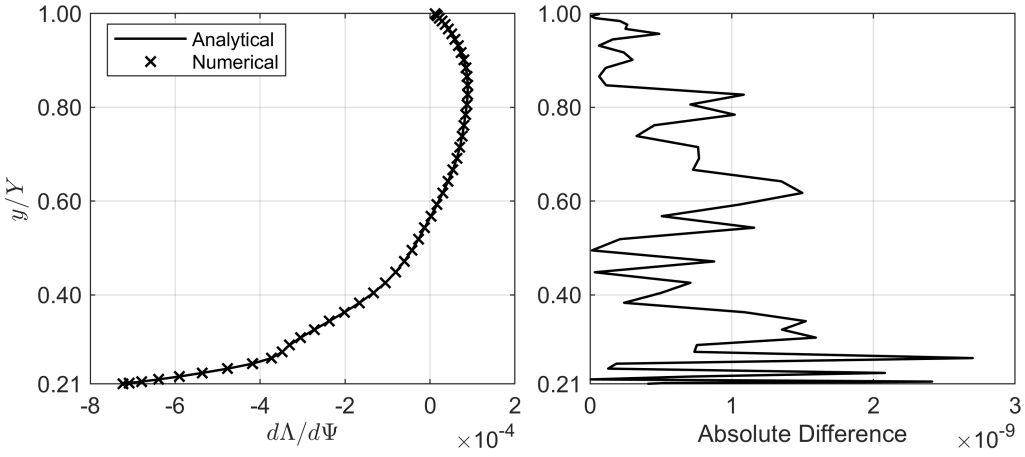

(d) Spanwise distribution of $d\Lambda/d\Psi$.

Figure D.6: Comparison between the analytically and numerically computed geometric lean sensitivities for the *XPROP* propeller at $\beta_{0.7R} = 20°$ and $V_\infty = 30$ m/s.

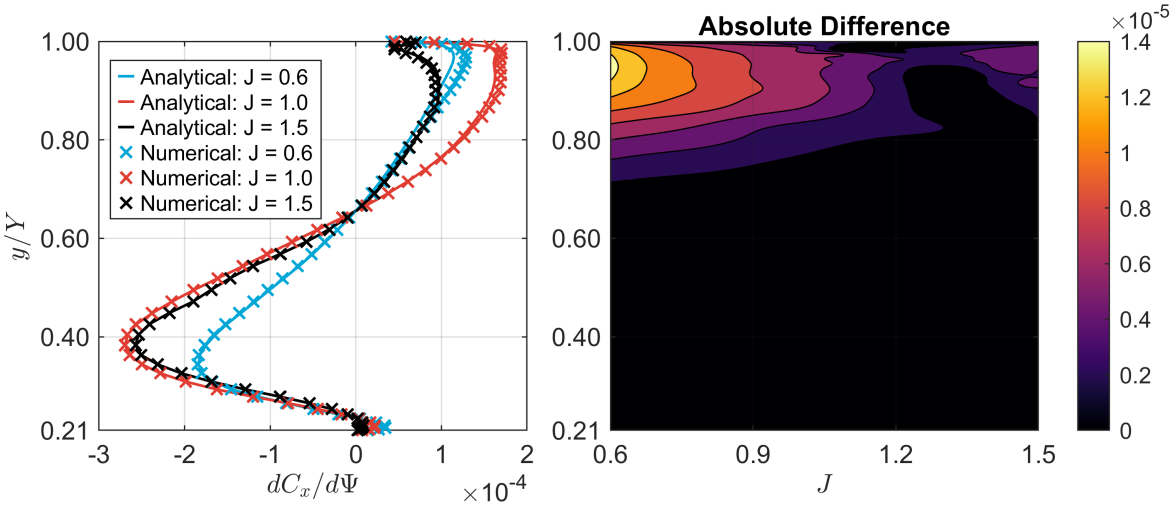

(a) Spanwise distribution of $dC_x/d\Psi$.

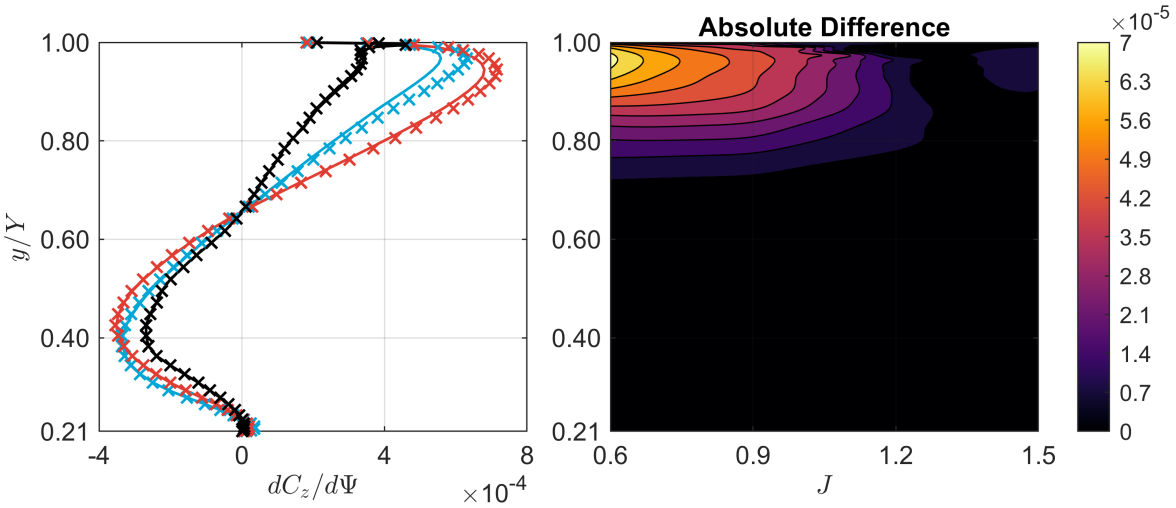

(b) Spanwise distribution of $dC_z/d\Psi$.

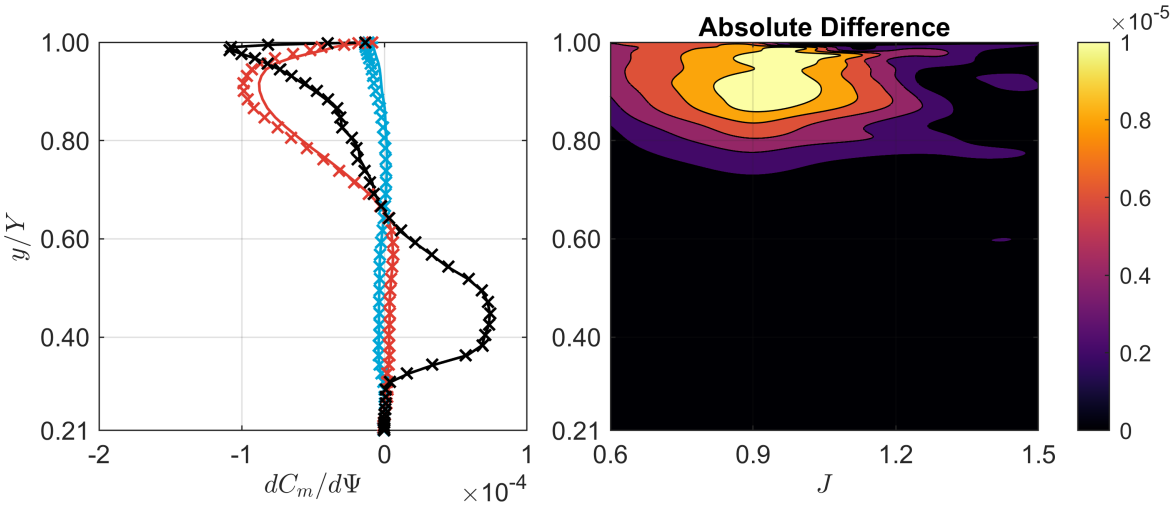

(c) Spanwise distribution of $dC_m/d\Psi$.

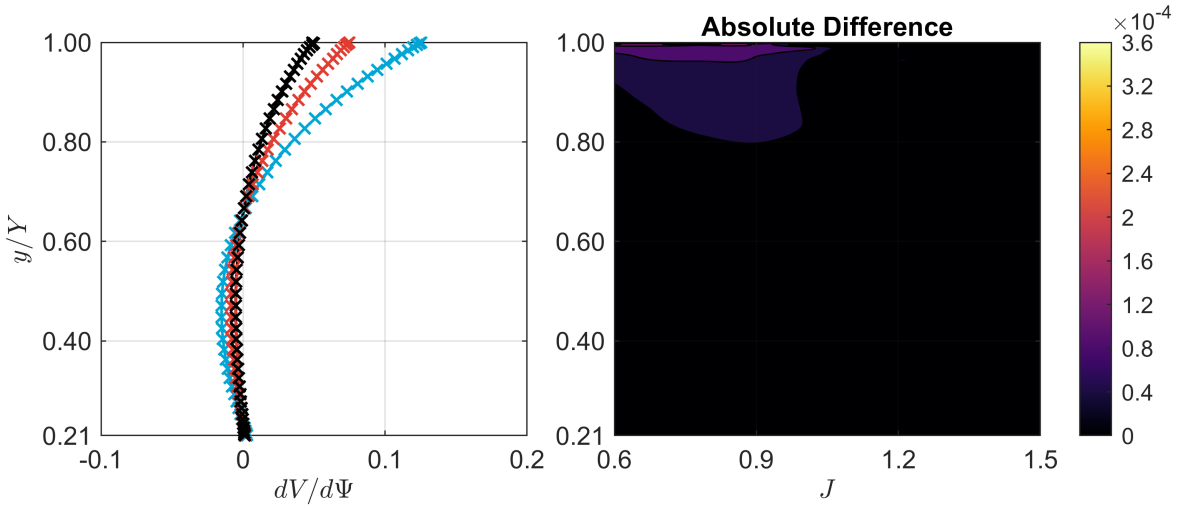

(d) Spanwise distribution of $dV/d\Psi$.

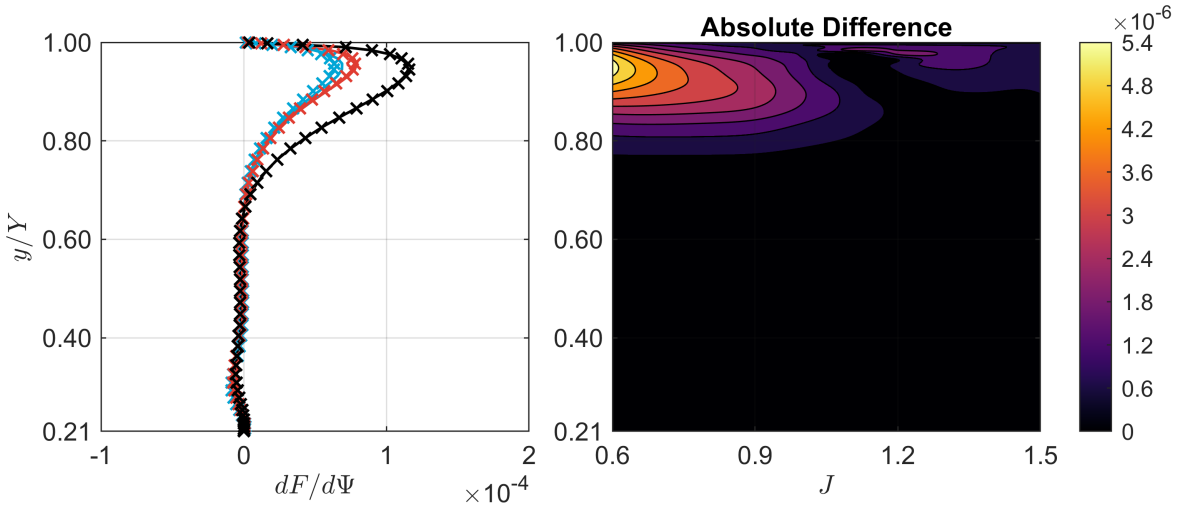

(e) Spanwise distribution of $dF/d\Psi$.

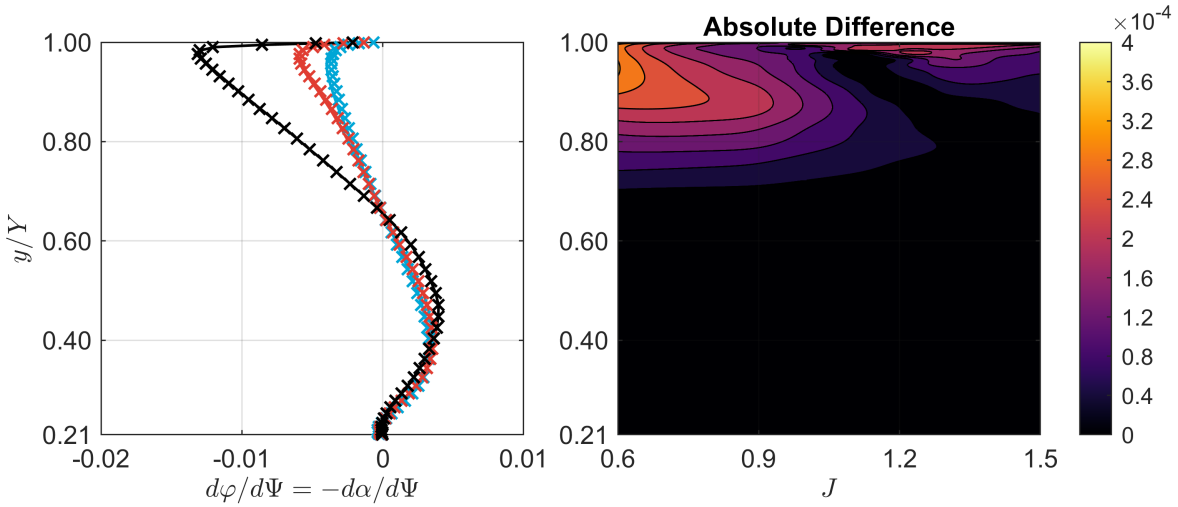

(f) Spanwise distribution of $d\varphi/d\Psi$.

Figure D.7: Comparison between the analytically and numerically computed lean sensitivities for the *XPROP*-Λ propeller at $\beta_{0.7R} = 20°$ and $V_\infty = 30$ m/s.

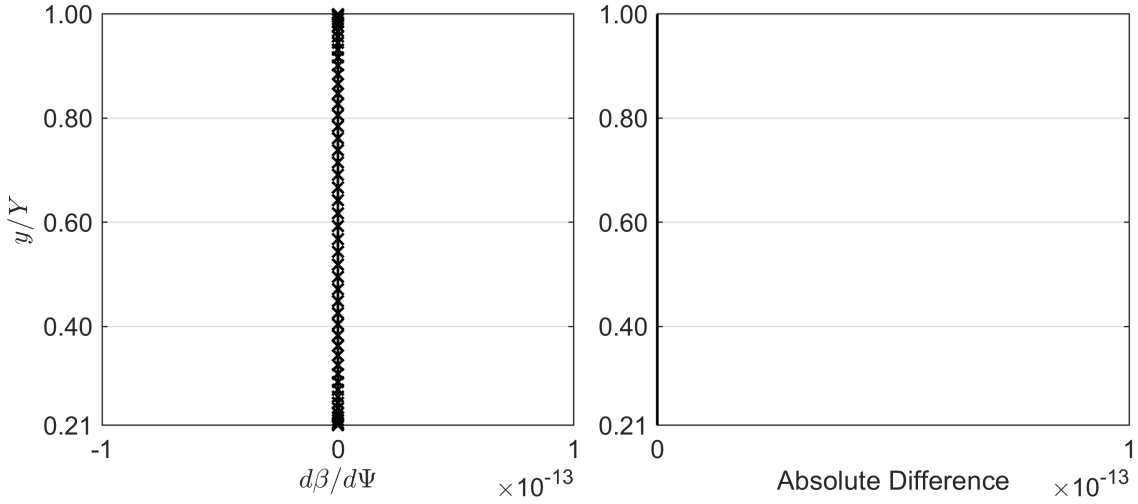

(a) Spanwise distribution of $d\beta/d\Psi$.

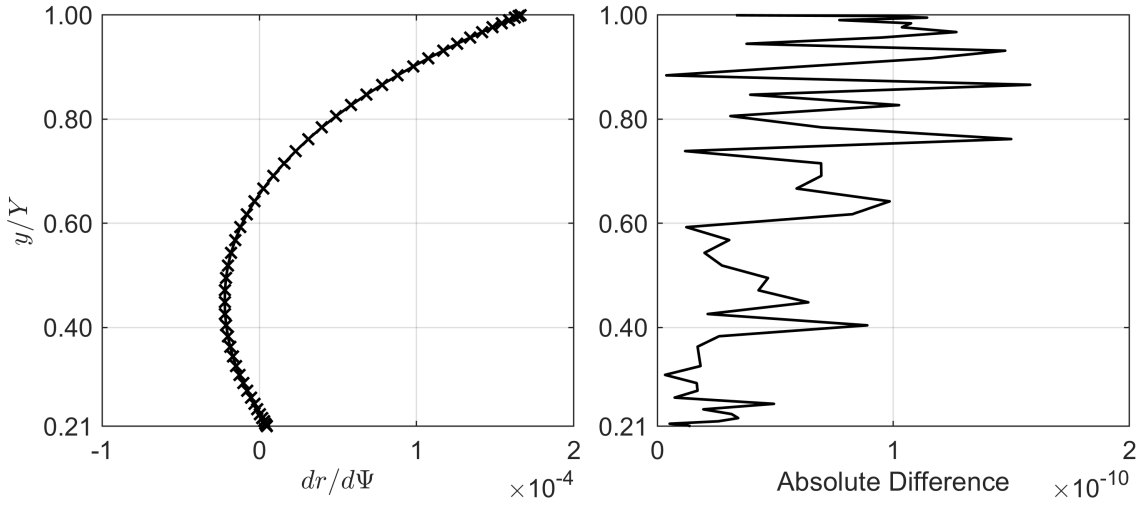

(b) Spanwise distribution of $dr/d\Psi$.

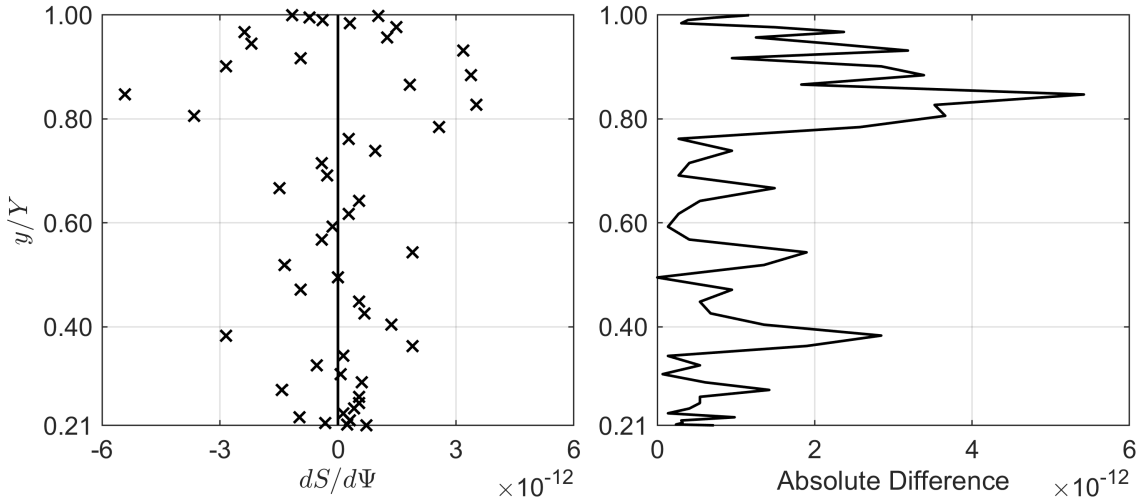

(c) Spanwise distribution of $dS/d\Psi$.

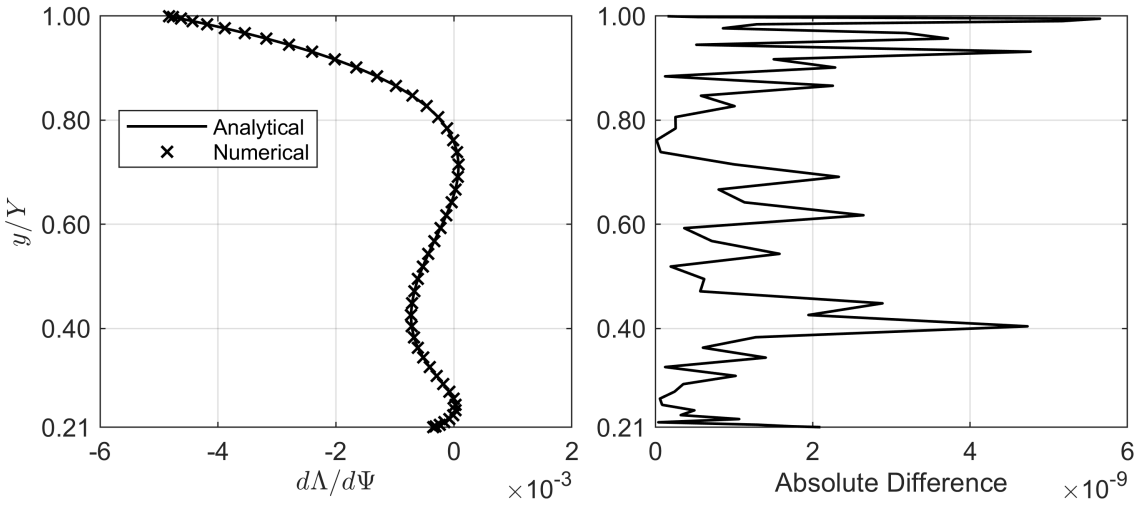

(d) Spanwise distribution of $d\Lambda/d\Psi$.

Figure D.8: Comparison between the analytically and numerically computed geometric lean sensitivities for the *XPROP*-Λ propeller at $\beta_{0.7R} = 20°$ and $V_\infty = 30$ m/s.

D.3. Radial Sensitivities

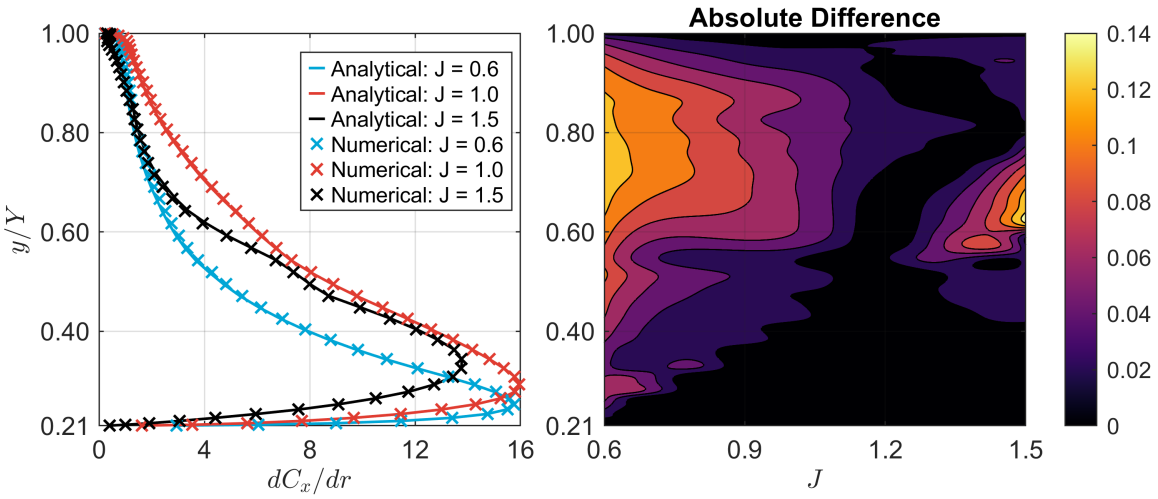

(a) Spanwise distribution of dC_x/dr.

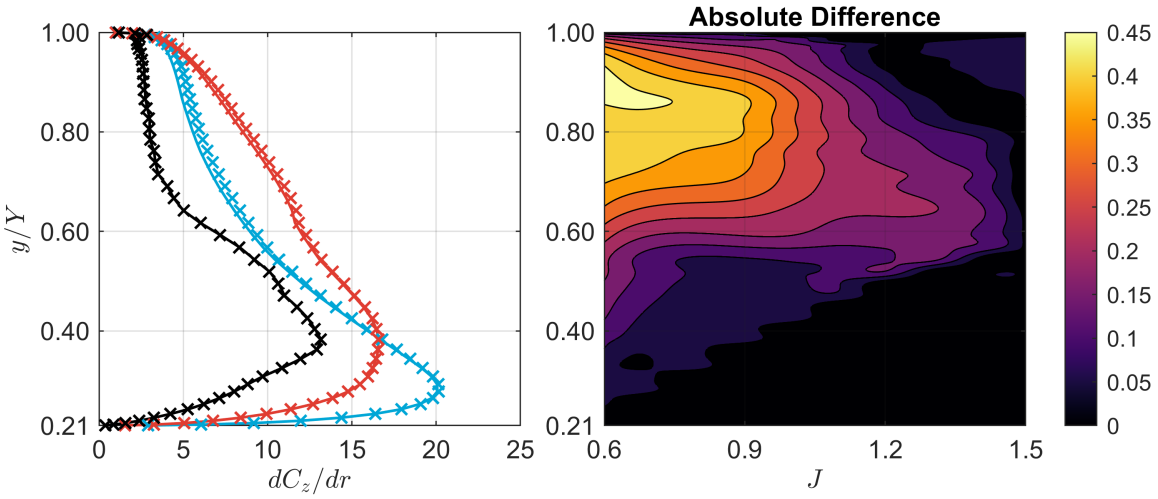

(b) Spanwise distribution of dC_z/dr.

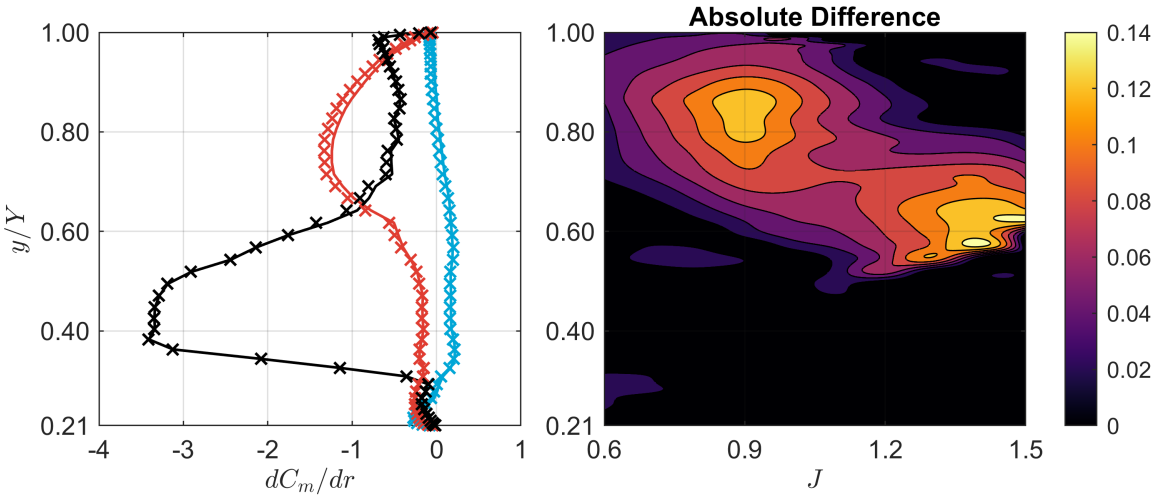

(c) Spanwise distribution of dC_m/dr.

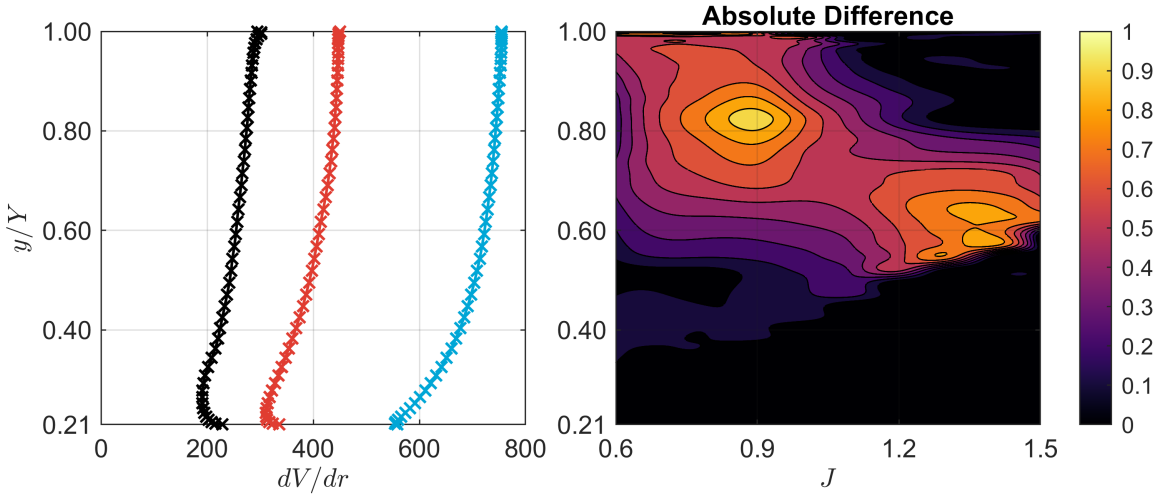

(d) Spanwise distribution of dV/dr.

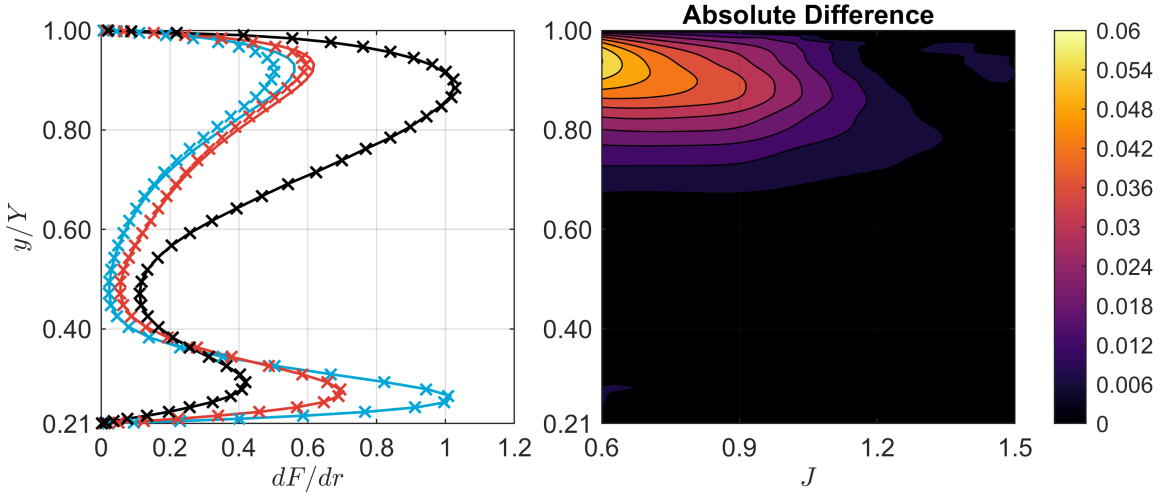

(e) Spanwise distribution of dF/dr.

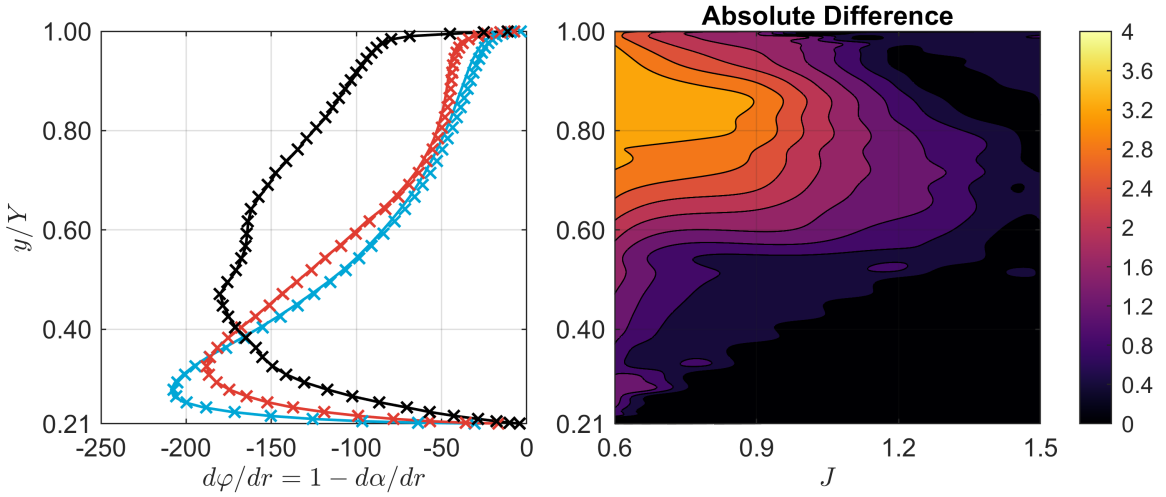

(f) Spanwise distribution of $d\varphi/dr$.

Figure D.9: Comparison between the analytically and numerically computed radial sensitivities for the *XPROP* propeller at $\beta_{0.7R} = 20°$ and $V_\infty = 30$ m/s.

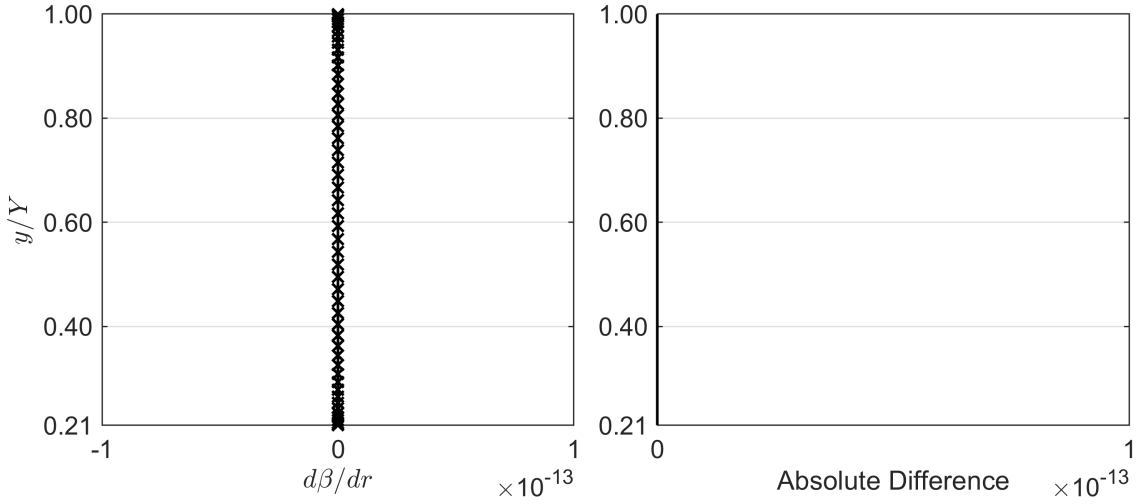

(a) Spanwise distribution of $d\beta/dr$.

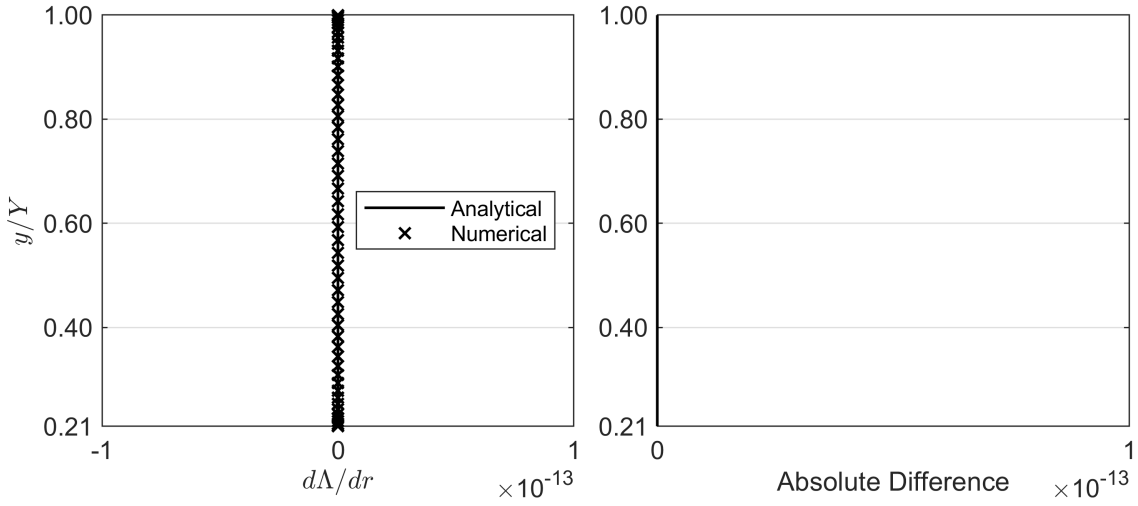

(b) Spanwise distribution of $d\Lambda/dr$.

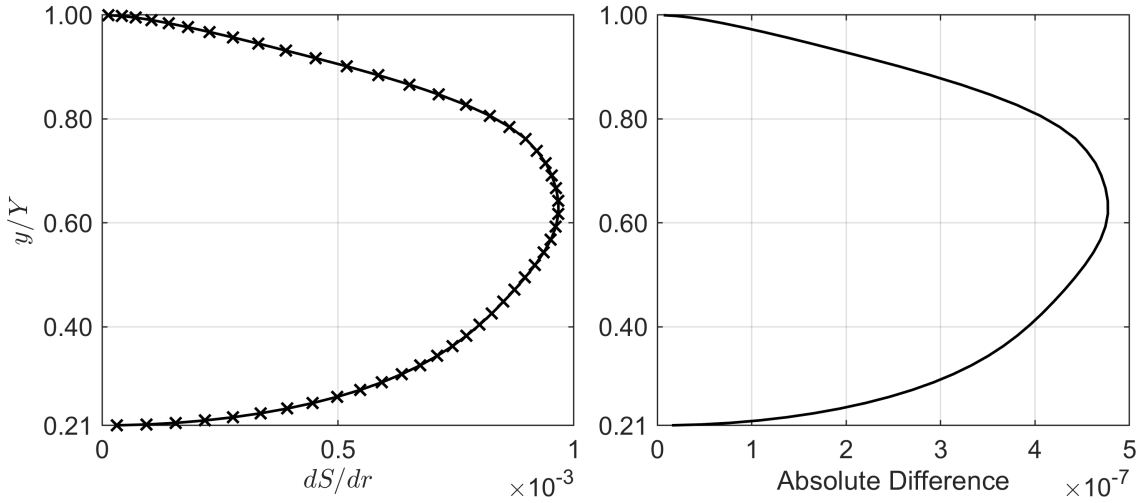

(c) Spanwise distribution of dS/dr.

Figure D.10: Comparison between the analytically and numerically computed geometric radial sensitivities for the *XPROP* propeller at $\beta_{0.7R} = 20°$ and $V_\infty = 30$ m/s.

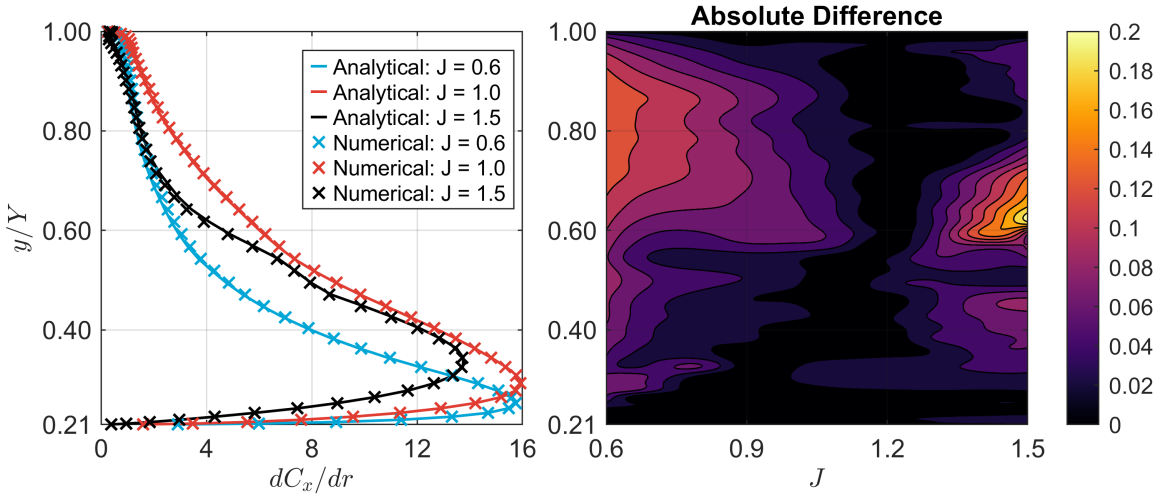

(a) Spanwise distribution of dC_x/dr.

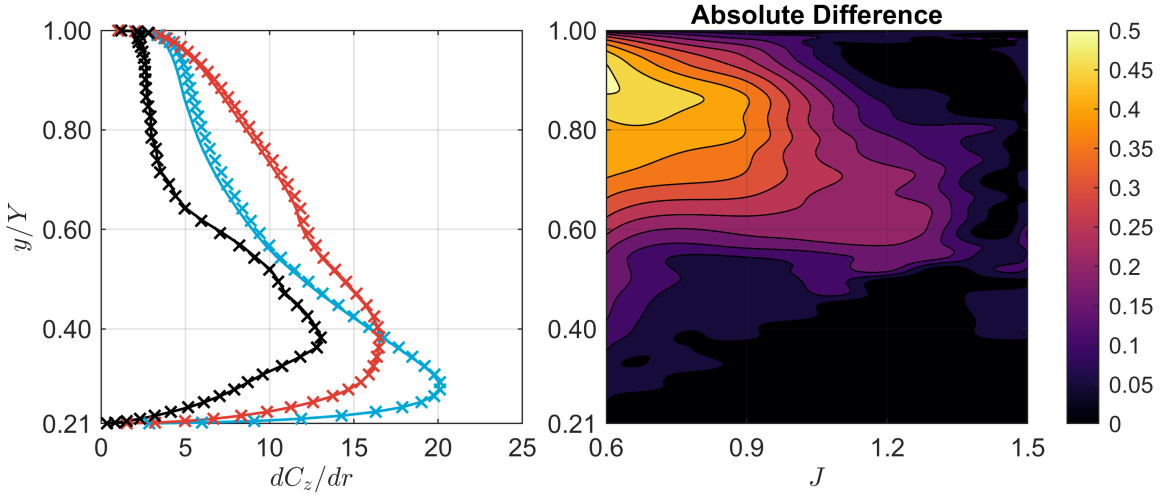

(b) Spanwise distribution of dC_z/dr.

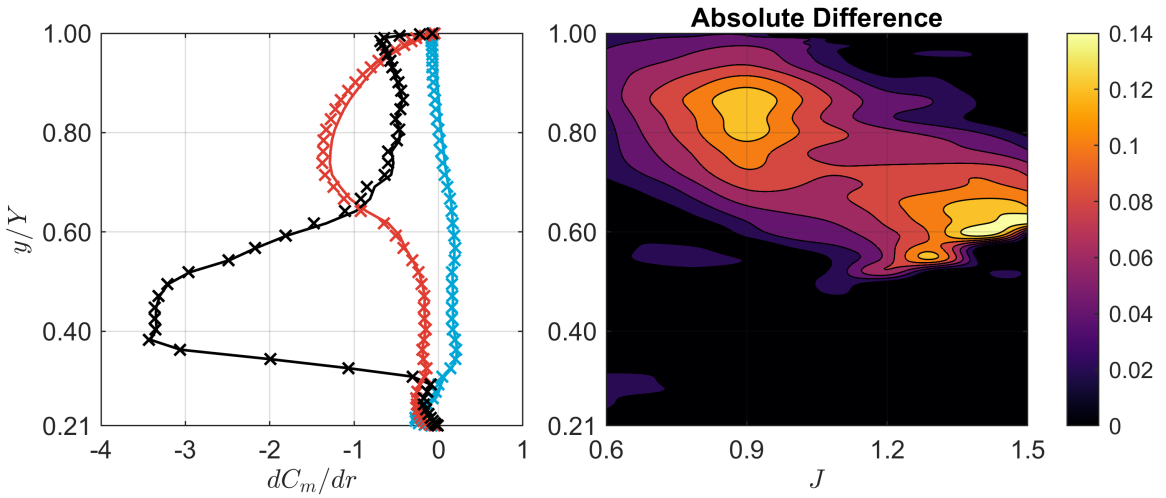

(c) Spanwise distribution of dC_m/dr.

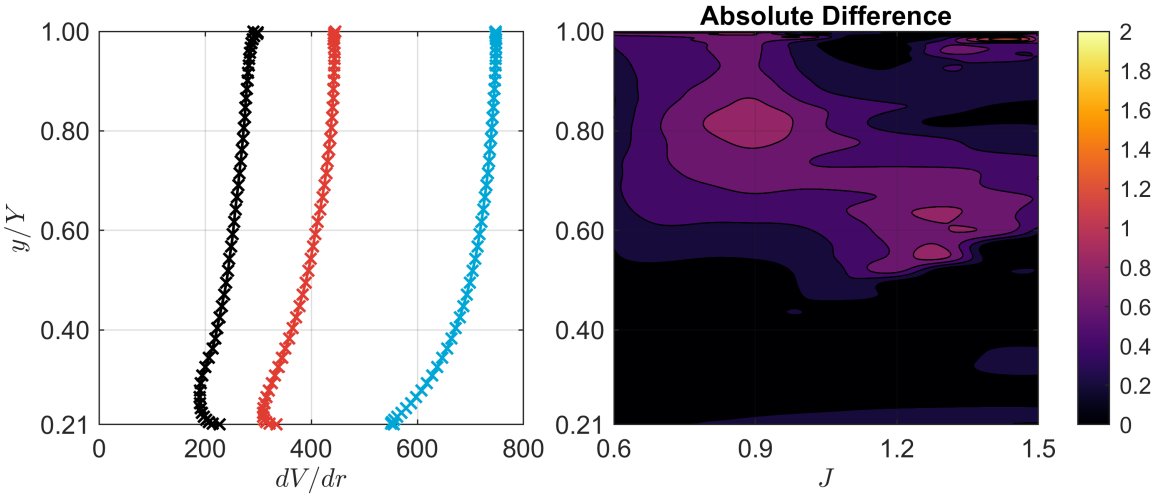

(d) Spanwise distribution of dV/dr.

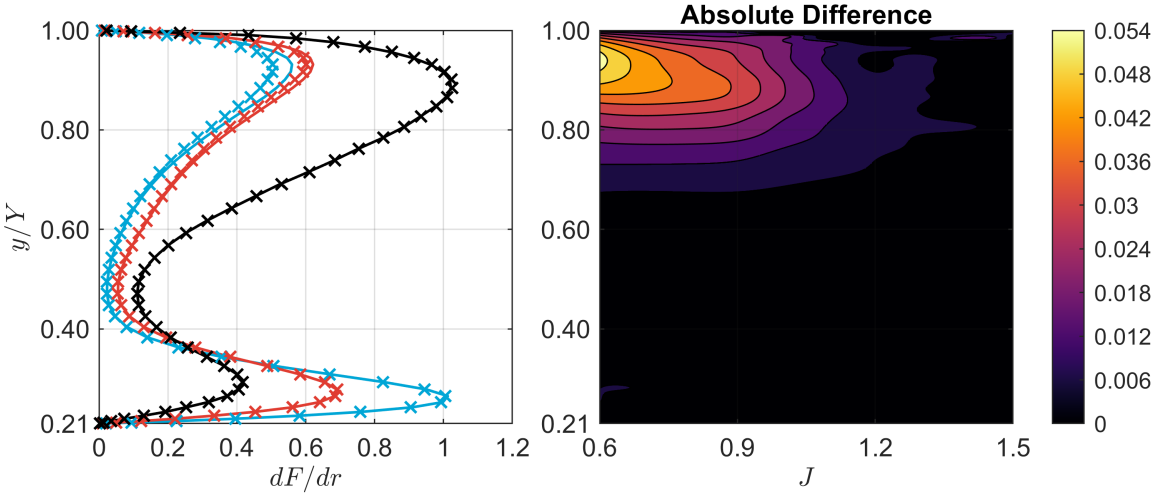

(e) Spanwise distribution of dF/dr.

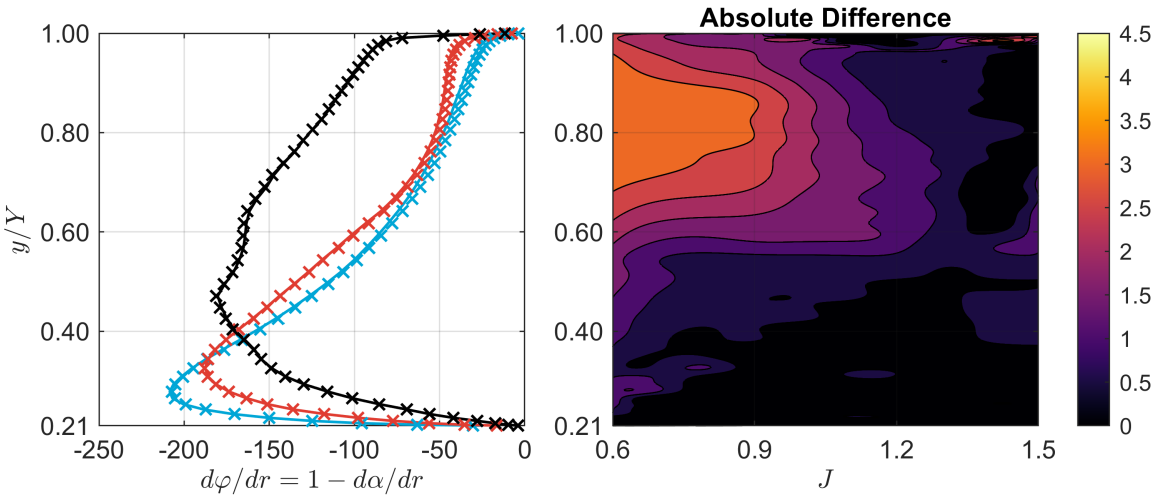

(f) Spanwise distribution of $d\varphi/dr$.

Figure D.11: Comparison between the analytically and numerically computed radial sensitivities for the *XPROP*-Λ propeller at $\beta_{0.7R} = 20°$ and $V_\infty = 30$ m/s.

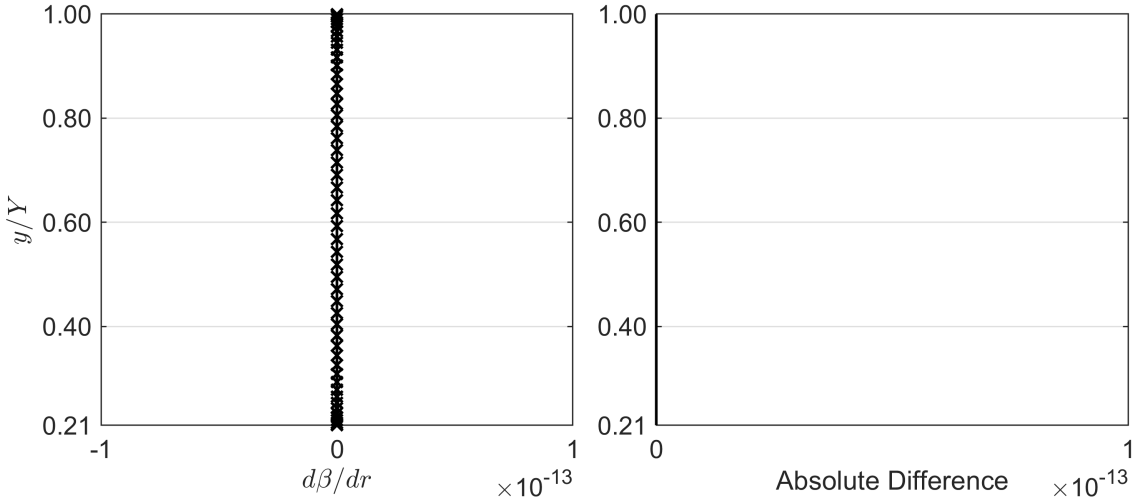

(a) Spanwise distribution of $d\beta/dr$.

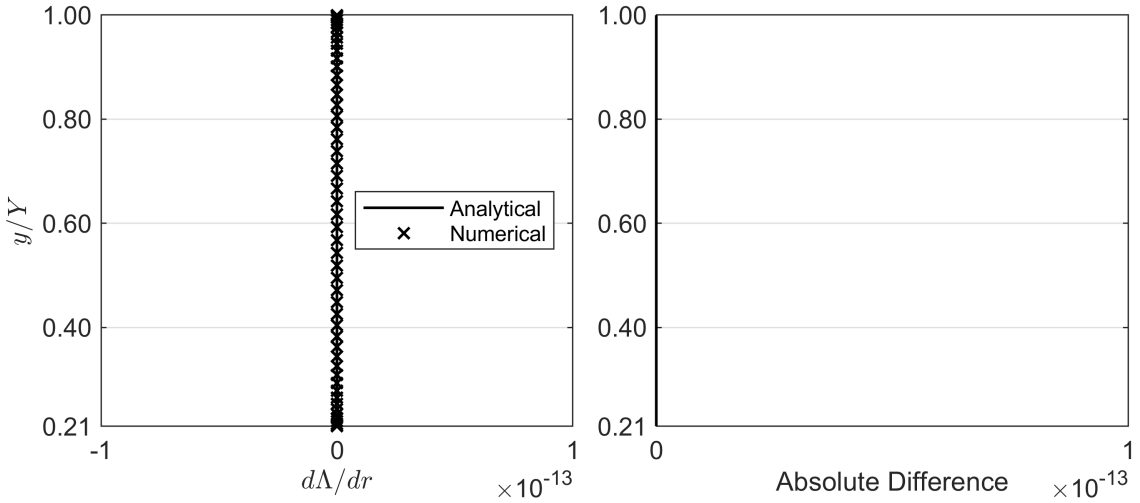

(b) Spanwise distribution of $d\Lambda/dr$.

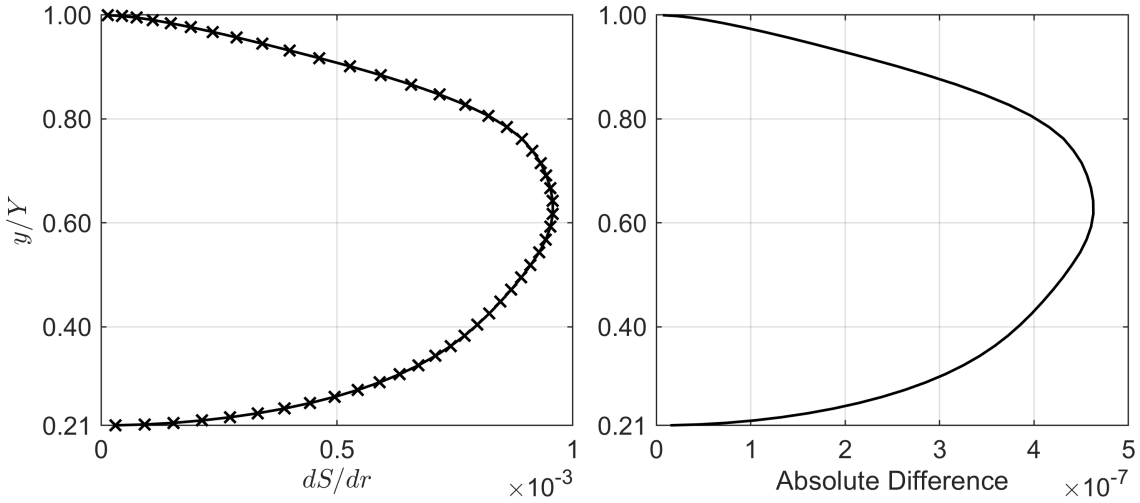

(c) Spanwise distribution of dS/dr.

Figure D.12: Comparison between the analytically and numerically computed geometric radial sensitivities for the *XPROP*-Λ propeller at $\beta_{0.7R} = 20°$ and $V_\infty = 30$ m/s.

E

Parametrization of Radially Distributed Design Variables

To represent a radially distributed design variable, a parametrization can be used to avoid the need to define numerous coordinate points along the blade span. Parametric curves offer several advantages in this context. First of all, they provide a flexible and efficient way to represent complex blade shapes using a small number of parameters, rather than a large set of coordinate points [50]. This makes parametric curves computationally efficient, which is important in design problems where computational time is a limiting factor. Second, because parametric curves are defined by basis functions, they inherently ensure smoothness of the curves which is essential to avoid infeasible designs. Lastly, parametric curves can facilitate constraint handling [51]. Since the curve is described by a set of control points, constraints can be applied directly by restriction of these points. This guarantees that the final design meets the requirements.

Various parametrization techniques have been developed to represent arbitrary complex curves by a minimum number of control points, some of which are outlined below. By applying these methods, the number of variables for the radially distributed QCA and FA in chapter 5 can be reduced significantly, while their distributions remain smooth and continuous.

E.1. Cubic Spline

Sodja et al. [5] implemented cubic splines to define the blade axis in polar coordinates.

$$\varphi(r) = \frac{\varphi_0}{2}\left(3\left(\frac{r - r_{\text{root}}}{r_{\text{tip}} - r_{\text{root}}}\right)^2 - \left(\frac{r - r_{\text{root}}}{r_{\text{tip}} - r_{\text{root}}}\right)^3\right) \tag{E.1}$$

$$z(r) = \frac{z_0}{2}\left(3\left(\frac{r - r_{\text{root}}}{r_{\text{tip}} - r_{\text{root}}}\right)^2 - \left(\frac{r - r_{\text{root}}}{r_{\text{tip}} - r_{\text{root}}}\right)^3\right) \tag{E.2}$$

In this case, φ_0 and z_0 are the parameters being optimized during the process. However, these curves cannot represent arbitrary complex shapes, as they are constrained to be either monotonically increasing or decreasing over the range $r \in [r_{\text{root}}, r_{\text{tip}}]$, depending on the sign of φ_0 and z_0.

E.2. 1-Cosine Curve

Möhren et al. [18] parametrized the quarter-chord line using a 1-cosine function.

$$x = x_{\text{tip}}\left(1 - \cos\left(\frac{\pi}{2}\frac{y}{y_{\text{tip}}}\right)\right) \tag{E.3}$$

The parameters x_{tip} and y_{tip} can be varied to adjust the curvature of the blade axis, but they also allow only monotonically increasing or decreasing geometries. This parametrization is applied only to sweep in the work of Möhren et al. [18], but it can also be used to model lean.

E.3. Power Law Function

A generic power law function to parametrize sweep was introduced by Thielen [6].

$$\frac{x}{R} = \frac{QCA_{\text{tip}}}{Y}\left(\frac{y}{R}\right)^{d\Lambda} + \kappa\left(\left(\frac{y}{R} - 0.5\right)^2 - 0.25\right) \tag{E.4}$$

Here, QCA_{tip} defines the tip offset of the quarter-chord line, $d\Lambda$ controls the curvature of the sweep distribution, and κ specifies the additional forward or backward sweep without affecting the tip sweep.

E.4. Bézier Curve

The Bézier curve is a widely used parametrization, constructed with Bernstein basis polynomials which serve as the basis functions of the parametric curve [52, 53]. A Bézier curve $\mathbf{C}(t)$ of degree *n* is defined by a set of *n+1* control points $P_0, P_1, ..., P_n$, also known as Bézier points, which determine the shape of the curve.

$$\mathbf{C}(t) = \sum_{i=0}^{n} \mathbf{P_i} B_{n,i}(t), \quad t \in [0,1] \tag{E.5}$$

$$B_{n,i}(t) = \binom{n}{i} t^i (1-t)^{n-i} \tag{E.6}$$

In 2D, each control point is defined by a set of (X,Y)-coordinates. The first and last control points, P_0 and P_n, specify the start and the end point of the curve, respectively, while the other control points typically do not lie on the curve. As previously mentioned, one of the advantages of parametric curves is the possibility to impose constraints to the design. For Bézier curves, this is achieved by restricting the coordinates of their control points, which ensures the design stays within the desired limits [13].

E.5. Parametrization Selection

The cubic spline and 1-cosine curve are not selected for further use, as they only allow either monotonically increasing or decreasing blade axis geometries. Since the Bézier curve can parametrize the same sweep and lean distributions as the power law parametrization of Thielen [6], the more generic Bézier curve is the selected parametrization method in this work. What remains is to verify whether these curves can accurately parametrize propeller blade geometries. Fortunately, Bézier curves are used extensively in literature. Margalida et al. [16] used them in their optimization study to describe radial distributions of geometric variables along the blade span. Geng et al. [11] successfully determined the radial distribution of sweep using a 4^{th} degree Bézier curve, as shown in Figure 1.2. Furthermore, Bézier curves were successfully applied by Burger [33], Gruijl [54], Keil [13] and Shen et al. [55].

Finally, Haan [20] conducted an error analysis on the Bézier parametrization of *XPROP*, in which, among other parameters, the chord distribution was specified at 25 radial positions along the blade span. His study evaluated how accurately the Bézier curve approximates the blade shape at these positions. With a maximum error for non-dimensional chord of approximately $2 \cdot 10^{-6}$, which corresponds to a chord discrepancy of 0.0001 mm [20], it can be concluded that the Bézier curve is able to parametrize the blade geometry accurately. Therefore, the Bézier curve can be used with confidence as the parametric curve for this work.

F

Additional Parameter Study Results

This appendix presents additional results from the parameter study on structural behaviour of flexible blades, as discussed in section 5.4. First, the maximum failure index based on Tsai-Wu failure theory is provided across the parameter space for both the leading edge and trailing edge spars in Figure F.1. Next, additional outcomes for an increased thrust setting of 100 N are shown, illustrating the blade's principal and shear strain in Figure F.2, which allows for a comparison with the 50 N operating condition.

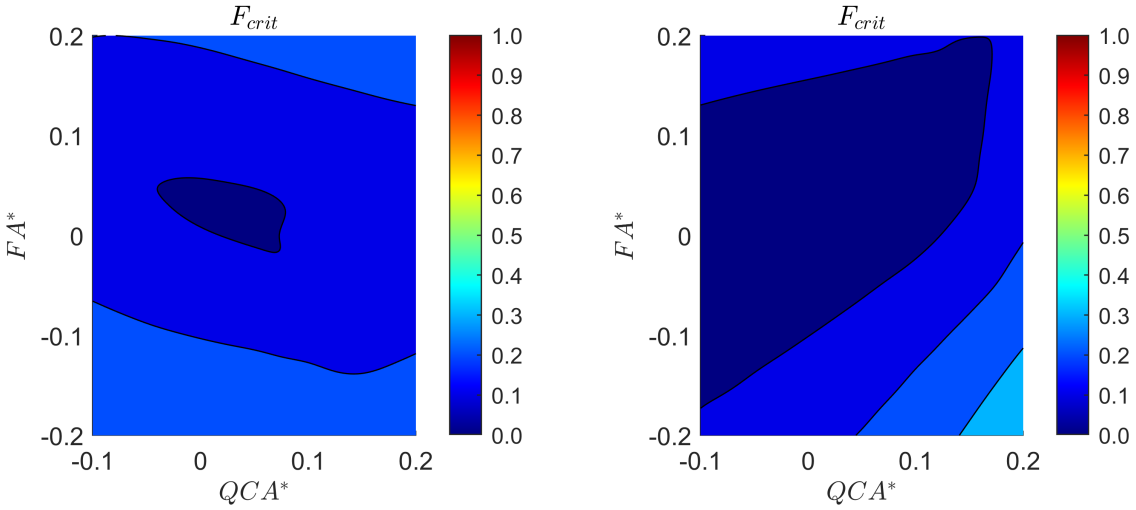

(a) Leading edge spar.

(b) Trailing edge spar.

Figure F.1: Maximum failure index for the leading edge and trailing edge spar laminates at a thrust of 50 N.

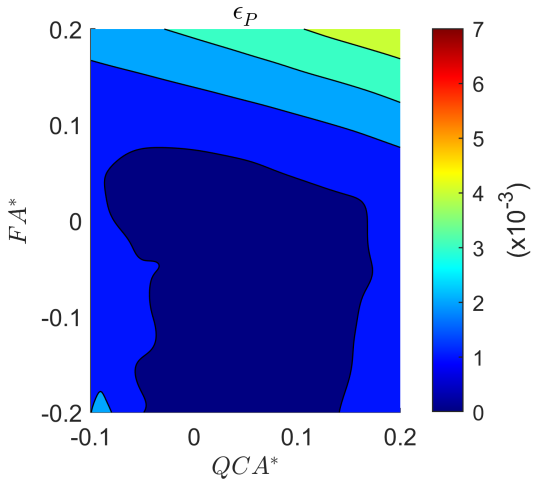

(a) Top skin principal strain.

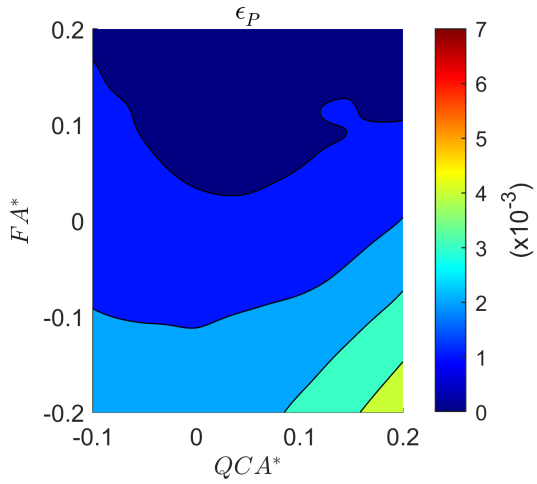

(b) Bottom skin principal strain.

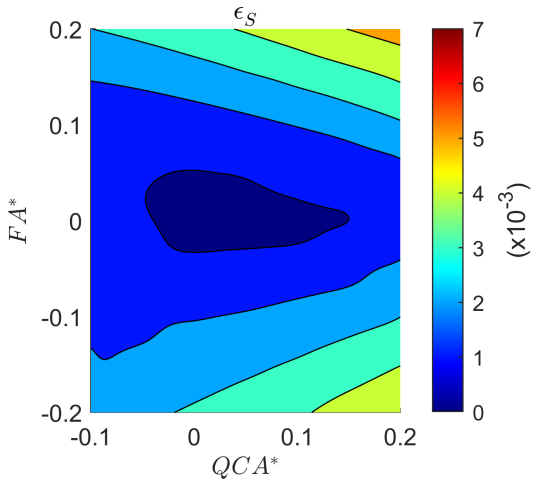

(c) Top skin shear strain.

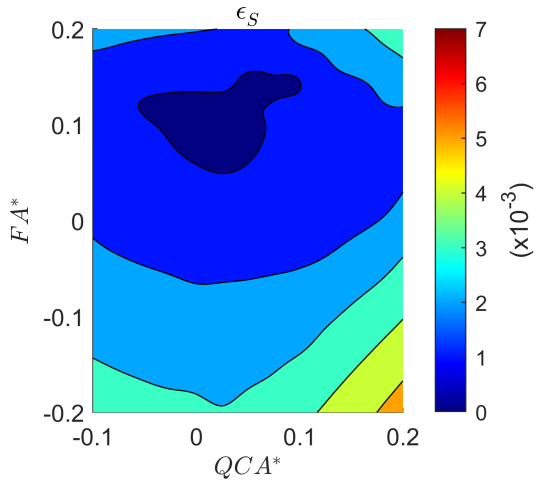

(d) Bottom skin shear strain.

Figure F.2: Strain at the location of maximum F_{crit} for a thrust setting of 100 N.